MSc Thesis

Investigation of the Effects of Steam Injection on NO_x Emissions in Hydrogen-Methane Blend Flames

Doruk Çelebi



TU Delft

MSc Thesis

Investigation of the Effects of Steam Injection on NO_X Emissions in Hydrogen-Methane Blend Flames

by

Doruk Çelebi

to obtain the degree of Master of Science
at the Delft University of Technology
to be defended publicly on 27th of October, 2025

Responsible Supervisor: Dr. Francesca De Domenico
Student number: 5332427

Faculty of Aerospace Engineering · Delft University of Technology



Copyright © Doruk Çelebi, 2025
All rights reserved.

Contents

List of Figures iv

List of Tables vii

Table of Symbols . . . 1

Abstract 4

1 Introduction 5
- 1.1 Characteristics of Conventional and Alternative Fuels . . . 6
- 1.2 Nitrogen Oxides in Combustion . . . 8
- 1.3 Strategies for NO_x Mitigation . . . 13

2 Behaviour and Characterisation of Hydrogen Flames 15
- 2.1 Flame Structure . . . 15
- 2.2 Temperature field and peak flame temperature . . . 19
- 2.3 Laminar flame speed . . . 21

3 Water/Steam Injection in Combustion 24
- 3.1 Steam and Water Injection: Mechanisms of NO_x Suppression . . . 24
- 3.2 Steam & Water Injection in Literature . . . 26

4 Research Proposal 31
- 4.1 Problem Definition . . . 31
- 4.2 Research Gap . . . 31
- 4.3 Research Objective and Research Questions . . . 32

5 Experimental Set-Up 34
- 5.1 Vertical Burner Set-Up . . . 34
- 5.2 Operating Range and Equivalence Ratio Determination . . . 40
- 5.3 Steam Injection Mechanism . . . 42

6 Measurement Techniques 49
- 6.1 Gas Analyzer System . . . 49
- 6.2 UV Camera . . . 50
- 6.3 DSLR Camera . . . 51

7 Methodology, Test Matrix & Experimental Points 53
- 7.1 Estimation of Adiabatic Flame Temperature and Laminar Flame Speed using Cantera . . . 53
- 7.2 Uncertainty Quantification . . . 54
- 7.3 Experimental Point Selection . . . 56

8 Data Processing 64
- 8.1 Statistical Approach for Data Accuracy . . . 64
- 8.2 Gas Analyzer Measurements in Dry and Wet Conditions . . . 67
- 8.3 Result Validation and Variability Analysis . . . 69
- 8.4 Emission Indices and Normalization (EINO, EICO O_2) . . . 71
- 8.5 UV Camera Processing . . . 75

9 Results 76
- 9.1 Simplified Estimation of Temperature and NO Reduction Due to Steam Injection . . . 76
- 9.2 Series A: Variation of Burner Power . . . 80
- 9.3 Series B: Variation of Blend Percentage . . . 91
- 9.4 Series C: Variation in Steam Injection Amount . . . 100
- 9.5 Series D: Variation in Steam Injection Location . . . 111

10 Discussion **127**

11 Conclusion & Recommendations **132**
11.1 Conclusion 132
11.2 Recommendations 134

References **143**

A Appendix: Additional Document **144**

B Appendix B: Steam Generator Characterization Experiment **158**

List of Figures

2.1 Curvature–diffusion schematic for lean premixed flames with $Le < 1$. Red arrows indicate heat diffusion, black arrows indicate fuel mass diffusion. Curvature is defined as $\kappa > 0$ for a front convex toward the reactants and $\kappa < 0$ for a front concave toward the reactants, and for $Le < 1$ the convex cusps are locally fuel-enriched while the concave troughs are fuel-depleted. The schematic summarises behaviour observed in laminar H_2/CH_4/air polyhedral (Bunsen-type) flames at atmospheric pressure with 50–83% H_2, $\phi = 0.53$–0.64, and bulk velocities 1.65–2.50 m s^{-1}, where cusps are enriched and troughs depleted due to differential diffusion [44]. 16

2.2 OH mole-fraction fields as reaction-zone markers for lean premixed flames at matched conditions. Panel (a) CH_4/air with $Le \approx 1$, panel (b) H_2/air with $Le < 1$. The hydrogen case shows a thinner reaction layer and pronounced cellular corrugations, consistent with thermo-diffusive imbalance. Fields reproduced from modelling of CH_4/H_2/air flames that includes stretch, heat loss and non-unity Le, applied to an atmospheric bluff-body-stabilised configuration [45]. 16

2.3 Instantaneous (left halves) and time-averaged (right halves) OH-PLIF for a premixed bluff-body/swirl burner at $U_{\text{in}} = 6$ m s^{-1} and $\phi = 0.6$, for swirl numbers $S = 0,\ 0.42,\ 0.73$ and hydrogen volume fractions $\eta_{H_2} = 0$–30% [46]. Increasing η_{H_2} produces a thinner, more corrugated reaction layer consistent with $Le < 1$ effects, while higher S strengthens large-scale shear/recirculation. The instantaneous frames show finer cellular structure at larger η_{H_2}, and the time-averaged frames indicate a broader flame brush at higher S. OH-PLIF is used here as a qualitative marker of the reaction zone; quantitative wrinkling would require front extraction and flame-surface-density analysis. 18

2.4 Schematic of a premixed swirl combustor showing the inner recirculation zone (IRZ) produced by vortex breakdown, and the inner and outer shear layers (ISL, OSL). Hot products in the IRZ recirculate upstream and ignite the incoming reactants along the ISL, which is the primary attachment line. In lean hydrogen flames, larger s_L, smaller δ_L, and sub-unity Le bias attachment closer to the ISL and reduce lift-off at a given bulk flow, which also tightens flashback margin. [47]. 19

2.5 Adiabatic flame temperature T_{ad} versus equivalence ratio ϕ for CH_4/air, H_2/air, and CO/air at $p = 1$ bar and $T_{\text{in}} \approx 300$ K. Hydrogen reaches higher T_{ad} than methane over lean to slightly rich conditions, consistent with a product slate dominated by H_2O and different dissociation behaviour relative to CO_2–rich hydrocarbon products. Figure adapted from ScienceDirect Topics [50]. 20

2.6 NOx emissions in ppm vs equivalence ratio and hydrogen content for a CH4/ H2 blend reacting with air [51] 21

2.7 Laminar burning velocity s_L versus equivalence ratio at $T_u \approx 295$ K and $p = 1$ bar, compiled from multiple studies [56]. Note the different vertical units, m/s for hydrogen and cm/s for methane. The non-monotonic dependence on ϕ and the substantially higher s_L for H_2 are evident across datasets. 22

5.1 Combustor set-up and operation location [78]. 34

5.2 Combustion chamber with ventilation hood and gas rack [78]. 34

5.3 Vertical combustor lab set-up without the steam injection mechanism. 35

5.4 Swirler with Swirl Number S_w = 1.1 [78] 36

5.5 Injector schematic showing the injection points of the air and the fuel 36

5.6 Connections to the baseplate 36

5.7 Pilot burner attached to the base plate of the main burner. 37

5.8 Top view of the steel baseplate. 37

5.9 Underside of the steel baseplate. 37

5.10 Exploded view of the main combustor assembly. 38
5.11 Gas rack used for methane and hydrogen distribution. The fuels are stored outside the building in cylinder bundles for safety. 38
5.12 Physical control panel of the combustor set-up. 39
5.13 LabView interface for setting and monitoring operating conditions. 40
5.14 The stability regime of the vertical combustor at 12 kW burner power. The x-axis denotes the hydrogen mole fraction while the y-axis denotes the equivalence ratio. Left figure is with 0 axial air injection, the right figure is with 20% AAI (denoted as χin the figures) [80] 41
5.15 The steam generator without the lid 44
5.16 The steam generator with the lid 44
5.17 Schematic of the water spray atomizer [86] 45
5.18 Picture of the unmodified atomizer 45
5.19 The atomizer after it has been drilled and modified for the steam set-up 45
5.20 Schematic of side steam injection configuration 46
5.21 Schematic of axial steam injection configuration 46
5.22 Detailed Schematic of the burner 46
5.23 Assembly test for the burner set-up 47
5.24 Vertical combustor set-up with the feed lines named. Side steam injection configuration present 48
5.25 Wide-view of the vertical combustor set-up with side injection configuration 48

6.1 Sampling port of the gas analyzer 49
6.2 Locations of cameras used in the lab set-up 51
6.3 Line of sight of cameras with respect to the combustion chamber and steam injection ports 52

9.1 Experiment-A1: NO (dry) vs burner power for 100% H_2 with and without side steam injection (Steam 9 = 24.4 g/min). The upper axis shows the corresponding equivalence ratio ϕ. . . . 80
9.2 Experiment-A1: Emission index of NO (EINO, mass basis) as a function of burner power for 100% H_2 combustion with and without side steam injection (Steam 9 = 24.4 g/min). The upper axis indicates the corresponding equivalence ratio ϕ. 82
9.3 Experiment-A2: NO (dry) vs burner power for 100% CH_4 with and without side steam injection (Steam 9 = 24.4 g/min). 84
9.4 Experiment-A2: NO (dry) vs equivalence ratio for 100% CH_4 with and without side steam injection (Steam 9 = 24.4 g/min). Point annotations indicate burner power. 84
9.5 Flame images for pure CH_4 combustion at constant equivalence ratio of 0.798 with varying burner power. No steam injection is used. 85
9.6 Experiment A2. Comparison of derived emission indices (EINO and EICO) on a mass basis for steam and non-steam cases. 88
9.7 Flame photographs for pure CH_4 combustion at 10.5 kW (top row) and 7.5 kW (bottom row), comparing no-steam (left) and Steam-9 (right) [=24.4 g/min steam] conditions (side steam injection). The images highlight differences in flame luminosity, shape, and flow field between operating points. 89
9.8 Experiment-B1: NO (dry) vs H_2 blend fraction at 11 kW with and without side steam injection (Steam 9 = 24.4 g/min). The upper axis shows the corresponding equivalence ratio ϕ. . . . 92
9.9 Experiment B1. Comparison of derived emission indices (EINO and EICO) on a mass basis for steam and non-steam cases. 94
9.10 Flame images for pure CH_4 and 80% H_2 cases at 11 kW, with and without side steam injection (Steam-9 = 24.4 g/min). 95
9.11 Experiment-B2: NO (dry) vs H_2 blend fraction at 9 kW with and without side steam injection (Steam 9 = 24.4 g/min). The upper axis shows the corresponding equivalence ratio ϕ. . . . 96
9.12 Experiment B2. Comparison of derived emission indices (EINO and EICO) on a mass basis for steam and non-steam cases. 98
9.13 Comparison of EINO (mass basis, g/kg fuel) between Experiment B1 (11 kW) and Experiment B2 (9 kW) for varying H_2 fuel fractions under no-steam and Steam-9 conditions. . . . 99
9.14 Comparison of EICO (mass basis, g/kg fuel) between Experiment B1 (11 kW) and Experiment B2 (9 kW) for varying H_2 fuel fractions under no-steam and Steam-9 conditions. . . . 99

9.15 Experiment-C1: NO (dry) vs H_2 blend fraction at 10 kW with and without side steam injection (Steam 7 = 17.7 g/min; Steam 9 = 24.4 g/min). The upper axis shows the corresponding equivalence ratio ϕ. 102
9.16 Experiment C1. Comparison of derived emission indices (EINO and EICO) on a mass basis for various steam injection cases. 104
9.17 Experiment-C2: NO (dry) vs H_2 blend fraction at 10 kW with and without side steam injection (Steam 6 = 13.7 g/min; Steam 7 = 17.7 g/min; Steam 8 = 22.8 g/min; Steam 9 = 24.4 g/min). The upper axis shows the corresponding equivalence ratio ϕ. 106
9.18 Experiment C2. Comparison of EINO on a mass basis for various steam injection cases. . 108
9.19 Experiment C2. Comparison of EICO on a mass basis for various steam injection cases. . 108
9.20 UV imaging of 10 kW 40% H2 blend flame under different steam injection settings. 109
9.21 UV imaging of 10 kW 60% H2 blend flame under different steam injection settings. 109
9.22 UV imaging of 10 kW 80% H2 blend flame under different steam injection settings. 110
9.23 Experiment-D1: NO (dry) vs H_2 blend fraction at 10 kW with and without axial steam injection (Steam 6 = 13.7 g/min; Steam 7 = 17.7 g/min; Steam 8 = 22.8 g/min; Steam 9 = 24.4 g/min). The upper axis shows the corresponding equivalence ratio ϕ. 113
9.24 Percentage reduction in NO emissions with Steam-7 (17.7 g/min) and Steam-9 (24.4 g/min) injection compared to the no-steam case, for D1 (axial) and C-series average (C1 and C2, side steam injection). Steam-7 cases are shown with dashed lines, while Steam-9 cases are solid. Constant 10 kW burner power 115
9.25 UV imaging at 10 kW, 40% H_2: axial (top row) vs side (bottom row) steam injection from No-Steam to Steam-9. 116
9.26 UV imaging at 10 kW, 60% H_2: axial (top row) vs side (bottom row) steam injection from No-Steam to Steam-9. 117
9.27 UV imaging at 10 kW, 80% H_2: axial (top row) vs side (bottom row) steam injection from No-Steam to Steam-9. 118
9.28 Abel-inverted UV imaging of a 10 kW flame with 40% H_2 blend under different axial steam injection settings. 120
9.29 Abel-inverted UV imaging of a 10 kW flame with 60% H_2 blend under different axial steam injection settings. 121
9.30 Abel-inverted UV imaging of a 10 kW flame with 80% H_2 blend under different axial steam injection settings. 121
9.31 Experiment D1. Comparison of EINO on a mass basis for various steam injection cases. . 123
9.32 DSLR camera images of flame fronts for H_2 blends from 10% to 100%, each shown under No Steam and Steam 9 injection conditions. Side steam injection was used. Steam addition influences flame luminosity and shape across the hydrogen blending range. 125

B.1 Experimental set-up to characterize the performance of the steam generator 158
B.2 Placement of the thermometer on the silicone hose 159
B.3 K-Type thermometer 1319A 159

List of Tables

1 List of Symbols, Qualifiers, and Abbreviations 1

5.1 Overview of flow controllers and sensors used in the setup [82]. 39
5.2 Definition of Variables Used in the Equivalence Ratio and Fuel Properties Calculations . . . 42

6.1 Working uncertainties (post-calibration), based on analyzer specifications and observed repeatability. 50

7.1 Full-scale values of the gas flow controllers of the main burner 55
7.2 Test matrix for Experiment-A1. 100% H_2 combustion with varying burner power. Side steam injection configuration was used. 56
7.3 Test matrix for Experiment-A2. 100% CH_4 combustion with varying burner power. Side steam injection configuration was used. 57
7.4 Test matrix for Experiment-B1. Constant 11 kW burner with varying blend percentage. Side steam injection configuration was used. 58
7.5 Test matrix for Experiment-B2. Constant 9 kW burner with varying blend percentage. Side steam injection configuration was used. 59
7.6 Test matrix for Experiment-C1. Constant 10 kW burner power with varying steam injection setting and H_2 blend fraction. Side steam injection configuration was used. 60
7.7 Test matrix for Experiment-C2. Constant 10 kW burner power with varying steam injection setting and H_2 blend fraction. A wider range of steam settings were used compared to previous experiments. Side steam injection configuration was used. 61
7.8 Test matrix for Experiment-D1. Constant 10 kW burner power with varying steam injection setting and H_2 blend fraction. Axial steam injection configuration was used. 62

8.1 Comparison of NO Concentrations Across Repeated Experiments (10 kW, Steam 9 vs. No-Steam) 70
8.2 Comparison of O_2 Concentrations Across Repeated Experiments (10 kW) 71

9.1 Estimated NO_{wet} for steam injection of 24.4 g/min (Steam-9) across T_{ad} and β. 78
9.2 Estimated NO_{wet} for steam injection of 17.7 g/min (Steam-7) across T_{ad} and β. 78
9.3 NO emissions and background O_2 for Experiment A1. 100% H_2 combustion with varying burner power. Side steam injection configuration was used. Values reported on a dry basis; analyzer wet readings are shown in parentheses. Dry conversion via Equation 8.5. 80
9.4 Experiment A1. Derived NO metrics (*dry*). NO values were normalized to 15% O_2 using Eq. (8.16). 81
9.5 NO emissions for Experiment A2. 100% CH_4 combustion with varying burner power. Side steam injection configuration was used. Values reported on a dry basis; analyzer wet readings are shown in parentheses. Dry conversion via Equation 8.5. 83
9.6 Full emissions for Experiment A2. 100% CH_4 combustion with varying burner power. Values reported on a *dry* basis for NO; analyzer wet readings are shown in parentheses. O_2, CO, CH_4, and CO_2 are measured dry by the analyzer. Dry conversion via Equation 8.5. Side steam injection configuration was used. 86
9.7 Experiment A2. O_2 normalized and derived NO and CO metrics (*dry*) as described in Section 8.4 87
9.8 NO emissions for Experiment B1. Constant 11 kW burner power with varying H_2 fuel fraction. Side steam injection configuration was used. Values reported on a dry basis; analyzer wet readings are shown in parentheses. Dry conversion via Equation 8.5. 91

9.9 Full emissions for Experiment B1. Constant 11 kW burner power with varying H_2 fuel fraction. Values reported on a *dry* basis for NO; analyzer wet readings are shown in parentheses. O_2, CO, CH_4, and CO_2 are measured dry by the analyzer. Dry conversion via Equation 8.5. Side steam injection configuration was used. 93
9.10 Experiment B1. O_2-normalized and derived NO and CO metrics (*dry*) as described in Section 8.4. 94
9.11 NO emissions for Experiment B2. Constant 9 kW burner power with varying H_2 fuel fraction. Side steam injection configuration was used. Values reported on a dry basis; analyzer wet readings are shown in parentheses. Dry conversion via Equation 8.5. 95
9.12 Full emissions for Experiment B2. Constant 9 kW burner power with varying H_2 fuel fraction. Values reported on a *dry* basis for NO; analyzer wet readings are shown in parentheses. O_2, CO, CH_4, and CO_2 are measured dry by the analyzer. CH_4 values close to the analyzer detection limit ($\sim$4 ppm) should be interpreted with caution. Dry conversion via Equation 8.5. Side steam injection configuration was used. 97
9.13 Experiment B2 (9 kW). O_2-normalized and derived NO and CO metrics (*dry*) as described in Section 8.4. 98
9.14 NO emissions for Experiment C1. Constant 10 kW burner power with varying H_2 fuel fraction and steam injection level (Steam-7 = 17.7 g/min, Steam-9 = 24.4 g/min). Values reported on a dry basis; analyzer wet readings are shown in parentheses. Dry conversion via Equation 8.5.101
9.15 Full emissions for Experiment C1. Constant 10 kW burner power with varying H_2 fuel fraction and steam injection level (Steam-7 = 17.7 g/min, Steam-9 = 24.4 g/min). Values reported on a *dry* basis for NO; analyzer wet readings are shown in parentheses. O_2, CO, CH_4, and CO_2 are measured dry by the analyzer. Dry conversion via Equation 8.5. Side steam injection configuration was used. 103
9.16 Experiment C1. O_2-normalized and derived NO and CO metrics (*dry*) as described in Section 8.4. 104
9.17 NO emissions for Experiment C2. Constant 10 kW burner power with varying H_2 fuel fraction and steam injection level (Steam-6 = 13.7 g/min, Steam-7 = 17.7 g/min, Steam-8 = 22.8 g/min, Steam-9 = 24.4 g/min). Side steam injection configuration was used. Values reported on a dry basis; analyzer wet readings are shown in parentheses. Dry conversion via Equation 8.5. 105
9.18 Full emissions for Experiment C2. Constant 10 kW burner power with varying H_2 fuel fraction and steam injection level (Steam-6 = 13.7 g/min, Steam-7 = 17.7 g/min, Steam-8 = 22.8 g/min, Steam-9 = 24.4 g/min). Values reported on a *dry* basis for NO; analyzer wet readings are shown in parentheses. O_2, CO, CH_4, and CO_2 are measured dry by the analyzer. Dry conversion via Equation 8.5. 107
9.19 Experiment C2. O_2-normalized and derived NO and CO metrics (*dry*) computed from analyzer readings. 108
9.20 NO emissions for Experiment D1. Constant 10 kW burner power with varying H_2 fuel fraction and steam injection level (Steam-6 = 13.7 g/min, Steam-7 = 17.7 g/min, Steam-8 = 22.8 g/min, Steam-9 = 24.4 g/min). Values reported on a *dry* basis; analyzer wet readings are shown in parentheses. Dry conversion via Equation 8.5. Axial steam injection configuration was used.112
9.21 Axial (D1) vs side (C1 and C2) comparisons at 10 kW, 250 NLPM total air. Values are dry NO; drops are computed series-by-series (i.e., against each series' own no-steam case). "—" indicates not tested. 114
9.22 Full emissions for Experiment D1. Constant 10 kW burner power with varying H_2 fuel fraction and steam injection level (Steam-6 = 13.7 g/min, Steam-7 = 17.7 g/min, Steam-8 = 22.8 g/min, Steam-9 = 24.4 g/min). Values reported on a *dry* basis for NO; analyzer wet readings are shown in parentheses. O_2, CO, CH_4, and CO_2 are measured dry by the analyzer. Dry conversion via Equation 8.5. Axial steam injection configuration was used. . 119
9.23 Experiment D1. Derived NO metrics (*dry*). NO values were normalized to 15% O_2 using Eq. (8.16). 123

B.1 Calculated steam mass flow rates for the power settings of the steam generator 160
B.2 Uncertainty analysis for steam mass flow rate measurements 161
B.3 Steam mass flow rates at different power settings 161

Table of Symbols

Table 1: List of Symbols, Qualifiers, and Abbreviations

Symbol	Units	Definition
Latin symbols (A–Z)		
$\mathrm{AFR}_{\mathrm{fuel}}^{\mathrm{mol}}$	–	Stoichiometric molar air–fuel ratio of the fuel blend.
C_2^*	–	Excited dicarbon chemiluminescence (visible).
CH^*	–	Excited methylidyne chemiluminescence (visible).
CH_4	ppm	Methane (analyzer).
CO	ppm	Carbon monoxide (analyzer).
CO_2	%vol	Carbon dioxide (analyzer).
CV	–	Coefficient of variation, σ/μ.
EICO	$\mathrm{g\,kg^{-1}}$	Emission index of CO (mass-of-fuel basis).
EICO^E	$\mathrm{mg\,MJ^{-1}}$	Emission index of CO (energy basis).
EINO	$\mathrm{g\,kg^{-1}}$	Emission index of NO (mass-of-fuel basis).
EINO^E	$\mathrm{mg\,MJ^{-1}}$	Emission index of NO (energy basis).
FS	device units	Full-scale value of a controller (flow-set uncertainty).
H_2	–	Hydrogen in fuel blend (molar/volumetric fraction as stated).
$\mathrm{LHV}_{\mathrm{CH_4}}$	$\mathrm{kJ\,mol^{-1}}$	Molar lower heating value of CH_4.
$\mathrm{LHV}_{\mathrm{H_2}}$	$\mathrm{kJ\,mol^{-1}}$	Molar lower heating value of H_2.
$\mathrm{LHV}_{\mathrm{mix}}$	$\mathrm{kJ\,mol^{-1}}$	Molar lower heating value of the fuel mixture.
$\mathrm{M}_{\mathrm{CH_4}}$	$\mathrm{g\,mol^{-1}}$	Molar mass of CH_4.
M_{CO}	$\mathrm{g\,mol^{-1}}$	Molar mass of CO.
$\mathrm{M}_{\mathrm{H_2}}$	$\mathrm{g\,mol^{-1}}$	Molar mass of H_2.
$\mathrm{M}_{\mathrm{mix}}$	$\mathrm{g\,mol^{-1}}$	Molar mass of the fuel mixture.
M_{NO}	$\mathrm{g\,mol^{-1}}$	Molar mass of NO.
n	–	Count (samples or data points).
n_{prod}	$\mathrm{mol\,mol^{-1}}$	Total (wet) product moles per mol fuel.
NO	ppm	Nitric oxide (analyzer).
O_2	%vol	Oxygen (analyzer).
R	units of x_i	Range of a signal, max(x_i)-min(x_i).
RD	device units	Read value set in the controller (flow-set uncertainty).
s	$\mathrm{mol\,mol^{-1}}$	Steam-to-fuel molar ratio (mol H_2O per mol fuel).
T_{ad}	K	Adiabatic flame temperature.
T_{flame}	K	Baseline flame temperature.
T_{new}	K	Estimated flame temperature with steam.
T_s	K	Steam injection temperature.
$\Delta\dot{Q}$	device units	Device uncertainty: $0.005\,RD + 0.001\,FS$.
$\dot{m}_{\mathrm{gas}}$	$\mathrm{kg\,s^{-1}}$	Total gas mass flow (air + fuel).

Continued on next page

Symbol	Units	Definition
$\dot{m}_s$	kg s^{-1}	Steam mass flow rate.
$\dot{m}_{\text{tot}}$	kg s^{-1}	Total mass flow of gases.
$\dot{m}_{\text{H}_2,\text{lpm}}$	L/min	H_2 volumetric flow (operating).
$\dot{m}_{\text{CH}_4,\text{lpm}}$	L/min	CH_4 volumetric flow (operating).
$\dot{m}_{\text{fuel,mix,lpm}}$	L/min	Fuel-blend volumetric flow (operating).
$\dot{V}_{\text{air,lpm}}$	L/min	Air volumetric flow (operating).
$u(\cdot)$	same as arg.	Standard uncertainty of the quantity in parentheses.
X_{CO}	ppmv	Mole fraction of CO (form: wet/dry by qualifier).
$X_{\text{H}_2\text{O}}$	–	Mole fraction of H_2O in products (wet).
X_{NO}	ppmv	Mole fraction of NO (form: wet/dry/by O_2 qualifier).
x_{CH_4}	–	CH_4 fraction in the fuel blend.
x_{H_2}	–	H_2 fraction in the fuel blend.
x_i	units of x_i	ith sample value in a time series.
Greek symbols (α–ω)		
β	–	Temperature-sensitivity coefficient for thermal NO model.
ΔT	K	Estimated flame temperature drop due to steam.
$c_{p,g}$	J kg^{-1} K^{-1}	Mean specific heat of combustion gases.
$c_{p,s}$	J kg^{-1} K^{-1}	Specific heat of steam.
μ	units of x_i	Mean of a time series.
ν_{dry}	mol mol^{-1}	Dry product moles (per mol fuel).
$\nu_{\text{O}_2,\text{stoich}}$	mol mol^{-1}	Stoichiometric O_2 demand per mol fuel (blend).
σ	units of x_i	Standard deviation of a time series.
ϕ	–	Global equivalence ratio.
ϕ_{mix}	–	Equivalence ratio of the fuel–air mixture.
Abbreviations and units (as used in text/tables)		
AAI	–	Axial Air Injection.
ABEL	–	(Inverse) Abel transform (image reconstruction).
AO2000	–	ABB Advance Optima gas analyzer platform.
CFD	–	Computational Fluid Dynamics.
CRZ	–	Central Recirculation Zone.
DSLR	–	Digital Single-Lens Reflex (camera).
EI	–	Emission Index (generic).
EICO	–	Emission Index of CO (see EICO/EICO^E).
EINO	–	Emission Index of NO (see EINO/EINO^E).
GRI-Mech 3.0	–	Gas Reaction Mechanism for NG/H_2 combustion.
HSL	–	High-Temperature Systems Lab (rig/facility).
HySIITE	–	GE “Hydrogen Steam-Injected, Inter-cooled Turbine Engine”.
HW	–	Hot–Wet (sampling/conditioning basis).

Continued on next page

Symbol	Units	Definition
kW	–	Kilowatt (thermal power).
LHV	–	Lower Heating Value.
LIF	–	Laser-Induced Fluorescence.
MFC	–	Mass Flow Controller.
NDIR	–	Non-Dispersive Infrared (gas analysis).
NLPM	–	Normal litres per minute (standardized volumetric flow).
NO-LIF	–	Nitric Oxide Laser-Induced Fluorescence.
OH^*	–	Excited hydroxyl chemiluminescence (UV).
OH-PLIF	–	Planar Laser-Induced Fluorescence of OH.
PIV	–	Particle Image Velocimetry.
PLIF	–	Planar Laser-Induced Fluorescence.
ppm	–	Parts per million (by volume unless stated).
ppmv	–	Parts per million by volume.
RAW	–	Uncompressed camera image format.
RMS	–	Root-Mean-Square.
RSS	–	Root-Sum-Square.
TDMS	–	Technical Data Management Streaming (LabVIEW).
TU Delft	–	Delft University of Technology.
Uras 26	–	ABB NDIR analyzer (CO, CO_2, CH_4).
Magnos 28	–	ABB paramagnetic O_2 analyzer.
Limas 11 HW	–	ABB UV analyzer (NO/NO_2).
UV	–	Ultraviolet (camera/imaging).
mg/MJ	–	Milligrams per megajoule.
g/kg	–	Grams per kilogram of fuel.
g/min	–	Grams per minute (steam flow).
L/min	–	Litres per minute (operating flow).

Abstract

The decarbonization of gas turbine technology requires combustion systems capable of operating with hydrogen and hydrogen–natural gas blends while maintaining low NO_x emissions. Hydrogen combustion increases flame temperature and reactivity, which might increase thermal NO formation through the Zeldovich mechanism and increase the flashback risk. Steam dilution is a promising strategy to mitigate NO_x and improve flashback resistance without major hardware modifications, yet its performance in partially premixed, swirl-stabilized flames with different fuel composition, steam delivery strategy, and operating conditions is not yet fully understood.

This thesis investigates the effect of steam injection on NO emissions in lean premixed CH_4/H_2 flames using a swirl-stabilized vertical combustor operating at 7–11 kW. Four experimental series were conducted to isolate the influence of (i) thermal load, (ii) H_2 blend fraction, (iii) steam injection amount, and (iv) injection location (side vs. axial). Emissions were measured using an ABB AO2000 analyzer, and the results are reported as raw, 15% O_2 normalized and mass- & energy-based emission indices (EINO). Flame structure was characterized using DSLR imaging and OH^* chemiluminescence. A simplified analytical estimate based on thermal NO scaling was developed to contextualize the measurements.

Steam injection consistently reduced NO under all operating conditions. Measured reductions ranged from 30–40% at moderate steam loadings (17.7 g/min) to 45–55% under higher steam addition (24.4 g/min), in close agreement with the simplified thermal prediction. NO reductions exceeded 80% in high methane fraction blends in lean conditions but approached local quench limits, as indicated by elevated CO and unburned CH_4 measured at the exhaust. High hydrogen blend fraction flames produced higher absolute NO but tolerated steam injection without evident oxidation penalties. Axial steam injection provided more uniform premixing than side injection and maintained stable operation across all H_2 blends, achieving comparable or improved NO reduction without CO rise. Flame Imaging revealed that steam addition cools and weakens the flame core, producing annular reaction zones consistent with reduced peak temperatures and suppressed radical pools.

The results demonstrate that steam injection is an effective NO control strategy for hydrogen partially-premixed combustion. Its effectiveness depends on injection strategy, blend ratio, and operating power. A more uniform steam–air partial-premixing have a more favorable effect on NO reduction and stability. The findings provide design guidance for implementing steam dilution in practical low-NO_x hydrogen combustion systems and highlight directions for future work, including high-pressure testing and resolved diagnostics of radical fields and local temperature.

1 Introduction

Fossil fuels, due to their high energy densities, have been used as primary energy sources for transportation, industrial activities and power generation for the last few centuries [1]. For much of modern history, these resources have been instrumental in driving industrialization, technological innovation, and economic growth worldwide. However, it is only in recent decades that the adverse effects of using fossil fuels have begun to gain prominence in collective public awareness.

This dependence of modern society on fossil fuels has come at significant environmental costs[2]. Their combustion releases large amounts of greenhouse gases, most notably carbon dioxide (CO_2), methane (CH_4), and nitrous oxide (N_2O), along with pollutants such as carbon monoxide (CO), nitrogen oxides (NO_x), sulfur oxides (SO_x), particulate matter, and volatile organic compounds [3]. These emissions intensify the greenhouse effect which drives global warming, sea-level rise, and more frequent extreme weather while also degrading air quality and human health. In particular, NO_x, a term used for nitrogen oxides such as NO, NO_2 and N_2O, is problematic because it contributes to ground-level ozone and fine particulate matter formation, aggravates respiratory and cardiovascular illnesses, and accelerates environmental damage [4, 5]. Since NO_x can form in any combustion system that relies on air as the oxidizer, due to the abundance of nitrogen in the atmosphere, strategies to mitigate these emissions are increasingly critical and continue to receive growing attention.

Combustion emissions from aviation, transportation and stationary power generation remain central to contemporary environmental challenges. Although aviation contributes a relatively smaller portion of total global greenhouse gas emissions compared to other sectors, its impact on climate forcing is disproportionately large due to the altitude at which emissions occur. Carbon dioxide (CO_2), with its long atmospheric lifetime, and nitrogen oxides (NO_x), which enhance ozone formation at cruise altitudes, both contribute significantly to radiative forcing effects on the climate system [6]. In addition, stationary gas turbines, particularly those used in large-scale power generation, constitute some of the most substantial point sources of NO_x at ground level. Their emissions directly influence local air quality and pose notable risks to public health, particularly in densely populated or industrialized regions. Collectively, these sectors exemplify the broader issue of combustion-related NO_x emissions and highlight the critical need for targeted mitigation strategies that address both atmospheric layers and sectors of origin.

The urgency to reduce combustion emissions in both aviation and land-based systems has led to intensified efforts in research and innovation aimed at transitioning to sustainable fuels and adopting alternative propulsion systems. Hydrogen has emerged as a promising candidate due to its high specific energy and potential to achieve near-zero carbon emissions when combusted [7]. However, hydrogen combustion poses important challenges, particularly the formation of NO_x which is promoted by the high flame temperature of hydrogen [8]. Addressing these challenges requires new strategies that align with global climate goals and increasingly stringent emission regulations.

Several ongoing efforts are exploring hydrogen combustion with direct relevance to NO_x emissions, flame stability, and engine integration. Recent subsonic, gas-turbine relevant studies use dual-swirl coaxial injectors, such as the HYLON burner, to investigate stabilization, lift-off, flashback, and NO_x formation under aero-engine conditions [9]. In parallel, Pratt & Whitney's HySIITE (Hydrogen Steam-Injected, Intercooled Turbine Engine) concept couples hydrogen combustion with steam injection and exhaust-water recovery;

component-level rig tests have reported up to a 99.3% reduction in NO_x and demonstrated onboard water recovery and evaporation subsystems [10].

These projects highlight both practical and modeling challenges in implementing hydrogen combustion: maintaining stable combustion while reducing NO_x, understanding flame front dynamics under different equivalence ratios and pressure regimes, and integrating hydrogen fuel-firing into existing propulsion or gas turbine platforms. They also demonstrate the growing commitment to hydrogen as a practical combustion fuel in aviation and power applications. At the same time, academic and laboratory studies focus more directly on the combustion challenges, investigating approaches such as steam or water injection, advanced diagnostics, and other techniques aimed at stabilizing hydrogen flames and reducing NO_x emissions.

As interest in reducing NO_x intensifies, water and steam injection are receiving growing attention as practical mitigation concepts. The approach is relatively simple to implement in laboratory flames and in many gas-turbine configurations, since it can be added without major redesign. Added H_2O increases the mixture heat capacity and lowers peak flame temperatures, which directly weakens thermal NO formation. It also alters the H/O/OH radical pool, which in turn reduces NO production under comparable conditions. Depending on the setup, water or steam can change stabilization behavior and shorten the effective exposure time to high temperatures. These trends are documented in both research studies and application settings. Specific mechanisms, trade-offs, and implementation strategies are discussed in detail in Chapter 3.

1.1. Characteristics of Conventional and Alternative Fuels

It is necessary to provide an initial overview of methane and hydrogen combustion because their fundamental thermochemical and transport properties set the conditions under which flame stability, heat release and pollutant formation emerge. This section gives a concise, physics-focused introduction to methane as an industrial baseline and to the contrasting behaviour of hydrogen.

1.1.1. Methane as a Baseline Fuel

Hydrocarbon fuels such as kerosene, gasoline and methane have historically been the dominant energy carriers for transportation and power generation because of their high volumetric energy density, well-developed supply chains and compatibility with existing combustion technologies. Their combustion characteristics have been studied extensively, and much of the foundational knowledge of flame chemistry, pollutant formation and combustor design derives from hydrocarbon research [11, 12]. In the context of gas turbines, both aviation engines and stationary power units are conventionally operated with hydrocarbon fuels, which makes their behaviour the natural reference point when evaluating alternative fuels such as hydrogen.

Among hydrocarbons, methane (CH_4) is particularly important because it is the principal constituent of natural gas and represents the simplest hydrocarbon molecule. Its combustion is comparatively clean relative to heavier hydrocarbons, as it produces negligible soot under most conditions and has relatively few intermediate species, which simplifies the chemical pathways to major products [12, 11, 13]. Complete stoichiometric combustion of methane in air can be written as:

$$CH_4 + 2\,O_2 \;\rightarrow\; CO_2 + 2\,H_2O,$$

with incomplete combustion leading to pollutants such as carbon monoxide (CO) and unburnt hydrocarbons (UHC) when oxygen is locally depleted or when residence times are insufficient [13]. The absence of aromatic intermediates in methane oxidation largely eliminates soot precursors, which is one of the reasons why natural gas is widely promoted as a “clean” transitional fuel in energy systems.

The combustion behaviour of methane is well characterised in terms of fundamental parameters. It has a laminar flame speed of approximately 0.4 m/s at stoichiometric conditions and atmospheric pressure, which is significantly lower than that of hydrogen but comparable to other light hydrocarbons [13]. Its flammability limits in air range from about 5 to 15% by volume, narrower than hydrogen but adequate for safe and controlled operation in lean-premixed configurations. The adiabatic flame temperature of stoichiometric methane–air mixtures is roughly 2220 K at 1 bar, lower than hydrogen–air flames but still sufficiently high to ensure complete oxidation under most operating conditions [11]. These values make

methane flames slower, cooler and narrower in flammability than hydrogen flames, and provide a useful benchmark for interpreting the impact of alternative fuels or dilution strategies.

The choice of methane as a baseline fuel in combustion studies is motivated by several factors. Methane is industrially relevant, since lean-premixed natural gas combustion represents the current standard in stationary power generation and serves as a logical reference point for comparison with prospective hydrogen-fuelled systems. It is also extensively documented in both experiments and detailed chemical-kinetic models, most notably the GRI-Mech 3.0 mechanism, which accurately predicts flame structure, adiabatic temperatures and major-species behaviour for CH_4/air mixtures [14]. This wealth of reference data allows laboratory measurements to be placed in context and interpreted with confidence. Finally, methane provides a stable and reproducible flame that can be systematically perturbed by introducing hydrogen or steam, enabling controlled investigation of the effects of altered chemistry, transport properties and dilution on flame structure and performance.

1.1.2. Concept of Hydrogen as Fuel for Transportation & Power Generation

Hydrogen has emerged as a leading candidate for decarbonising aviation and stationary power systems due to its absence of carbon in the fuel molecule and its high gravimetric energy density. With an energy content of approximately 120 MJ/kg, hydrogen contains nearly three times more energy per unit mass than conventional hydrocarbon fuels such as methane or kerosene [15]. This property makes it attractive in applications where fuel mass is critical, particularly for aircraft. However, hydrogen also suffers from a very low volumetric energy density, which necessitates specialised storage either as a compressed gas at pressures up to 700 bar or as a cryogenic liquid below $-253\,^{\circ}$C. Both options introduce significant engineering and economic challenges for integration into existing aircraft and turbine systems [16, 17].

Storage

Since hydrogen has very low volumetric energy density compared to current aviation fuels, it occupies a much larger volume. To address this, hydrogen is typically stored in either compressed gaseous form or as a cryogenic liquid. Compressed storage at up to 700 bar requires heavy, high-pressure tanks that increase structural weight and complexity, while cryogenic storage demands advanced insulation technologies to minimise boil-off and maintain safety at extremely low temperatures [16]. Both approaches remain technologically challenging and economically demanding for aviation-scale use.

Safety

Hydrogen's chemical and physical properties introduce distinct safety considerations. Its very low ignition energy makes it highly susceptible to unintended ignition, while its small molecular size enables leakage through fittings and contributes to material embrittlement in certain metals [18]. In addition, hydrogen flames are nearly invisible, complicating detection and emergency response. These properties require robust safety protocols, advanced leak detection systems, and careful selection of compatible materials.

Infrastructure & Transportation

Unlike conventional fossil fuels, hydrogen lacks a mature global infrastructure for production, transportation, and storage. Large-scale adoption therefore requires new facilities for producing "green hydrogen" via electrolysis powered by renewable energy, distribution networks such as pipelines or cryogenic tankers, and modifications to existing airports and power plants to safely accommodate hydrogen operations [19]. These logistical challenges are a central barrier to its near-term integration into aviation and stationary energy systems.

Combustion Properties and Challenges

In addition to system-level issues, hydrogen's combustion behaviour differs fundamentally from hydrocarbons and directly impacts its suitability for practical combustors. Complete stoichiometric combustion of hydrogen in air can be represented as:

$$2\,H_2 + O_2 \;\rightarrow\; 2\,H_2O.$$

Unlike hydrocarbon combustion, no carbon dioxide is formed, and water vapour is the sole major product under ideal conditions. This absence of carbon-based products eliminates soot and unburnt hydrocarbon emissions, which is a major environmental advantage over conventional fuels.

Hydrogen's laminar flame speed at stoichiometric conditions is approximately 2.0–2.5 m/s at atmospheric pressure, nearly an order of magnitude higher than methane [13]. This promotes stable flame anchoring even under lean conditions but also increases the risk of flashback into premixing passages. Its wide flammability limits in air (4–75% by volume) enable operation across a broader range of equivalence ratios than hydrocarbons, allowing lean combustion strategies but complicating flame control and stability [11].

Hydrogen also exhibits strong preferential diffusion effects due to its high molecular diffusivity. The Lewis number (the ratio of thermal to mass diffusivity) is substantially below unity for hydrogen–air mixtures, meaning that hydrogen diffuses faster than heat. This imbalance produces local inhomogeneities at the flame front, driving thermo-diffusive instabilities, cellular flame structures, and high sensitivity to stretch and curvature [20]. Furthermore, hydrogen flames are thinner than those of hydrocarbons and more responsive to aerodynamic strain, with flame thickness and strain rate being key parameters governing their stabilisation and extinction.

Pressure further influences hydrogen combustion. While most laboratory investigations are performed at atmospheric pressure, practical aero-engines and gas turbines operate at elevated pressures. Increasing pressure accelerates chemical kinetics, reduces flame length scales, and shifts the relative influence of transport and chemical timescales. Consequently, instability behaviour observed in atmospheric flames may not directly represent that in high-pressure combustors, underscoring the need to interpret laboratory-scale findings with caution.

A further environmental consideration unique to hydrogen combustion in aviation is the formation of contrails. Because hydrogen has a higher mass-specific water yield than hydrocarbons, its combustion releases more water vapor per unit energy. At cruise altitudes, where temperatures and pressures favor condensation, this enhances the likelihood and persistence of contrails. While contrails are composed primarily of ice crystals, they alter the radiative balance of the atmosphere, often producing a net warming effect that can rival or exceed the climate forcing of the CO_2 saved by switching to hydrogen [6, 21]. This underlines that the climate impact of hydrogen-fueled aviation is not solely tied to NO_x but also to water-vapor-induced contrails, which remain an active area of research and uncertainty.

A final and critical distinction of hydrogen combustion is its higher flame temperature compared to hydrocarbons. The adiabatic flame temperature of stoichiometric hydrogen–air mixtures is roughly 2400 K at 1 bar, compared with about 2220 K for methane–air flames under similar conditions [11]. This difference of nearly 200 K, while beneficial for complete oxidation and high reactivity, creates conditions that strongly favour the formation of thermal NO_x through high-temperature pathways. Thus, while hydrogen eliminates carbon-based emissions, its combustion is intrinsically more prone to NO_x production due to its higher flame temperature. These characteristics provide the direct motivation for the following section, which discusses the mechanisms of NO_x formation in greater detail.

1.2. Nitrogen Oxides in Combustion

Nitrogen oxides (NO_x) represent a family of compounds primarily consisting of nitric oxide (NO), nitrogen dioxide (NO_2), and nitrous oxide (N_2O). Among these, NO and NO_2 are the most abundant products of combustion processes, while N_2O is formed under specific low-temperature or catalytic conditions [11, 12]. NO_x formation is almost unavoidable in any air-breathing combustion system due to the overwhelming presence of molecular nitrogen in the oxidiser stream. Although nitrogen is inert under standard conditions, high flame temperatures and radical-driven reactions enable its conversion to reactive oxides, which then persist in exhaust streams.

The environmental relevance of NO_x stems from its multifaceted impacts. In the troposphere, NO_x acts as a precursor to ozone (O_3) and secondary particulate matter, both of which degrade air quality and contribute to smog formation [22]. Ozone and fine particles are linked to adverse health outcomes including respiratory illnesses, cardiovascular disease, and increased mortality [23]. At the same time, NO_x emissions contribute to acid deposition when converted to nitric acid in the atmosphere, which can harm ecosystems and corrode infrastructure. From a regulatory standpoint, these health and environmental burdens have made NO_x one of the most tightly controlled pollutants in both stationary and mobile combustion sources.

Beyond local air-quality concerns, NO_x also plays a role in climate forcing. Although NO and NO_2 are not themselves potent greenhouse gases, they influence atmospheric chemistry in ways that alter the concentrations of longer-lived radiatively active species. For example, NO_x enhances ozone formation in

the upper troposphere, where ozone acts as a greenhouse gas [6]. In aviation, the altitude of emissions magnifies this effect: NO_x released from aircraft engines accelerates ozone formation at cruise levels, producing a non-negligible radiative forcing component in addition to the direct CO_2 emissions. Meanwhile, N_2O is itself a strong greenhouse gas with a global warming potential nearly 300 times greater than CO_2, and although it is less prominent in high-temperature flames, it can be significant in lean, low-temperature gas turbine conditions [24].

From a combustion science perspective, NO_x is particularly important because it is strongly dependent on the detailed thermo-chemical environment of the flame. Unlike CO or unburnt hydrocarbons, which primarily reflect incomplete oxidation, NO_x is formed even in fully stoichiometric or lean conditions where oxidation is otherwise complete. Its production is governed by a set of distinct pathways; thermal, prompt, fuel-bound, and N_2O-intermediate, that depend differently on temperature, equivalence ratio, pressure, and flame structure. The exponential temperature sensitivity of thermal NO in particular makes small variations in flame temperature or residence time translate into large changes in emission levels. For this reason, NO_x serves as a sensitive diagnostic of flame behaviour and a key target in designing clean combustion systems.

In the context of hydrogen and methane fuels, the significance of NO_x becomes even sharper. Hydrogen combustion eliminates CO_2 emissions entirely, but the higher flame temperatures relative to methane intensify thermal NO production. Methane combustion, while producing less thermal NO per unit energy than hydrogen, still generates NO_x through multiple channels including prompt pathways via hydrocarbon radicals [25]. Both fuels therefore raise the same central challenge: any transition away from carbon-containing fuels does not inherently eliminate nitrogen oxide emissions, and in the case of hydrogen, may even exacerbate them. Understanding the mechanisms by which NO_x forms, and the parameters that control its production, is thus central to evaluating the environmental viability of hydrogen-fuelled combustion and motivates the following detailed discussion.

1.2.1. Thermal NO Formation (Zeldovich Mechanism)

The dominant pathway for nitrogen oxide formation in high-temperature flames is thermal NO, described by the extended Zeldovich mechanism. First proposed by Zeldovich in 1946, this mechanism captures the dissociation of molecular nitrogen in the presence of oxygen radicals at elevated temperatures [26, 11, 12]. Because molecular nitrogen is strongly bound (bond energy 941 kJ/mol), its conversion to NO requires activation energies that are only accessible in regions where flame temperatures exceed approximately 1800 K [11, 12]. For this reason, thermal NO is most significant in stoichiometric and lean-premixed flames where adiabatic flame temperatures are high, and it is particularly pronounced in hydrogen flames, which reach higher peak temperatures than hydrocarbons under similar conditions.

The extended Zeldovich mechanism consists of three key elementary reactions:

$$\begin{aligned} N_2 + O &\rightleftharpoons NO + N \\ N + O_2 &\rightleftharpoons NO + O \\ N + OH &\rightleftharpoons NO + H \end{aligned}$$

The first step, the dissociation of N_2 by atomic oxygen, is the rate-limiting reaction due to the high bond strength of molecular nitrogen. Once nitrogen atoms are formed, they are rapidly oxidised through reactions with O_2 and OH, driving the production of NO. The third reaction involving OH is particularly important in premixed flames, where high radical concentrations are present. Collectively, these reactions define the thermal NO pathway and establish its sensitivity to both temperature and radical pool concentrations.

The rate of thermal NO formation exhibits an exponential dependence on flame temperature, consistent with the Arrhenius form of the rate-determining step. As a result, relatively modest increases in temperature (on the order of 100–200 K) can produce disproportionately large increases in NO production. For instance, the difference in stoichiometric adiabatic flame temperature between hydrogen–air (≈2400 K) and methane–air flames (≈2220 K) is sufficient to make thermal NO yields significantly higher in hydrogen combustion, despite hydrogen producing no prompt NO due to the absence of hydrocarbon fragments [27, 25].

Zeldovich mechanism is extremely sensitive to temperature. Because the rate-limiting step is the dissociation of N_2 by atomic oxygen, the forward rate constant follows an Arrhenius expression:

$$k_1(T) = A_1\, T^{n_1}\, \exp\!\left(-\frac{E_{a,1}}{RT}\right), \tag{1.1}$$

where $k_1(T)$ is the rate constant of the dissociation reaction (R1), A_1 is the pre-exponential factor, n_1 is the temperature exponent, $E_{a,1}$ is the activation energy for N_2 dissociation, R is the universal gas constant, and T is the absolute temperature. The large activation energy reflects the strong triple bond of N_2, which is difficult to break except at very high flame temperatures.

The parameters A_1, n_1, and $E_{a,1}$ are not universal constants but are determined specifically for each elementary reaction from a combination of experimental measurements and theoretical calculations. Typical sources of data include shock-tube ignition studies, flow-reactor experiments, and laminar flame measurements, which provide rate information across combustion-relevant temperature ranges. These datasets are then fitted using Arrhenius-type expressions to extract the pre-exponential factor, temperature exponent, and activation energy. The resulting parameters are compiled in detailed chemical-kinetic mechanisms such as GRI-Mech 3.0 and the San Diego mechanism, where they are validated and, in some cases, optimized against a broader set of experimental targets. In practice, these tabulated values provide an effective representation of the temperature dependence of the reaction rate and are widely used in both combustion modeling and mechanism development [14, 28, 29, 30, 31].

Under the quasi-steady approximation for atomic nitrogen, the NO production rate can be expressed as:

$$\dot{\omega}_{\mathrm{NO}} \;\propto\; k_1(T)\,[\mathrm{N_2}]\,[\mathrm{O}], \tag{1.2}$$

where $\dot{\omega}_{\mathrm{NO}}$ is the volumetric production rate of NO (commonly reported in $\mathrm{mol \cdot m^{-3} \cdot s^{-1}}$, or equivalently $\mathrm{kg \cdot m^{-3} \cdot s^{-1}}$ on a mass basis), $[\mathrm{N_2}]$ is the molar concentration of nitrogen ($\mathrm{mol \cdot m^{-3}}$), and $[\mathrm{O}]$ is the molar concentration of atomic oxygen ($\mathrm{mol \cdot m^{-3}}$). This relation highlights that NO production scales exponentially with T through the rate constant, with additional, weaker dependencies on species concentrations.

A useful measure of this sensitivity can be written as the logarithmic temperature derivative of the rate:

$$\frac{\partial \ln \dot{\omega}_{\mathrm{NO}}}{\partial T} \;\approx\; \frac{E_{a,1}}{RT^2}, \tag{1.3}$$

where the right-hand side defines an effective temperature sensitivity parameter, often denoted $\beta_T(T)$. At typical flame-zone temperatures ($T \approx 2200$–2400 K), β_T is about $7 \times 10^{-3}\,\mathrm{K^{-1}}$, implying that a 100 K rise in temperature can approximately double thermal NO production, while a 200 K rise can increase it by nearly a factor of four.

The integrated NO concentration in a combustor depends not only on the local rate but also on the residence time of gases in the high-temperature zone. This can be expressed as:

$$Y_{\mathrm{NO}} \;\sim\; \int_{\mathrm{htz}} \dot{\omega}_{\mathrm{NO}}(T(t))\, dt \;\;\approx\;\; \dot{\omega}_{\mathrm{NO}}(T_{\mathrm{peak}})\, \tau_{\mathrm{htz}}, \tag{1.4}$$

where Y_{NO} is the total NO yield, T_{peak} is the peak flame temperature, and τ_{htz} is the effective residence time in the high-temperature zone. This expression shows that aerodynamics (e.g., recirculation in swirl-stabilised flames), dilution, and pressure influence NO formation both by changing T_{peak} and by altering how long reactants are exposed to these high-temperature conditions.

The dependence of thermal NO on flame residence time is equally important. In practical combustors, gases remain in the high-temperature zone for finite durations determined by mixing, turbulence, and flow structure. Longer residence times in these zones allow thermal NO pathways to proceed further, increasing emissions. This explains why burner design, swirl stabilisation, and dilution strongly affect NO formation even at the same global equivalence ratio and firing condition. Elevated pressures, as found in gas turbines, also shift the balance of reaction rates, generally favouring higher NO levels compared to atmospheric conditions [11, 12].

In summary, the Zeldovich mechanism establishes thermal NO as a high-temperature, radical-driven process that is the dominant pathway in lean-premixed combustion [12][29]. Its exponential sensitivity to temperature makes it the principal challenge for hydrogen-fuelled systems, where peak adiabatic flame temperatures exceed those of methane by nearly 200 K. For this reason, most NO reduction strategies—such as lean operation, dilution, and steam injection—can be interpreted in terms of their ability to reduce peak flame temperatures or shorten the residence time of gases in the high-temperature core.

1.2.2. Prompt NO Formation (Fenimore Mechanism)

In addition to the high-temperature Zeldovich pathway, nitrogen oxides can also be produced via the so-called *prompt NO* route, first identified by Fenimore in 1971 [32]. Unlike thermal NO, which requires flame-zone temperatures exceeding ~ 1800 K, prompt NO arises at the very leading edge of hydrocarbon flames, even under comparatively lower temperature conditions. It originates from reactions between molecular nitrogen and hydrocarbon-derived radicals, primarily CH, which are abundant in the thin flame front region. This makes prompt NO characteristic of hydrocarbon combustion and essentially absent in pure hydrogen flames, where no carbon-containing intermediates exist [12, 29].

The fundamental initiation step of the prompt mechanism is

$$\mathrm{CH} + \mathrm{N_2} \rightarrow \mathrm{HCN} + \mathrm{N} \tag{1.5}$$

where CH is the methylidyne radical, an important transient species in hydrocarbon flames. The nitrogen atom produced in this step is then available to participate in oxidation reactions similar to those of the Zeldovich sequence, while hydrogen cyanide (HCN) acts as a stable intermediate that further oxidises toward NO:

$$\mathrm{HCN} + \mathrm{O} \rightarrow \mathrm{NCO} + \mathrm{H} \tag{1.6}$$

$$\mathrm{NCO} + \mathrm{H} \rightarrow \mathrm{NH} + \mathrm{CO} \tag{1.7}$$

$$\mathrm{NH} + \mathrm{O} \rightarrow \mathrm{NO} + \mathrm{H} \tag{1.8}$$

Through this pathway, carbon–nitrogen intermediates such as HCN, NCO, and NH serve as the carriers of nitrogen from the fuel–air interface into NO.

The defining feature of prompt NO is its localisation: it is formed almost immediately downstream of the reaction zone, where CH radicals are at their highest concentration. Since CH abundance strongly depends on mixture stoichiometry, prompt NO is most pronounced in near-stoichiometric or fuel-rich flames, where hydrocarbon fragments persist. Under lean-premixed conditions, CH concentrations diminish rapidly, causing prompt NO to contribute only marginally to total NO emissions compared to the thermal pathway [32, 12].

In practical terms, prompt NO is therefore an important baseline contributor in methane and other hydrocarbon flames, but its role declines as the equivalence ratio decreases or as the hydrogen fraction in a fuel blend increases. For pure hydrogen combustion, prompt NO is essentially absent. For methane or methane-rich blends, it contributes to the initial stages of NO formation but is generally outweighed by thermal NO at the high flame temperatures typical of lean-premixed gas turbines. This mechanistic distinction explains why the transition from methane to hydrogen not only changes the overall magnitude of NO emissions but also shifts the dominant pathway of formation.

1.2.3. N_2O-Intermediate Pathway

A third pathway for nitrogen oxide formation is the so-called *N_2O-intermediate mechanism*, sometimes referred to as the nitrous oxide pathway. This route becomes important under lean, low-to-moderate temperature conditions, particularly in premixed combustion at equivalence ratios $\phi < 0.8$ [33, 29]. Unlike

the thermal Zeldovich mechanism, which requires flame-zone temperatures above about 1800 K, the N_2O pathway can proceed efficiently at lower temperatures where radical concentrations are limited. As such, it provides a secondary route to NO_x formation in lean-premixed flames where thermal NO production is suppressed.

The mechanism proceeds through the formation of nitrous oxide (N_2O) as an intermediate, which can then either decompose or react to yield NO. A representative initiation step involves the recombination of N_2 with an oxygen atom in the presence of a third body:

$$N_2 + O + M \rightarrow N_2O + M, \tag{1.9}$$

where M is a third body (typically N_2, O_2, or another collision partner) that stabilises the newly formed N_2O molecule. Once formed, nitrous oxide can undergo competing reactions:

$$N_2O + O \rightarrow 2\,NO, \tag{1.10}$$

$$N_2O + H \rightarrow N_2 + OH. \tag{1.11}$$

The first channel represents the conversion of N_2O into NO, while the second acts as a terminating step that suppresses NO yield by recycling nitrogen back into N_2. The relative importance of these channels depends strongly on temperature, equivalence ratio, and radical pool composition.

A key feature of the N_2O pathway is its sensitivity to pressure. At elevated pressures, collisional stabilisation of N_2O is more efficient, increasing its steady-state concentration and enhancing its overall contribution compared to thermal NO. This makes the mechanism particularly relevant for lean-premixed gas turbines and aero-engine combustors, which operate at high pressures and moderate flame temperatures [33]. In hydrocarbon flames such as methane, the N_2O pathway is most active under lean conditions where CH radical concentrations are low (limiting prompt NO) and peak temperatures are insufficient to drive large thermal NO production. In hydrogen flames, however, higher flame temperatures and more abundant radicals tend to suppress the N_2O pathway, reducing its relative role.

While the majority of N_2O formed in flames is consumed to produce NO, a fraction can remain unreacted and be emitted directly. This is environmentally relevant since nitrous oxide is itself a potent greenhouse gas with a global warming potential approximately 300 times that of CO_2 on a 100-year timescale [34]. Thus, the N_2O-intermediate mechanism not only provides an auxiliary pathway for NO_x formation but also introduces the possibility of direct N_2O emissions under certain conditions, particularly in lean, low-temperature flames.

Overall, although the N_2O-intermediate pathway does not dominate total NO_x formation, it plays an important secondary role in lean-premixed systems. Its inclusion in chemical-kinetic models is necessary to accurately capture emission trends, especially for low-emission combustors, and its dual relevance to both NO and N_2O highlights its importance in combustion research.

1.2.4. Fuel NO

A fourth pathway for NO formation is *fuel NO*, which originates from nitrogen chemically bound within the fuel itself. In coal, heavy oils, and biomass, nitrogen occurs in the form of heteroatomic functional groups (e.g. pyridines, amines, nitriles). During devolatilisation and pyrolysis, these groups form reduced nitrogen species such as HCN, NH_3, and NNH, which can subsequently oxidise to NO through reaction sequences analogous to those of prompt and thermal NO [33, 29]. The overall conversion of fuel-bound nitrogen to NO is highly sensitive to local stoichiometry: under fuel-lean conditions, oxidation pathways dominate and NO yields are high, whereas under fuel-rich conditions, partial reduction of NO to N_2 can occur through reburning reactions.

In contrast to solid and liquid fossil fuels, gaseous fuels such as methane and hydrogen contain no chemically bound nitrogen. As a result, the fuel-NO pathway is not relevant to hydrogen and methane flames. However, it remains a major source of NO in systems firing coal, heavy oils, and biomass, and is therefore an important mechanism to consider in the broader context of combustion emissions.

1.2.5. NNH Mechanism

Another minor pathway for NO formation is the *NNH mechanism*, which proceeds through the nitrogen hydride radical (NNH). It begins with the association of molecular nitrogen with a hydrogen atom:

$$N_2 + H \rightarrow NNH, \tag{1.12}$$

followed by oxidation of NNH through reactions such as

$$NNH + O \rightarrow NO + NH. \tag{1.13}$$

Through this sequence, nitrogen is activated by hydrogen radicals and subsequently oxidised to NO [33, 29].

The NNH pathway is generally less significant than thermal, prompt, or N_2O-intermediate mechanisms. Its overall contribution is typically small under practical combustion conditions but can become more noticeable in hydrogen-rich environments, where high concentrations of H radicals promote NNH formation. For this reason, the NNH route is often included in detailed chemical-kinetic mechanisms of NO_x chemistry, even though it usually represents only a secondary contribution compared to the dominant thermal pathway.

1.2.6. NO_2 Formation Mechanisms

Although nitric oxide (NO) is the primary product of nitrogen fixation in flames, nitrogen dioxide (NO_2) also contributes to total NO_x emissions and warrants separate discussion. Unlike NO, which forms in the high-temperature flame zone through thermal, prompt, or N_2O pathways, NO_2 is typically generated downstream in cooler post-flame regions. Its formation proceeds mainly via the oxidation of NO:

$$NO + \tfrac{1}{2}O_2 \rightarrow NO_2, \tag{1.14}$$

$$NO + HO_2 \rightarrow NO_2 + OH. \tag{1.15}$$

The first reaction dominates under conditions where excess oxygen is present, while the second becomes significant in environments with high radical concentrations, such as turbulent flames or regions with substantial intermediate chemistry. Because both reactions are slow at elevated temperatures, NO_2 formation is generally limited within the flame itself and is instead favoured in the cooler post-combustion zones or during mixing with ambient air.

In typical gas turbine or laboratory-scale premixed flames, NO_2 accounts for only a small fraction of total NO_x, often less than 10% [11, 12]. However, its relative contribution can rise under low-temperature combustion modes (e.g. staged combustion, HCCI engines) or in the exhaust plume, where sufficient time and oxygen are available for conversion of NO into NO_2. Furthermore, NO_2 is of particular environmental concern, as it is directly toxic and acts as a precursor to tropospheric ozone and secondary particulate matter [35].

For this reason, emissions are usually reported in terms of the aggregate quantity NO_x = NO + NO_2

1.3. Strategies for NO_x Mitigation

Given the near-inevitability of NO_x formation in high-temperature, air-breathing combustion systems, considerable research has been devoted to developing methods that suppress emissions while maintaining stable and efficient operation. The strategies employed span operating practices, dilution approaches, and advanced combustor concepts, each targeting different aspects of the formation pathways discussed previously.

A widely used operational strategy is lean premixing, in which fuel and air are thoroughly mixed before combustion to achieve overall lean equivalence ratios. This lowers the flame temperature and thereby reduces the exponential sensitivity of thermal NO formation [11]. However, lean premixing increases susceptibility to flame instability and flashback, especially for highly reactive fuels such as hydrogen. Other established methods include staged combustion, which distributes heat release across multiple zones to avoid localized temperature peaks, and exhaust gas recirculation (EGR), in which part of the exhaust is mixed back with the incoming charge to dilute oxygen and add heat capacity, both of which suppress NO production [36, 37].

In addition to operational control, dilution methods are frequently employed to reduce NO_x. Injection of inert species such as nitrogen, carbon dioxide, or water increases the effective heat capacity of the working fluid, thereby lowering adiabatic flame temperatures and slowing NO formation rates. Among these, steam

or water injection has attracted particular attention due to its effectiveness in both laboratory and practical combustors. Unlike gaseous diluents, water undergoes phase change, providing additional cooling through latent heat absorption and modifying radical chemistry in the flame zone [36, 38, 39].

More advanced combustor concepts pursue architectural solutions to NO_x control. Rich-quench-lean (RQL) combustors are the most widely adopted low-NO_x architecture in aero-engine applications, where fuel-rich primary zones are followed by rapid dilution to limit peak flame temperatures [37]. Other approaches include low-swirl burners, which promote stable, distributed flames under lean conditions, and catalytic combustors, which oxidize fuels at lower temperatures than conventional flames [36, 37]. While effective, many of these designs require dedicated hardware layouts and are generally integrated at the engine design stage rather than as retrofit solutions.

In contrast, steam or water injection offers a practical alternative that can be implemented with limited modification to existing combustion hardware, especially for power generation systems. This approach is therefore attractive both in experimental research and in industrial systems where external control of NO_x is required without redesigning the combustor. Steam and water addition have been investigated extensively as direct NO_x suppression strategies in laboratory-scale flames and gas turbine environments.

A notable example is Pratt & Whitney's HySIITE (Hydrogen Steam Injected Intercooled Turbine Engine) concept, which couples hydrogen combustion with exhaust water recovery and re-injection of steam. According to the company this approach has demonstrated the potential for a 35% improvement in energy efficiency relative to current single aisle propulsion systems, while rig tests showed up to a 99.3% reduction in NO_x emissions [40]. The system design reclaims approximately one gallon of water every three seconds from the exhaust stream, feeding it back into the steam loop to create a closed cycle that mitigates weight penalties.

Having established the theoretical background of NO_x formation and its mitigation, the next chapter turns to the behavior and characterization of hydrogen flames. This provides the necessary foundation for understanding how the unique properties of hydrogen, including high diffusivity, wide flammability limits, and strong thermo-diffusive instabilities, shape flame structure and stability in both laboratory and practical contexts. These characteristics are essential to interpret not only the baseline behavior of hydrogen combustion but also its response to dilution and mitigation strategies such as steam injection.

2

Behaviour and Characterisation of Hydrogen Flames

As discussed in the previous chapter, hydrogen combustion leads to unique flame and combustion properties. In this chapter, different aspects of hydrogen flames will be investigated in depth.

2.1. Flame Structure

Premixed hydrogen flames comprise a thin reaction zone embedded within a broader preheat layer, and their structure is governed by transport–chemistry coupling that differs markedly from hydrocarbon baselines. The principal distinctions stem from the high molecular diffusivity of H_2 and the resulting effective Lewis number below unity in lean mixtures, which amplifies preferential diffusion, curvature and stretch sensitivity, cellular front formation, and local variations in burning rate [20, 41, 13]. These effects control how the flame anchors, wrinkles, and responds to strain, thereby setting stability margins in canonical jets and in swirl-stabilised configurations relevant to gas turbines [20, 42].

Preferential diffusion and cellularity at $Le < 1$

A defining feature of lean premixed hydrogen flames is an effective Lewis number below unity, $Le = \alpha/D_{\mathrm{H_2}} < 1$, where α is the thermal diffusivity and $D_{\mathrm{H_2}}$ is the mass diffusivity of hydrogen in the mixture. When $Le < 1$, fuel diffuses toward the reaction zone faster than heat diffuses away, which enriches convex flame segments that face the incoming reactants and depletes concave segments. This imbalance couples with flame curvature and stretch, producing spatial variations in local burning rate and predisposing the front to thermo-diffusive instability [41, 20, 13]. In practical terms, lean hydrogen flames become thinner and more corrugated than hydrocarbon baselines, and they display enhanced sensitivity to aerodynamic strain and to geometric confinement [42, 43].

Figure 2.1 illustrates how $Le < 1$ couples fuel diffusion with curvature, enriching cusps and depleting troughs and thereby modifying the local burning velocity.

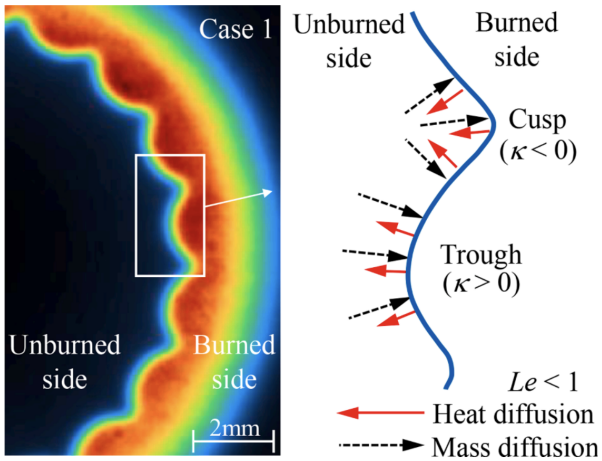


Figure 2.1: Curvature–diffusion schematic for lean premixed flames with $Le < 1$. Red arrows indicate heat diffusion, black arrows indicate fuel mass diffusion. Curvature is defined as $\kappa > 0$ for a front convex toward the reactants and $\kappa < 0$ for a front concave toward the reactants, and for $Le < 1$ the convex cusps are locally fuel-enriched while the concave troughs are fuel-depleted. The schematic summarises behaviour observed in laminar H_2/CH_4/air polyhedral (Bunsen-type) flames at atmospheric pressure with 50–83% H_2, $\phi = 0.53$–0.64, and bulk velocities 1.65–2.50 m s^{-1}, where cusps are enriched and troughs depleted due to differential diffusion [44].

Linear stability analyses of premixed flames, together with weakly nonlinear theory and direct numerical simulation, show that for sufficiently sub-unity Le small perturbations on an initially planar front grow rather than decay. The growth rate increases with mixture reactivity and with the magnitude of transport imbalance, and a finite band of unstable wavenumbers leads to the emergence of cellular structures on the flame surface. These cells increase flame-surface area and integrated consumption rate, while creating negatively curved pockets prone to near-extinction under high stretch [41, 20]. Experiments at lean equivalence ratios confirm the appearance of cellularity and fine-scale wrinkling in hydrogen and hydrogen-enriched flames under conditions where comparable methane flames remain smooth, which is consistent with the lower Le of hydrogen mixtures and the associated curvature–diffusion coupling [13, 43].

Figure 2.2 contrasts CH_4/air and H_2/air at matched conditions and shows the thinner and more cellular hydrogen reaction zone that results from thermo-diffusive imbalance.

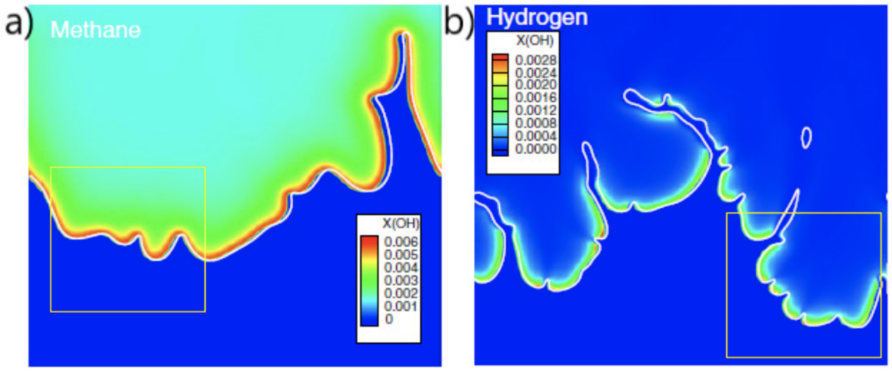


Figure 2.2: OH mole-fraction fields as reaction-zone markers for lean premixed flames at matched conditions. Panel (a) CH_4/air with $Le \approx 1$, panel (b) H_2/air with $Le < 1$. The hydrogen case shows a thinner reaction layer and pronounced cellular corrugations, consistent with thermo-diffusive imbalance. Fields reproduced from modelling of CH_4/H_2/air flames that includes stretch, heat loss and non-unity Le, applied to an atmospheric bluff-body-stabilised configuration [45].

Preferential diffusion also sets the sign and magnitude of the flame's response to curvature and stretch, commonly summarised by a Markstein-type sensitivity: for $Le < 1$, positively curved elements (convex toward the reactants) accelerate, while negatively curved elements are fuel-starved and decelerate. This asymmetry broadens the distribution of instantaneous burning rates across the front and explains the frequent observation of alternating bright and dim reaction zones in planar imaging of lean hydrogen flames. In hydrogen-enriched methane mixtures the same mechanisms appear with reduced intensity, and the threshold for visible cellularity shifts to leaner conditions as the hydrogen fraction is lowered [20, 13, 42].

The implications for combustor-relevant configurations are twofold. First, in shear layers and near swirl-induced recirculation zones, curvature and strain are naturally large, so $Le < 1$ effects strongly influence anchoring location and stability margins. Second, in turbulent flows that lie in the thin-reaction-zone regime, small-scale motions wrinkle the preheat layer while the reaction sheet remains thin, and the differential diffusion characteristic of hydrogen alters classical turbulent-flame scalings by shifting curvature statistics and local extinction criteria. These consequences have been documented in atmospheric laboratory flames and are expected to persist at elevated pressure with quantitative shifts in the instability bounds, which is important when interpreting engine-relevant conditions [43, 20, 42].

Turbulence–flame interaction in lean hydrogen flames

The curvature–diffusion effects described above do not disappear in turbulence, they are redistributed by eddies across many scales. In laboratory burners, lean hydrogen–air flames often sit in the thin–reaction–zone regime, where turbulence wrinkles the preheat layer while the inner reaction sheet remains thin [42, 20, 43]. In this setting, $Le < 1$ does not introduce a new regime, it modifies how local geometry and kinematics influence the burning rate, with positively curved cusps tending to accelerate and negatively curved troughs tending to slow.

Two time–scale ratios help organise this picture. The Damköhler number compares the time needed for chemistry with the time of the large eddies, $Da = \tau_{\text{chem}}/\tau_{\text{turb}}$. When Da is large, chemistry keeps pace with the flow and the flame behaves like a wrinkled sheet. When Da is small, large eddies rearrange the mixture before reactions can complete [42, 20]. The Karlovitz number compares the flame time with the time of the smallest eddies, $Ka = (\tau_F/\tau_\eta)^{1/2}$. Small Ka means the smallest eddies are too slow to disturb the thin reaction layer, intermediate Ka corresponds to thin–reaction–zone behaviour, large Ka approaches conditions where even the smallest eddies disrupt the inner layer [42, 20]. For lean hydrogen at 1 bar, a larger laminar flame speed s_L and a smaller thermal thickness δ_L than methane shift these boundaries for quenching and wrinkling, yet many canonical configurations still fall within the thin–reaction–zone band [42, 13, 43].

The statistical outcome is consistent across measurements and simulations. Lean H_2 and H_2–enriched flames exhibit higher flame–surface density and broader distributions of curvature, strain, and instantaneous normal propagation speed s_n than CH_4 at matched (Da, Ka) [43, 20]. The sub–unity Lewis number biases the local response, cusps are more likely to carry high burning rates and troughs are more likely to host pockets that evolve toward near–extinction. The resulting heat–release field often appears patchy or cellular, even when global conditions place the flame in the thin–reaction–zone regime [42, 43].

These trends matter for practical combustors. At fixed bulk flow and equivalence ratio, raising the hydrogen fraction increases wrinkling and the spread of s_n, which narrows blow–off margins through greater exposure to local strain in troughs, while the larger s_L tends to reduce global lift–off. In confined swirl burners, where strong mean curvature and shear are intrinsic, anchoring shifts toward the inner shear layer and the upstream edge of the central recirculation zone, and aerodynamic adjustments that push vortex breakdown downstream are often used to recover flashback margin under hydrogen enrichment [20, 43]. Similar behaviours are expected at elevated pressure, although quantitative thresholds for local extinction and instability shift with pressure and temperature, which should be noted when extrapolating atmospheric results to engine conditions [20, 42].

Figure 2.3 compares instantaneous and time-averaged OH-PLIF across swirl numbers and hydrogen fractions. As η_{H_2} increases, the instantaneous fields exhibit finer cellular corrugations and a thinner reaction layer, consistent with sub-unity Lewis number behaviour. Increasing S enhances shear and recirculation, which broadens the time-averaged reaction zone (flame brush). These trends are qualitative; rigorous quantification of wrinkling requires front detection and statistics such as flame-surface density.

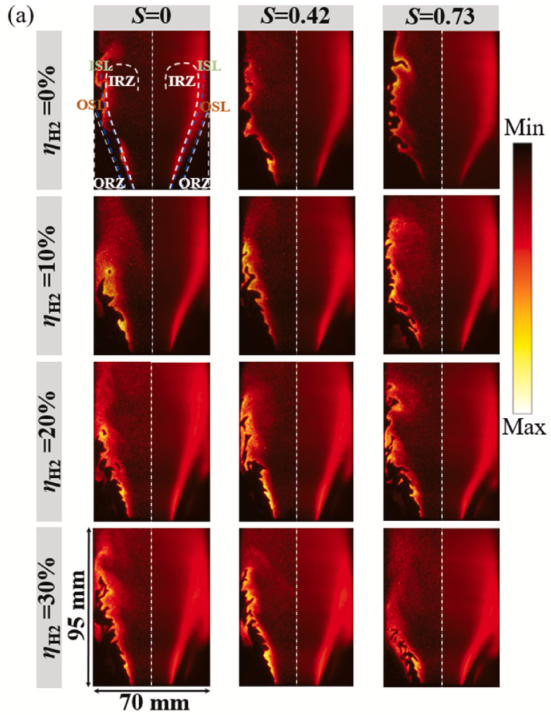


Figure 2.3: Instantaneous (left halves) and time-averaged (right halves) OH-PLIF for a premixed bluff-body/swirl burner at $U_{\text{in}} = 6$ m s^{-1} and $\phi = 0.6$, for swirl numbers $S = 0,\ 0.42,\ 0.73$ and hydrogen volume fractions $\eta_{\text{H}_2} = 0$–30% [46]. Increasing η_{H_2} produces a thinner, more corrugated reaction layer consistent with $Le < 1$ effects, while higher S strengthens large-scale shear/recirculation. The instantaneous frames show finer cellular structure at larger η_{H_2}, and the time-averaged frames indicate a broader flame brush at higher S. OH-PLIF is used here as a qualitative marker of the reaction zone; quantitative wrinkling would require front extraction and flame-surface-density analysis.

Stabilisation and anchoring in swirl/shear flows

In premixed hydrogen–air swirl combustors, anchoring is set by the interaction between the central recirculation zone (CRZ) created by vortex breakdown and the fast, thin H_2 flame. Hot products in the CRZ ignite incoming reactants along the inner shear layer (ISL), which is the primary attachment line; secondary attachment can occur on the outer shear layer (OSL) at the injector lip or bluff body [42, 20, 43]. For H_2 mixtures the larger laminar flame speed s_L, smaller thermal thickness δ_L, and $Le < 1$ bias, which accelerates positively curved cusps, all favor upstream attachment on the ISL and shorter lift-off at a given bulk flow.

Figure 2.4 summarizes the flow features that govern flameholding in premixed swirl combustors. Vortex breakdown creates an inner recirculation zone (IRZ) bounded by the inner and outer shear layers (ISL, OSL); hot products recirculating in the IRZ ignite incoming reactants along the ISL, establishing the primary attachment line. In lean hydrogen mixtures, higher s_L, smaller δ_L, and sub-unity Le bias attachment closer to the ISL and shorten lift-off at a given bulk flow, which has direct implications for flashback margin.

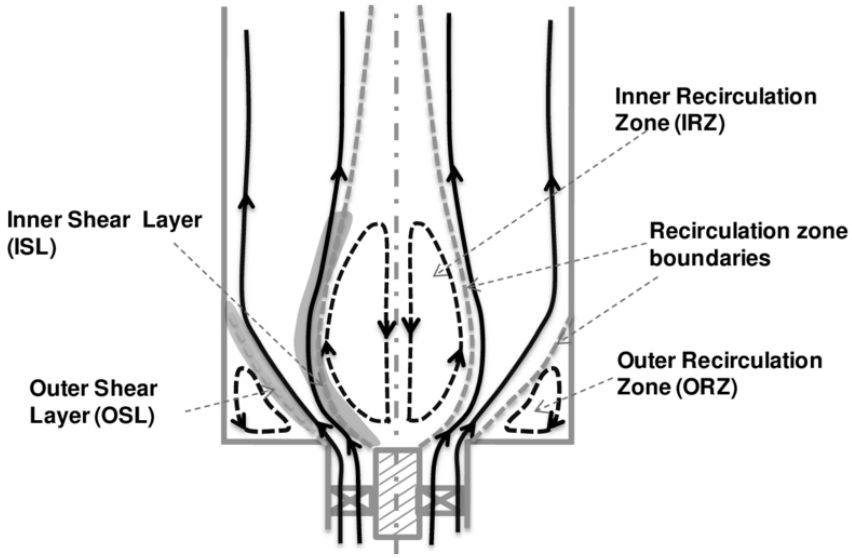


Figure 2.4: Schematic of a premixed swirl combustor showing the inner recirculation zone (IRZ) produced by vortex breakdown, and the inner and outer shear layers (ISL, OSL). Hot products in the IRZ recirculate upstream and ignite the incoming reactants along the ISL, which is the primary attachment line. In lean hydrogen flames, larger s_L, smaller δ_L, and sub-unity Le bias attachment closer to the ISL and reduce lift-off at a given bulk flow, which also tightens flashback margin. [47].

Swirl level controls the CRZ and therefore the anchoring point. Increasing swirl enlarges the CRZ and moves the stagnation point upstream, which strengthens recirculation and reduces lift-off height; excessive swirl, together with H_2's high reactivity, can bring the reaction zone close to the injector, narrowing flashback margin [20, 42]. Geometric confinement and lip shape set shear and heat loss near the attachment line, which are more influential for thin H_2 flames than for methane because conductive and convective losses more readily perturb a thin reaction zone [43].

Hydrogen properties also alter failure modes. Boundary-layer and core flashback are promoted by high s_L and by the adverse pressure gradient near breakdown, and combustion-induced vortex breakdown can occur at lower thresholds than with methane under comparable conditions [48, 43]. Practical levers that recover stability include moderating swirl, adding an axial jet to shift breakdown downstream, smoothing or cooling near-wall regions, operating slightly leaner, and applying controlled dilution (e.g., steam) to reduce peak temperature and reactivity without eliminating the CRZ [20, 43].

In summary, swirl stabilization mechanisms are generic, but hydrogen's higher s_L, thinner δ_L, and sub-unity Le shift attachment toward the ISL and reduce lift-off while simultaneously tightening flashback margins. These trends motivate careful control of swirl, confinement, and local heat losses in hydrogen-capable premixed combustors.

2.2. Temperature field and peak flame temperature

Temperature governs reaction rates, species partitioning, and pollutant formation in premixed flames. Locally along the flame normal, reactants at T_{in} are heated through a diffusive preheat layer where chemistry is slow, then pass a thin reaction layer where heat release and radical production are concentrated, and finally relax toward a post-flame state near the adiabatic flame temperature T_{ad} [13, 20]. The thickness of the thermal layer δ_L and the location of the temperature peak depend on transport, elementary kinetics, and heat loss. In low-loss flames the temperature rise is monotonic and the post-flame temperature approaches T_{ad}, whereas confinement and radiation lower the attained temperature and can shift the peak toward the reaction zone [13, 11].

A useful starting point is the adiabatic limit. For a specified mixture, T_{ad} follows from an enthalpy balance assuming complete heat release and no losses, and it varies systematically with equivalence ratio ϕ, initial temperature T_{in}, pressure p, and any diluents. At $p = 1$ bar and $T_{\text{in}} \approx 300$ K, stoichiometric H_2/air reaches

$T_{ad} \approx 2400$ K, while CH_4/air reaches $T_{ad} \approx 2220$ K, differences that arise from product heat capacities and dissociation behaviour [11, 12]. For both fuels, T_{ad} increases from lean to near-stoichiometric conditions, peaks slightly on the rich side, then decreases in very rich mixtures as incomplete oxidation and dissociation grow [13, 11]. Raising T_{in} increases T_{ad} approximately linearly for small changes, and increasing p at fixed ϕ and T_{in} generally raises T_{ad} modestly because higher pressure suppresses dissociation, with mixture-dependent magnitude [11, 49]. Added diluents such as N_2, CO_2, or H_2O reduce T_{ad} through heat capacity, and liquid water injection introduces an additional latent-heat sink upstream of the flame [11].

Against this backdrop, the thermochemistry of hydrogen and methane leads to systematic differences in the attained temperatures. For the same p, T_{in} and ϕ, equilibrium calculations show that H_2/air reaches a higher adiabatic flame temperature than CH_4/air [11, 12]. Part of this difference comes from the product mixture. Hydrogen–air combustion yields products that are mainly H_2O with N_2, whereas methane–air produces a CO_2 plus H_2O mixture with N_2. At flame temperatures CO_2 has a higher effective heat capacity than H_2O, therefore the same released chemical energy produces a smaller temperature rise when CO_2 is abundant. A second contribution is inert dilution. Per unit heat released, methane requires more O_2 than hydrogen, so stoichiometric CH_4/air carries more accompanying N_2 into the products, which further lowers T_{ad}. A third contribution is high temperature dissociation. CO_2 dissociates appreciably to CO and O_2, which is endothermic and provides an additional energy sink compared with the dissociation pattern in water rich hydrogen flames. A further contribution is the higher heat release per unit oxidizer for hydrogen, since H_2 releases about 484 kJ per mol of O_2 compared with about 401 kJ per mol of O_2 for CH_4, so for the same amount of air the hydrogen flame deposits more sensible energy into the products. Taken together, these effects place stoichiometric H_2/air near ~ 2400 K and CH_4/air near ~ 2220 K at 1 bar and room temperature inlets [11, 12].

The trend described above is illustrated in Figure 2.5, which compares equilibrium adiabatic flame temperature versus equivalence ratio for H_2/air, CH_4/air, and CO/air at 1 bar and $T_{in} \approx 300$ K. Hydrogen lies systematically above methane across lean to slightly rich mixtures, peaking a little to the rich side and then decreasing as dissociation grows at very rich conditions. The plot captures the combined influence of product heat capacities and high–temperature dissociation on T_{ad}; exact values depend on p, T_{in}, and diluents.

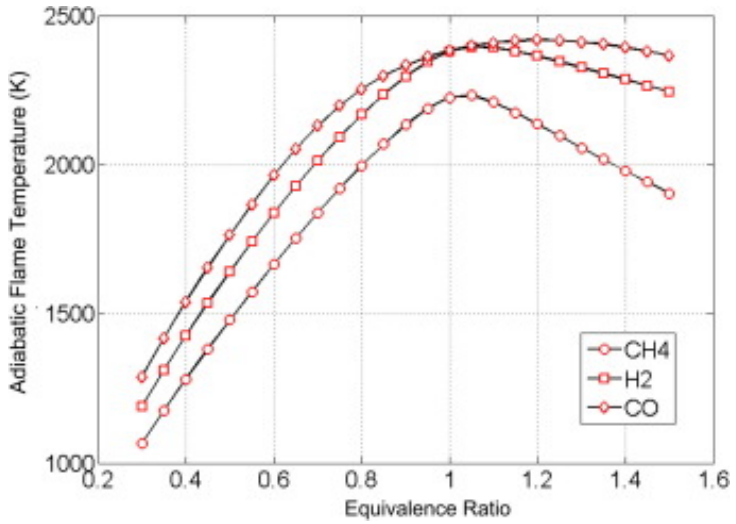


Figure 2.5: Adiabatic flame temperature T_{ad} versus equivalence ratio ϕ for CH_4/air, H_2/air, and CO/air at $p = 1$ bar and $T_{in} \approx 300$ K. Hydrogen reaches higher T_{ad} than methane over lean to slightly rich conditions, consistent with a product slate dominated by H_2O and different dissociation behaviour relative to CO_2–rich hydrocarbon products. Figure adapted from ScienceDirect Topics [50].

The higher T_{ad} of hydrogen, combined with its shorter chemical time scales and thinner thermal layer, yields a steeper temperature rise across the reaction zone in lean premixed operation. This steepening increases the propensity for high–temperature pathways of NO formation, a topic developed in Section 1.2.1 [13, 11, 12]. When hydrogen is blended into methane, T_{ad} at fixed ϕ and T_{in} shifts toward the hydrogen limit,

whereas added diluents such as steam counteract that trend by raising the mixture heat capacity and, for liquid injection upstream, adding a latent–heat sink; the net effect depends on blend fraction and dilution level [11].

Below in Figure 2.6, an image from Troiani et al. is presented, showing the NO_x emissions against equivalence ratio and H_2 blend fraction variables in H_2-CH_4 blend fuels. As NO_x emissions are very sensitive the flame temperature, the NO_x emissions results are a great indication of the flame temperatures. As it can be observed in Figure 2.6, the NO_x emissions are highest around equivalence ratio of 1 and the emissions get higher as the H_2 fraction increases, indicating higher flame temperatures for H_2 flames.

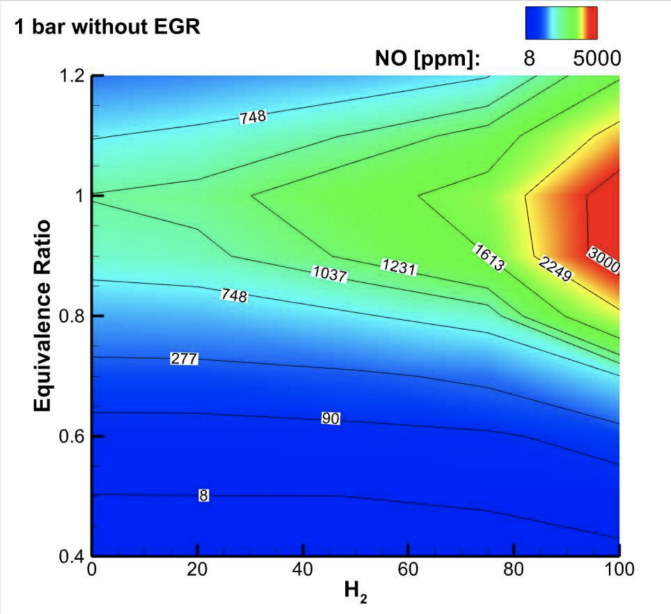


Figure 2.6: NOx emissions in ppm vs equivalence ratio and hydrogen content for a CH4/ H2 blend reacting with air [51]

Real combustors depart from the adiabatic ideal because heat is lost and residence times are finite. Wall conduction, radiation, and gas-side convection lower the measured peak, and these effects are more influential for thin hydrogen flames because the reaction layer often lies close to walls or bluff bodies in compact geometries. Aerodynamic stretch further modifies local temperature by reducing residence time in the high-temperature zone and by altering radical pools [43, 20]. Consequently, post-flame temperatures should be interpreted together with the thermal environment and flow topology when extrapolating laboratory measurements to engine-relevant conditions.

These temperature trends have direct implications for both emissions and operability. Peak temperature controls the exponential sensitivity of thermal NO production and co-determines stability margins through its influence on reaction rates. Accurate temperature characterisation is therefore central in hydrogen flame studies. Common diagnostics include Rayleigh thermometry for absolute fields, line-of-sight absorption or emission thermometry for path-averaged values, and thermocouples with radiation and conduction corrections; OH^* chemiluminescence is a useful qualitative heat-release marker but does not provide temperature directly [43, 20, 13]. Reported temperatures should be accompanied by T_{in}, p, ϕ, and dilution levels to enable comparison with equilibrium calculations or NASA CEA outputs [49].

2.3. Laminar flame speed

The laminar burning velocity s_L is the normal propagation speed of a steady, planar, one–dimensional premixed flame relative to the unburned mixture. It sets the intrinsic reactivity scale of a mixture, enters flame–stability and anchoring criteria, and is a key input to turbulent–flame regime maps [13, 20, 42]. For given fuel–air composition, s_L depends on equivalence ratio ϕ, unburned temperature T_u, pressure p, and any diluents. In low–loss conditions at $p = 1$ bar, stoichiometric H_2/air has $s_L \approx 2.0$–2.5 m/s, whereas

CH_4/air has $s_L \approx 0.35$–0.45 m/s, consistent with faster chemistry and thinner thermal layers for hydrogen [13, 43, 12].

The dependence on ϕ is non-monotonic. For both fuels s_L rises from lean mixtures to a maximum near, but not necessarily exactly at, stoichiometry, then decreases on the rich side as incomplete oxidation and product dilution grow. The location and height of the peak reflect the competition between increased radical production at higher fuel availability and reduced thermal diffusivity and heat release in very rich mixtures [13, 11]. At fixed p and T_u, hydrogen–air curves lie above methane–air curves and retain appreciable values farther into the lean regime, which is consistent with the wider flammability range of hydrogen.

Representative measurements at $T_u \approx 295$ K and $p = 1$ bar are compiled in Figure 2.7. For hydrogen–air, datasets from Dowdy et al. [52], Kwon and Faeth [53], Tse et al. [54], and Kuznetsov et al. [55], as collated by Ghosh et al. [56], cluster around $s_L \sim 2$–2.7 m/s near slightly rich conditions, with appreciable values persisting far into the lean regime. For methane–air, measurements from Hermanns et al. [57], Goswami et al. [58], and Mazas et al. [59] peak around $s_L \sim 0.35$–0.40 m/s. The figure also illustrates typical inter-study scatter due to diagnostics and stretch corrections, yet the trends are robust: H_2/air propagates substantially faster than CH_4/air at comparable ϕ, consistent with faster chain-branching chemistry and thinner thermal layers discussed earlier.

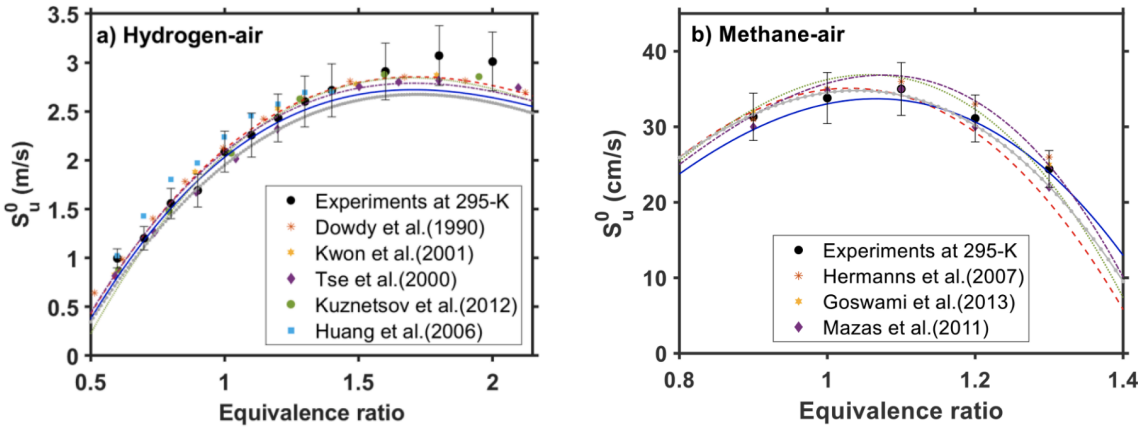


Figure 2.7: Laminar burning velocity s_L versus equivalence ratio at $T_u \approx 295$ K and $p = 1$ bar, compiled from multiple studies [56]. Note the different vertical units, m/s for hydrogen and cm/s for methane. The non-monotonic dependence on ϕ and the substantially higher s_L for H_2 are evident across datasets.

Temperature and pressure exert strong parametric on the flame speed. Over practical ranges the variation is often captured with power-law scalings following Metghalchi and Keck's work and studies [60]:

$$s_L(\phi, T_u, p) \;\approx\; s_{L,0}(\phi) \left(\frac{T_u}{T_{\text{ref}}}\right)^{\alpha(\phi)} \left(\frac{p}{p_{\text{ref}}}\right)^{\beta(\phi)} \tag{2.1}$$

where $s_{L,0}(\phi)$ is the burning velocity at reference conditions $(T_{\text{ref}}, p_{\text{ref}})$, $\alpha > 0$ is a temperature exponent, and $\beta < 0$ is a pressure exponent [60]. Typical values are $\alpha \sim 1.5$–2.0 and $\beta \sim -0.2$ to -0.5, with exact exponents depending on fuel, ϕ, and kinetic mechanism [20, 13, 11]. Physically, higher T_u accelerates elementary reactions and steepens thermal gradients, while higher p enhances three-body recombination and raises product heat capacities, both of which lengthen chemical times and reduce s_L.

Dilution and composition changes modify s_L through heat capacity loading and chemistry. Adding diluents such as N_2, CO_2, or H_2O lowers flame temperature and slows chain branching, which reduces s_L. At equal volume fraction, CO_2 typically suppresses s_L more than N_2 because of its higher heat capacity and participation in recombination chemistry [12, 11]. Water vapor exerts a similarly strong influence, it increases the mixture heat capacity and, through high third body efficiencies, it promotes radical recombination (e.g. H + OH + M $\rightarrow$ H_2O + M, H + O_2 + M $\rightarrow$ HO_2 + M), which lowers the H and O pools and shifts the OH/HO_2 balance, further reducing s_L; measurements in oxygen enriched and air flames show that at matched volumetric addition H_2O can depress s_L more than N_2 and comparably to CO_2 [59, 61, 62, 12].

Conversely, enriching CH_4/air with H_2 increases s_L at fixed ϕ and T_u, both because hydrogen chemistry is faster and because the effective Lewis number decreases toward unity or below, which reduces diffusive inhibition on the lean side [13, 43]. The same enrichment that raises s_L also narrows flashback margin in premixers and shifts anchoring upstream in shear and swirl flows, points returned to in the stabilization subsection.

Dilution and composition changes modify s_L through heat-capacity loading and chemistry. Adding inert N_2, CO_2, or H_2O lowers flame temperature and slows chain-branching, which reduces s_L; CO_2 typically has a stronger effect than N_2 at equal volume fraction due to higher heat capacity and participation in recombination reactions [12, 11]. Conversely, enriching CH_4/air with H_2 increases s_L at fixed ϕ and T_u, both because hydrogen chemistry is faster and because the effective Lewis number decreases toward unity or below, which reduces diffusive inhibition on the lean side [13, 43]. The same enrichment that raises s_L also narrows flashback margin in premixers and shifts anchoring upstream in shear and swirl flows, points returned to in the stabilization subsection.

The trends above provide two takeaways for hydrogen-relevant combustors. First, at otherwise similar conditions hydrogen mixtures propagate substantially faster than methane mixtures, which supports stable lean operation but increases flashback risk in premixing passages. Second, s_L can be tailored by inlet heating, pressure, and controlled dilution, allowing a degree of reactivity management independent of equivalence ratio. These points will be used later when discussing stability margins and the interplay between flame speed, residence time, and NO formation.

Summary and outlook

This chapter clarified how lean premixed hydrogen flames differ from hydrocarbon baselines in ways that govern stability, reactivity, and emissions. Sub-unity effective Lewis number couples diffusion to curvature and stretch, which produces thinner, more cellular fronts and a broader spread of local burning rates than in methane. Thermochemistry explains the higher adiabatic flame temperatures of H_2/air at matched p, T_{in}, and ϕ, through lower effective product heat capacity, different high-temperature dissociation, higher heat release per unit oxidizer, and less inert dilution. Consistent with this, laminar burning velocities of H_2/air exceed CH_4/air by factors of several, remain appreciable deeper into the lean regime, and show well documented dependences on unburned temperature and pressure.

Following from this, the next chapter reviews steam and water injection as NO_x mitigation strategies in premixed systems relevant to hydrogen. The focus is on three interacting mechanisms, reduction of peak flame temperature, chemical modification of the H/O/OH radical pool including the strong third-body efficiencies of H_2O, and flow or residence-time changes in the high-temperature region. The review distinguishes land-based gas turbines from aviation concepts and highlights cases where H_2O addition can simultaneously reduce NO_x and, with appropriate cycle integration, improve overall efficiency.

3

Water/Steam Injection in Combustion

This chapter examines the role of water and steam injection in premixed combustion with emphasis on NO_x formation mechanisms and gas-turbine–relevant configurations. The first part explains how H_2O addition modifies flame temperature, residence time, and radical chemistry, establishing the physical and chemical basis for NO_x suppression. The second part reviews experimental and numerical findings from the literature on hydrogen and hydrogen–methane mixtures, comparing steam injection strategies, injector configurations, and operating conditions at both atmospheric and elevated pressures. Particular attention is given to how reported NO_x trends should be interpreted when changes in equivalence ratio or adiabatic flame temperature are involved, and to practical implementation factors such as injection location and evaporation completeness. This chapter provides the framework required to connect fundamental mechanisms with combustor-scale behavior and motivates the experimental approach developed in the next chapter.

3.1. Steam and Water Injection: Mechanisms of NO_x Suppression

Steam and water injection reduce NO_x by acting on the core levers that control nitrogen fixation in flames: peak temperature, radical pool composition, and residence time in the high-temperature zone. In contrast to large architectural changes, dilution with H_2O can be implemented with limited hardware modifications and is therefore of practical interest across laboratory and industrial systems [36, 37].

Thermal effect: lowering the adiabatic flame temperature

The most direct way in which steam or water injection suppresses NO_x formation is through a reduction of the adiabatic flame temperature. Because thermal NO is exponentially sensitive to temperature (Sec. 1.2.1), even modest decreases of 100–200 K can reduce NO production by several fold [11, 36].

The adiabatic flame temperature T_{ad} is obtained from an overall energy balance in which the chemical enthalpy released by the fuel is distributed into heating the combustion products and any injected streams:

$$\sum_{k\in\mathrm{prod}} n_k \int_{T_{\mathrm{in}}}^{T_{\mathrm{ad}}} c_{p,k}(T)\,dT = -\Delta h_{\mathrm{rxn}}(T_{\mathrm{in}}) - \dot{m}_\ell\, h_{\mathrm{vap}}(T_{\mathrm{inj}}) - \sum_{j\in\mathrm{inj}} \dot{m}_j \int_{T_{\mathrm{in}}}^{T_{\mathrm{inj}}} c_{p,j}(T)\,dT. \tag{3.1}$$

Here n_k and $c_{p,k}$ denote the mole number and heat capacity of each combustion product, Δh_{rxn} is the enthalpy of reaction of the fuel–air mixture at the inlet temperature T_{in}, and the additional terms on the right-hand side account for the energy required to heat and, if necessary, evaporate the injected fluid. In the case of liquid water injection, the latent heat of vaporization h_{vap} represents a strong cooling sink, in addition to the sensible heating required to raise the liquid from injection temperature T_{inj} to its evaporation point. When steam is injected instead, the latent-heat term is absent, but the sensible heating contribution remains if the steam enters colder than the flame gases. In both cases, the added H_2O substantially increases the total heat capacity of the mixture, forcing the equilibrium temperature T_{ad} to shift downward.

Thus, while liquid water injection achieves stronger temperature reductions per unit mass flow because of the additional latent heat sink, both water and steam injection reduce flame temperature through dilution and heat-capacity effects. The resulting decrease in T_{ad} directly suppresses thermal NO formation and represents the most robust and well-documented mechanism of NO_x control by H_2O addition.

Dilution and residence-time effects
In addition to lowering flame temperature, the presence of water or steam can influence NO formation through modifications to the residence time in high-temperature regions. A commonly used control-volume estimate for the residence time is

$$\tau_{\mathrm{htz}} \sim \frac{V_{\mathrm{htz}}}{\dot{m}/\bar{\rho}}, \tag{3.2}$$

where V_{htz} is the effective volume of the high-temperature zone, $\dot{m}$ is the bulk mass flow rate, and $\bar{\rho}$ is the mean gas density in that region. This relation follows from the definition of residence time as the ratio of control volume to volumetric flow rate and should be interpreted as an approximate global measure rather than a local property, since real flames exhibit strong spatial variations in both velocity and density [11, 42, 37]. The dependence on $\bar{\rho}$ highlights the role of dilution: adding steam or water increases the average gas density, which, for fixed $\dot{m}$ and V_{htz}, leads to a lower volumetric flow rate and therefore a longer mean residence time.

In practice, however, the impact of H_2O addition on effective residence time is more complex than this bulk estimate suggests. Experimental and numerical studies have shown that steam injection can alter the flow field itself, for example by weakening the recirculation zone in swirl-stabilized combustors or by lifting the flame front downstream [25, 63]. Such aerodynamic modifications tend to reduce the actual time that fluid elements spend in the peak-temperature zone where NO production is most rapid, even if the mean density has increased. The result is that steam addition may simultaneously increase the nominal residence time of the mixture while decreasing the effective residence time relevant for thermal-NO formation.

Overall, the effect of steam or water injection on residence time depends on how it is defined. From a bulk control-volume perspective, adding H_2O increases the mean gas density $\bar{\rho}$, which for fixed V_{htz} and $\dot{m}$ reduces the volumetric flow rate and therefore increases the nominal residence time τ_{htz}. However, experimental and numerical studies consistently show that steam also alters the flow field, for example by weakening recirculation or lifting the flame downstream, which reduces the actual time that gases spend in the high-temperature core where NO is produced most rapidly [25, 63]. Thus, while bulk estimates suggest longer residence times, the effective residence time relevant to NO formation is often shortened in practice. The combined effect of lower peak temperatures and reduced high-temperature exposure explains much of the NO suppression observed under steam- or water-diluted conditions.

Chemical effect: modification of the radical pool
Steam affects key H/O/OH radical pathways that couple to NO formation:

$$\mathrm{H} + \mathrm{OH} + \mathrm{M} \rightarrow \mathrm{H_2O} + \mathrm{M}, \tag{3.3}$$
$$\mathrm{H} + \mathrm{O_2} + \mathrm{M} \rightarrow \mathrm{HO_2} + \mathrm{M}, \tag{3.4}$$
$$\mathrm{NO} + \mathrm{OH} \rightleftharpoons \mathrm{NO_2} + \mathrm{H}, \tag{3.5}$$
$$\mathrm{NO} + \mathrm{HO_2} \rightarrow \mathrm{NO_2} + \mathrm{OH}. \tag{3.6}$$

By promoting three-body recombination and HO_2 formation, added H_2O generally lowers the concentrations of highly reactive H and O atoms while altering the OH/HO_2 balance. Reduced [O] and [OH] directly slow the extended Zeldovich sequence (especially $\mathrm{N} + \mathrm{OH} \rightarrow \mathrm{NO} + \mathrm{H}$), complementing the thermal suppression. In hydrogen-rich flames, steam also shifts the H/O/OH pool via reactions like $\mathrm{H} + \mathrm{H_2O} \rightleftharpoons \mathrm{H_2} + \mathrm{OH}$, typically reducing H and O atom availability at a given T [61, 62]. The net outcome is a chemically mediated decrease of thermal-NO production beyond what is achieved by temperature reduction alone [36].

Third-body efficiencies of H_2O
Water is an efficient third body in key recombination reactions, commonly represented by an effective collider concentration,

$$[\mathrm{M}] = \sum_i \alpha_i [X_i], \tag{3.7}$$

where α_i are third-body collision efficiencies. Detailed H_2/O_2 mechanisms report $\alpha_{\mathrm{H_2O}}$ substantially greater than unity for reactions such as $\mathrm{H} + \mathrm{OH} + \mathrm{M} \rightarrow \mathrm{H_2O} + \mathrm{M}$ and $\mathrm{H} + \mathrm{O_2} + \mathrm{M} \rightarrow \mathrm{HO_2} + \mathrm{M}$, meaning H_2O enhances radical recombination rates relative to N_2 or O_2 as bath gases [61, 62]. This third-body effect

further depletes the radical pool that feeds thermal and NNH-related NO routes. A related consequence is increased collisional stabilization in termolecular steps (e.g. HO_2 formation), which can modestly shift NO/NO_2 partitioning in the cooler post-flame zone; since emissions are reported as NO_x = NO + NO_2, the net NO_x reduction still predominantly reflects the large decrease in thermal-NO production.

Water versus steam injection
Liquid-water injection provides the strongest local cooling because evaporation adds a latent-heat sink and enhances micro-mixing, but it risks local quenching, wall wetting, and increased CO/UHC if overused. Steam injection avoids evaporation transients and can be metered precisely; although it offers less cooling per unit mass, it still reduces NO_x effectively via heat capacity, dilution, and third-body chemistry. Both approaches have demonstrated substantial NO_x reductions in premixed methane and hydrogen flames at atmospheric pressure, with steam-to-air mass fractions up to ~ 20–30% delivering large decreases without catastrophic loss of stability when properly staged [38, 39]. Practical trade-offs include potential efficiency penalties, altered blow-off/flashback margins, and materials concerns due to elevated moisture levels [37]. Some studies also found that water injection can be a viable strategy for suppressing flashback occurrence in hydrogen while also causing significant reduction in NOx emissions [64].

Interaction with non-thermal NO routes
Under very lean, moderate-temperature conditions, the N_2O-intermediate pathway can contribute a measurable fraction of NO_x. Steam generally lowers its contribution by reducing temperature and radical availability; however, because H_2O is an effective collider, collisional stabilization processes (e.g. for HO_2 or, at pressure, N_2O) can compete. Experiments and reactor-network analyses indicate that the net effect of steam remains strongly favorable for NO_x reduction across methane and hydrogen premixed flames, including at constant flame temperature where purely chemical effects are isolated [38, 36].

The mechanistic framework above shows why steam and water injection are effective for NO_x control, but their broader role depends on the system of application. In stationary gas turbines, water injection is typically introduced to suppress emissions at the cost of efficiency, since the added mass flow and heat management reduce cycle performance [36, 37]. In aviation the focus has shifted toward integrating steam injection into the propulsion cycle in a way that delivers both environmental and performance benefits. This combined effect of emissions control and efficiency gain illustrates the different design philosophy between stationary and aviation contexts and underscores why steam and water injection continue to receive attention in hydrogen propulsion research.

In summary, steam and water injection provide a robust and multifaceted means of suppressing NO_x emissions by lowering flame temperatures, altering residence times in high-temperature zones, and modifying radical chemistry through third-body effects. Their effectiveness has been confirmed across both laboratory flames and practical gas turbine systems, with aviation-oriented concepts such as Pratt & Whitney's HySIITE program demonstrating that H_2O addition can simultaneously reduce NO_x and improve overall cycle efficiency. While the precise balance of thermal, chemical, and aerodynamic effects depends on operating conditions and injection strategies, the consistent outcome is a measurable reduction in NO_x emissions without requiring disruptive combustor redesigns.

3.2. Steam & Water Injection in Literature

This section surveys the available literature on adding water or steam to premixed flames in gas-turbine–relevant settings to establish what has been tried, under which conditions, what was found, and what those findings imply. The review spans atmospheric and pressurized studies on hydrogen and hydrogen–methane mixtures, compares steam against inert dilution, and covers both combustor-scale implementation (premixing versus direct injection, injector location and targeting, spray quality, evaporation completeness) and engine-level strategies (injection ahead of compressors versus in the combustor). For each study, the emphasis is on the reported NO_x outcomes together with carbon monoxide and operability, and on how to interpret results when equivalence ratio or adiabatic flame temperature are not held the same. From these comparisons, the chapter extracts common mechanisms and practical lessons that connect chemistry and thermal effects to hardware choices. It concludes by identifying a focused research gap: a consistent premixed, swirl-stabilized dataset for hydrogen and hydrogen–methane blends with steam at representative conditions that reports both ppm and $EINO_x$ and interprets CO and stability with temperature effects accounted for, which motivates the experiments presented in this thesis.

Mechanisms at atmospheric conditions. Lu et al. [65] investigated humidification effects in premixed hydrogen by operating a H_2/air micromix combustor at atmospheric pressure with steam or N_2 premixed on the oxidizer side while sweeping dilution ratio and equivalence ratio. Measurements show that, at matched operating points, the NO level with steam dilution is about 20–50% of the NO level with N_2 dilution. Of the total reduction, 50.8–92.1% is attributed to thermal and dilution effects and 5.8–15.8% to a direct chemical influence of H_2O on the radical pool. The remaining "third-body" effect is small; in their analysis it may slightly decrease or slightly increase NO depending on ϕ because added H_2O changes third-body collision efficiencies in key recombination steps, but its magnitude is minor compared with the thermal and direct-chemical contributions. Overall, the non-thermal terms act to weaken the NNH pathway, and the flame remained stable across the tested dilution and ϕ ranges, indicating that steam provides both the expected thermal benefit and a measurable chemical suppression of NO in premixed hydrogen flames [65].

Evidence that the reduction of NO_x is not purely thermal comes from atmospheric swirl-burner measurements on natural gas and hydrogen where steam or N_2 was premixed into the air up to about 30% of the air mass in a study by Göke and Paschereit [38]. The researchers explicitly report NO_x and CO < 10 ppm for both fuels at steam-injected conditions up to near-stoichiometric, whereas nitrogen dilution at comparable levels did not reduce NO_x. They attribute the extra benefit of steam to changes in the radical pool that limit thermal, N_2O, and NNH pathways via reduced O-atom availability, with prompt-NO increases noted for steam-injected natural gas cases. Interpreting these findings alongside the micromix results, this indicates that steam retains an advantage over an inert both when cooling dominates and when temperature effects are held approximately constant [38].

Complementary laminar data and kinetics are provided by Göckeler [66], who measured burning velocities of premixed methane, hydrogen-enriched methane, and hydrogen with steam dilution and developed a semi-empirical correlation for the decrease in burning velocity with steam mole fraction at fixed preheat temperature and equivalence ratio. One-dimensional simulations with a "virtual" inert species were used to separate pure dilution and thermal effects from chemistry; the comparison showed a non-negligible chemical influence of H_2O. Mechanistically, steam enhances chain-terminating recombination through higher third-body efficiency and shifts radical levels, yielding lower H and O and slightly higher OH compared with inert dilution. This change weakens thermal, N_2O, and NNH NO pathways over a broad range of conditions, consistent with the chemical component inferred in premixed hydrogen by Lu et al. [65] and with the advantage of steam over N_2 observed in the swirl-burner data of Göke and Paschereit [38].

Concetti et al. [63] analyze the chemical influence of steam on NO formation in premixed hydrogen while explicitly controlling for thermal effects by holding the adiabatic flame temperature approximately constant through compensating adjustments in either equivalence ratio or unburned-mixture temperature. Within that constant-T_{ad} framework, simulations of freely propagating flames show that increasing steam reduces NO even when temperature severity is controlled, with reductions on the order of one-half near stoichiometric conditions at high water loading. The mechanism is traced to water's impact on the radical pool (O/H/OH) and third-body efficiencies in key recombination steps, which weakens downstream thermal and NNH pathways. A reported temperature crossover in the flame-speed response to steam further indicates that stability margins depend on whether humidification is applied at lower or higher T_{ad}. Read together with the decomposition in Lu et al. [65] and the near-constant-temperature comparison in Göke and Paschereit [38], this consolidates the conclusion that steam's benefit is not only thermal but also chemical in premixed H_2 flames.

Elevated-pressure behavior in premixed combustors. At pressures typical of gas-turbine rigs, the same tendencies appear while the usable window narrows. Stathopoulos et al. [67] operated a swirl combustor with axial-air injection on natural gas and on a hydrogen-enriched mixture containing 10% H_2 by mass at absolute pressures up to 9 bar and steam-to-air mass ratios up to 0.25. They observed that NO rises with pressure in no-steam operation, that adding 10% steam already reduces NO, and that the highest tested steam ratios bring emissions to consistently low levels, reported as < 10 ppm for natural gas and < 5 ppm for the hydrogen-enriched case across the highest investigated pressure and equivalence-ratio range. The same dataset clarifies carbon monoxide trends: when CO is compared at fixed ϕ, the steam-injected cases often appear lower because steam cools the flame at the same ϕ and shifts the CO curve; however, when the comparison accounts for temperature, the intrinsic effect of adding steam is a small increase in CO, attributable to slower oxidation kinetics and additional dilution at a given thermal severity [67]. This

temperature-accounted interpretation is consistent with atmospheric swirl experiments with liquid water injection, where improved atomization mitigated CO penalties at comparable thermal severity [68].

Injector placement and spray interaction in combustors. Beyond intrinsic chemistry, injector placement and spray and flow interaction determine how much of the potential NO reduction is realized in practical combustors. Using an Eulerian–Lagrangian CFD model of a swirl-stabilized premixed combustor and natural gas as fuel, Farokhipour et al. [69] varied injection location, direction, water-to-fuel ratio, and swirl number. Injecting near the inlet nozzles drives droplets into cold wall flows where they under-evaporate and contribute little; aiming the spray at the end of the primary (post-ignition) zone increases residence in hot gases, promotes complete evaporation and uniform cooling, and maximizes NO_x suppression. Axial targeting outperformed tangential injection because it avoided uneven cooling and recirculation pockets, and higher swirl numbers extended droplet residence near the hot core. Reported trends show large NO_x reductions for WFR ≈ 0.3–0.4 with diminishing returns and power penalties if quenching sets in at still higher ratios, which provides practical bounds for design.

Experimental evidence for how liquid atomization couples to emissions in premixed swirl flames is provided by Lellek [68]. Atmospheric single-burner tests with liquid water injection mapped global NO_x and CO versus steam-to-air fraction, equivalence ratio, and adiabatic flame temperature, and combined OH^* chemiluminescence with droplet diagnostics. At moderate steam-to-air ratios, NO_x decreased strongly, but incomplete evaporation or coarser sprays increased CO due to local over-dilution and quenching; finer atomization expanded the usable window and reduced the CO penalty at comparable thermal severity. The study further shows that when data are compared at fixed ϕ the steam-injected cases can appear to have lower CO because the flame is colder, while comparisons that account for temperature reveal the intrinsic tendency of CO to increase slightly with steam due to slower oxidation kinetics and added dilution. These findings align with the placement and evaporation guidance from modeling [69] and explain the CO behavior observed in pressurized rigs.

Engine-architecture strategies for water and steam. At engine level, NASA's assessment using kerosene compares three architectures: fine misting ahead of the low-pressure compressor (LPC), misting ahead of the high-pressure compressor (HPC), and direct combustor injection [70]. For well-atomized LPC misting with complete evaporation, the study reports substantial turbine-inlet-temperature relief and commensurate NO_x decreases while also improving cycle efficiency in warm-day operation; HPC misting shows similar but smaller benefits, and combustor injection yields the strongest immediate NO_x reduction with potential penalties in stability and maintenance unless carefully engineered. The analysis emphasizes droplet sizes of a few micrometers and uniform distribution to avoid liner impingement or casing cooling, and it frames where in the engine one can balance NO_x reduction, efficiency, stability, and system complexity.

Experimental compressor-path data by Novelo et al. [71] complement the NASA system picture on a single-shaft gas-turbine rig. Water-to-air ratios of 0.5, 1, and 2% lowered compressor-discharge temperature by up to 34 K and reduced NO_x by approximately 25%. At the higher ratios, incomplete pre-combustor evaporation allowed liquid carry-through, which added combustor-side cooling but also increased CO due to local over-dilution and quenching. These results bound practical ratios for upstream injection and highlight that evaporation completeness is a first-order control on the NO–CO trade-off when water is introduced ahead of the flame.

Bridging rig studies to aircraft missions, Zahid [72] combines engine-cycle and combustor modeling to co-optimize water-injection location and rate across mission segments. Upstream strategies in the compressor path can deliver large NO_x reductions (up to about 80% in the modeling) while preserving or improving specific fuel consumption because cooler, denser air reduces compressor work; downstream strategies near or in the combustor achieve the strongest immediate NO_x cuts but tend to penalize fuel burn unless tightly constrained. The analysis further shows configuration dependence: architectures with richer front ends yield larger absolute NO_x benefits for a given water fraction, whereas modern lean systems must balance humidification against stability and CO when temperature effects are accounted for. This suggests a mapping from laboratory variables such as steam fraction, T_{ad}, and ϕ to mission-level trade-offs.

Taken together, the architecture-level studies (NASA [70], Novelo et al. [71], and Zahid [72]) show that where water or steam is introduced in the cycle sets the trade between NO_x benefit, efficiency, and stability. These findings frame the combustor-scale and engine evidence discussed next and motivate using steam

as a control variable in hydrogen-rich premixed systems, where very-lean operation can be constrained by stability and flashback margins.

Hydrogen and H_2–CH_4 engines as supporting evidence. Although the geometric and control constraints differ from gas-turbine combustors, hydrogen engine studies reinforce core trends for steam-injected operation. Mohamed et al. [73] characterized intake port water injection in a direct-injection hydrogen spark-ignition engine at 2000 rpm. At 10 bar IMEP (Indicated Mean Effective Pressure), injecting 5 kg/h water lowered NO_x by 79% while moderating pressure rise; at higher load it extended the attainable IMEP and improved torque with small gains in indicated thermal efficiency, partly by relaxing boost requirements. Xu et al. [74] performed single-cylinder tests with direct water injection and showed that increasing per-cycle water mass to 4.5 mg/cycle at $\lambda = 1.15 (= \frac{1}{\phi})$ reduced NO_x by 53.7%, lengthened the main heat-release period, and slightly improved indicated thermal efficiency; advancing water injection timing produced further NO_x benefits, highlighting timing as a primary control. Dhyani and Subramanian [75] compared cooled EGR (Exhaust Gas Recirculation) and port water injection in a multi-cylinder hydrogen engine and found that a water-to-hydrogen mass ratio near 7.5 reduced NO_x by 97% at similar brake thermal efficiency, whereas 25% EGR achieved a 57% reduction, indicating stronger NO_x effect from water than from inert recirculation. For hydrogen–methane blends, Novella et al. [76] used a calibrated medium-duty engine model to show that water injection can match EGR's NO_x suppression at about 80% reduction while lowering intake boost requirement and maintaining efficiency at high specific power. Taken together, these studies support the generality of steam-injected NO_x control in hydrogen-rich mixtures, and they underscore quantity and timing as key parameters for balancing NO_x, CO, and efficiency.

Broader context and reporting practice. For context outside aero combustors, Londerville et al. [77] survey water and steam injection in industrial burners and turbines, collating typical NO_x decreases in the 40–70% range, with benefits contingent on how humidity is introduced and recovered. Without heat recovery or careful staging, efficiency losses, higher CO or UHC, and stability issues can emerge. The review supports the practice of reporting ppm for steam-injected cases alongside $EINO_x$ and assessing CO and stability with attention to temperature effects to avoid misinterpretation. This aligns with the reporting approach adopted in the present work.

Synthesis and research gap. The combined evidence establishes that steam injection reduces NO in premixed hydrogen flames through both thermal and chemical effects. At atmospheric pressure, steam-injected operation outperforms inert dilution for hydrogen and for hydrogen-enriched natural gas, and this advantage persists in datasets that control, at least approximately, for temperature effects [65, 38, 63]. In pressurized swirl combustors, steam remains effective and low-ppm outcomes are attainable at suitable steam-to-air ratios, with CO behavior dependent on whether comparisons are made at fixed ϕ or with temperature effects accounted for [67]. Implementation details matter: injector location, targeting, and swirl govern evaporation and residence time in the reacting core [69, 68], and at engine level the point of introduction trades NO_x benefit, efficiency, stability, and system complexity [70, 71, 72].

Despite this progress, several limitations remain for gas-turbine–relevant hydrogen systems. A large fraction of prior work is either atmospheric or based on internal combustion engines, often using liquid water sprays with incomplete or configuration-dependent evaporation. Such studies are valuable for identifying trends, but spray evaporation and near-wall quenching can confound interpretation of intrinsic flame chemistry and make it difficult to generalize to fully premixed turbine combustors. Where hydrogen appears, it is frequently as a minor enrichment to natural gas rather than as the dominant fuel, and consistent comparisons to an inert diluent at matched temperature level are uncommon. Even when steam is used, datasets rarely provide a unified map in equivalence ratio and steam injection amount (or steam-to-air fraction) at a representative pressure with joint reporting of ppm and $EINO_x$, together with CO and operability metrics interpreted with temperature effects explicitly accounted for. Stability is often treated qualitatively rather than with a reproducible margin referenced to measured flame or acoustic indicators, and phase effects are not cleanly separated, leaving open questions about how liquid water sprays versus premixed steam influence NO, CO, and stability when temperature effects are normalized.

A practical motivation is that some engines already circulate water to manage liner and combustor heat loads; that stream can be converted to steam and introduced near the combustor inlets, which makes steam addition implementable with existing hardware. What is missing in the literature is a quantitative assessment

of how this implementation route affects emissions and stability for hydrogen and hydrogen–methane mixtures in premixed, swirl stabilized combustors. In particular, there are few studies that compare this approach with staged or spray introductions once temperature effects are considered, and there are limited datasets that report ppm and EINO$_x$ together with CO and stability within one protocol. This practical pathway reinforces the need for targeted experiments rather than resolving the gap by itself.

The next chapter formulates the research proposal by stating the specific questions and objectives that follow from this review and by outlining the experimental methodology and measurement protocol used to address them.

4

Research Proposal

This chapter outlines the motivation for the study, summarizes the specific gaps identified in the literature review, states the research objectives and questions, and introduces the proposed experimental approach.

4.1. Problem Definition

Aviation and power generation face increasingly stringent limits on nitrogen oxides (NO_x) due to their impact on air quality and regulated emissions inventories. Hydrogen is a promising fuel because it removes carbon from the exhaust and enables very lean operation. At the same time, hydrogen's high reactivity and high flame temperatures promote NO formation through thermal and related pathways. The literature review shows that adding water or steam can lower flame temperature and adjust the radical pool, which reduces NO in premixed flames. It also shows that practical outcomes depend on how and where the diluent is introduced, on equivalence ratio, and on mixing and evaporation details.

Most low-emission gas turbine practice on natural gas relies on lean premixed operation without diluent, while many studies that use water or steam focus on internal combustion engines or on hydrocarbon flames. For hydrogen and hydrogen–methane mixtures, there are far fewer data in premixed, swirl stabilized combustors that map the combined influence of equivalence ratio, blend fraction, and steam addition. There is also limited guidance on how to interpret carbon monoxide and stability when temperature changes with steam are not held constant in a comparison. These gaps motivate a controlled, combustor-scale investigation that resolves NO, CO, and operability trends under a single, consistent protocol.

4.2. Research Gap

The review highlights several gaps that are directly relevant to hydrogen and hydrogen–methane premixed combustors:

- A lack of consistent, combustor-scale datasets for hydrogen and hydrogen–methane blends with steam addition in premixed, swirl stabilized configurations at representative laboratory conditions, with joint reporting of NO in ppm and as $EINO_x$ together with CO and stability indicators.
- Limited parametric maps that span the key controls of interest in one campaign, namely equivalence ratio, hydrogen fraction in H_2–CH_4 blends, steam injection amount, and steam injection location.
- Few studies that interpret NO and CO while explicitly treating temperature effects, for example by reporting an estimated adiabatic flame temperature and using it to clarify whether observed trends arise from cooling or from non-thermal influences associated with steam.
- Insufficient comparison of practical introduction strategies for steam in premixed combustors, for example distributed introduction near the inlets versus more localized addition, and how these choices influence emissions and operability when temperature effects are considered.

These gaps motivate an experimental investigation to systematically evaluate how steam injection affects hydrogen and hydrogen–methane premixed combustion, with emphasis on flame structure, NO_x suppression, carbon monoxide and efficiency trade-offs, and stability. The next chapter states the research objective and questions that follow from this review and outlines the experimental methodology and measurement protocol that will be used to address them.

4.3. Research Objective and Research Questions

The objective of this thesis is to experimentally determine how steam injection affects NO emissions in premixed CH_4–H_2 flames stabilized by swirl, with emphasis on the roles of steam flow rate, injection location, fuel composition, and burner power. The study quantifies emission outcomes in ppm and as $EINO_x$, assesses CO and other relevant products, and interprets the dominant NO-suppression mechanisms using emissions trends together with OH^* chemiluminescence imaging. The test matrix spans 7–11 kW burner power, 0–100% H_2 in the fuel, and multiple steam injection levels and configurations (side and axial).

Research Objective

The research objective of this thesis was to experimentally investigate the effect of steam injection on NO emissions in premixed CH_4–H_2 flames within a swirl-stabilized burner, with a focus on how steam flow rate, injection location, fuel composition, and burner power influence emission outcomes, and on understanding the underlying mechanisms of NO suppression.

The investigation is organized around three research questions aligned with the experimental program and the way results are synthesized in the conclusions.

Research Question 1

What are the design considerations for steam injection in a lab-scale model gas turbine combustor operating on hydrogen-methane blends?

Relevant subquestions include:

- How do injection location and fuel composition set the trade between NO suppression and stability, and what practical limits result for side and axial configurations?
- Which laboratory constraints and hardware choices are most likely to bias steam delivery and measurements, and how should they be addressed in practice?

Research Question 2

How does steam injection impact NO emissions in hydrogen and hydrogen–methane blended combustion?

Relevant subquestions include:

- What NO reductions are achieved across methane, hydrogen, and blended fuels as steam flow rate increases?
- How do reductions differ when expressed in ppm versus $EINO_x$ across 7–11 kW and for side and axial injection?
- How does injection location (side versus axial) change the NO response for each blend and power level, and which location provides greater NO reduction per unit of added steam?

Research Question 3

How does steam injection affect overall combustion characteristics and stability in fully hydrogen and hydrogen–methane flames?

Relevant subquestions include:

- How do CO and unburned fuel indicators respond to steam addition for different blends and injection locations?
- How does flame structure change with steam, and how do these changes relate to stability margins and operability?
- Which combinations of blend fraction, steam rate, and injection location provide low NO together with acceptable CO and robust attachment over the tested power range?

The next chapter describes the experimental setup used to address these questions. It introduces the premixed, swirl stabilized burner and fuel handling system, the steam delivery hardware and injection configurations, and the measurement suite for NO, CO, and supporting diagnostics. Test conditions, calibration procedures, and uncertainty estimates are specified together with the operating and data acquisition protocol.

5

Experimental Set-Up

5.1. Vertical Burner Set-Up

General Facility and Operation

The experimental campaign is conducted in the Compressor Hall at the High-Speed Laboratory (HSL) of the Faculty of Aerospace Engineering, TU Delft. Due to safety requirements, reacting-flow experiments are performed in a defined ATEX zone (ATmosphere EXplosible). A ventilation hood above the zone and ducted exhaust lines remove hot product gases safely to the outside of the building. The operator console is located behind a protective shield; all tests are run remotely via a LabView-based interface that controls pilot/main ignition, shutdown, and set-points for burner power, total air flow, axial air injection (AAI) fraction, and hydrogen blend percentage.

Overall Combustor Layout

An overview of the lab set-up with the swirl-stabilized burner used in this thesis (without steam injection modifications) is provided in Figure 5.1 and Figure 5.2. The modifications done for the steam injection mechanism will be discussed later.

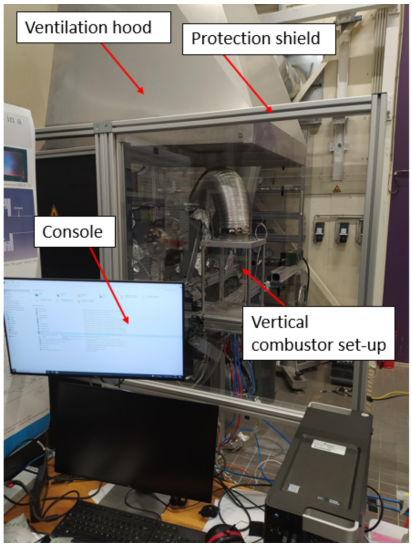


Figure 5.1: Combustor set-up and operation location [78].

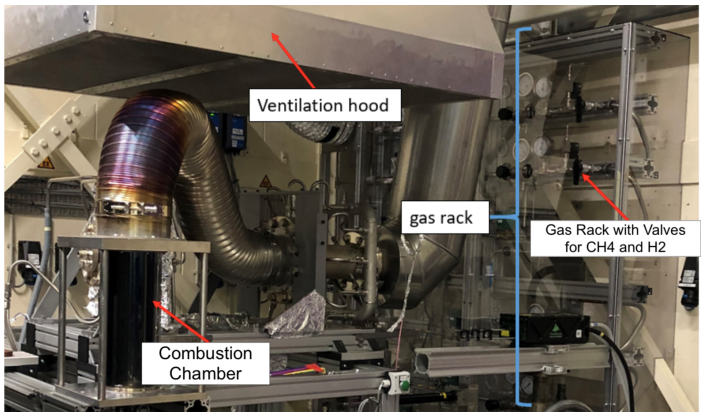


Figure 5.2: Combustion chamber with ventilation hood and gas rack [78].



Figure 5.3: Vertical combustor lab set-up without the steam injection mechanism.

Swirler and the Axial Air Injection

Premixed combustion systems are often used in many power generation applications due to their low NOx emissions [79]. In premixed combustion, the fuel and oxidizer are fully mixed before ignition. This results in a uniform fuel–air mixture that burns as a flame front propagates through the mixture. In contrast, diffusion (non-premixed) combustion injects fuel into an air stream where mixing and burning occur simultaneously. Premixed combustion, especially when operated under lean conditions, leads to lower peak flame temperatures compared to non-premixed (diffusion) combustion. Since NOx formation is highly sensitive to temperature, primarily forming via the thermal (Zeldovich) mechanism at temperatures above 1800K, temperature reduction significantly decreases NOx production. Moreover, the homogeneous nature of a fully premixed mixture helps avoid local hot spots or fuel-rich zones, which are otherwise convenient locations for NOx generation. However, when operating with hydrogen, such fully premixed operation poses significant flashback risks due to the very high laminar flame speed of H_2. For this reason, the present burner is designed as a partially premixed system, where the fuel is injected as late as possible upstream of the chamber to limit pre-flame residence time and reduce the likelihood of flashback.

Swirl stabilization is a commonly used flame stabilization technique in combustors and burners due to its effectiveness in anchoring flames under lean and partially premixed conditions. The core principle relies on inducing angular momentum to the incoming airflow using a swirler. The swirler consists of a set of vanes arranged to induce rotation. This swirling motion creates a central low pressure region and promotes the formation of an inner recirculation zone (IRZ). In addition, an outer recirculation zone (ORZ) forms near the chamber walls. The IRZ recirculates hot combustion products and reactive radicals back toward the flame root, while the ORZ helps confine and stabilize the flame along the chamber boundaries. When enclosed in a combustion chamber, the interaction of the IRZ and ORZ forms a large central recirculation region that helps anchor the flame and extend its stability limits.

In the present setup, an axial swirler with a geometric swirl number $S_w = 1.1$ is used, mounted upstream of the mixing tube. The swirler is 3D printed in 420 stainless steel and infused with bronze. Its main function is to generate the recirculation flow and enhance turbulent mixing. Downstream of the swirler outlet, the fuel (CH_4–H_2) is injected radially into the swirling air stream. This arrangement promotes partial premixing within the mixing tube before the reactants enter the combustion chamber. While the swirler alone does not fully premix the fuel and air, its combination with radial fuel injection ensures sufficient mixing while mitigating flashback risks. For this reason, the combustor is categorized as a partially premixed system [80]. The strength of the swirl directly affects the shape, position, and the stability limits of the flame. An image of the swirler used in the experimental campaign is given in Figure 5.4.



Figure 5.4: Swirler with Swirl Number S_w = 1.1 [78]

Due to low velocities present in the IRZ, there is a higher likelihood of flashback. This risk is more pronounced in hydrogen flames because of their high laminar flame speed, whereas methane flames generally do not exhibit flashback under similar conditions. In swirling flows, the velocity deficit on the centerline further increases this tendency [81]. To mitigate the issue, axial air injection of a central air jet (AAI) is utilized. While keeping the total airflow into the combustion constant, a certain percentage of the air is injected directly through the center of the burner without going through the swirler. This provides additional stabilization in high–hydrogen-fraction cases, preventing the flame from propagating upstream into the mixing tube.

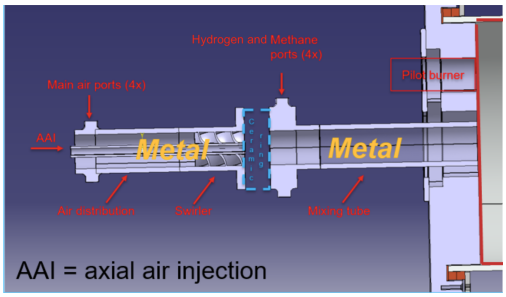


Figure 5.5: Injector schematic showing the injection points of the air and the fuel

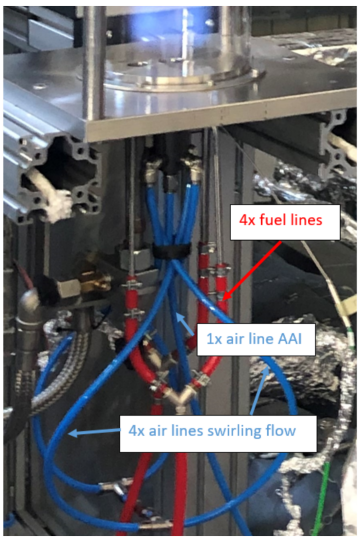


Figure 5.6: Connections to the baseplate

Pilot Burner

Ignition of the system is achieved using a dedicated pilot burner, which serves as a stable ignition source and as a transition stage between the low-power start-up flame and the higher-power main burner flame. Once stabilized, the pilot flame is used to ignite the main burner. The pilot burner operates on methane and air, with its own spark plug for ignition. The spark plug also functions as an ionization probe, providing a DC signal that confirms flame presence through the detection of combustion radicals.

The pilot burner is manufactured by Kramschroder, type ZMI 16B200R, with a nominal power capacity of 1–2 kW. 2 kW was used to start up the main burner in this experimental campaign. The pilot burner is designed to operate near atmospheric conditions. Ignition control is performed by an IFD 258-5/1W automatic burner controller in single-electromode [78]. The pilot air and methane supply lines are each regulated by dedicated Bronkhorst mass flow controllers (MFCs), identified in the P&ID as FCV units. In

addition, the methane line is equipped with a manual regulator to provide an extra level of safety and redundancy.

Figure 5.7 shows the pilot burner's integration with the baseplate of the main burner.



Figure 5.7: Pilot burner attached to the base plate of the main burner.

Main Combustion Chamber

The combustion process takes place inside a cylindrical quartz chamber with an inner diameter of 155 mm and a length of 400 mm. The chamber is mounted on a 30 mm thick steel baseplate, which serves as the main interface for the fuel, air, and auxiliary injection lines. The baseplate accommodates five inlets: one central inlet for the main burner fuel–air mixture, one inlet for the pilot burner flame, and three auxiliary inlets that can be configured for different purposes. For the steam injection campaign, two of these side inlets were used to supply steam, while the third remained available for future modifications.

Figures 5.8 and 5.9 show the baseplate from the top and underside, respectively. An exploded view of the entire chamber assembly is provided in Figure 5.10, highlighting the integration of the quartz tube, swirler, and mixing tube with the steel baseplate.

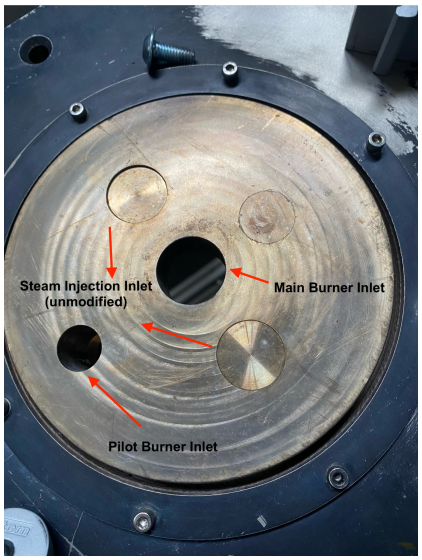


Figure 5.8: Top view of the steel baseplate.

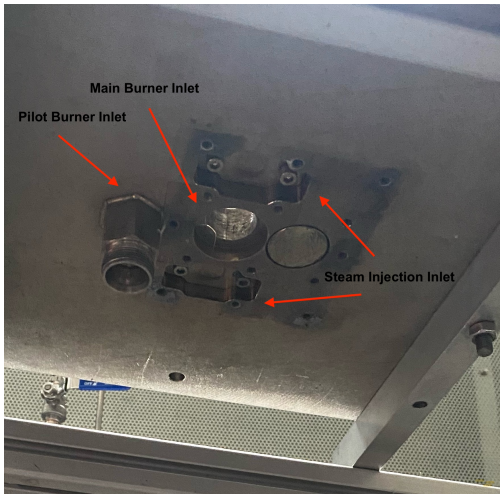


Figure 5.9: Underside of the steel baseplate.

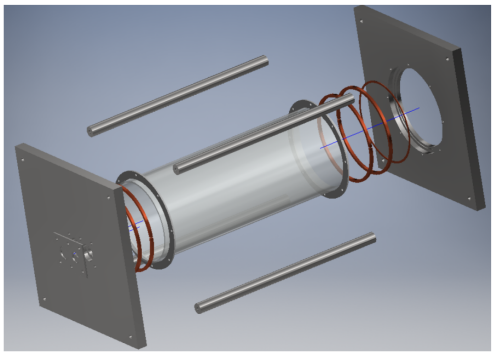


Figure 5.10: Exploded view of the main combustor assembly.

At the center of the baseplate, the main burner fuel–air mixture enters through a mixing tube with an inner diameter of 24 mm and a length of 55 mm. At the inlet of this tube, a fuel injection ring is positioned. The ring contains four evenly spaced ports that inject fuel radially into the swirling air stream created by the upstream swirler. This configuration allows for effective turbulent mixing and establishes a partially premixed flame before the mixture enters the combustion chamber.

The quartz cylinder provides optical access for diagnostic measurements, while the steel baseplate ensures mechanical stability and reliable integration with the injection hardware. Together, the chamber design allows safe and controlled operation of the swirl-stabilized flame under different fuel compositions and injection configurations.

Gas Supply and Flow Control

The burner operated for the experimental campaign can run on both H_2 and CH_4, or on a blend of these two fuels. The air supply is provided from a pressurized tank located outside the laboratory building, while the fuel is supplied from gas racks positioned beneath the ATEX zone behind the combustor. The gases are fed into the pilot and main burners through electronically controlled valves, which are actuated via the LabView interface at the operator console. An image of the gas rack used for fuel distribution is shown in Figure 5.11.

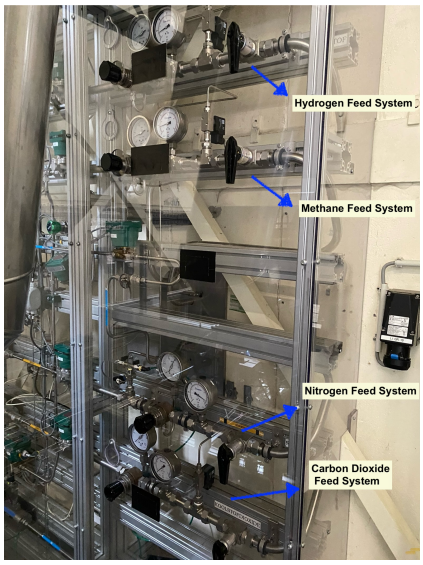


Figure 5.11: Gas rack used for methane and hydrogen distribution. The fuels are stored outside the building in cylinder bundles for safety.

All fuel and air lines in the setup are regulated by Bronkhorst mass flow controllers (MFCs). Each MFC is assigned a functional code in the P&ID for identification. The pilot burner uses one MFC for air and one

for methane, while the main burner is equipped with separate MFCs for air, methane, and two ranges of hydrogen flow. In addition, the axial air injection (AAI) line is controlled by a dedicated MFC. An overview of the controllers and their ranges is provided in Table 5.1.

Name	Manufacturer	Model	Working fluid	Range
Pilot air	Bronkhorst	F-206AI-RAD-55-V	Air	10 – 500 nlpm
Pilot fuel – CH_4	Bronkhorst	F-202AV-M20-RAD-55-V	CH_4	1.76 – 85 nlpm
Main burner – air	Bronkhorst	F-107CI-RGD-13-V	Air	300 – 3000 nlpm
Main burner – CH_4	Bronkhorst	F-113AC-M50-RAD-55-V	CH_4	7 – 350 nlpm
Main burner – H_2 low	Bronkhorst	F-201AV-50K-RAD-55-V	H_2 gas	0.36 – 60 nlpm
Main burner – H_2 high	Bronkhorst	F-113AC-1M0-RAD-55-V	H_2 gas	20 – 1000 nlpm
Axial air injection (AAI)	Bronkhorst	F-203AV-M50-RAD-55-V	Air	10 – 250 nlpm

Table 5.1: Overview of flow controllers and sensors used in the setup [82].

The accuracy of flow measurements is tied to the manufacturer specifications of the Bronkhorst MFCs. Each device defines a set-point error as a function of the read value (RD) and the full-scale value (FS). The associated uncertainty in volumetric flow rate can be expressed as:

$$\Delta\dot{Q} = 0.005RD + 0.001FS \tag{5.1}$$

At low flow rates relative to the device range, the full-scale component dominates the uncertainty, leading to higher relative errors. The combined effect of these uncertainties is treated further in Chapter 7.

In practice, the MFCs and valves are operated remotely from the control station. This setup ensures safe operation within the ATEX zone while giving the operator full authority over burner power, total airflow, hydrogen fraction, and AAI percentage. An overview of the control hardware and the LabView interface is shown in Figure 5.12 and Figure 5.13.

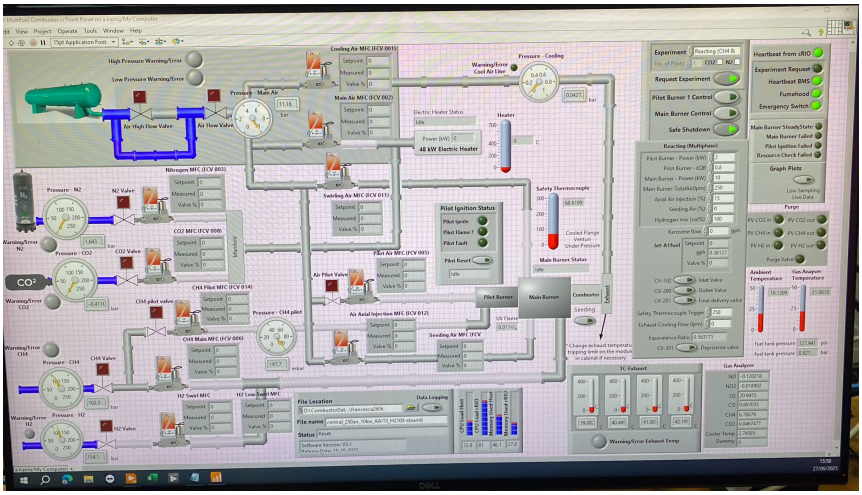


Figure 5.12: Physical control panel of the combustor set-up.

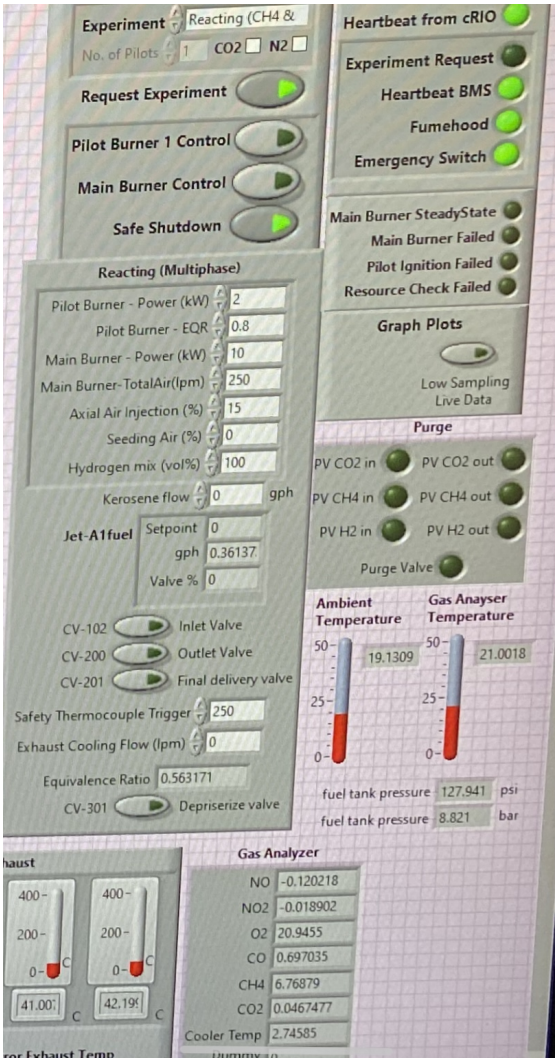


Figure 5.13: LabView interface for setting and monitoring operating conditions.

5.2. Operating Range and Equivalence Ratio Determination

The operating regime of the Swirl-Stabilized Vertical Combustor, as defined in its manual [78], provides the recommended burner power range and corresponding stability limits. These accessible conditions are summarized below to characterize the range used in the experimental campaign.

Hydrogen flames have higher adiabatic flame temperatures compared to conventional hydrocarbon fuels at the same equivalence ratios. Since higher flame temperatures are strongly associated with higher NOx emissions, it is expected that the effect of steam addition will be more pronounced for hydrogen flames. Nevertheless, the HSL facility is capable of operating with both H_2 and CH_4, and both fuels were included in the present campaign. This choice reflects not only scientific completeness but also practical relevance, as future gas turbines are expected to operate flexibly on hydrogen, methane, or their blends. In addition, hydrocarbon operation enables measurement of CO emissions, which provides an important diagnostic of combustion efficiency and complements the NOx measurements. The experimental campaign therefore encompasses pure H_2, pure CH_4, and blended H_2–CH_4 flames. It should also be noted that the high flame speed and reactivity of hydrogen can alter the flame position in the burner, potentially leading to flashback. Hence, certain operating points may not be achievable in stable conditions due to flashback or blow-off. Moreover, the introduction of steam modifies the underlying combustion processes, so some conditions may be stable without steam injection but become unstable when steam is added.

The vertical combustor has a recommended burner power range of 7-12 kW and can vary the fuel from 100% hydrogen & 0% methane to 0% hydrogen & 100% methane. A stability limit test has been previously

conducted by PhD candidates and University staff to characterize the stability regime of the vertical combustor [80]. The findings indicate that at lower equivalence ratios high methane percentage blend fuels tend to blow-out while the higher hydrogen percentage blend fuels tend to flashback without any axial air injection [83](100% of the air is injected through the nozzle). As the equivalence ratio is increased the blowout for the methane flame is mitigated, while the flashback issue for the higher hydrogen fraction flames persisted. This implied that axial air injection (AAI) was necessary for high hydrogen fraction flames to sustain stable combustion. A chart for the stability regime of the vertical combustor can be found in Figure 5.14:

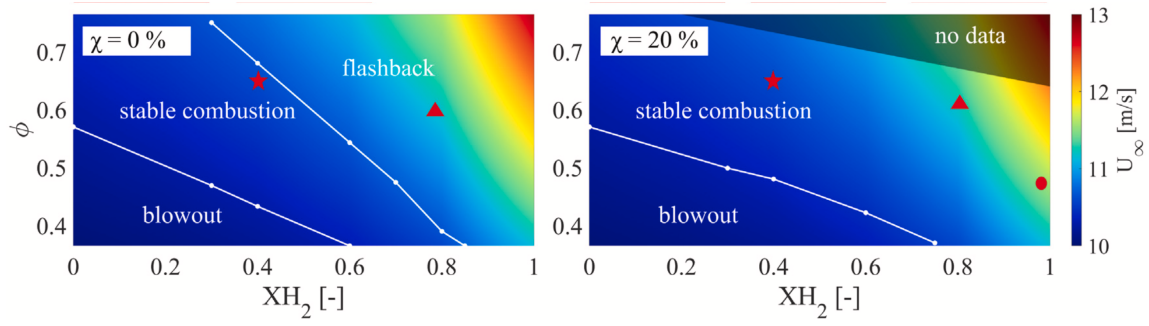


Figure 5.14: The stability regime of the vertical combustor at 12 kW burner power. The x-axis denotes the hydrogen mole fraction while the y-axis denotes the equivalence ratio. Left figure is with 0 axial air injection, the right figure is with 20% AAI (denoted as χin the figures) [80]

The figure in Figure 5.14 describes the static stability of the flame, meaning if it can burn without flashback or blow-off. It does not account for any dynamic instabilities or thermo-acoustic instabilities. It should be noted that the equivalence ratio of the flame can be changed by adjusting both the burner power (which changes the fuel injection amounts) and the total amount of air injected into the burner.

The equivalence ratio is not a direct control variable in this facility as the control inputs directly control the mass flow controllers. Instead, the equivalence ratio must be derived from the controller set-points: the burner power in kW, the total air flow rate in nlpm, and the hydrogen molar fraction of the fuel. The steps to calculate the equivalence ratio for a given test point is given as:

The equivalence ratio is not a direct control variable in this facility as the control inputs directly control the mass flow controllers. Instead, the equivalence ratio must be derived from the controller set-points: the burner power in kW, the total air flow rate in nlpm, and the hydrogen molar fraction of the fuel. The steps to calculate the equivalence ratio for a given test point is given as:

$$\dot{V}_{\text{air,lpm}} = \dot{V}_{\text{air,nlpm}} \cdot \frac{T_{\text{air}}}{T_{normal}} \quad [\text{lpm}] \tag{5.2}$$

$$AFR_{fuel_{mol}} = AFR_{H2_{mol}} \cdot f_{H2} + AFR_{CH4_{mol}} \cdot (1 - f_{H2}) \quad [\text{mole/mole}] \tag{5.3}$$

$$\dot{V}_{\text{fuel,mix,lpm}} = \frac{P_{burner}}{\eta_{cc} \cdot LHV_{mix_{kg}} \cdot \rho_{mix,fuel}} \cdot 60 \cdot 10^{6} \quad [\text{lpm}] \tag{5.4}$$

$$\rho_{mix,fuel} = \frac{P \cdot M_{mix} \cdot 10^{-3}}{R_{universal} \cdot T_{\text{fuel}}} \quad [\text{kg/m}^3] \tag{5.5}$$

$$LHV_{mix_{mol}} = LHV_{H2_{mol}} \cdot f_{H2} + LHV_{CH4_{mol}} \cdot (1 - f_{H2}) \quad [\text{J/mol}] \tag{5.6}$$

$$LHV_{mix_{kg}} = \frac{LHV_{mix_{mol}}}{M_{mix} \cdot 10^{-3}} \quad [\text{J/kg}] \tag{5.7}$$

$$M_{mix} = M_{H2} \cdot f_{H2} + M_{CH4} \cdot (1 - f_{H2}) \quad [\text{g/mol}] \tag{5.8}$$

$$\phi_{mix} = \frac{\dot{V}_{\text{fuel,mix,lpm}}}{\dot{V}_{\text{air,lpm}}} \cdot AFR_{fuel_{mol}} \quad [-] \tag{5.9}$$

Notation clarification (one-time): $\dot{V}_{\text{air,nlpm}}$ is volumetric air flow at normal conditions (nlpm), $\dot{V}_{\text{air,lpm}}$ is volumetric air flow at operating conditions (lpm), and $\dot{V}_{\text{air}}$ (without subscript) denotes SI volumetric flow in m^3/s.

Where the meaning of each symbol with their units are given in Table 5.2. If the variable is a constant, the value used in the calculations are given.

Variable	Name	Unit	Value
$AFR_{fuel_{mol}}$	Molar Air-to-Fuel Ratio of the Fuel Mix (stoichiometric)	-	
$AFR_{H2_{mol}}$	Molar Air-to-Fuel Ratio of H_2 (stoichiometric)	-	2.38
$AFR_{CH4_{mol}}$	Molar Air-to-Fuel Ratio of CH_4 (stoichiometric)	-	9.52
f_{H2}	Hydrogen Molar Fraction	-	
$\dot{V}_{\text{fuel,mix,lpm}}$	Volumetric Flow Rate of Fuel Mixture	lpm	
$\dot{V}_{\text{air,lpm}}$	Volumetric Flow Rate of Air (operating)	lpm	
$\dot{V}_{\text{air,nlpm}}$	Volumetric Flow Rate of Air (normal)	nlpm	
T_{normal}	Reference Temperature at Normal Conditions	K	273.15
T_{air}	Air Temperature (operating)	K	288
T_{fuel}	Fuel Temperature (injection)	K	288
P_{burner}	Burner Power	kW	
η_{cc}	Combustion Efficiency	-	1
$LHV_{mix_{kg}}$	Lower Heating Value of the Fuel Mixture (per kg)	J/kg	
$\rho_{mix,fuel}$	Density of the Fuel Mixture	kg/m^3	
P	Pressure of the Fuel Gases (at injection)	Pa	101325
$R_{universal}$	Universal Gas Constant	J/mol·K	8.3145
M_{mix}	Molar Mass of the Fuel Mixture	g/mol	
$LHV_{H2_{mol}}$	Lower Heating Value of H_2 (per mol)	J/mol	241920
$LHV_{CH4_{mol}}$	Lower Heating Value of CH_4 (per mol)	J/mol	802000
$LHV_{mix_{mol}}$	Lower Heating Value of the Fuel Mixture (per mol)	J/mol	
M_{H2}	Molar Mass of H_2	g/mol	2.016
M_{CH4}	Molar Mass of CH_4	g/mol	16.04
ρ_{air}	Density of Air (at 288 K, 1 atm)	kg/m^3	1.226
ϕ_{mix}	Equivalence Ratio of the Fuel Mixture	-	

Table 5.2: Definition of Variables Used in the Equivalence Ratio and Fuel Properties Calculations

With this calculation, the equivalence ratio of a selected point with the available inputs can be calculated.

5.3. Steam Injection Mechanism

To perform a productive experiment, it was important to select a device that can inject the correct amount of steam into the flame. If the steam was too much, the flame could be blown-off from too much dilution, and if the steam was too little, the injected steam would not affect the flame in a significant way. To determine the desired amount of steam injection into the flame, a literature study was conducted to investigate what

is the steam-to-air or steam-to-fuel ratios have been tested and produced substantial changes in NOx emissions.

It was found that a range of steam values were tested in literature, but the steam injection values did indicate a trend. It was found in a study that steam injection rate of up to 10% of the product gases produced significant decrease in NOx emissions [63]. Another study conducted on H2-CH4 blend fuels found that steam-to-fuel ratio of around 1 to 2 produced noticeable changes in NOx emissions [84]. In another study, it was found that water-to-gas (product gas) ratios of up to 16% have shown significant decrease in NOx emissions. In the light of these information, some preliminary calculations were conducted [85].

An example point from the vertical combustor was chosen as a reference point for the literature values mentioned above. The burner power of 10 kw, total air injection of 250 nlpm and a hydrogen molar fraction of 0.5 was taken as a reference point for the burner. From these, the mass flow rates of air and fuel can be calculated to be used to estimate the required steam flow rate of the steam generator:

Given and assuming:

- Burner Power: $10\,\text{kW}$
- Air Flow Rate: $250\,\text{nlpm}$
- Hydrogen Molar Fraction: $f_{\text{H}_2} = 0.5$
- Combustion Efficiency: $\eta_{\text{cc}} = 1.0$
- Normal Temperature: $T_{\text{normal}} = 273.15\,\text{K}$
- Air Density: $\rho_{\text{air}} = 1.226\,\text{kg/m}^3$

1. Convert air flow to actual volume flow rate (at $15°C$):

$$\dot{V}_{\text{air,lpm}} = 250 \cdot \frac{288}{273.15} \approx 263.66\,\text{lpm} \tag{5.10}$$

$$\dot{V}_{\text{air}} = \frac{263.66}{1000 \cdot 60} \approx 4.394 \times 10^{-3}\,\text{m}^3/\text{s} \tag{5.11}$$

2. Air mass flow rate:

$$\dot{m}_{\text{air}} = \rho_{\text{air}} \cdot \dot{V}_{\text{air}} = 1.226 \cdot 4.394 \times 10^{-3} \approx 5.39 \times 10^{-3}\,\text{kg/s} = 5.39\,\text{g/s} \tag{5.12}$$

3. Fuel blend properties (50% H_2, 50% CH_4):

$$M_{\text{mix}} = 0.5 \cdot 2.016 + 0.5 \cdot 16.04 = 9.028\,\text{g/mol} \tag{5.13}$$

$$LHV_{\text{mix,mol}} = 0.5 \cdot 241920 + 0.5 \cdot 802000 = 521960\,\text{J/mol} \tag{5.14}$$

$$LHV_{\text{mix,kg}} = \frac{521960}{9.028 \cdot 10^{-3}} \approx 5.78 \times 10^{7}\,\text{J/kg} \tag{5.15}$$

4. Fuel mass flow rate (from energy balance):

$$\dot{m}_{\text{fuel}} = \frac{10 \cdot 1000}{5.78 \times 10^{7}} \approx 1.73 \times 10^{-4}\,\text{kg/s} = 0.173\,\text{g/s} \tag{5.16}$$

Here, $\dot{V}_{\text{air,lpm}}$ is the actual volumetric air flow rate in liters per minute, corrected from normal liters per minute using the temperature ratio. $\dot{V}_{\text{air}}$ is the same volumetric flow expressed in SI units of m^3/s. $\dot{m}_{\text{air}}$ is the corresponding air mass flow rate obtained using the air density ρ_{air}. M_{mix} is the molar mass of the 50% H_2–50% CH_4 fuel mixture, $LHV_{\text{mix,mol}}$ is the lower heating value of the mixture on a molar basis, and $LHV_{\text{mix,kg}}$ is the same expressed on a mass basis. Finally, $\dot{m}_{\text{fuel}}$ is the required fuel mass flow rate to deliver the target burner power of 10 kW at the given mixture heating value.

The preliminary calculations indicate that for the reference point taken, the air flow rate is around 5.39 g/s and the fuel flow rate is 0.173 g/s. So according to the literature, a steam flow rate of around 0.2 to 0.5 g/s would be desirable for the conditions of the vertical combustor. However, most steam generators did not

explicitly indicate their steam mass flow rate but instead stated their power settings. So another preliminary calculation was required to estimate the steam mass flow rate of the steam generators from power ratings.

Commercially, the most available steam generators were in the range of 1-2 kW power ratings. So, a preliminary estimation of the steam flow rate of a 1 kW steam generator was conducted.

The steam mass flow rate can be estimated from the energy balance by considering the latent heat of vaporization of water. Assuming all the electrical power is used to vaporize liquid water at 100 °C:

- Electrical Power Input: $P = 1000\,\text{W}$
- Latent Heat of Vaporization: $\Delta H_{\text{vap}} = 2257\,\text{kJ/kg} = 2257\,\text{J/g}$
- Assumed Efficiency: $\eta = 1.0$ (ideal case)

Steam Mass Flow Rate:

$$\dot{m}_{\text{steam}} = \frac{P}{\Delta H_{\text{vap}}} = \frac{1000}{2257} \approx 0.443\,\text{g/s} \tag{5.17}$$

Therefore, a 1 kW steam generator operating at full efficiency is expected to produce approximately:

$$\dot{m}_{\text{steam}} \approx \mathbf{0.443}\,\text{g/s} \tag{5.18}$$

This result indicates that the 1 kW steam generators satisfy the steam mass flow rate requirement for the test cases in the vertical combustor. Since 1 kW steam generators were commercially accessible, it was decided to use them for the experimental campaign. After extensive research on what is available commercially, it was decided that steam generators intended for in-house sauna applications were the best fit for the experiment requirements. The chosen device was a small 1kW powered 3L capacity steam generator. The device is simple to use, it has a removable lid to fill the water in and the lid is equipped with an outlet hole to direct the steam through its 10mm diameter silicone hose and a pressure relief holes in case the steam hose is obstructed. The device has a CE certification so no additional commissioning was required for the device itself. However, the overall combustor system still had to be commissioned to ensure all safety protocols are abode by and any risk factors are mitigated. An image of the steam generator is given below in Figs. 5.15 and 5.16:



Figure 5.15: The steam generator without the lid



Figure 5.16: The steam generator with the lid

The steam generator has controllable time and power settings. It also arrives with a remote controller to control the settings, which is very convenient as getting close to the combustor during its operation is extremely dangerous and not allowed. The steam generator has 9 power settings, from the lowest power setting 1 to the highest power setting of 9. However, no documentation was available on the difference

between different power settings. Knowing amount of steam mass flow rate injected into to combustor is very important to characterize the effect of steam injection, so it was necessary to quantify the mass flow rates of steam and the temperature of steam at each different power setting. To achieve this, a side experiment was conducted to characterize performance of the steam generator. The details of this side-experiment is described in Appendix B.

Once the performance of the steam generator was characterized, the steam generator could be incorporated into the current burner set-up at HSL facility. The steam generator is equipped with a heat resistant silicone hose to direct the steam outwards. To fully incorporate the steam generator into the burner set-up several modifications were conducted. Heat resistant Swagelok components, tubes and connectors were used as they are known for their reliable leak tight properties. Through these tubes and connectors, the steam is directed into modified atomizer fits that inject the steam into the combustion chamber. The atomizers used are Fluidic Instruments BV FI-0.15-80°-SF atomizer made from SS 416 & sintered brass[86]. However, the atomizers are built for water spray injection and allow for only 0.95 g/min of nominal flow rate, much lower than what is outputted by the steam generator. To accommodate this, 6 mm diameter holes that allow larger flow rates of steam were drilled into the atomizers using industrial scale precision drills. Images of the non-drilled and drilled atomizers are given below Figs. 5.17 to 5.19:

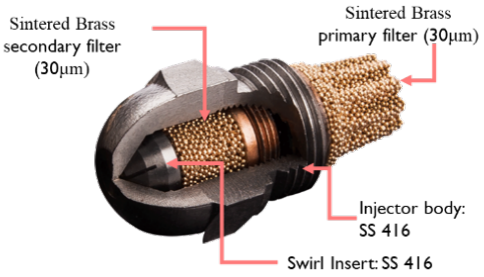


Figure 5.17: Schematic of the water spray atomizer [86]



Figure 5.18: Picture of the unmodified atomizer



Figure 5.19: The atomizer after it has been drilled and modified for the steam set-up

One of the variables chosen for the experimental campaign is the location of the steam injection. 2 different steam injection configurations were planned: the **side injection configuration**, and the **axial (steam) injection configuration**. In the side injection configuration, the steam is injected through the 2 holes around the main burner inlet as described in Figure 5.8, meaning the steam and the fuel-air injection systems are completely separate. In axial injection configuration, the steam is injected through the axial air injection hole, which is at the center of the baseplate, while the 2 side holes previously used for steam injection were sealed shut. With 2 different configurations, 2 separate set-up were needed to be assembled. The schematics for both of the configurations are given below in Figure 5.20 and Figure 5.21

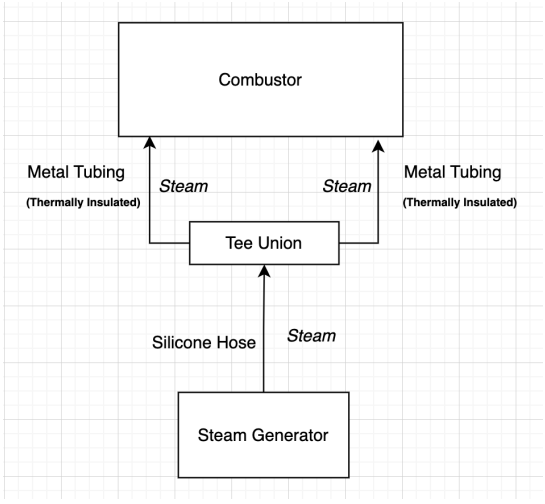


Figure 5.20: Schematic of side steam injection configuration

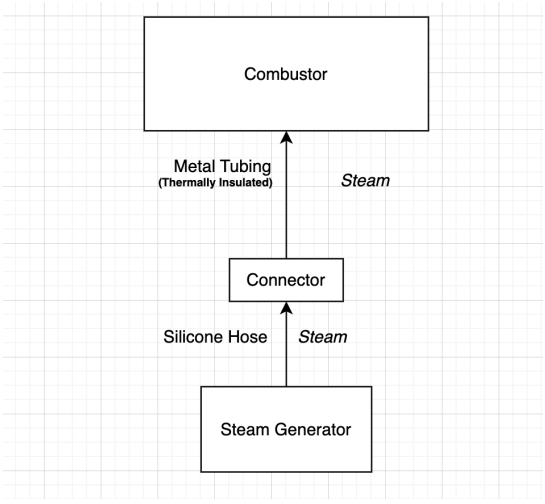


Figure 5.21: Schematic of axial steam injection configuration

A more detailed schematic of the burner is given below in Figure 5.22:

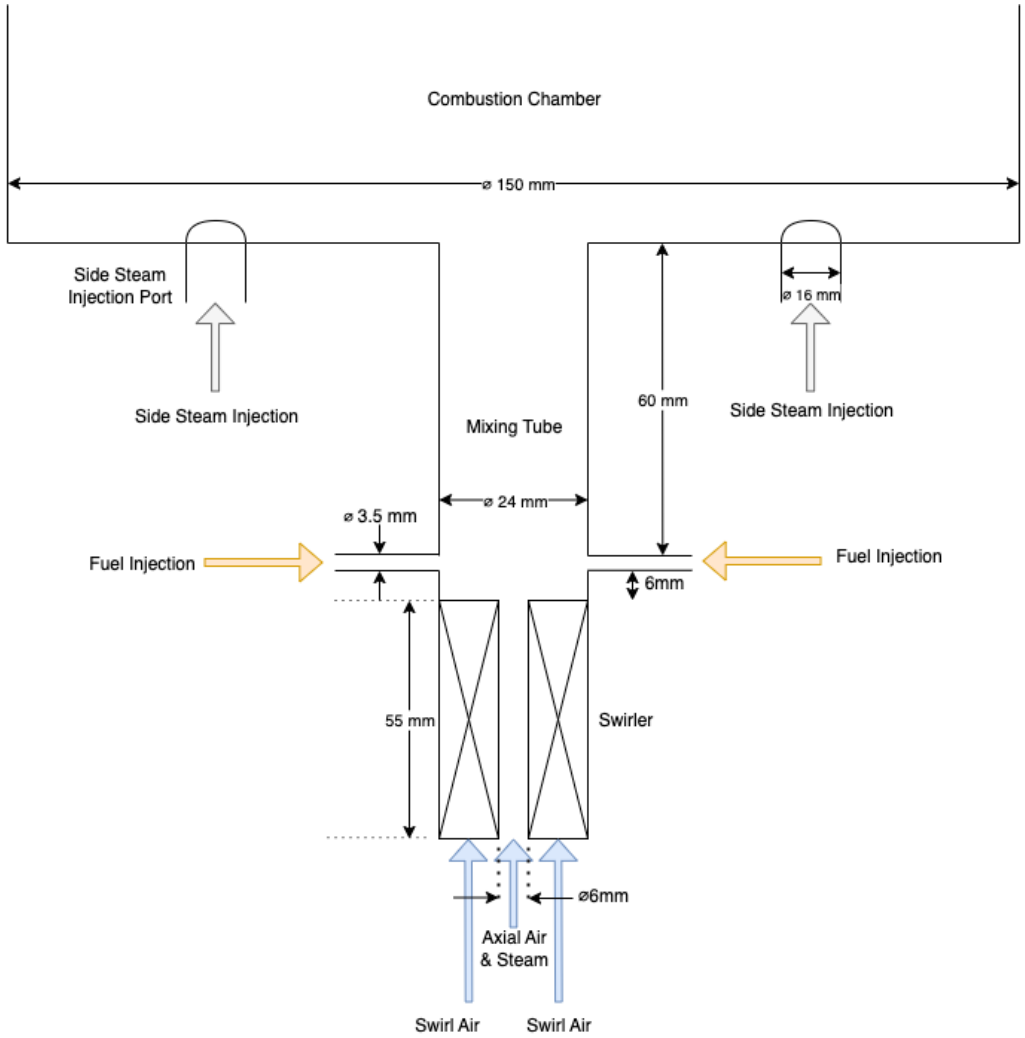


Figure 5.22: Detailed Schematic of the burner

General assembly of the burner set-up can be seen in Figure 5.23. It should be noted that in the image below, both the side injection and the axial injection configurations are attached to test if the fittings work well. During operation, only one of the configurations will be present. When the side injection configuration is used, the axial steam injection line will instead be replaced with axial air injection (AAI) line, which is used to stabilize the flame. When axial steam injection configuration is used, the AAI will not be present due to compatibility issues with the steam and air being in the same line, hence no AAI will be possible during axial steam injection configuration. During this configuration, the side steam injection holes in the baseplate will be plugged with caps. Additionally, to limit thermal losses and mitigate dangers for hot surfaces, Techflex insulation sleeves were used on the tubing and connectors.

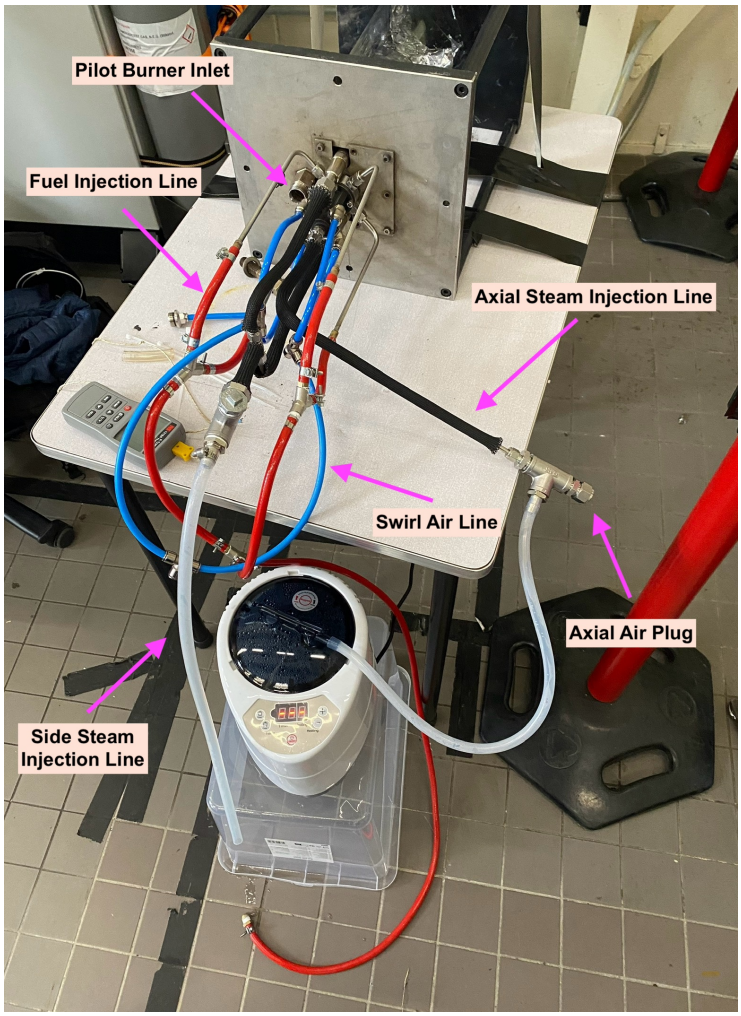


Figure 5.23: Assembly test for the burner set-up

A closer look to the burner set-up with steam injection mechanism incorporated can be seen in Figure 5.24. The set-up in the image is for side steam injection configuration and the axial air injection line can be seen in the image.

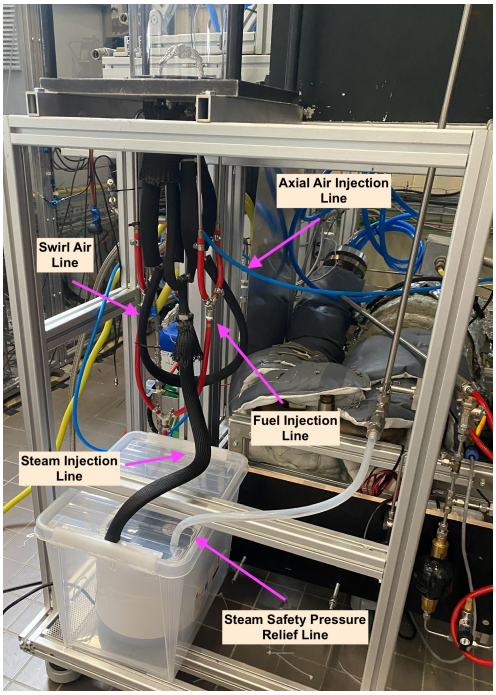


Figure 5.24: Vertical combustor set-up with the feed lines named. Side steam injection configuration present

A wider view of the combustor set-up is presented in Figure 5.25.

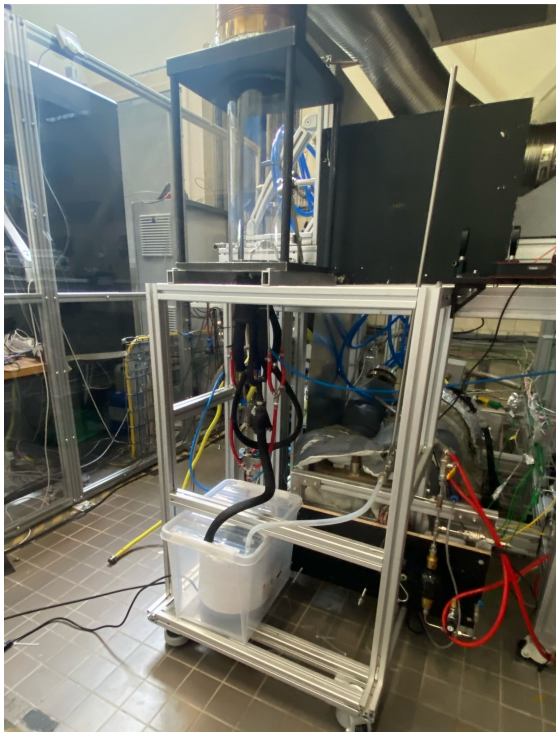


Figure 5.25: Wide-view of the vertical combustor set-up with side injection configuration

6

Measurement Techniques

In this chapter, the measurement techniques used in the experimental campaign to gather data is presented.

6.1. Gas Analyzer System

The gas analyzer was the primary emissions instrument used in this campaign. Combustion products were continuously withdrawn through a dedicated sampling port located at the top of the combustion chamber and routed directly to the analyzer via a heat-traced, insulated stainless-steel line to avoid condensation prior to conditioning. Data were logged at 0.1 Hz (one point every 10 s), after allowing sufficient stabilization time when operating conditions were changed. The sampling port of the gas analyzer is pictured below:

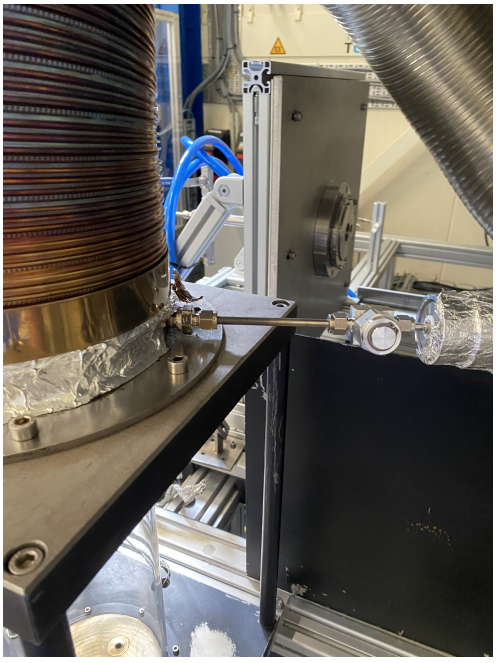


Figure 6.1: Sampling port of the gas analyzer

6.1.1. Platform and Modules

An ABB Advance Optima AO2000 modular system was employed [87, 88]. The configuration comprised:

- **Uras26** (NDIR) for CO, CO_2, and CH_4. The Uras26 is a non-dispersive infrared photometer (2.5–8 μm) with 1–2 beam paths and reference/measurement receivers. Gas-selective optical filters and a dual-beam arrangement suppress common-mode drift and temperature effects [87].
- **Magnos28** (paramagnetic) for O_2. The sensor exploits oxygen's paramagnetism; a magneto-mechanical element (microwing/dumbbell) placed in a magnetic field experiences a torque pro-

portional to O_2 concentration. Optical readout and on-board analog-to-digital conversion yield fast, low-noise measurements across wide ranges [89, 87].

- **Limas11 HW** (UV) for NO and NO_2. The module uses ultraviolet absorption (Beer–Lambert law) in a hot-wet configuration to minimize NO_x losses and interferences associated with condensation and dissolution [90].

6.1.2. Gas Path, Conditioning, and Measurement Basis

The raw exhaust stream is extracted from the chamber and routed to the analyzer through a heat-traced line. For the dry channels (Uras26 for CO, CO_2, CH_4 and Magnos28 for O_2), the sample is dehumidified upstream so that water vapor is removed prior to analysis; the reported values are therefore dry gas volume fractions.

For the wet channel (Limas11 HW for NO and NO_2), the sampling path is kept hot to prevent condensation along the route to the UV cell, and the measurements are taken directly on the wet gas. This approach minimizes NO_x losses associated with condensation/dissolution and avoids wet-to-dry conversion for these species.

Since H_2O is removed ahead of the dry channels and is not measured by the analyzer, any wet-basis interpretation (e.g., reference-O_2 normalization or comparison to equilibrium “wet” compositions) uses the water fraction obtained from combustion stoichiometry and the known steam-injection rates.

This configuration and procedure ensure that reported O_2, CO_2, CO, and CH_4 values represent dry gas composition at the analyzer inlet, while NO and NO_2 represent the hot-wet composition in the UV cell. Any conversion to wet-basis totals or to reference O_2 is performed in post-processing using the independently determined water fraction.

A full calibration was performed at the start of each experimental day. Five certified calibration gases were used: four cylinders with known concentrations of NO, NO_2, CO, CO_2, and CH_4 (balance N_2), and ambient air used for O_2. Cylinders that did not contain a given species served as the corresponding zero gas for that channel. Zero and span checks were executed for each module before measurements commenced.

The working uncertainties used in this campaign (post-calibration) are summarized in Table 6.1. These values are deliberately conservative, reflecting both manufacturer specifications and practical repeatability limits observed during operation.

Species	Module	Basis	Uncertainty
NO	Limas11 HW	wet	± 0.10 ppm
NO_2	Limas11 HW	wet	± 0.10 ppm
CO	Uras26	dry	± 1.00 ppm
CO_2	Uras26	dry	± 0.10 vol%
CH_4	Uras26	dry	± 1.00 ppm
O_2	Magnos28	dry	± 0.10 vol%

Table 6.1: Working uncertainties (post-calibration), based on analyzer specifications and observed repeatability.

6.2. UV Camera

Flame imaging was performed with a monochrome FL-20BW camera. The target signal was OH^* chemiluminescence near 309 nm. The camera viewed the flame through a UV-transmitting fused-silica window using a UV-capable lens. A narrow bandpass filter centered near 310 nm was used to isolate the OH^* band and suppress broadband background.

OH^* imaging is used as a fast, non-intrusive proxy for heat release. The excited OH^* band near 309 nm is produced in high temperature reaction zones, so its emission highlights the flame front rather than the cold

mixed reactants. From these images we extract: (i) overall flame shape and anchoring location, (ii) lift-off height relative to the nozzle, (iii) regions of intense reaction, and (iv) qualitative changes in stability with steam addition or operation point shifts.

6.3. DSLR Camera

Nikon D7500 DSLR camera was used to document qualitative changes in flame shape, color, and overall luminosity under each operating point. Images were taken through the furnace window on a fixed tripod with manual focus and manual exposure to ensure comparability across shots. White balance was fixed for a given series. Exposure time, aperture, and ISO were kept consistent within each test matrix when possible, but were occasionally adjusted within a narrow range to accommodate brightness differences between operating points and to avoid saturation. All photos were recorded in RAW format to preserve dynamic range and enable consistent post-processing.

These photographs provide visual context complementary to the UV images and gas analysis: they show flame anchoring and lift-off, visible luminosity variations with steam addition and equivalence ratio, and the presence of any incandescence or stray reflections. Because the DSLR observes broadband visible light rather than a specific emission band, the images are used for qualitative comparison only (not for quantitative heat-release or species inference).

The placements of the cameras in the overall lab set-up is presented below in Figure 6.2:

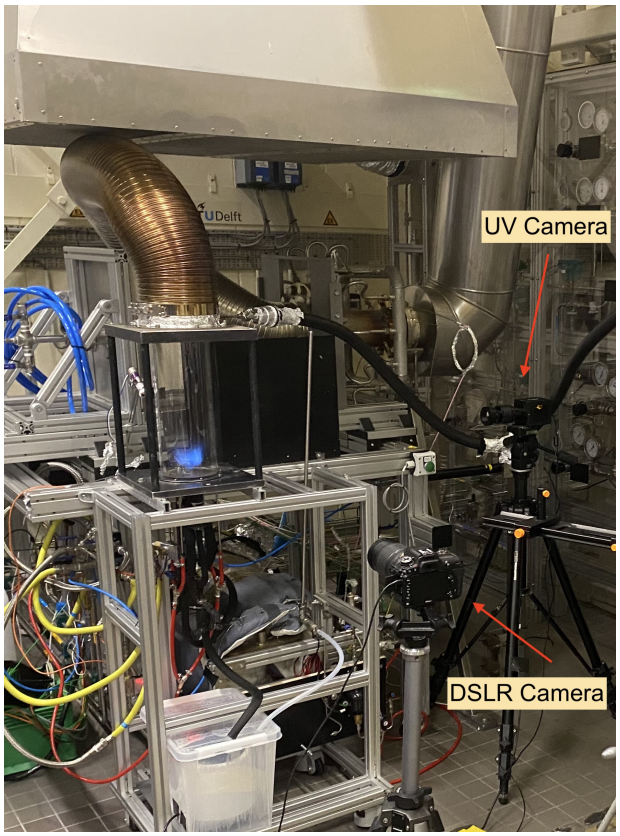


Figure 6.2: Locations of cameras used in the lab set-up

Since side steam injection configuration is not axi-symmetrical, it is important to clarify which direction the cameras are looking at with respect to the side steam injection. A schematic of this is given below in Figure 6.3:

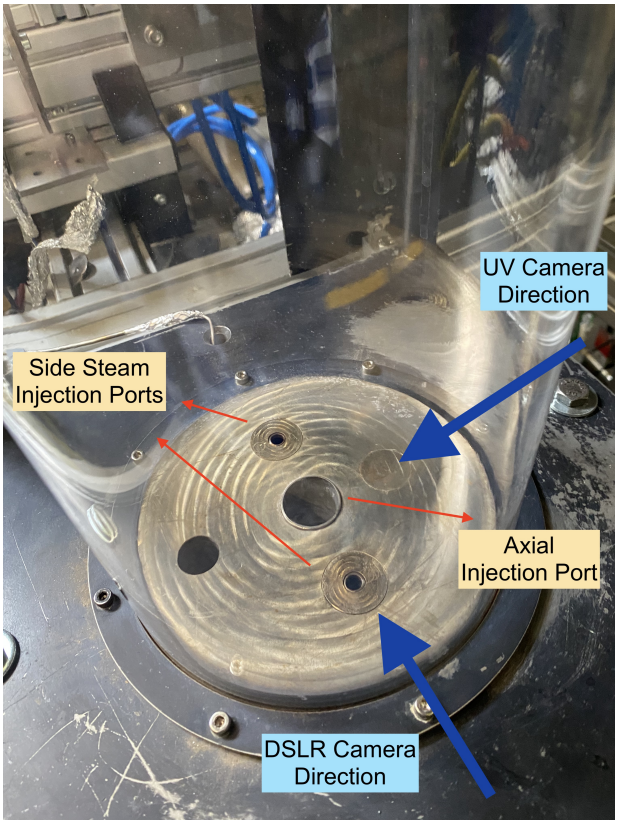


Figure 6.3: Line of sight of cameras with respect to the combustion chamber and steam injection ports

It should be noted that all images from both cameras are taken while the lights are off and window blinds down to ensure minimal interference of ambient light with the camera images.

7

Methodology, Test Matrix & Experimental Points

This chapter describes the methodology applied to support and guide the experimental campaign. It begins with Cantera simulations that were used to estimate adiabatic flame temperature and laminar flame speed, providing reference values that could not be measured directly in the setup. Next, the uncertainties in the equivalence ratio are quantified based on the specifications of the flow controllers to assess the reliability of the test conditions. The experimental point selection is then presented in a structured test matrix, organized into series that isolate the effects of burner power, fuel blend, steam amount, and injection location. Finally, a simplified analytical approach is introduced to estimate the impact of steam injection on flame temperature and NO reduction, complementing both the experimental results and the numerical simulations.

7.1. Estimation of Adiabatic Flame Temperature and Laminar Flame Speed using Cantera

One of the key aspects in characterizing a premixed flame is understanding its thermal and kinetic behavior. Parameters such as the adiabatic flame temperature and the laminar flame speed are fundamental indicators of flame structure, reactivity, and stability. Hence, these parameters are important for characterizing a flame.

Direct measurement of either flame temperature or flame speed was not carried out in this study, although such diagnostics are possible with advanced optical techniques. The HSL test rig was equipped with gas analyzers, mass flow controllers, and thermocouples; however, the thermocouples were only used to monitor hardware and boundary conditions, not to measure flame temperature. Since the flames under investigation are turbulent, the relevant propagation velocity is the turbulent flame speed. Nevertheless, laminar flame speed remains a useful baseline quantity because it is well-defined, widely reported in literature, and strongly correlated with reactivity and stability.

To obtain reference values for the conditions investigated, numerical simulations were performed with the open-source software Cantera [91]. Cantera provides detailed thermodynamic and kinetic models for hydrogen, methane, and their blends, and allows simulations under constant-pressure conditions with controlled temperature, pressure, equivalence ratio, and fuel composition. This made it possible to replicate the experimental operating points and extract the adiabatic flame temperature and unstretched laminar flame speed, which serve as reference values to contextualize the measurements. The reproducibility and transparency of Cantera's framework also contribute to its wide adoption in combustion research.

Simulation Methodology:

1. For each test condition defined by burner power, air flow, and hydrogen fraction, the equivalence ratio was first calculated using the methods discussed in Equation 5.9.
2. Using the calculated equivalence ratio and the known inlet conditions (temperature, pressure, fuel composition), the Cantera simulation was set up.

3. A one-dimensional freely propagating premixed flame model was used, implemented via the `FreeFlame` class in Cantera.
4. The simulations were based on the GRI-Mech 3.0 mechanism, which has been extensively validated for natural gas, hydrogen, and methane combustion at atmospheric pressure. This mechanism includes detailed kinetic pathways for oxidation and NOx formation, making it well-suited for the present study.
5. The inlet temperature was set to ambient temperature, taken as 288 K. Simulations were run at 1 atm, consistent with the experimental conditions.
6. Mesh refinement was handled automatically with the following refinement criteria: maximum ratio = 3.0, slope = 0.06, and curvature = 0.12. Simulations were run until a converged steady-state flame profile was obtained, with residuals below 10^{-9}.
7. these the steady-state simulation results, the following parameters below were extracted. It should be noted that these results are obtained for only the case with no steam injection, the values will be different for steam injected cases.
    - **Adiabatic Flame Temperature**: The peak temperature obtained from the equilibrium calculation at constant enthalpy and pressure.
    - **Laminar Flame Speed**: The unstretched flame speed obtained directly from the FreeFlame solver output.
8. These values were associated with each test point and used for interpreting trends related to flame behavior and emissions.

To verify the plausibility of the simulated results, the output values were briefly compared with literature data available for similar equivalence ratios and fuel compositions. The simulated adiabatic flame temperatures and laminar flame speeds were found to be in reasonable agreement with experimentally measured values reported in prior studies[56] [92][93] [94]. While this cross-check was not exhaustive, it provides added confidence in the validity of the simulation results.

It is important to acknowledge the assumptions and limitations of the simulation approach. The simulations are based on a one-dimensional, adiabatic, laminar flame model. Consequently, effects such as turbulence, flame stretch, and all forms of heat loss are not captured. In the experiments, heat is dissipated through radiation and conduction to the quartz tube and the base plate, which lowers the actual flame temperature compared to the adiabatic prediction. While such effects influence flame behavior in practice, the idealized simulation results still provide a consistent and valuable reference for interpreting experimental trends and comparing operating conditions.

Utilizing simulation data offers several key advantages in the analysis of combustion behavior. First, it enables a deeper investigation into the thermochemical effects of varying fuel compositions, particularly across different hydrogen–methane blends. This is essential for understanding how shifts in fuel mixture influence flame characteristics. The data also provide valuable insight into NOx formation mechanisms, particularly in relation to adiabatic flame temperature, which directly influences thermal NOx formation. However, it should be noted that residence time is another important factor governing NOx production, but this effect cannot be accounted for within the Cantera framework used here. A more comprehensive CFD (computational fluid dynamics) simulations can estimate residence times, but it was deemed out of scope of this current research.

Although simulations do not replace experimental measurements, they serve as a reliable and consistent tool for supporting the analysis when physical diagnostics are unavailable.

7.2. Uncertainty Quantification

To have a more comprehensive analysis, the potential effects of the uncertainties shall also be discussed. The uncertainty characterization for the steam injection was discussed in Section 5.3. In this section, the uncertainties arising from the fuel and air injection will be discussed. As previously mentioned before, the uncertainties of the Bronkhorst mass flow controllers are defined as:

$$\Delta\dot{Q} = 0.005RD + 0.001FS \tag{7.1}$$

Where RD is the read value and the FS is the full-scale value. The read value is the value inputted in the controller GUI for the given test point. The full-scale value is the maximum range for the respective mass flow controller. For the vertical (main) combustor, there are 4 relevant mass flow controllers that affect the calculation of the set-point equivalence ration:

Name	Max Range [nlpm]
Main Burner – air	3000
Main Burner CH_4	350
Main Burner H_2 low	60
Main Burner H_2 high	1000

Table 7.1: Full-scale values of the gas flow controllers of the main burner

As it can be observed from Table 7.1, there are 2 mass flow controllers for the hydrogen. This is done to cover a larger range of hydrogen flow rates. When the fuel is either pure hydrogen or pure methane, the calculation for the flow uncertainty is straightforward. However, when the fuel is a blend of H2 and CH4, an extra step is needed to calculate the total uncertainty of the fuel flow rate. According to the input H2 fraction value, the respective uncertainties of the H2 and CH4 flows are independently calculated. Then the root-sum-square (RSS) method is utilized to calculate the total uncertainty of the fuel flow rate:

$$u(\dot{m}_{fuel,mix,lpm}) = \sqrt{u(\dot{m}_{H2,lpm})^2 + u(\dot{m}_{CH4,lpm})^2} \tag{7.2}$$

Once the uncertainties of the volumetric flow rates for both fuel and air are determined, the uncertainty in the equivalence ratio can be calculated. The set-point equivalence ratio, ϕ, is defined as:

$$\phi_{mix} = \frac{\dot{V}_{\text{fuel,mix,lpm}}}{\dot{V}_{\text{air,lpm}}} \cdot AFR_{fuel_{mol}} \tag{7.3}$$

where $\dot{V}_{fuel}$ and $\dot{V}_{air}$ are the volumetric flow rates of the fuel mixture and air respectively, and $AFR_{fuel_{mol}}$ denotes the stoichiometric molar air-to-fuel ratio of the mixture, calculated from the H_2 and CH_4 fractions as given in Equation 5.3. Since the $AFR_{fuel_{mol}}$ is a deterministic value based on fuel composition, the uncertainty in ϕ arises from the uncertainties in the flow rates. The relative uncertainty in ϕ is given by the propagation of uncertainties:

$$\left(\frac{u(\phi)}{\phi}\right)^2 = \left(\frac{u(\dot{V}_{fuel,mix,lpm})}{\dot{V}_{fuel,mix,lpm}}\right)^2 + \left(\frac{u(\dot{V}_{air,lpm})}{\dot{V}_{air,lpm}}\right)^2 \tag{7.4}$$

and the absolute uncertainty in ϕ is then:

$$u(\phi) = \phi \cdot \sqrt{\left(\frac{u(\dot{V}_{fuel,mix,lpm})}{\dot{V}_{fuel,mix,lpm}}\right)^2 + \left(\frac{u(\dot{V}_{air,lpm})}{\dot{V}_{air,lpm}}\right)^2} \tag{7.5}$$

where $u(\dot{V}_{fuel,mix,lpm})$ is either the directly computed uncertainty of pure fuel (H_2 or CH_4), or, in case of a fuel blend, the root-sum-square (RSS) of both components as shown previously. The air flow uncertainty $u(\dot{V}_{air,lpm})$ is calculated from Equation 7.1 using the input air flow rate and the corresponding full-scale value.

While the calculation of the uncertainty of each set-point is possible, it is unnecessarily laborious and offers diminishing returns in terms of accuracy. Moreover, reporting individual uncertainty values for each data point would make the data presentation cluttered and impractical. Therefore, the uncertainty in the equivalence ratio is calculated using a representative value derived from the root-mean-square (RMS) method, as shown in Equation 7.6:

$$u(\phi) = \sqrt{\frac{1}{n}\sum_{i=1}^{n} u_i(\phi)^2} \tag{7.6}$$

This method is applied to each test group individually, where all calculated uncertainties within the group are aggregated to determine a single representative uncertainty value. This group-level uncertainty is then uniformly applied to all data points within the same test group, ensuring consistency while preserving readability and interpretability in data presentation.

The root-mean-square (RMS) method is chosen over other aggregation approaches such as the maximum or simple mean for its balanced treatment of variability. The maximum method, while conservative, can overstate the uncertainty if a single outlier has an unusually high value, thus misrepresenting the overall trend. On the other hand, a simple arithmetic mean may underestimate the impact of higher uncertainties. RMS provides a middle ground by giving greater weight to larger uncertainties without allowing any single value to dominate the result. This makes it particularly well-suited for representing the overall uncertainty within a test group, especially when the individual uncertainties vary moderately around a central value.

The final uncertainty value for ϕ is computed for each test group using the RMS method in this next section. The equivalence ratio and the corresponding uncertainties are provided with the test points.

7.3. Experimental Point Selection

The purpose of this experimental investigation is to explore the effect of steam on flame structure and emissions at different conditions. To investigate a wide range of conditions, several experimental conditions have been changed throughout the experimental campaign. All the experiments are conducted in ”side (steam) injection configuration” explained in Section 5.3 unless stated otherwise.

To make a more cohesive structure with the collected data, the experiments are divided into ”series”, where each series intend to investigate a different aspect of the experimental settings. The experimental series and the relevant test points are provided in the following sections.

It should also be noted that the adiabatic flame temperature and the laminar flame speeds described in the tables are for no steam injection cases.

Series A: Variation of Burner Power

The first area of interest is the change of the burner power while keeping the hydrogen blend fraction of the fuel mixture and the main air flow rate constant. For this first campaign, the power setting is changed from 10 kW to 7 kW, while keeping the total air flow at 250 lpm and testing for full hydrogen fuel (hydrogen fraction of 1). To see the effect of steam injection, the highest steam power setting of 9 is selected. The selected points are given below in Table 7.2.

Power [kW]	H_2 Fraction [-]	Total Air [nlpm]	AAI [%]	Equivalence Ratio [-] $\pm$ 0.009	Adiabatic Flame Temperature [K]	Laminar Flame Speed [cm/s]	Steam
10	1.0	250	15	0.529	1691.7	44.77	No-Steam Steam-9
9	1.0	250	15	0.476	1582.8	28.98	No-Steam Steam-9
8	1.0	250	10	0.423	1468.2	17.18	No-Steam Steam-9
7	1.0	250	10	0.370	1347.6	7.93	No-Steam Steam-9

Table 7.2: Test matrix for Experiment-A1. 100% H_2 combustion with varying burner power. Side steam injection configuration was used.

For these experimental groups, when the rms method for the uncertainty is applied in Equation 7.6, the uncertainty of the equivalence ratio is found to be 0.009, which is applied to all the points in this test group.

To complement this initial study with pure hydrogen, another set of experiments were conducted with pure methane. The combustor was set to 0 % H2 fraction (100% CH4) and the burner power was changed from 10 kW to 7 kW in 0.5 kW increments. To investigate the effect of steam injection, steam power 9 was once again used in this experiment group. The experimental points for this test group is given below in Table 7.3:

Power [kW]	H_2 Fraction [-]	Total Air [nlpm]	AAI [%]	Equivalence Ratio [-] ±0.031	Adiabatic Flame Temperature [K]	Laminar Flame Speed [cm/s]	Steam
11.0	0.0	180	0	0.976	2204.9	35.10	No-Steam Steam-9
10.5	0.0	180	0	0.931	2163.1	33.37	No-Steam Steam-9
10.0	0.0	180	0	0.887	2110.9	31.16	No-Steam Steam-9
9.5	0.0	180	0	0.843	2051.6	28.50	No-Steam Steam-9
9.0	0.0	180	0	0.798	1985.9	25.41	No-Steam Steam-9
8.5	0.0	180	0	0.754	1917.8	22.20	No-Steam Steam-9
8.0	0.0	160	0	0.798	1985.9	25.41	No-Steam Steam-9
7.5	0.0	160	0	0.748	1908.2	21.74	No-Steam Steam-9
7.0	0.0	140	0	0.798	1985.9	25.41	No-Steam Steam-9

Table 7.3: Test matrix for Experiment-A2. 100% CH_4 combustion with varying burner power. Side steam injection configuration was used.

As it can bee seen from the table, no AAI was used in the pure methane experiment as the stability regime plot at Figure 5.14 indicates flashback is not a concern for pure methane flames, hence the use of AAI is not needed. However, blowout is a huge concern for pure methane flames, so while decreasing the power of the burner the equivalence ratio of the flame also decreases, which put the flame in the blowout zone. To accommodate this, the total air mass flow rate is decreased to keep a stable flame at low power settings. This consequently increased the equivalence ratio of the flame, and placed the test point in the stable combustion region. Hence, it is important to analyze this set of data also in the perspective of equivalence ratio and not purely on the power setting of the burner. More on this will be discussed in Chapter 9.

The equivalence ratio values (ϕ) are subject to uncertainty due to flow meter limitations and calibration tolerances. Based on the specifications of the fuel and air flow controllers, the combined uncertainty in ϕ is estimated to be approximately ± 0.031. This level of uncertainty can occasionally result in partial overlap between adjacent operating points, especially when the burner power is adjusted in small increments (e.g., 0.5 kW). The impact of this overlap on the interpretation of emission trends will be examined in (Chapter 9.

Series B: Variation of Blend Percentage

In the next set of experiments, the hydrogen blend percentage of the fuel is varied while keeping the burner power the same. In Experiment B1, the power is set at 11kW and the main total airflow is kept at 250 nlpm. Data for no-steam and steam power 9 are collected for the test matrix given below in Table 7.4.

As presented in Table 7.4, the axial air injection (AAI) was kept at 0% for blends up to 50% H_2, since flashback was not an issue in this range. At higher hydrogen fractions, however, AAI was progressively increased up to 20% to provide additional axial momentum and reduce the risk of flashback. This adjustment ensured that stable flames could be sustained across the full range of blend percentages tested.

Power [kW]	H_2 Fraction [-]	Total Air [nlpm]	AAI [%]	Equivalence Ratio [-] $\pm$ 0.017	Adiabatic Flame Temperature [K]	Laminar Flame Speed [cm/s]	Steam
11.0	0.0	250	0	0.702	1833.3	18.25	No-Steam Steam-9
11.0	0.2	250	0	0.694	1831.3	20.24	No-Steam Steam-9
11.0	0.3	250	0	0.689	1830.0	21.60	No-Steam Steam-9
11.0	0.4	250	0	0.682	1826.9	23.24	No-Steam Steam-9
11.0	0.5	250	0	0.675	1825.6	25.54	No-Steam Steam-9
11.0	0.6	250	10	0.665	1821.7	28.42	No-Steam Steam-9
11.0	0.7	250	15	0.653	1818.1	32.32	No-Steam Steam-9
11.0	0.8	250	20	0.637	1813.1	38.04	No-Steam Steam-9

Table 7.4: Test matrix for Experiment-B1. Constant 11 kW burner with varying blend percentage. Side steam injection configuration was used.

As seen in Table 7.4, varying the hydrogen fraction in the fuel mixture while keeping constant air and power significantly affects the resulting equivalence ratio. This is a direct consequence of the differing lower heating values and stoichiometric air-to-fuel ratios of hydrogen and methane. Hydrogen has a higher molar lower heating value (LHV) and requires less oxidizer per mole compared to methane. Therefore, increasing the hydrogen content in the mixture reduces the total molar fuel flow required to maintain the same thermal power input. As a result, the fuel-to-air ratio decreases, leading to a lower equivalence ratio. This trend is evident in the data, where increasing the hydrogen fraction from 0.0 to 0.8 causes the equivalence ratio to drop from 0.702 to 0.637. Despite this decrease, the adiabatic flame temperature remains nearly constant, decreasing only slightly from 1841.9 K to 1822.2 K. In contrast, the laminar flame speed increases noticeably as the hydrogen fraction rises, which is consistent with the faster combustion kinetics of hydrogen compared to methane.

To complement the previous experiment group, another set of points were tested at constant 9 kW power and 250 nlpm total air injection. No-steam vs steam power 9 was compared. The test matrix for Experiment-B2 is given in Table 7.5:

Power [kW]	H_2 Fraction [-]	Total Air [lpm]	AAI [%]	Equivalence Ratio [-] $\pm$ 0.014	Adiabatic Flame Temperature [K]	Laminar Flame Speed [cm/s]	Steam
9.0	0.2	250	0	0.568	1609.5	9.89	No-Steam Steam-9
9.0	0.3	250	0	0.563	1607.0	10.57	No-Steam Steam-9
9.0	0.4	250	0	0.558	1605.9	11.45	No-Steam Steam-9
9.0	0.5	250	0	0.552	1604.8	12.63	No-Steam Steam-9
9.0	0.6	250	10	0.544	1602.2	14.02	No-Steam Steam-9
9.0	0.7	250	10	0.534	1599.4	15.94	No-Steam Steam-9
9.0	0.8	250	10	0.521	1596.0	18.69	No-Steam Steam-9
9.0	1.0	250	15	0.476	1582.8	28.98	No-Steam Steam-9

Table 7.5: Test matrix for Experiment-B2. Constant 9 kW burner with varying blend percentage. Side steam injection configuration was used.

In Table 7.5, AAI values were similarly adjusted at higher hydrogen fractions (10–15%) to mitigate flashback tendencies. At lower H_2 fractions, AAI was not required, so it was set to 0%.

Series C: Variation in Steam Injection Amount

In the next set of experiments, the amount of steam injected into the combustor is varied. This allows the isolated effect of steam quantity on flame behavior and emissions to be studied more directly. The tests are conducted at fixed burner power of 10 kW and fixed total air injection of 250 nlpm. Test points for no-steam, steam power 9 and power 7 are tested for each test point. To have a more comprehensive study, a range of hydrogen fractions are used and injected with steam levels 9 and 7.

Power [kW]	H_2 Fraction [-]	Total Air [nlpm]	AAI [%]	Equivalence Ratio [-] ±0.015	Adiabatic Flame Temperature [K]	Laminar Flame Speed [cm/s]	Steam
10.0	0.1	250	0	0.635	1724.1	14.05	No-Steam Steam-9
10.0	0.2	250	0	0.631	1723.0	14.89	No-Steam Steam-9 Steam-7
10.0	0.3	250	0	0.626	1721.3	15.91	No-Steam Steam-9 Steam-7
10.0	0.4	250	0	0.620	1719.1	17.16	No-Steam Steam-9 Steam-7
10.0	0.5	250	0	0.613	1717.0	18.78	No-Steam Steam-9 Steam-7
10.0	0.6	250	10	0.604	1713.8	20.76	No-Steam Steam-9 Steam-7
10.0	0.7	250	10	0.593	1710.6	23.68	No-Steam Steam-9 Steam-7
10.0	0.8	250	15	0.579	1707.3	27.61	No-Steam Steam-9 Steam-7
10.0	1.0	250	15	0.529	1691.7	44.77	No-Steam Steam-9 Steam-7

Table 7.6: Test matrix for Experiment-C1. Constant 10 kW burner power with varying steam injection setting and H_2 blend fraction. Side steam injection configuration was used.

Experiment-C1 investigates the effect of steam injection amount in a wide range of hydrogen fraction, and in essence acts as a complementary study for the ”variation of blend percentage” set of experiments. While this experiment provides insight on the effect of the amount of steam injection, a more comprehensive study was also initiated, this time conducting experiments with the full available power range of the steam generator to further investigate the effect of the amount of steam injected.

It should be noted that due to time constraints, 0.1 H2 fraction steam-7 data point was not tested. Instead of removing the 0.1 H2 fraction point completely from the test matrix and the results analysis, it was instead decided to keep the results for no-steam and steam-9 cases since they still provide valuable insights on the objective of the whole experimental campaign.

In this next experiment called Experiment-C2, no-steam, steam 9, 8, 7 and 6 cases were tested using a constant burner power of 10kW. Due to larger test points with more steam variation, only hydrogen fractions of 0.4, 0.6 and 0.8 were tested in this experiment group. The test matrix for Experiment-C2 is given in Table 7.7:

Power [kW]	H_2 Fraction [-]	Total Air [nlpm]	AAI [%]	Equivalence Ratio [-] ± 0.013	Adiabatic Flame Temperature [K]	Laminar Flame Speed [cm/s]	Steam
10.0	0.4	250	0	0.620	1719.1	17.16	No-Steam Steam-6 Steam-7 Steam-8 Steam-9
10.0	0.6	250	10	0.604	1713.8	20.76	No-Steam Steam-6 Steam-7 Steam-8 Steam-9
10.0	0.8	250	15	0.579	1707.3	27.61	No-Steam Steam-6 Steam-7 Steam-8 Steam-9

Table 7.7: Test matrix for Experiment-C2. Constant 10 kW burner power with varying steam injection setting and H_2 blend fraction. A wider range of steam settings were used compared to previous experiments. Side steam injection configuration was used.

It is expected that Experiment-C2 could provide a deeper insight in the effect of quantity of steam injection on the characteristics of a flame.

Series D: Variation in Steam Injection Location

So far, all the previous experiments in each experimental group were conducted in side steam injection configuration. However, literature indicates that the injection location of dilutants such as steam can have a huge impact on the structure, the dynamics and the emissions of a flame. To investigate this effect, Experiment-D1 was conducted after modifying the experimental set-up to the axial steam injection configuration. To allow for a comparison with side injection experiments, 10 kW burner power was kept constant while varying the hydrogen fraction of the fuel. Steam power 9, 8, 7, 6 and no-steam cases were tested to also act as a complementary study on the effect of amount of steam injection. The test matrix for Experiment-D1 is given in Table 7.8.

Axial Steam Injection Configuration							
Power [kW]	**H_2 Fraction [-]**	**Total Air [nlpm]**	**AAI [%]**	**Equivalence Ratio [-]** $\pm$ 0.014	**Adiabatic Flame Temperature [K]**	**Laminar Flame Speed [cm/s]**	**Steam**
10.0	0.4	250	0	0.620	1719.1	17.16	No-Steam Steam-6 Steam-7 Steam-8 Steam-9
10.0	0.5	250	0	0.613	1717.0	18.78	No-Steam Steam-6 Steam-7 Steam-8 Steam-9
10.0	0.6	250	0	0.604	1713.8	20.76	No-Steam Steam-6 Steam-7 Steam-8 Steam-9
10.0	0.7	250	0	0.593	1710.6	23.68	No-Steam Steam-6 Steam-7 Steam-8 Steam-9
10.0	0.8	250	0	0.579	1707.3	27.61	No-Steam Steam-6 Steam-7 Steam-8 Steam-9

Table 7.8: Test matrix for Experiment-D1. Constant 10 kW burner power with varying steam injection setting and H_2 blend fraction. Axial steam injection configuration was used.

One important aspect that should be clarified about the axial steam injection case is the lack of axial air injection (AAI) in this configuration. During the planing phase of the experiment, it was assumed that both steam and AAI can be directed through the same channel in to the combustor chamber. However, during the experiment it was found that the AAI stream was much stronger than the steam stream, hence the AAI was both blowing into the combustor and the steam generator, meaning the steam was not reaching into the combustion chamber in this set-up. To accommodate this, the AAI line was removed and the connection to that port was plugged with a sealed (steam leak resistant) cap, which was discussed in Section 5.3. This is the reason that none of the test points have AAI in this experimental group.

In the previous experimental points at 10 kW, AAI injection was used in hydrogen fraction 0.6 and above. This is due to the fact that due to hydrogen's high laminar flame speeds, the flame was burning further upstream and at times just after the swirler, which can potentially be damaging to the experimental set-up components. At 0.8 hydrogen fraction, the flame flashbacks without AAI. However, one interesting finding of this experiment was that the test point of 0.8 H2 fraction with steam injection ranges of power setting 9 to 6 allowed for a stable flame. This indicates that the axial steam injection acted as the AAI that stabilized the flame previously.

The no-steam cases for Experiment-7 was conducted without any AAI. This was done to have a more fair comparison on NOx emissions as the AAI affects the flame structure and tend to decrease NOx emissions [80]. This is true except for the 0.8 H2 fraction test point, as without the AAI, flashback occurs. To compare

the axial steam injection test-points with a no-steam test point, the 10 kW 0.8 H2 fraction test-point from Experiment-5 was used. Even though this method introduces a minor inconsistency it is believed that the ability of steam injection alone to stabilize the 0.8 H2 fraction flame without auxiliary air has a significant and noteworthy result in terms of aerodynamic and thermal impact on the flame structure.

8

Data Processing

This chapter describes how the experimental data were processed and validated prior to analysis. It includes baseline correction, signal filtering, and statistical screening to ensure stable and physically meaningful measurements. The wet–dry basis of each analyzer channel is clarified, and the corresponding conversions are outlined. Emission index calculations for NO (EINO) and CO (EICO) are presented on both mass-of-fuel and energy bases, together with the normalization procedure to 15% O_2. Additional data processing steps relevant to the interpretation of emission results are discussed, followed by an overview of the ultraviolet (UV) image processing methods used for visualization and analysis.

This chapter outlines the data handling procedures and statistical evaluation methods used to ensure the reliability and interpretability of the experimental results. Key topics include baseline correction, gas analyzer reliability, criteria for filtering noisy or unstable data, and the statistical tools used to validate observed trends in NO emissions. The chapter also presents repeatability checks across independent experimental campaigns and explains the rationale behind the inclusion or exclusion of specific data points. These procedures form the foundation for the accuracy and robustness of the combustion emission results discussed in subsequent chapters.

8.1. Statistical Approach for Data Accuracy

Baseline Measurements

The gas analyzer was calibrated at the beginning of each experimental day to ensure accuracy. Before every experimental set, flame-off baseline measurements were taken to check for residual sensor drift or offset. These baseline values were then subtracted from the flame-on data to correct any remaining deviation and maintain consistency across all measurements.

The baseline measurements were taken with the combustion chamber fully purged and no flame present. Under these conditions, the expected concentrations of combustion-related species such as NO, CO, CO_2, and NO_2 should be essentially zero, while O_2 levels should reflect the atmospheric concentration, typically around 20.9% by volume.

These baseline values were used for normalization purposes, particularly for NO, which is the primary emission species of interest in this study. Since NO should be absent without a flame, any residual NO signal in the baseline was attributed to sensor offset or drift and was subtracted from the flame-on measurements. Similarly, any measured concentrations of CO, CO_2, or NO_2 during the baseline runs were also treated as offsets and subtracted from the respective flame-on data. O_2 readings during the baseline were used to verify analyzer accuracy against the ambient oxygen level, and any significant deviation from ambient values would indicate a need for recalibration or inspection.

Gas Analyzer and Reliability of Emission Measurements

As mentioned in Chapter 6, all emission measurements in this study were conducted using the ABB AO2020 gas analyzer system, installed in the outlet line of the combustion chamber. The exhaust gases were sampled from the exhaust line downstream of the combustor, ensuring representative mixing of the flue gases. The readings were recorded once stable flow and flame conditions were reached. The readings were logged over a time span of approximately 60 to 100 seconds per test point, ensuring that fluctuations due to transient behavior were excluded from the reported results.

To ensure measurement accuracy and minimize drift effects, the gas analyzer system was calibrated at the start of each experimental day using calibration gases with known concentrations. This step was especially important for NO and NO_2 measurements, as the LIMAS21 HW UV photometer is known to be more susceptible to long-term drift and optical alignment sensitivity than the other modules. Daily calibration helped ensure repeatability across different test campaigns and allowed detection of any systematic shift in analyzer response over time.

The AO2020 system uses gas-specific modules, each with a distinct detection principle. NO and NO_2 are measured by the Limas11 HW UV photometer operating hot-wet to limit condensation losses. The module applies the Beer–Lambert law by measuring the attenuation of UV light through a sample cell at species-selective wavelengths; NO is typically detected near 214 nm and NO_2 near 400 nm.

CO, CO_2, and CH_4 are measured with the Uras26, a non-dispersive infrared analyzer. It observes the mid-infrared region, about 2.5 to 8 µm, where these gases absorb light. A reference path and gas-selective filters keep the signal stable against temperature changes and drift. The instrument also compensates for water vapor, which reduces cross-sensitivity to H_2O [87]. O_2 is measured by the Magnos28 paramagnetic analyzer, which senses the torque on a magneto-mechanical microwing (dumbbell) in a magnetic field; optical readout with on-board A/D conversion provides fast, low-noise response and is inherently immune to steam-related optical or chemical interferences [89, 87].

The focus of this study is on NO_x emissions, particularly nitric oxide (NO), as NO is known to be the dominant NO_x species in high-temperature combustion. Literature and experimental precedent both indicate that NO is typically present in significantly higher concentrations than NO_2 in such conditions, especially for dry, high-temperature flames with low residence times. This makes NO the primary contributor to total NO_x, and the most reliable indicator of NO_x formation and suppression.

Unfortunately, NO_2 readings from the gas analyzer were found to be unreliable in cases involving steam injection. Under dry conditions (no steam injection), NO_2 values were typically within the expected range of 0–10 ppm: lower for pure CH_4 flames and higher as the H_2 fraction increased. However, upon the introduction of steam, NO_2 values increased several fold, in many cases surpassing NO levels entirely. This behavior is chemically implausible. Under high-temperature, short-residence-time conditions such as those in the present setup, steam primarily reduces total NO_x by lowering flame temperature and enhancing radical-driven reduction of NO (e.g., NO + H $\leftrightarrow$ N + OH). These processes suppress both thermal and prompt NO formation, and do not promote oxidation of NO to NO_2. Although steam addition decreases flame temperature, the reduction is modest (typically a few hundred kelvin) and still well above the range where significant post-flame NO $\rightarrow$ NO_2 conversion occurs, which generally requires temperatures below 1100–1200 K and long residence times. Therefore, an increase of NO_2 exceeding NO during steam injection is physically unrealistic. Moreover, NO_2 readings in these cases were often highly unstable, showing sharp oscillations and sudden spikes or drops even after flame stabilization. This erratic behavior was not observed in any other species and further indicates unreliable detection.

To test whether these elevated NO_2 readings were real or due to measurement interference, a control test was performed using only steam injection without any combustion. In this test, the NO_2 reading reached approximately 130 ppm, despite the absence of any flame. This strongly indicates that the LIMAS21 HW UV analyzer is susceptible to interference in the presence of high moisture content, likely due to optical scattering, refractive index shifts, or possible condensation in the optical cell. Additionally, NO_2 is known to be water-soluble and can form nitric and nitrous acid when dissolved in liquid water, further complicating its measurement in humid environments.

Interestingly, this interference appeared to be specific to NO_2. The NO readings remained consistent and chemically reasonable across all tests. In steam injection cases, NO concentrations dropped progressively with increasing steam flow, as expected from thermal NO_x suppression. This behavior, along with the absence of any spike in NO during the steam-only control test, reinforces the conclusion that NO readings are not affected by the presence of steam and remain reliable throughout the campaign.

The other gas species, CO and CH_4, showed an increase in emissions during steam injection for fuel mixtures containing CH_4, which aligns with known combustion behavior. The presence of steam lowers the flame temperature and slows down oxidation reactions, particularly for the relatively slower-burning CH_4 component. As a result, CO and unburned CH_4 levels increase. However, in pure H_2 flames, this increase was not observed, supporting the conclusion that the analyzer measurements for CO and CH_4

are not being distorted by steam, but rather reflect real combustion phenomena. The absence of any artificial rise in CO or CH_4 during steam-only control tests further confirms the robustness of the URAS26 module against water vapor interference.

In summary, the following conclusions were drawn regarding the gas analyzer performance and data reliability:

- **NO readings are reliable and consistent across all conditions and are used as the primary metric for NO_x analysis.**
- **NO_2 readings are unreliable in the presence of steam and are excluded from analysis.**
- **Steam-only test confirmed severe NO_2 measurement interference (130 ppm of NO_2 reading with no combustion, which can not be true).**
- **NO_2 instability: readings during steam injection were often higher than NO and showed sharp oscillations even under steady-state conditions, making them physically implausible and analytically unusable.**
- **Detection sensitivity: the UV-based NO_2 detection method is particularly sensitive to steam due to its operating wavelength, water solubility of NO_2, and potential condensation effects.**
- **Daily calibration was performed to minimize drift errors, especially for NO and NO_2 which are more sensitive to alignment and aging effects in the UV photometer.**
- **CO and CH_4 trends under steam injection were only observed when CH_4 was present in the fuel mix, consistent with expected combustion chemistry.**
- **No steam interference was observed in CO, CH_4, O_2 or NO readings.**

Therefore, the combustion performance and NO_x mitigation analysis presented in this thesis are based solely on the validated NO emission data, excluding NO_2 due to its demonstrated measurement unreliability in humid conditions.

Statistical Stability of Gas Analyzer Signals

To ensure the reliability and consistency of the recorded emission data, a statistical evaluation was performed on the time-resolved gas analyzer signals extracted from the TDMS files. Each test point included 60 to 100 seconds (sometimes higher) of steady-state measurement during which species concentrations were logged continuously with 10 Hz sampling frequency.

For each species (e.g., NO, NO_2, CO, CH_4, O_2), the following statistical metrics were computed:

- **Mean** (μ): the time-averaged value over the stable window, used as the representative emission level.

$$\mu = \frac{1}{n}\sum_{i=1}^{n} x_i \tag{8.1}$$

- **Standard deviation (std)** (σ): quantifies the variation or fluctuation of the signal around the mean.

$$\sigma = \sqrt{\frac{1}{n-1}\sum_{i=1}^{n}(x_i - \mu)^2} \tag{8.2}$$

- **Coefficient of variation (CV)**: the ratio of the standard deviation to the mean, providing a normalized measure of variability.

$$\text{CV} = \frac{\sigma}{\mu} \tag{8.3}$$

- **Range** (R): the difference between the maximum and minimum values in the measurement window.

$$R = max(x_i) - min(x_i) \tag{8.4}$$

Although the standard deviation gives a basic measure of signal variability, it is not always sufficient on its

own to determine the quality of the data. In cases where the mean value is low (e.g., low-emission test points), even a small absolute standard deviation can represent significant relative fluctuation. Therefore, the coefficient of variation (CV) was used alongside standard deviation to provide a more robust and scale-independent assessment of signal stability. Meanwhile, the range was helpful in identifying whether a large oscillation or sharp deviation occurred—even if briefly—which may not be captured through the mean or CV alone.

These metrics were used as quantitative criteria to assess the quality of each test point. Data were flagged as unreliable or “bad” if any of the following were observed:

- **High CV or standard deviation**, indicating excessive signal instability.
- **Large range** relative to the mean value, suggesting unsteady operation or transient disturbances.
- **Oscillating or drifting trends** visible during visual inspection of the signal, often coupled with elevated statistical spread.
- **Negative values** for species that should not be present without combustion (e.g., NO, CO), typically treated as zero but noted as a sign of low signal-to-noise ratio.

Bad or unstable data points were relatively rare and were often identified during the measurement phase of the experiment through real-time observation of the gas analyzer output. In such cases, the same test point was repeated after allowing the readings to stabilize, and new measurements were taken.

Most of the problematic signals were associated with NO and NO_2 readings. The issues with NO_2 were explained separately previously and are largely attributed to measurement interference in steam-rich conditions. In contrast, abnormal NO readings were occasionally observed when the flame was not yet fully stabilized or during transient changes in operating conditions. In some cases, the NO signal showed unphysical large oscillations or spikes that could not be attributed to combustion behavior. Such data points were identified as artifacts of analyzer delay and were therefore discarded from the analysis.

Only data that demonstrated consistent signal behavior, low variability, and a clear steady-state mean were retained for final analysis. This filtering process was especially important for interpreting low-emission cases where minor fluctuations could significantly affect the reported concentration. In summary, the statistical screening served both as a validation tool and as a method to enforce objective thresholds for data inclusion.

Negative Gas Analyzer Readings

During the experiments, particularly in the steam injection test points, instances of negative readings were occasionally observed in the gas analyzer output. This was most commonly seen in NO measurements, where values dropped from significantly positive levels in the no-steam cases to slightly negative values, typically between 0.00 and –2.00 ppm when steam was introduced. Notably, baseline (flame-off) NO readings were consistently near zero, confirming that these negative values were not due to incorrect baseline subtraction.

This behavior is attributed to measurement uncertainty in the gas analyzer at very low concentration levels. When steam injection effectively reduces NO formation, the resulting NO concentrations can fall close to or below the instrument’s detection threshold, leading to occasional numerical artifacts in the recorded data. These negative values are not physically meaningful and were therefore treated as 0.00 ppm during data processing.

The same logic was applied to occasional negative readings in NO_2 and CO, which also occurred sporadically under steam-injected conditions. This consistent handling ensures that low-concentration emission results remain physically plausible and are not skewed by limitations of the measurement system.

8.2. Gas Analyzer Measurements in Dry and Wet Conditions

As mentioned before, ABB AO2020 gas analyzer was used in the experiments to measure the species content in the flue gasses. 6 species of interest were measured with ABB AO2020 gas analyzer. Due to the operating principles of the gas analyzer 4 of these species were measured in dry conditions: CH_4, CO, CO_2 and O_2, while NO and NO_2 were measured in ”wet-hot” conditions. This means that the results for the CH_4, CO, CO_2 and O_2 measurements are conducted after the H_2O content in the flue gas was removed, while for NO and NO_2 measurements the H_2O is still present in the flue gas.

The reason for this dry and hot-wet measurement discrepancy can be explained due to the nature of the measured species and the measurement methods. NDIR cells quantify CH_4, CO and CO_2 from narrow mid-IR absorption bands, but water vapour has dense, overlapping bands across the same region. As the humidity changes, the H_2O absorption within the channel's filter window varies which can create cross-sensitivity that the analyzer interprets as apparent changes in CH_4/CO/CO_2. Humidity may also affect the baseline of the device by altering the density and refractive index of the gas sample which can cause zero drift and lead to skewed measurements. Drying the sample removes H_2O which suppresses spectral interference and stabilizes zero/span. The drying is achieved through cooling the the gas below the dew point and condensing the water out. Consequently, CH_4, CO, CO_2 and (paramagnetic) O_2 measurements are conducted and reported on a dry basis

On the other hand, NO and especially NO_2 are susceptible to losses during sample drying. Due to this, NO and NO_2 measurements are done in hot-wet conditions. The sampling line is maintained at a temperature of $180°C$ and the Limas module for NO and NO_2 measurements is kept at $80°C$ to prevent the condensation of H_2O during NO_x measurements. When the wet flue gas stream is cooled the water condenses. NO_2 is soluble in liquid water and once dissolved undergoes rapid aqueous reactions (disproportionation/hydrolysis) to nitrite and nitrate (HNO_2 and HNO_3). Consequently, any condensed water in the sampling line behaves as a sink for gas-phase NO_2, depleting it before detection and biasing the measurement low. Although much less soluble than NO_2, NO is also sampled hot–wet to avoid artifacts introduced by drying. In coolers or on moist metal/oxide surfaces, NO can be partially oxidized to NO_2 and the NO/NO_2 partition is altered during transport, meaning any condensate further promotes heterogeneous reactions. In addition, the NO_x bench determines NO and NO_x (total) on the same sample stream. Keeping that stream above the dew point prevents NO_2 scrubbing upstream of the total measurement and preserves matrix consistency (humidity) for the detector.

However, this also means the analyzer outputs are not on a single basis: NO_x is recorded on a hot-wet basis, whereas CH_4, CO, CO_2 and O_2 are dry. Under ordinary (no-steam) operation with fixed fuel and only modest changes in equivalence ratio, the water-vapour fraction of the exhaust is nearly constant, so a wet-basis NO_x value is essentially a fixed scaling of the corresponding dry value. In that regime, relative comparisons of NO_x between points are still meaningful even if the channel itself is wet.

With steam injection, the water fraction in the sampled gas rises sharply and varies between points. The same absolute amount of NO_x is now diluted into a larger wet total, so the hot-wet ppm falls for dilution reasons, not necessarily because less NO_x was formed. Directly comparing wet-basis NO_x between steam and no-steam cases therefore skews the interpretation. To make a fair comparison both against the dry-basis species and across operating points, the NO readings are converted into dry readings from wet readings.

Hot–wet NO measurements were converted to a dry basis by removing the water-vapor fraction of the sampled (wet) gas. Since in Section 8.1 it was explained that NO_2 readings are unreliable and hence unusable, only the conversion of NO from wet to dry is required. Let X_{NO} denote the mole fraction (ppm/ppmv) of NO in the analyzer stream. The dry-basis value of can be directly calculated from mass conservation on the denominator:

$$X_{NO,\text{dry}} \;=\; \frac{X_{NO,\text{wet}}}{1 - X_{\text{H}_2\text{O,wet}}} \tag{8.5}$$

The water-vapour fraction $X_{\text{H}_2\text{O,wet}}$ is computed from operating conditions assuming lean, complete combustion and dry air $(O_2 + 3.76\,N_2)$, with injected steam included explicitly. Consider one mole of blended fuel composed of an H_2 molar fraction x_{H_2} and $(1 - x_{H_2})$ CH_4. The stoichiometric O_2 demand per mole of fuel is:

$$\nu_{O_2,\text{stoich}} \;=\; 2\,(1 - x_{H_2}) \;+\; \tfrac{1}{2}\,x_{H_2} \;=\; 2 - \tfrac{3}{2}x_{H_2} \tag{8.6}$$

This is for the demand of O_2 for the blend fuel of H_2-CH_4. This can be calculated from the pure components of H_2 and CH_4 combustion independently, and then merging them together. Pure-component stoichiometries

are given as:

$$\mathrm{CH_4} + 2\,\mathrm{O_2} \;\rightarrow\; \mathrm{CO_2} + 2\,\mathrm{H_2O} \qquad \Rightarrow \quad 2 \text{ mol } \mathrm{O_2}/\text{mol } \mathrm{CH_4} \tag{8.7}$$

$$\mathrm{H_2} + \tfrac{1}{2}\,\mathrm{O_2} \;\rightarrow\; \mathrm{H_2O} \qquad \Rightarrow \quad \tfrac{1}{2} \text{ mol } \mathrm{O_2}/\text{mol } \mathrm{H_2} \tag{8.8}$$

Where one mole of blended fuel is:

$$\text{Fuel (per mol)}: \quad x_{\mathrm{H_2}}\,\mathrm{H_2} \;+\; (1 - x_{\mathrm{H_2}})\,\mathrm{CH_4} \tag{8.9}$$

8.3. Result Validation and Variability Analysis

In any experimental campaign, the reliability of collected data is fundamental to the scientific rigor of the conclusions drawn. To act as a sanity check and validation of the experiments conducted, some of the experimental tests were repeated on different days. Particularly, Experiment-C1 with 10 kW constant power and changing the blend percentage was used in this validation procedure. The test points of Experiment-C1 was repeated in an experiment called Experiment-C1.2. In Experiment-C1.2, some of the points present were repeated for both steam and no-steam conditions. The purpose of repeating these experimental points was to examine whether a clear and consistent trend would emerge when the experiments were repeated under the same conditions, and if there is some variation in results, try to quantify it.

Ideally, a full validation study would involve repeating each test condition multiple times (typically 3 or more) to enable proper statistical hypothesis testing, such as a paired t-test. However, due to the limitations of this experimental campaign, including time-consuming flame stabilization, steam line startup delay, and limited access to the lab, this approach was not practical. The available time was instead prioritized for mapping a broader range of hydrogen fractions and steam rates. As a result, only a select number of points from Experiment-C1 were repeated in Experiment-C1.2.

While the number of repeats is too small for meaningful t-test application, these repetitions are still highly valuable when used to observe general consistency and trend behavior. In this case, the main objective is to confirm that the observed NO reduction with steam injection is not a one-off result, but a physically repeatable and observable phenomenon. Therefore, rather than relying on formal p-value statistics with limited data points, a more descriptive comparison approach was taken. This includes checking for consistency in the NO drop magnitude and whether steam injection always leads to a downward trend in NO, which is indeed confirmed by the repeated points.

Additionally, Experiment-D1 which was mainly designed to explore steam variability and not specifically aimed at repeatability happened to include three hydrogen blend ratios (40 %, 60 %, 80 %) that overlap with Experiment-C1. These cases were also incorporated into the validation effort. While the system settings and environmental conditions on that day were not guaranteed to be identical, the same measurement protocols and calibration procedures were followed, allowing these points to provide secondary confirmation of the repeatability of NO behavior under steam injection.

To give an overview of the repeated points and their respective results, Table 8.1 is presented below in Table 8.1. It should be noted that the results are compared in wet NO, which is the raw data acquired from the gas analyzer.

H_2 (%)	Experiment	No-Steam NO_{wet} (ppm)	Steam 9 NO_{wet} (ppm)	NO_{wet} Drop (%)
20	Experiment-C1.2	2.02	0.73	63.9
20	Experiment-C1	2.23	0.57	74.4
40	Experiment-C1.2	4.62	2.48	46.3
40	Experiment-C1	4.21	0.77	81.8
40	Experiment-D1	3.96	2.36	40.3
60	Experiment-C1.2	6.21	2.41	61.2
60	Experiment-C1	5.61	1.80	67.9
60	Experiment-D1	5.70	1.19	79.1
70	Experiment-C1.2	8.60	4.07	52.7
70	Experiment-C1	8.13	3.13	61.5
80	Experiment-C1.2	13.41	8.29	38.1
80	Experiment-C1	14.14	7.07	50.0
80	Experiment-D1	13.04	7.98	38.9
100	Experiment-C1.2	33.66	18.62	44.7
100	Experiment-C1	35.32	17.64	50.1

Table 8.1: Comparison of NO Concentrations Across Repeated Experiments (10 kW, Steam 9 vs. No-Steam)

From the table above, several key observations can be made. First and foremost, the trend of NO reduction with steam injection is clearly consistent across all repeated points and experiments. For every H_2 blend ratio tested, the introduction of steam led to a measurable decrease in NO emissions. This trend is preserved not only across different experimental points, but also across different experimental days as all three datasets (Experiment-C1, Experiment-C1.2, and Experiment-D1) were conducted independently. This strengthens the argument that the observed NO reduction is not merely an artifact of a single test session, but a physically real and repeatable phenomenon under varied but controlled conditions.

Another notable feature is the very strong consistency observed in the No-Steam cases across experiments. For nearly all blend ratios, the NO levels without steam are in close agreement across repeated tests, often within less than 10 % variation. This suggests that the measurement protocol, burner control, air-fuel ratio regulation, and system stability were reliable and repeatable under dry conditions.

In contrast, the Steam 9 cases exhibit noticeably more variability. While the direction of NO change is always downward, the magnitude of reduction fluctuates between experiments. For instance, at 40 % H_2, the NO drop ranges from 40.3 % to 81.8 %; similarly, at 100 % H_2, it ranges from 44.7 % to 50.1 %. This variation is attributed to the inherently more complex and less stable nature of steam injection in the current setup. Steam was introduced using an open-loop system without active mass flow control, making it sensitive to pressure fluctuations, transient heating behavior, and potential condensation in the lines. Additionally, steam affects flame speed and anchoring behavior, meaning that even minor shifts in flow fields can result in measurable changes in local NO formation rates. Another aspect to consider is that the steam injection was not perfectly symmetric, as the side-injection configuration could lead to uneven steam distribution around the burner, locally altering flame temperature and mixing characteristics. Combined with the influence of steam on flame speed and anchoring behavior, even small asymmetries or shifts in flow fields can result in measurable changes in local NO formation rates.

Despite these sources of variation, the consistency in trend direction, always showing NO reduction with steam, combined with the physical magnitude of reduction (often exceeding 50 %) suggests that the observed effects are robust. The fact that No-Steam values are tightly grouped while steam values show a broader spread also reinforces the idea that the variability is not due to random system noise or measurement error, but due to the known physical sensitivities introduced by steam. Therefore, even though the steam-injected measurements carry more uncertainty, the overall trends remain valid, and the data set can be considered reliable for interpreting the influence of steam on NO formation.

In addition to NO measurements, oxygen (O_2) concentrations were also monitored for each test condition.

O_2 is a valuable diagnostic parameter in combustion systems, serving as an indicator of excess air and mixture stoichiometry. While O_2 itself is not a direct driver of NO formation, stable O_2 values across repeated experiments provide a useful reference to assess whether air–fuel mixing and burner control were consistent between tests. In particular, a mismatch in O_2 could suggest a shift in equivalence ratio or a deviation in burner setup, both of which could influence NO emissions.

Table 8.2 presents O_2 concentrations recorded for all repeated conditions in both dry and steam 9 cases. These values consistently fall within a narrow range across experiments.

H_2 (%)	Experiment	No-Steam O_2 (% vol)	Steam 9 O_2 (% vol)
20	Experiment-C1.2	10.34	10.46
20	Experiment-C1	10.31	10.32
40	Experiment-C1.2	9.30	9.35
40	Experiment-C1	9.27	9.30
40	Experiment-D1	8.64	8.69
60	Experiment-C1.2	9.07	9.11
60	Experiment-C1	9.27	9.30
60	Experiment-D1	8.64	8.69
70	Experiment-C1.2	8.51	8.64
70	Experiment-C1	8.50	8.62
80	Experiment-C1.2	7.76	7.89
80	Experiment-C1	7.78	7.84
80	Experiment-D1	7.47	7.56
100	Experiment-C1.2	6.33	6.55
100	Experiment-C1	6.24	6.48

Table 8.2: Comparison of O_2 Concentrations Across Repeated Experiments (10 kW)

The O_2 values in dry conditions are remarkably consistent across the three experiments. For example, at 60 % H_2, the dry O_2 ranges between 9.07 % and 9.27 %, while at 100 % H_2 it ranges between 6.24 % and 6.33 %. Similar consistency is observed in the steam 9 cases, with typical spreads remaining within ± 0.2–0.3 % vol.

These narrow variations, well within the expected analyzer accuracy and system stability limits, provide strong evidence that the air-fuel ratio was controlled reliably throughout all test days. In turn, this reinforces the validity of the NO comparison between experiments, as the equivalence ratio and combustion completeness were not significantly changing. Therefore, the observed NO reductions can be confidently attributed to steam injection effects rather than to drift in operating conditions.

8.4. Emission Indices and Normalization (EINO, EICO O_2)

Accurate comparison of emission data requires consistent normalization practices. This section introduces the emission index of NO (EINO) as a fuel-based metric for quantifying emissions, and outlines the oxygen normalization procedure used to report concentrations at standardized O_2 reference levels.

8.4.1. EINO

The emission index (EI) of a species is defined as the mass of that species emitted per unit of fuel consumed. Aviation and gas-turbine standards define EI on the basis of the mass of the fuel (g / kg of fuel) and treat NO_x as NO + NO_2, which is typically reported as NO_2 equivalent mass [95, 96, 97, 98]. In this work, both CH_4, H_2 and their blend fuels have been experimented with, and since CH_4 and H_2 have very different molecular masses, the EI will also be reported on an energy basis (g / MJ based on LHV) alongside the mass basis. This energy-based emission-index approach has been widely adopted in both regulatory frameworks and combustion studies, where NO_x emissions are normalized by the fuel's energy input or

output (e.g., g NO_x per GJ or mg NO_x per MJ) to enable comparison across different fuels and systems [99, 100, 101, 102].

This method aims to provide an additional outlook and acts as a tool to normalize the emissions with respect to the power output of the combustion process. In standard practice, both NO and NO_2 emissions are evaluated to form EINOx (Emission Index NO_x). However, since NO_2 readings were proven to be unreliable in this set of experiments, only NO will be the species of interest. Hence, the emission index will be called EINO rather than EINOx.

The energy basis EI formula for the NO species is given in Equation 8.10. This is standard for EI calculations and for the general form, NO can be replaced with any other species to get the EI of any other desired species.

$$\text{EINO}^{E}\ [\text{g/MJ}] \;=\; \frac{10^3}{\text{LHV}_{\text{mix}}}\, M_{NO}\, X_{NO,\text{dry}}\, \nu_{\text{dry}} \tag{8.10}$$

where M_{NO} is the molecular mass of NO (g/mol)), $X_{NO,\text{dry}}$ is the dry mole fraction from the analyzer, ν_{dry} is the number of dry product moles per mole of fuel, and LHV_{mix} is the molar lower heating value of the fuel mixture (kJ/mol); the factor 10^3 converts kJ to MJ.

To calculate the EINO for a given test point, the dry molar flow ratio, ν_{dry}, must be determined reliably. While the main exhaust species such as O_2 and CO_2 could in principle be used to construct a simplified carbon or oxygen balance, equilibrium simulations were performed in Cantera to ensure a chemically consistent treatment of all combustion and dilution effects. For each condition, adiabatic constant-pressure equilibrium was calculated by mixing 1 mol of fuel with air at the measured equivalence ratio ϕ and the corresponding steam injection rate s (mol H_2O per mol fuel). From the resulting equilibrium composition, the total number of product moles and the wet H_2O mole fraction, $X_{\text{H}_2\text{O,wet}}$, were extracted. The number of dry moles was then computed as $(1 - X_{\text{H}_2\text{O,wet}})\, n_{\text{prod}}$, where n_{prod} is the total product moles:

$$\nu_{\text{dry}} \;=\; n_{\text{prod}}\,(1 - X_{\text{H}_2\text{O}}) \tag{8.11}$$

The validity of this approach was verified by comparing the modeled major species (O_2 and CO_2) against the measured values. The agreement was very close, confirming that the equilibrium calculations yield realistic exhaust compositions. Under lean conditions, this also implies that the calculated N_2 content is consistent with the measured data, since it follows directly from the air composition. The mole fraction of water was determined from the simulated equilibrium including both the combustion-generated H_2O and the injected steam fraction s, which is added to the reactant mixture prior to equilibrium. This ensures that both chemical and dilution effects of steam are captured in the computed $X_{\text{H}_2\text{O,wet}}$ used for EINO normalization.

equilibrium:

This is equivalent to using dry analyzer fractions with a dry product-mole count (i.e., $n_{\text{NO}} = X_{\text{NO, dry}}\nu_{\text{dry}}$). In certification practice, the number of dry product moles is determined by a carbon balance using measured wet $[CO_2], [CO], [HC]$ rather than by equilibrium. However, provided the same wet/dry basis and fuel are used, the two approaches are equivalent [96, 95].

The molar LHV of the H_2/CH_4 mixture is also given as:

$$\text{LHV}_{\text{mix}} = x_{\text{H}_2}\,\text{LHV}_{\text{H}_2} + (1 - x_{\text{H}_2})\,\text{LHV}_{\text{CH}_4} \quad [\text{kJ/mol}] \tag{8.12}$$

with $x_{\text{H}_2} + x_{\text{CH}_4} = 1$. To convert this energy basis EI to mass-of-fuel EI, Equation 8.13 can be used:

$$\text{EINO}\,[\text{g/kg}] \;=\; \text{EINO}^{E}\,[\text{g/MJ}]\,\frac{\text{LHV}_{\text{mix}}}{M_{\text{mix}}} \quad \text{with} \quad M_{\text{mix}} = x_{\text{H}_2} M_{\text{H}_2} + x_{\text{CH}_4} M_{\text{CH}_4} \tag{8.13}$$

In this report, both energy basis and mass-of-fuel basis EINO values will be reported in the results to provide insight with both of these parameters. However, the methodology presented above have some differences with the standard procedure of EINOx quantification that should be fully disclosed [95, 96, 97, 98].

Difference between standardized EINOx calculations and how it is treated in this analysis:

Determination of ν_{dry}: In standard practice, ICAO Annex 16, FAA AC 34-1B, and SAE ARP1533 [95] define ν_{dry} as the number of dry product moles per mole of fuel, determined through a carbon balance using measured wet (or consistently converted dry) $[CO_2], [CO], [HC]$. In the present study, hydrocarbon concentrations were negligible because the flames operated lean, and CO levels were low, indicating near-complete combustion. Although a simplified carbon balance could therefore have been applied, ν_{dry} was instead obtained from adiabatic constant-pressure equilibrium simulations in Cantera to maintain consistency across all operating points and to account for both combustion and steam-dilution effects in a chemically complete manner. Each equilibrium case was computed by mixing 1 mol of fuel with air at the measured equivalence ratio ϕ and the imposed steam injection rate s. After equilibrium, the wet products were converted to a dry basis using $\nu_{\text{dry}} = n_{\text{prod}}(1 - X_{H_2O})$. When the fuel composition and the measurement basis (wet/dry) are the same, the equilibrium-based and carbon-balance routes are algebraically consistent.

Ambient CO_2 correction. In standard practice, an ambient CO_2 correction is applied when forming the carbon balance to account for intake CO_2 entrained into the exhaust stream, since CO_2 is already present in the atmosphere. In this work, this factor is neglected because, under the present lean conditions, its effect on the overall carbon balance is typically less than 1% in concentration terms (corresponding to a correction factor of about 1.00–1.01), which can be considered negligible.

Reference-condition corrections. In standard practice, a set of multiplicative corrections are used to reduce the specified reference conditions (pressure, temperature, humidity, and in some cases a reference fuel–air ratio). In this work, no reference-condition corrections are applied and the results are reported at actual test conditions.

Steam Addition. In standard practice, external steam injection is not explicitly parameterized in the Annex algebra, but the carbon-balance itself remains valid provided measured product fractions are used consistently on a defined wet/dry basis. In this work, steam is handled directly in the equilibrium computation of ν_{dry} by adding s mol H_2O per mol fuel before equilibration. The method captures the dilution and chemistry effects of steam on n_{prod} and X_{H_2O}; a carbon-balance route would yield the same ν_{dry} when applied to consistent wet fractions.

NO_2 channel and converter efficiency. In standardized reductions, NO_x is defined as NO + NO_2 and reported as NO_2 equivalent mass; when a single-channel chemiluminescence NO_x analyzer with a catalytic converter is used, a converter efficiency correction is applied [95, 97, 96]. In this analysis, separate NO and NO_2 channels were available but NO_2 readings were not reliable; consequently, only EINO (NO only) is reported, and no converter efficiency correction is applied. If robust NO_2 measurements become available, NO_x as NO_2 equivalent can be computed and reported using the standard convention.

Effect of methodological differences. The deviations from standardized Annex 16 procedures have only a minor quantitative influence on the reported EINO values but improve internal consistency for the present dataset. Using equilibrium-derived ν_{dry} instead of a carbon-balance approach introduces at most sub-percent differences under lean, well-burnt conditions where CO and HC are low. Neglecting the ambient CO_2 correction alters the effective carbon balance by less than 1%, which translates to an error of the same order in EINO. Omitting reference-condition corrections means that the results are reported at the actual laboratory pressure, temperature, and humidity, rather than being adjusted to standardized certification reference values. This choice does not affect the physical trends observed but means that the reported EINO values correspond to the specific test environment rather than normalized reference conditions. Finally, restricting the analysis to NO (excluding NO_2) slightly underestimates the total NO_x but provides a reliable trend indicator because NO dominates the NO_x fraction under the high-temperature, short-residence flames investigated here. Overall, the combined effect of these methodological differences is expected to be minimal and does not affect the main conclusions of this study.

8.4.2. EICO

In parallel with EINO, the emission index of CO (EICO) is also evaluated in this work. EICO quantifies the mass of CO emitted per unit of fuel consumed, reported on both an energy basis (g/MJ) and a fuel-mass basis (g/kg). The formulation is identical to that used for EINO, with M_{CO} and $X_{CO,\text{dry}}$ replacing the NO parameters in Equation 8.10 and Equation 8.13. Thus,

$$\mathrm{EICO}^{E}\ [\mathrm{g/MJ}] \;=\; \frac{10^3}{\mathrm{LHV_{mix}}}\, M_{CO}\, X_{CO,\mathrm{dry}}\, \nu_{\mathrm{dry}} \tag{8.14}$$

$$\mathrm{EICO}\,[\mathrm{g/kg}] \;=\; \mathrm{EICO}^{E}\,[\mathrm{g/MJ}]\,\frac{\mathrm{LHV_{mix}}}{M_{\mathrm{mix}}} \tag{8.15}$$

EICO serves as a complementary metric to EINO: while NO formation is strongly linked to flame temperature and thermal pathways, CO emissions reflect incomplete oxidation processes and are highly sensitive to local stoichiometry, residence time, and dilution effects. Reporting both EINO and EICO allows a more comprehensive assessment of combustion performance, pollutant formation, and the effects of hydrogen blending and steam injection on flame chemistry.

Differences from standardized EICO calculations
The same considerations as for EINO apply regarding determination of ν_{dry}, omission of ambient CO_2 correction, neglect of reference-condition corrections, and explicit parameterization of steam injection. Unlike NO/NO_2 reporting, no converter efficiency correction is needed because CO is measured directly by the analyzer.

8.4.3. O_2 Normalization

Another normalization technique used in this work is the O2 normalization method. Reported NO concentrations (in ppm) depend not only on formation chemistry but also on how much the exhaust is diluted by excess air. To enable fair, standardized comparisons across test points with different excess-air levels and steam injection levels, NO is corrected to a reference dry oxygen level. In this work $15\,\%$ O_2 (dry) method is adopted as the reference condition. This is a common baseline in premixed burner and appliance literature.

On a dry molar basis, dilution by excess air scales with the fraction of inert gasses and unreacted oxygen.

Under the standard assumption that dilution is the dominant effect, the dry-basis concentration of a pollutant is inversely proportional to $(21 - O_{2,\mathrm{meas,dry}})$, where $21\,\%$ is taken as the nominal oxygen content of air. The correction from a measured dry oxygen level $O_{2,\mathrm{meas,dry}}$ to a chosen reference $O_{2,\mathrm{ref}}$ is

$$X_{\mathrm{NO}}@O_{2,\mathrm{ref}} \;=\; X_{\mathrm{NO,\,dry}}\;\frac{21 - O_{2,\mathrm{ref}}}{21 - O_{2,\mathrm{meas,dry}}}\,, \tag{8.16}$$

with all oxygen values in % (dry) and X_{NO} in volumetric ppm (dry).

Different regulatory bodies apply slightly different nominal oxygen values when normalizing pollutant concentrations to a dry-reference O_2 level. In the U.S., EPA Method 19 specifies the use of 20.9% O_2 in the normalization factor—e.g., using the multiplier $\frac{20.9}{20.9-O_{2,\mathrm{meas,dry}}}$ to correct for dilution effects [103]. In contrast, many European frameworks adopt a rounded value of 21%, applying correction factors of the form $\frac{21-O_{2,\mathrm{ref}}}{21-O_{2,\mathrm{meas,dry}}}$ for normalizing emissions to reference oxygen levels [104]. In this work, a reference value of $21\,\%$ O_2 is adopted, following the convention in European regulatory practice and for consistency with other combustion studies employing the same normalization basis.

Since the gas analyzer readings for NO are given in wet-basis, the NO readings are first converted into dry-basis as explained in Section 8.2. The readings of O_2 are already given in dry-basis in the gas analyzer, so no additional steps are needed. A reference concentration of $15\,\%$ O_2 is adopted for reporting NO emissions, since this is the standard practice for stationary gas turbines and large combustion plants. Both U.S. EPA regulations and European guidance documents specify 15% O_2 as the normalization basis for gas turbine emission compliance testing [105, 106].

The purpose of this method is to remove dilution effects associated with varying excess air. The normalization ensures that the changes in NO values are due to differing NO values and changes due to O_2 dilution are factored out.

8.5. UV Camera Processing

The ultraviolet (UV) camera images were first recorded in grayscale `.tif` format. For visualization, these were converted into false-color representations using a scientific colormap, which makes the flame front structures and gradients more discernible while preserving the relative intensity distribution.

To extract radially resolved information from the line-of-sight camera images, the inverse Abel transform was applied. The Abel inversion mathematically reconstructs the radial emission field under the assumption of axial symmetry, effectively recovering the true spatial distribution of the flame from its integrated projection. This approach could only be used for the axial steam injection configuration, which is axisymmetric by design. The side-injection cases lack cylindrical symmetry, and therefore Abel inversion is not applicable for those.

Several image artefacts had to be addressed prior to inversion. The flame axis (centerline) was not always perfectly aligned with the image center, so an automatic symmetry-based algorithm was combined with manual correction to ensure accurate placement of the centerline. A vertical stripe artefact along this axis, introduced by the inversion procedure, was suppressed by replacing the affected pixels with interpolated values from the neighboring regions. In addition, a left–right averaging about the chosen axis was performed, which enforced symmetry and improved the stability of the inversion.

The final output consisted of Abel-inverted flame fields visualized in false color. These images are used in the following sections to analyze the effect of steam injection on the flame structure.

9 Results

This chapter presents the key findings of the thesis. First, a preliminary estimation of expected NO reduction via steam injection is presented. Then, the NO emissions results for all the experiments are first presented to investigate the trend of NO emissions with steam injection. Later, all the readings from the gas analyzer are presented to provide a more comprehensive discussion on the effect of steam on combustion dynamics. After that, images of the flames at different conditions are provided to compare the physical differences of different flames.

9.1. Simplified Estimation of Temperature and NO Reduction Due to Steam Injection

To complement the experiments and to provide an intuitive understanding of the impact of steam injection on flame temperature and NO emissions, a simplified analytical method is used. This approach is based on a first-principles energy balance and the exponential sensitivity of thermal NO formation to temperature. It allows for quick estimates of how much steam injection affects the adiabatic flame temperature and consequently the NO emissions, without solving the full chemical kinetics.

Energy Balance and Flame Temperature Drop

The first step is to estimate the drop in flame temperature resulting from the thermal absorption by the injected steam. Assuming adiabatic conditions, perfect mixing, and constant specific heats, the temperature drop ΔT can be approximated as:

$$\Delta T = \frac{\dot{m}_{steam} \cdot c_{p,steam} \cdot (T_{flame} - T_{steam})}{\dot{m}_{gas} \cdot c_{p,gas}} \tag{9.1}$$

where:

- $\dot{m}_{steam}$ is the steam mass flow rate [kg/s]
- $\dot{m}_{gas}$ is the total gas mass flow rate (air + fuel) [kg/s]
- $c_{p,steam}$ is the specific heat capacity of steam [J/kg·K]
- $c_{p,gas}$ is the average specific heat of the combustion gases [J/kg·K]
- T_{flame} is the baseline adiabatic flame temperature [K]
- T_{steam} is the steam injection temperature [K]

The new estimated flame temperature is then:

$$T_{new} = T_{flame} - \Delta T \tag{9.2}$$

NO Estimation Based on Temperature Sensitivity

Thermal NO formation, governed by the extended Zeldovich mechanism, exhibits an exponential dependence on temperature. Hence, the ratio of NO concentrations with and without steam can be approximated

as [107, 108]:

$$\frac{NO_{steam}}{NO_{no-steam}} \approx \exp\left(-\beta \cdot \frac{\Delta T}{T_{flame}}\right) \tag{9.3}$$

which gives:

$$NO_{steam} = NO_{nosteam} \cdot \exp\left(-\beta \cdot \frac{\Delta T}{T_{flame}}\right) \tag{9.4}$$

Here, β is an empirical coefficient representing the sensitivity of NO to flame temperature, typically ranging from 6 to 10 [11] (though actual values depend on activation energy, fuel, and conditions). $NO_{no-steam}$ is the NO emission level without steam, and NO_{steam} is the estimated NO level after steam injection.

Worked Example

For a baseline adiabatic flame temperature of 1713.8 K, corresponding to a thermal power of 10 kW and a fuel blend of 60% hydrogen by volume with an equivalence ratio of 0.604, steam is injected at 393 K with a mass flow rate of 0.0004067 kg/s (equivalent to 24.4 g/min) into a total gas flow rate of 0.005473 kg/s (air plus fuel). The specific heat capacity of steam is taken as 2000 J/kg·K, reflecting its value at elevated temperatures typical of steam injection [109]. For the combustion gases, an effective average specific heat capacity of 1300 J/kg·K is used. This value is higher than the 1005 J/kg·K commonly cited for dry air at room temperature because combustion products, such as water vapor and carbon dioxide, have higher heat capacities, and specific heat capacity increases with temperature. Thus, 1300 J/kg·K represents an approximate average for hot combustion products near flame temperatures [11]. Using these values, the temperature drop is calculated as:

$$\Delta T = \frac{0.0004067 \cdot 2000 \cdot (1713.8 - 393)}{0.005473 \cdot 1300} = 151.0 \text{ K} \tag{9.5}$$

Then, the new flame temperature becomes:

$$T_{new} = 1713.8 - 151.0 = 1562.8 \text{ K} \tag{9.6}$$

Assuming a baseline NO concentration of 10 ppm and using $\beta = 7.5$, the estimated NO level with steam injection is:

$$NO_{wet} = 10 \cdot \exp\left(-7.5 \cdot \frac{151.0}{1713.8}\right) \approx 5.17 \text{ ppm} \tag{9.7}$$

This corresponds to an approximate NO reduction of 48.3%.

Parametric Analysis

To evaluate the sensitivity of the predicted NO reduction to the assumed parameters, the same analytical formulation is applied across a wider range of baseline and injection conditions. The objective is to determine how the estimated NO suppression depends on the baseline adiabatic flame temperature (T_{ad}), the steam mass flow rate ($\dot{m}_s$), the temperature sensitivity coefficient (β), and the baseline NO concentration (NO_0). This comparison helps establish the range of NO reductions that can be expected for realistic variations in these quantities.

Parameter ranges. The selected values reflect the experimental conditions and typical literature ranges:

- $T_{\text{ad}} = \{1610, 1710, 1810, 1910\}$ K, representing a range of flame temperatures;
- $\dot{m}_s = \{17.7, 24.4\}$ g/min, corresponding to the experimental Steam-7 and Steam-9 cases;
- $\beta = \{6.5, 7.5, 8.5\}$, representing the lower, nominal, and upper values of thermal NO temperature sensitivity;

- $NO_0 = \{5, 10, 15\}$ ppm, capturing the range of baseline NO levels measured across fuels and powers.

All other quantities are kept the same as in the worked example: $\dot{m}_{\text{tot}} = 0.005473$ kg/s, $T_s = 393$ K, $c_{p,s} = 2000$ J/(kg · K), and $c_{p,g} = 1300$ J/(kg · K). Steam is injected at consistent $T_s = 393$ K throughout the experiments and $\dot{m}_{\text{tot}} = 0.005473$ kg/s has it most contribution from total air injection, which is kept at 250 nlpm for most experimental points. For each condition, the temperature drop ΔT is recalculated using the energy-balance equation, and NO_{wet} is determined using the exponential relation.

Tables 9.1 and 9.2 summarize the results for the two steam injection rates. Each cell reports the predicted steam injected flame NO level in ppm, with the percentage reduction relative to the baseline value shown in parentheses. The larger steam flow (24.4 g/min) yields a higher temperature drop and consequently a stronger exponential suppression of NO.

T_{ad} [K]	β	ΔT [K]	NO_{wet} @ 5 ppm	NO_{wet} @ 10 ppm	NO_{wet} @ 15 ppm
1610	6.5	139	2.85 (43%)	5.70 (43%)	8.55 (43%)
	7.5	139	2.62 (48%)	5.23 (48%)	7.85 (48%)
	8.5	139	2.40 (52%)	4.80 (52%)	7.20 (52%)
1710	6.5	151	2.82 (44%)	5.64 (44%)	8.46 (44%)
	7.5	151	2.58 (48%)	5.17 (48%)	7.75 (48%)
	8.5	151	2.36 (53%)	4.72 (53%)	7.08 (53%)
1810	6.5	162	2.79 (44%)	5.58 (44%)	8.37 (44%)
	7.5	162	2.55 (49%)	5.10 (49%)	7.65 (49%)
	8.5	162	2.32 (54%)	4.63 (54%)	6.95 (54%)
1910	6.5	173	2.76 (45%)	5.53 (45%)	8.29 (45%)
	7.5	173	2.52 (50%)	5.04 (50%)	7.57 (50%)
	8.5	173	2.29 (54%)	4.58 (54%)	6.87 (54%)

Table 9.1: Estimated NO_{wet} for steam injection of 24.4 g/min (Steam-9) across T_{ad} and β.

T_{ad} [K]	β	ΔT [K]	NO_{wet} @ 5 ppm	NO_{wet} @ 10 ppm	NO_{wet} @ 15 ppm
1610	6.5	101	3.33 (34%)	6.65 (34%)	9.98 (34%)
	7.5	101	3.12 (38%)	6.25 (38%)	9.37 (38%)
	8.5	101	2.93 (41%)	5.87 (41%)	8.80 (41%)
1710	6.5	109	3.30 (34%)	6.60 (34%)	9.90 (34%)
	7.5	109	3.10 (38%)	6.19 (38%)	9.29 (38%)
	8.5	109	2.92 (42%)	5.84 (42%)	8.76 (42%)
1810	6.5	118	3.27 (35%)	6.54 (35%)	9.81 (35%)
	7.5	118	3.07 (39%)	6.14 (39%)	9.21 (39%)
	8.5	118	2.88 (42%)	5.75 (42%)	8.63 (42%)
1910	6.5	126	3.24 (35%)	6.49 (35%)	9.73 (35%)
	7.5	126	3.04 (39%)	6.08 (39%)	9.12 (39%)
	8.5	126	2.86 (43%)	5.73 (43%)	8.59 (43%)

Table 9.2: Estimated NO_{wet} for steam injection of 17.7 g/min (Steam-7) across T_{ad} and β.

Higher steam flow rates yield a larger ΔT and thus a stronger exponential decrease in NO. Increasing β has a comparable effect, as it amplifies the thermal sensitivity of the Zeldovich mechanism. The influence of T_{ad} is milder because both ΔT and the denominator of the exponential term scale with temperature. Nonetheless, even moderate temperature reductions of 100–170 K predict NO decreases of 35–55%, which aligns well with values present in literature.

Discussion on the Validity of the Simplified Estimation Method

The simplified approach outlined above offers several practical advantages that make it particularly useful in early-stage analysis and interpretation. One of its main strengths lies in its intuitiveness and computational speed. It provides a rapid means to evaluate the expected trend of NO reduction due to steam injection, without the need for detailed chemical mechanisms or numerical solvers. By focusing on the thermal aspect of NO formation, specifically the exponential dependence of thermal NO on flame temperature, it

captures the dominant physics for lean high hydrogen fraction flames, where thermal NO is typically the primary formation pathway. This makes it especially relevant for hydrogen combustion systems, where fuel-bound nitrogen is absent and prompt NO is comparatively less significant.

However, the method is also subject to several important limitations. Most notably, it neglects detailed chemical kinetics. The model assumes that NO formation is governed entirely by the thermal Zeldovich mechanism, which may not be accurate in cases involving rich mixtures or where prompt NO becomes relevant. Additionally, the assumption of perfect mixing and uniform temperature distribution overlooks real-world effects such as jet penetration limits, incomplete mixing, or spatial temperature gradients within the flame. The use of constant specific heats for both the steam and combustion gases further simplifies the energy balance but introduces potential inaccuracies, especially over large temperature ranges.

Another limitation is the absence of residence time effects. NO formation is both temperature- and time-dependent, and the current method does not account for how long the reacting gases remain at elevated temperatures. Moreover, at high steam injection levels, nonlinearities may arise due to increased dilution and flame quenching effects, which are not captured by this linearized model. Therefore, while the method performs well under moderate injection conditions, its accuracy diminishes as steam flow rates become excessive.

Despite these limitations, the method remains highly useful in practice when applied under the right conditions. It is best suited for lean hydrogen or hydrogen–methane blends, where thermal NO is the dominant mechanism and steam injection levels are within a reasonable range. It provides valuable insight into expected trends and supports the validation or interpretation of more complex results. When clearly contextualized, the simplified approach enhances the overall understanding of steam injection effects and complements the experimental and simulation-based findings of this work.

9.2. Series A: Variation of Burner Power

Experiment-A1: Pure Hydrogen Flames

The first set of results to be presented are from Experiment-A1 from Series A: Variation of Burner Power. Experiment-A1 serves as the foundational case in this campaign because it isolates the behavior of a fully hydrogen-fueled flame under different power levels with and without steam injection using the side injection configuration. Unlike the blend cases in later series, the chemistry here is carbon-free, meaning that the only meaningful pollutant to track is NO, while CH4, CO, and CO2 channels are inherently irrelevant. As established in Chapter 8 the NO2 channel results are disregarded due to poor reliability of the analyzer. For this reason, the raw results focus solely on NO and O2. However, this limitation highlights the clean-burning nature of hydrogen. The dry and wet emissions results for NO and the dry O2 results for Experiment-A1 is given below in Table 9.3:

Power [kW]	**AAI [%]**	$\phi \pm$ **0.009**	**NO (ppm, *dry*) (wet in parentheses)**		**Dry reduction**		**O_2 [%]**	
			No-Steam	Steam-9	Abs [ppm]	%	No-Steam	Steam-9
10	15	0.529	8.46 (6.77 wet)	6.38 (4.60 wet)	2.08	24.6	11.19	11.09
9	15	0.476	4.68 (3.83 wet)	2.46 (1.81 wet)	2.22	47.4	12.22	12.13
8	10	0.423	2.20 (1.84 wet)	0.00 (0.00 wet)	2.20	100.0	13.27	13.32
7	10	0.370	0.58 (0.50 wet)	0.00 (0.00 wet)	0.58	100.0	14.28	14.34

Table 9.3: NO emissions and background O_2 for Experiment A1. 100% H_2 combustion with varying burner power. Side steam injection configuration was used. Values reported on a dry basis; analyzer wet readings are shown in parentheses. Dry conversion via Equation 8.5.

The dry NO readings of Table 9.3 is visualized in Figure 9.1. It should be noted that the uncertainty of NO readings are $\pm$0.1 ppm. Since this value is low compared to the values observed in the gas analyzer, the error bars in the graph is too small to be noticeable, so error bars in all subsequent NO graphs are omitted.

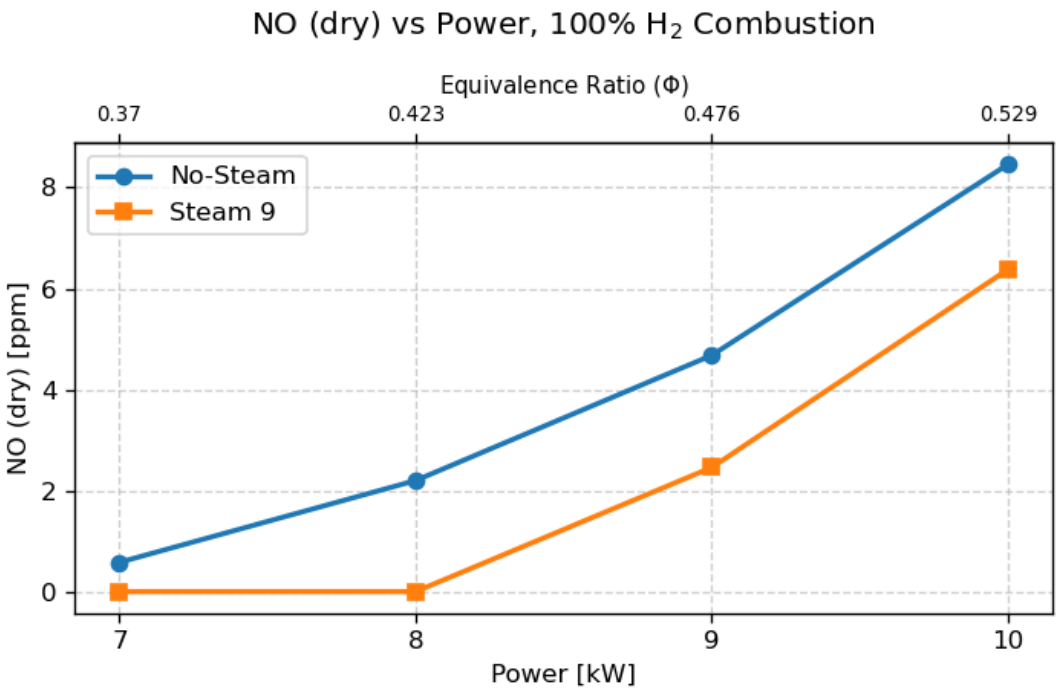


Figure 9.1: Experiment-A1: NO (dry) vs burner power for 100% H_2 with and without side steam injection (Steam 9 = 24.4 g/min). The upper axis shows the corresponding equivalence ratio ϕ.

Table 9.3 presents the NO emissions measured across four burner power levels under dry and steam-

injected conditions (Steam 9). Since the main air injection is kept at constant 250 nlpm, the change in burner power directly indicates a change in the equivalence ratio of the flame. The test point at 7 kW describes a very lean condition at $\phi = 0.370$ and the test point 10 kW describes a comparatively richer, but still lean condition at $\phi = 0.529$. As expected, as the equivalence ratio gets closer to $\phi = 1$, the adiabatic flame temperature gets higher, which promotes stronger thermal NO mechanism. Consequently, it can be observed in no-steam case that the NO emissions steadily rise with increasing equivalence ratio (burner power).

The results in Table 9.3 and Figure 9.1 indicate that steam injection is successful at mitigating NO emissions. When steam is injected, the NO levels at low burners of 7 and 8 kW dropped below the detection limit of the gas analyzer. At the higher power levels of 9 and 10 kW, the absolute dry NO drop is around 2.1 ppm, which corresponds to about 25 to 47% reduction in NO emissions respectively. However, it should be noted that these experimental points are at relatively lean conditions and NOx emissions are often a concern at or near stoichiometric conditions. Hence, while the data at 7 and 8 kW technically correspond to a 100% reduction relative to the measured no-steam reference, this does not imply complete elimination of NO emissions, but rather that the concentrations dropped below the detection limit of the analyzer at these already very lean conditions. However, combined with the significant NO reductions in higher burner powers at 9 and 10 kW, these results indicate steam injection is a successful and viable strategy to mitigate NO emissions in H_2, even at extremely lean conditions.

To complement the absolute emissions data, the derived (dry) NO metrics are presented below in Table 9.4 to provide an insight on the normalized emission performance and allow a fair comparison across different operating conditions. To provide better visualization, the EINO plot for Experiment-A1 is provided in Figure 9.2.

Power [kW]	ϕ	**Steam**	**NO (dry) [ppm]**	**NO@15% O_2 [ppm]**	**EINO [mg/MJ]**	**EINO [g/kg]**	**ΔEINO [%]**
10.0	0.529	No-Steam	8.46	5.16	4.200	0.504	0.00
		Steam-9	6.38	3.85	3.166	0.380	-24.6
9.0	0.476	No-Steam	4.68	3.19	2.614	0.314	0.00
		Steam-9	2.46	1.66	1.374	0.165	-47.4
8.0	0.423	No-Steam	2.20	1.70	1.400	0.168	0.00
		Steam-9	0.00	0.00	0.000	0.000	-100.0
7.0	0.370	No-Steam	0.58	0.52	0.427	0.051	0.00
		Steam-9	0.00	0.00	0.000	0.000	-100.0

Table 9.4: Experiment A1. Derived NO metrics (*dry*). NO values were normalized to 15% O_2 using Eq. (8.16).

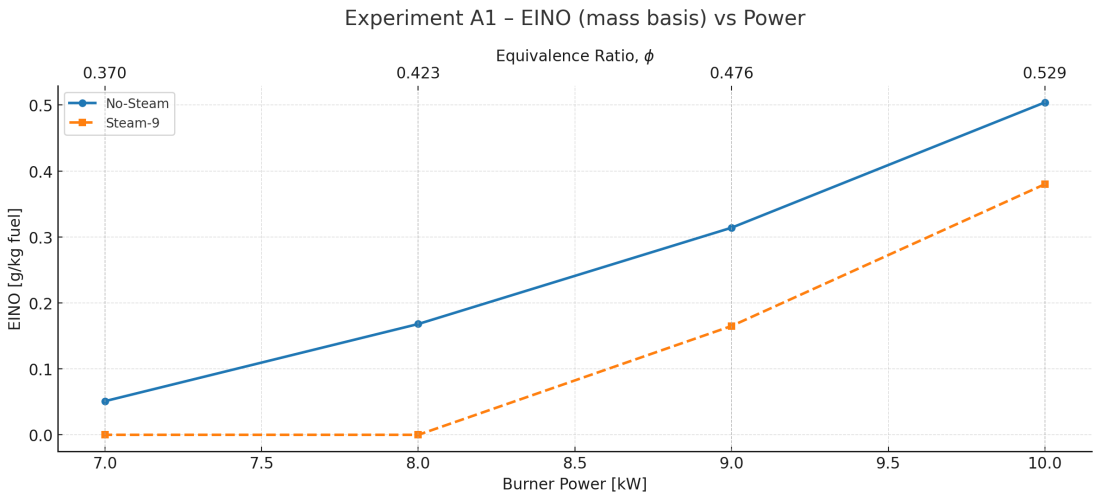


Figure 9.2: Experiment-A1: Emission index of NO (EINO, mass basis) as a function of burner power for 100% H_2 combustion with and without side steam injection (Steam 9 = 24.4 g/min). The upper axis indicates the corresponding equivalence ratio ϕ.

For Experiment-A1, the O_2 concentrations remained within a relatively narrow band (11.2–14.3%) across the investigated power range, and the difference between no-steam and steam cases at a given power was typically less than 0.1%. This stability in background oxygen implies that the raw NO values are already directly comparable between conditions, and the normalization serves as a formal confirmation rather than a correction.

After applying Equation 8.16, the normalized NO concentrations closely followed the dry readings: at 10 kW, the value decreased from 5.16 ppm (no steam) to 3.85 ppm (Steam-9), while at 9 kW it dropped from 3.19 to 1.66 ppm. At the lowest powers, the normalized values dropped below the detection limit, consistent with the apparent complete suppression already evident in the raw data. It should be noted, however, that this reflects concentrations falling beneath the measurement sensitivity, not necessarily a true elimination of NO formation. The important insight is that the percentage reduction induced by steam remained consistent before and after normalization, demonstrating that the suppression is thermochemical in origin and not attributable to altered air dilution.

The EINO metrics provided in Table 9.4 and Figure 9.2 provide energy-specific and mass-specific views on the emissions. By definition, EINO scales the measured NO to the chemical energy input of the burner, thereby removing the trivial dependence on absolute power level. It can be observed from the EINO results that the trend for both raw absolute ppm values of NO emissions and the EINO metrics are identical. EINO rises with increasing burner power level and steam injection achieves significant reduction at all power levels. The agreement between the normalized indices and the raw ppm values provides strong validation. Not only do the absolute NO concentrations decrease, but the emissions per unit of released energy also decline, indicating that steam directly modifies the combustion thermochemistry rather than simply diluting the flue gases.

These results carry several broader implications. First, they show that the measurement conclusions are robust across different metrics, since the same qualitative and quantitative trends appear whether the data are expressed in raw ppm, O_2-normalized concentration, or energy/mass-normalized EINO. Second, they demonstrate that even for 100% H_2 flames operated under lean conditions, where adiabatic flame temperatures are moderated and baseline NO formation is already low, steam injection still produces a substantial reduction in energy-specific NO formation. Finally, they emphasize that the impact of steam cannot be attributed solely to dilution. If dilution were the dominant effect, the O_2-normalized values would remain nearly unchanged yet the fact that they decline together with the raw ppm values points instead to physical mechanisms such as reduced flame temperature, shorter high-temperature residence times, and shifts in radical chemistry. The presence of steam lowers the peak flame temperature through both dilution and increased heat capacity, which reduces the thermal window in which NO can form. It may also shorten the residence time of combustion products in the high-temperature zone, although this effect

cannot be directly confirmed with the present setup. At the same time, steam alters the concentrations of OH, H, and O radicals, which are central to the chain-branching reactions sustaining the flame and to the extended Zeldovich mechanism responsible for thermal NO formation [11]. By lowering the radical pool and promoting recombination rather than NO-producing pathways, steam contributes directly to the observed suppression of emissions.

Experiment-A2: Pure Methane Flames

Experiment-A2 explores pure methane operation, serving as the hydrocarbon counterpart to A1. Compared to hydrogen, methane flames have a lower laminar flame speed, burn at lower adiabatic flame temperatures for the same equivalence ratio, and exhibit a higher lean flammability limit. As a result, they require richer operation to achieve stable combustion at the same thermal input. These characteristics lead to fundamentally different dynamics and emission profiles, making this experiment a critical benchmark for understanding how steam interacts with carbon-based fuels.

The NO emission results of Experiment-A2 are provided below in Table 9.5:

Power [kW]	**Total Air [nlpm]**	$\phi \pm$ **0.031**	**NO (ppm, *dry*) (wet in parentheses)**		**Dry reduction**	
			No-Steam	Steam-9	Abs [ppm]	%
11.0	180	0.976	37.01 (30.13 wet)	29.39 (20.75 wet)	7.62	20.6
10.5	180	0.931	34.07 (28.00 wet)	20.92 (14.90 wet)	13.15	38.6
10.0	180	0.887	25.05 (20.78 wet)	16.04 (11.53 wet)	9.01	36.0
9.5	180	0.843	21.86 (18.30 wet)	9.44 (6.84 wet)	12.42	56.8
9.0	180	0.798	13.98 (11.82 wet)	2.20 (1.61 wet)	11.78	84.3
8.5	180	0.754	7.95 (6.78 wet)	0.00 (0.00 wet)	7.95	100.0
8.0	160	0.798	12.45 (10.52 wet)	0.00 (0.00 wet)	12.45	100.0
7.5	160	0.748	5.16 (4.41 wet)	0.00 (0.00 wet)	5.16	100.0
7.0	140	0.798	6.60 (5.58 wet)	0.00 (0.00 wet)	6.60	100.0

Table 9.5: NO emissions for Experiment A2. 100% CH_4 combustion with varying burner power. Side steam injection configuration was used. Values reported on a dry basis; analyzer wet readings are shown in parentheses. Dry conversion via Equation 8.5.

In addition, relevant plots for (dry) NO emissions are provided in Figure 9.3 and Figure 9.4:

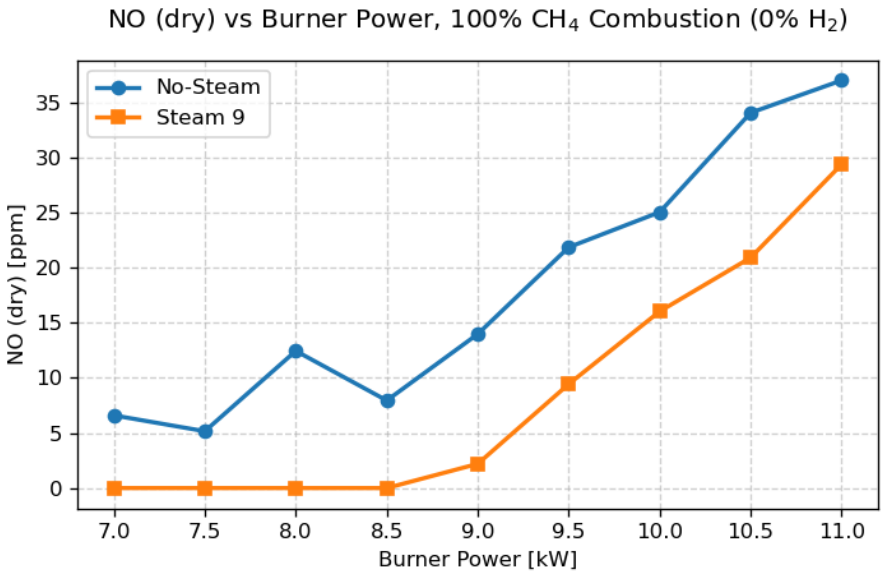


Figure 9.3: Experiment-A2: NO (dry) vs burner power for 100% CH_4 with and without side steam injection (Steam 9 = 24.4 g/min).

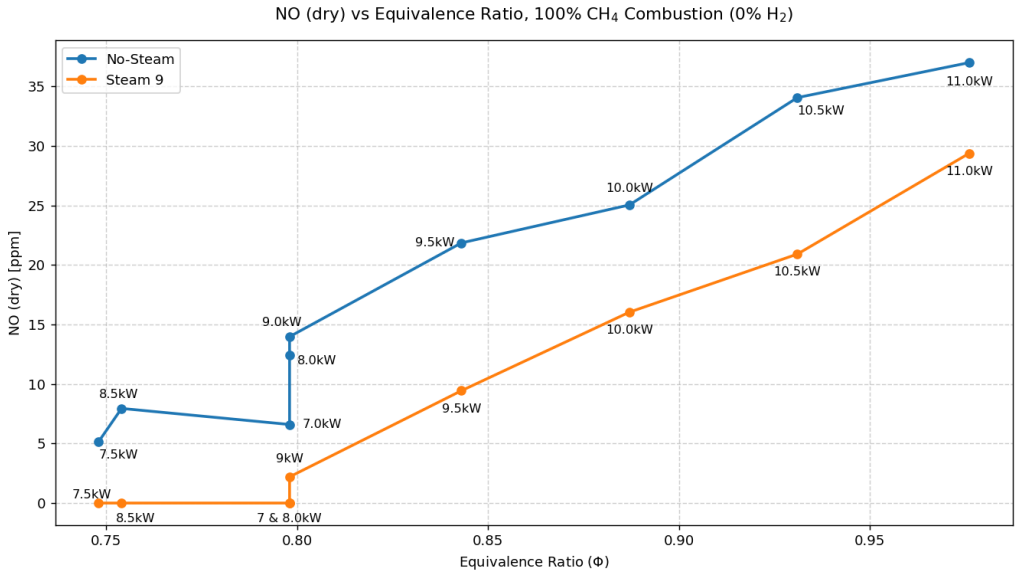


Figure 9.4: Experiment-A2: NO (dry) vs equivalence ratio for 100% CH_4 with and without side steam injection (Steam 9 = 24.4 g/min). Point annotations indicate burner power.

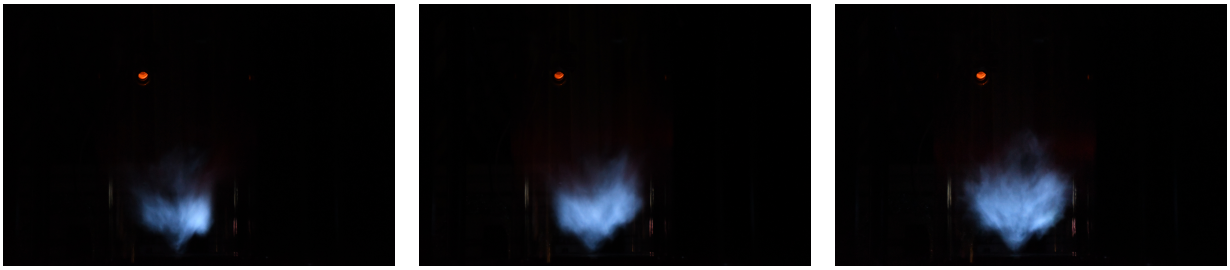
Across the power range of 7–11 kW, NO emissions increase in an almost linear manner with burner power, rising from approximately 5 ppm at the lowest to more than 35 ppm at 11 kW. This trend is more pronounced than in A1, where NO remained below 10 ppm even at the highest power. The higher levels here are directly linked to the richer equivalence ratios of the test points, even at similar burner power levels compared to pure H_2 in Experiment-A1. The richer operation leads to higher flame temperatures, which in turn promote stronger thermal NO formation. The calculated equivalence ratio values, however, carry an uncertainty of about ± 0.031 due to flow meter limitations and calibration tolerances. This uncertainty

can occasionally cause partial overlap between adjacent operating points, particularly when burner power is incremented in small steps (e.g., 0.5 kW). Even so, the increasing trend in NO remains clear and consistent. This suggests that the actual values of ϕ likely follow the expected trend closely enough for meaningful interpretation, and the impact of ϕ uncertainty is therefore acknowledged but does not obscure the observable changes in emission behavior.

It is important to note that the equivalence ratio ϕ did not vary in a perfectly consistent manner with burner power. At several operating points, adjustments in the total air injection were required to remain within the stability limits of the burner. At lower powers, the methane flame approached blow-off, so the total air flow was reduced to sustain stable combustion. As a result, there are cases with nearly identical ϕ values but different absolute air and fuel flows. This complicates a purely ϕ-based interpretation, since NO formation is influenced not only by mixture composition but also by boundary conditions such as heat losses, stability constraints, and flow field.

This becomes evident when comparing NO emissions at the same ϕ but different power levels. While theory identifies ϕ as the main parameter governing emissions, the data show that NO still increases with power. A key reason is the effect of heat losses: although the total heat transfer to the burner walls and surroundings may not remain strictly constant with power, since increased flow velocity, temperature gradients, and radiation can alter convective and radiative heat exchange, the smaller thermal input and limited heat capacity at low powers make these losses proportionally more significant, leading to a larger effective temperature drop and reduced NO formation. At higher powers, the larger heat release reduces the relative influence of these losses, allowing the flame to sustain a higher effective temperature and thereby promoting stronger thermal NO kinetics. In addition, the adjustments in air injection required for stability modify the velocity field and flame shape, which in turn affect the mixing pattern and the thickness of the high-temperature zone where Zeldovich NO can form. Finally, the higher flow rates associated with increased power also elevate turbulence and strain levels, enhancing radical production and mixing, and indirectly supporting additional NO formation. These effects together explain why ϕ alone cannot provide a complete description of the experimental data and why burner configuration, thermal environment, and fluid dynamics must also be considered.

To better illustrate these effects, flame photographs were taken at constant equivalence ratio but varying burner power, as shown in Figure 9.5.



7 kW, 140 nlpm air | 8 kW, 160 nlpm air | 9 kW, 180 nlpm air

Figure 9.5: Flame images for pure CH_4 combustion at constant equivalence ratio of 0.798 with varying burner power. No steam injection is used.

As shown in Figure 9.5, increasing the burner power alters the flame appearance even when the equivalence ratio is held constant. At lower power, the flame is compact, faint, and relatively stable, whereas at higher powers it widens, becomes more luminous, and displays stronger fluctuations in the shear layer. The increase in luminosity reflects the higher absolute heat release rate, which enhances chemiluminescence from visible radicals such as CH* and C_2^*, while OH emission lies in the ultraviolet range and is not captured by the DSLR camera. These observations indicate that absolute flow rates and thermal input affect both the velocity field and the radiative characteristics of the flame, thereby modifying its structure, turbulence intensity, and luminosity. This further supports the conclusion that ϕ alone is not sufficient to describe the combustion behavior, as flow dynamics, heat losses, and radical pool intensities also play a decisive role.

Looking at the the NO emission results in Figure 9.4 it can be observed that steam injection once again results in significant reduction in NO emissions. The trend seems clearer in the equivalence ratio vs dry

NO emissions graph. At lower equivalence ratios, the NO emissions were already low in the no-steam reference, and with steam injection the NO emissions readings dropped below the detection limit of the analyzer. In the intermediary to high H_2 fractions,steam injection consistently achieved absolute NO drops of 7.5 to 13 ppm which correspond to 84 to 20% reduction in NO emissions. These results are similar to the ones observed in Experiment-A1: steam injection achieves significant reductions in absolute ppm terms in mostly similar ranges, but the relative percentage drops differ greatly depending on the reference no-steam NO emissions. This results in lowest percentage NO drops in the high power ranges, even though those ranges still result in significant reductions in NO emissions. Nevertheless, these results combined with Experiment-A1 indicate that steam injection is a viable and efficient strategy to mitigate NO emissions.

To provide a broader picture of the effects of steam injection, the full emissions table for Experiment-A2 is provided in Table 9.6:

Power [kW]	Air [nlpm]	$\phi \pm$ 0.031	Steam	NO (ppm, *dry*) (wet in parentheses)	O_2 [%]	CO [ppm]	CH_4 [ppm]	CO_2 [%]
11.0	180	0.976	No-Steam	37.01 (30.13 wet)	0.60	27.73	0.00	11.45
			Steam-9	29.39 (20.75 wet)	0.72	51.25	0.00	11.38
10.5	180	0.931	No-Steam	34.07 (28.00 wet)	1.58	0.00	0.00	10.90
			Steam-9	20.92 (14.90 wet)	1.63	0.00	0.00	10.88
10.0	180	0.887	No-Steam	25.05 (20.78 wet)	2.53	0.00	0.00	10.38
			Steam-9	16.04 (11.53 wet)	2.58	4.05	0.03	10.34
9.5	180	0.843	No-Steam	21.86 (18.30 wet)	3.50	0.00	0.14	9.83
			Steam-9	9.44 (6.84 wet)	3.53	53.02	8.41	9.81
9.0	180	0.798	No-Steam	13.98 (11.82 wet)	4.46	0.00	0.63	9.28
			Steam-9	2.20 (1.61 wet)	4.52	214.08	86.55	9.25
8.5	180	0.754	No-Steam	7.95 (6.78 wet)	5.44	0.00	1.00	8.73
			Steam-9	0.00 (0.00 wet)	5.56	384.44	314.08	8.65
8.0	160	0.798	No-Steam	12.45 (10.52 wet)	4.69	0.00	0.00	9.17
			Steam-9	0.00 (0.00 wet)	4.81	493.04	397.27	9.06
7.5	160	0.748	No-Steam	5.16 (4.41 wet)	5.80	0.00	0.00	8.55
			Steam-9	0.00 (0.00 wet)	6.08	930.30	950.36	8.31
7.0	140	0.798	No-Steam	6.60 (5.58 wet)	5.01	3.84	0.00	8.99
			Steam-9	0.00 (0.00 wet)	5.30	848.11	1035.76	8.75

Table 9.6: Full emissions for Experiment A2. 100% CH_4 combustion with varying burner power. Values reported on a *dry* basis for NO; analyzer wet readings are shown in parentheses. O_2, CO, CH_4, and CO_2 are measured dry by the analyzer. Dry conversion via Equation 8.5. Side steam injection configuration was used.

The expanded emissions data in Table 9.6 add context to the NO behavior by reporting O_2, CO, CH_4, and CO_2 alongside NO. The dry O_2 fractions increase steadily as burner power decreases, rising from below 1% at 11 kW to over 5% at 7 kW. This is expected, since the richer ϕ points at higher power consume more oxygen, while the relatively leaner conditions at lower power leave more excess oxygen in the exhaust. The difference between no-steam and steam injection cases for O_2 is minimal and within the analyzer error margin. This shows that steam injection did not affect the underlying air–fuel ratio, but instead influenced the thermochemical environment, primarily flame temperature and radical pool without altering stoichiometry. With steam injection, at higher power levels the CO emissions are significantly lower compared to the lower power levels. The CO emissions are below the detection limit for most no-steam cases. However, in almost all points the CO emissions have increased with steam injection. This result is even more refined in lower power levels where the CO measurements rise from around 0-4 ppm to values around 800-900 ppm. This rise in CO emissions with steam injection indicate incomplete combustion at low powers of steam, where quenching, reduced flame temperature and shorter residence times suppress formation of fully oxidized flame. This consequently indicates steam injection has observable adverse effects on combustion efficiency at lower powers. This is also supported by the CH_4 emissions. CH_4 emissions are either below the detection limit or negligible for all no-steam points and at higher burner powers the CH_4 emissions are also below the detection limits. However, with steam injection at lower

powers CH_4 emissions shoot up to several hundreds of ppm or even over 1000 ppm for the 7 kW point. This is in agreement with the findings of CO emissions that steam injection results in lower combustion efficiency for lower burner powers. It should be noted that the burner power does not exactly scale with equivalence ratio here as previously mentioned, so this effect has more to do with local steam dilution effect due to relatively large amounts of steam injected at lower burner powers. Concurrently, CO_2 concentration decreases steadily with power, from about 11.5% at 11 kW to below 9% at 7 kW, as it is expected from the lesser fuel input and lesser carbon conversion at more lean conditions. At each power, steam injection only slightly modifies CO_2, suggesting that the gross carbon balance is maintained even though quenching within the flame leads to greater CO and CH_4. Interactions of these species demonstrate an apparent trade-off: where steam significantly reduces NO, especially below 9.5 kW, incomplete combustion products are formed in high yields while at higher powers, NO reductions are more modest in relative terms but completeness of combustion is maintained. Broadly speaking, the combined emissions data confirm that the effect of steam in A2 is regime-dependent: it reduces NO effectively, but at low powers it does so at the expense of oxidation efficiency, producing higher CO and unburned methane. These results highlight the importance of considering the whole emission profile when we consider steam injection strategies.

It should be noted that the same combustion efficiency penalties observed in pure CH_4 flames may also be present in pure H_2 flames, however since H_2 flames don't emit any carbon and the gas analyzer used in this experimental campaign is not suitable for H_2 measurements in the flue gas, whether H_2 combustion penalties present with steam injection or by how much can not be confirmed in this paper. Hence further research needs to be conducted to investigate the effect of combustion penalties in H_2 flames with steam injection and compare it to the combustion penalties of CH_4 flames.

After the raw emission results for Experiment-A2, the derived (dry) NO metrics are presented in Table 9.7. To provide a clear visualisation of the emission indices, Figure 9.6 provides the plots of EICO and EINO in mass basis.

Power [kW]	ϕ	Steam	NO				CO			
			(dry) [ppm]	@15% O_2 [ppm]	EINO [mg/MJ]	EINO [g/kg]	(dry) [ppm]	@15% O_2 [ppm]	EICO [mg/MJ]	EICO [g/kg]
11.0	0.976	No-Steam	37.01	10.82	12.261	0.615	27.73	8.11	8.575	0.429
		Steam-9	29.39	8.64	9.671	0.485	51.25	15.07	15.743	0.787
10.5	0.931	No-Steam	34.07	10.47	11.844	0.594	0.00	0.00	0.000	0.000
		Steam-9	20.92	6.44	7.239	0.363	0.00	0.00	0.000	0.000
10.0	0.887	No-Steam	25.05	8.09	9.163	0.459	0.00	0.00	0.000	0.000
		Steam-9	16.04	5.20	5.849	0.293	4.05	1.31	1.379	0.069
9.5	0.843	No-Steam	21.86	7.45	8.442	0.423	0.00	0.00	0.000	0.000
		Steam-9	9.44	3.22	3.638	0.182	53.02	18.11	19.075	0.954
9.0	0.798	No-Steam	13.98	5.04	5.726	0.287	0.00	0.00	0.000	0.000
		Steam-9	2.20	0.80	0.900	0.045	214.08	77.53	81.748	4.089
8.5	0.754	No-Steam	7.95	3.05	3.461	0.174	0.00	0.00	0.000	0.000
		Steam-9	0.00	0.00	0.000	0.000	384.44	148.63	156.108	7.808
8.0	0.798	No-Steam	12.45	4.56	5.100	0.256	0.00	0.00	0.000	0.000
		Steam-9	0.00	0.00	0.000	0.000	493.04	181.76	188.254	9.415
7.5	0.748	No-Steam	5.16	2.03	2.266	0.114	0.00	0.00	0.000	0.000
		Steam-9	0.00	0.00	0.000	0.000	930.30	372.25	381.022	19.056
7.0	0.798	No-Steam	6.60	2.46	2.703	0.136	3.84	1.43	1.468	0.073
		Steam-9	0.00	0.00	0.000	0.000	848.11	322.44	323.795	16.194

Table 9.7: Experiment A2. O_2 normalized and derived NO and CO metrics (*dry*) as described in Section 8.4

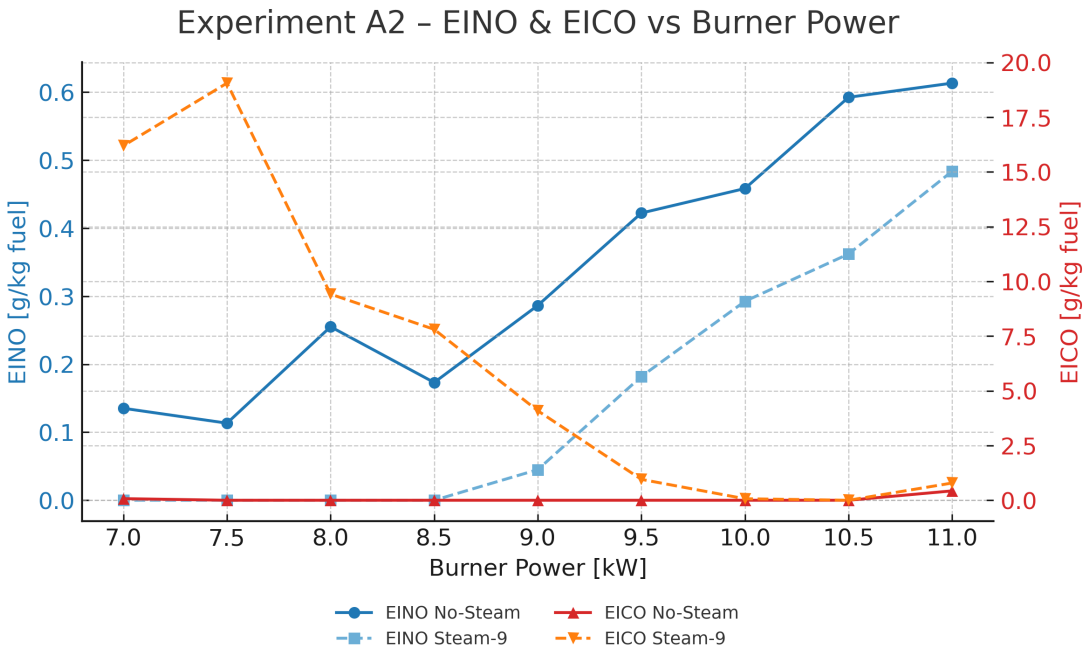
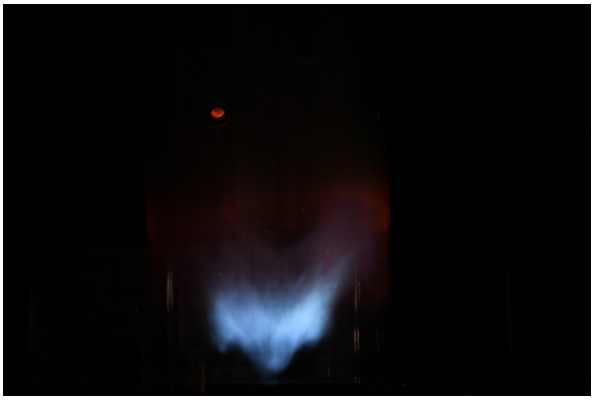


Figure 9.6: Experiment A2. Comparison of derived emission indices (EINO and EICO) on a mass basis for steam and non-steam cases.

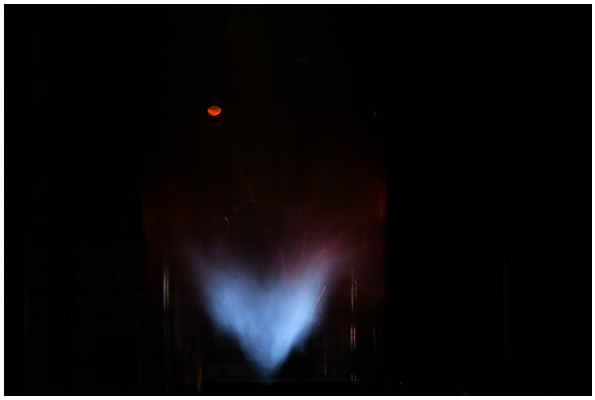
O_2 normalized values of NO and CO reflect the same results that were observed in raw ppm emissions results. O_2 normalization reduced the range of NO and CO values in a comparatively tighter range so the absolute differences between points are not as drastic as they are for raw values, nevertheless the trend is still clear. NO emissions drop with steam injection at all levels and the NO emissions tend to increase with increasing burner power, which is closely related to equivalence ratio. O_2 normalized CO emissions also follow the same trend observed in raw CO emissions: steam injection causes increase in CO emissions in lower burner powers. These O_2 normalized results indicate that the difference in CO and NO emissions observed in different points are not due to O_2 dilution due to different O_2 levels in the products but is due to the physical effect steam has on the flame.

These findings are also reinforced with the emissions indices results. EINO results confirm that NO formation per unit energy is reduced by steam injection. The trends observed in these derived emissions indices are very similar to those in the raw emissions results. This overall alignment between raw, normalized, and energy/mass-specific results strengthens the conclusion that the influence of steam is thermochemical rather than an artifact of excess-air variation or simple dilution effects.

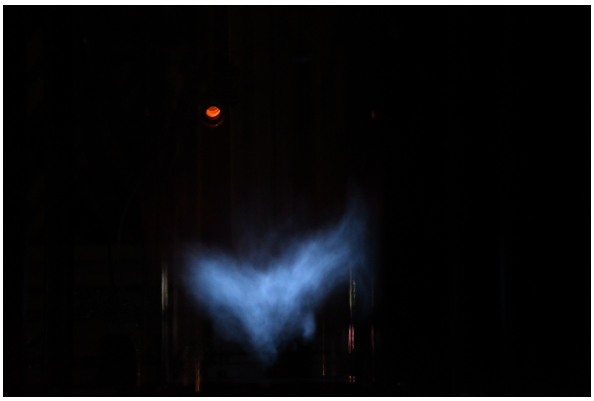
To illustrate the visual effect of steam injection in methane flames, DSLR camera images of steam and no-steam injection cases are provided below in Figure 9.7:



No-Steam (10.5 kW, $\phi \approx 0.93$)



Steam-9 (10.5 kW, $\phi \approx 0.93$)



No-Steam (7.5 kW, $\phi \approx 0.75$)



Steam-9 (7.5 kW, $\phi \approx 0.75$)

Figure 9.7: Flame photographs for pure CH_4 combustion at 10.5 kW (top row) and 7.5 kW (bottom row), comparing no-steam (left) and Steam-9 (right) [=24.4 g/min steam] conditions (side steam injection). The images highlight differences in flame luminosity, shape, and flow field between operating points.

The impact of steam injection on flame characteristics can be observed from the images in Figure 9.7. For the lower-power flame at 7.5 kW, steam injection results in a noticeably higher flame lift-off height, likely due to the upward momentum of the injected steam having a stronger relative influence under conditions of reduced fuel and air flow, where the overall gas throughput is lower. At 10.5 kW, no significant lift-off is observed, likely because the higher mass throughput of the flame reduces the relative influence of the same steam injection, making its effect weaker compared to the 7.5 kW case.

However, in the 10.5 kW flame the flame appears stretched upward, which indicates that steam injection modifies the local flow field and shear-layer dynamics rather than producing a distinct lift-off. The injected steam introduces additional momentum into the near-burner region, altering recirculation and entrainment patterns that influence the flame shape. It should be noted that this deformation does not necessarily imply that steam penetrates the core reaction zone where most heat release occurs. In swirl-stabilized configurations, the flame may anchor either in the inner or outer shear layer depending on the operating condition. If stabilization occurs in the inner shear layer, the centreline reaction zone near the burner rim may remain partially shielded from side steam injection, whereas the off-axis reaction zones are more exposed and therefore more likely to interact with the injected steam. However, a definitive assessment of which regions of the flame are reached by steam would require resolved measurements of the flow field and scalar transport (e.g., PIV or OH-PLIF), which are beyond the scope of the present study. Therefore, caution is required when visually interpreting flame deformation as direct interaction with high-temperature reaction regions.

It is important to note that in the current setup, steam was injected through two ports in the baseplate, positioned at the front and behind the flame as seen in the images. This configuration directs steam preferentially from the sides. A more uniform distribution, for example through a ring of ports encircling the

flame, could potentially provide more even coverage of the hot reaction zones and thereby enhance NO mitigation.

Additionally, at both 10.5 kW and 7.5 kW, the flames with steam appear more diffuse and less luminous, consistent with dilution and reduced radical chemiluminescence. The flame edges also appear more turbulent and irregular under steam addition, indicating modified shear layer dynamics. Comparing power levels, the higher-power case shows a brighter and more compact flame core, while the lower-power case appears wider and less intense, reflecting the lower heat release and stronger relative heat losses.

In conclusion, these results observed in Experiment-A2, combined with the results of Experiment-A1, indicate that steam injection is a successful strategy for mitigating NO emissions, both in H_2 and CH_4 flames.

9.3. Series B: Variation of Blend Percentage

Experiment-B1: H_2 Fraction Variation with Constant 11 kW Power

In Series B, the effect of change of (H_2–CH_4) fuel blend is investigated with and without side steam injection (Steam 9 = 24.4 g/min). In Experiment-B1, the flame is kept at a constant of 11 kW, and the hydrogen blend percentage is changed from 0% to 80%. To maintain the stability of the flame, axial air injection is used for points at 60, 70 and 80% hydrogen content. A 100% H_2 case was not included in this series because the flame was unstable even before steam injection. Although a flame could be ignited, it stabilized dangerously close to the burner rim and repeatedly approached flashback into the mixing tube. Due to the associated safety risks and the likelihood of hardware damage, this operating point was not investigated further.

The NO emission data for Experiment-B1 is given in Table 9.8. The change in equivalence ratio while increasing the H_2 fraction is a direct outcome of the differing fuel properties: at constant burner power, less fuel is required as the hydrogen content rises due to its higher energy density, and the corresponding air-to-fuel ratio shifts. As a result, ϕ decreases gradually across the sweep, which needs to be kept in mind when interpreting the emission trends.

H_2 Blend [%]	**AAI [%]**	**$\phi \pm$ 0.017**	**NO (ppm, *dry*) (wet in parentheses)**		**Dry reduction**	
			No-Steam	Steam-9	Abs [ppm]	%
0	0	0.702	5.78 (4.99 wet)	3.64 (2.82 wet)	2.14	37.0
20	0	0.694	8.12 (6.96 wet)	2.55 (1.96 wet)	5.57	68.6
30	0	0.689	10.34 (8.82 wet)	3.97 (3.04 wet)	6.37	61.6
40	0	0.682	11.91 (10.11 wet)	5.50 (4.20 wet)	6.41	53.9
50	0	0.675	12.86 (10.84 wet)	4.99 (3.78 wet)	7.87	61.2
60	10	0.665	10.36 (8.67 wet)	5.82 (4.38 wet)	4.54	43.8
70	15	0.653	24.11 (19.97 wet)	17.73 (13.22 wet)	6.38	26.5
80	20	0.637	21.12 (17.27 wet)	14.84 (10.93 wet)	6.28	29.7

Table 9.8: NO emissions for Experiment B1. Constant 11 kW burner power with varying H_2 fuel fraction. Side steam injection configuration was used. Values reported on a dry basis; analyzer wet readings are shown in parentheses. Dry conversion via Equation 8.5.

Relevant plot for (dry) NO emissions for Experiment-B1 are provided in Figure 9.8:

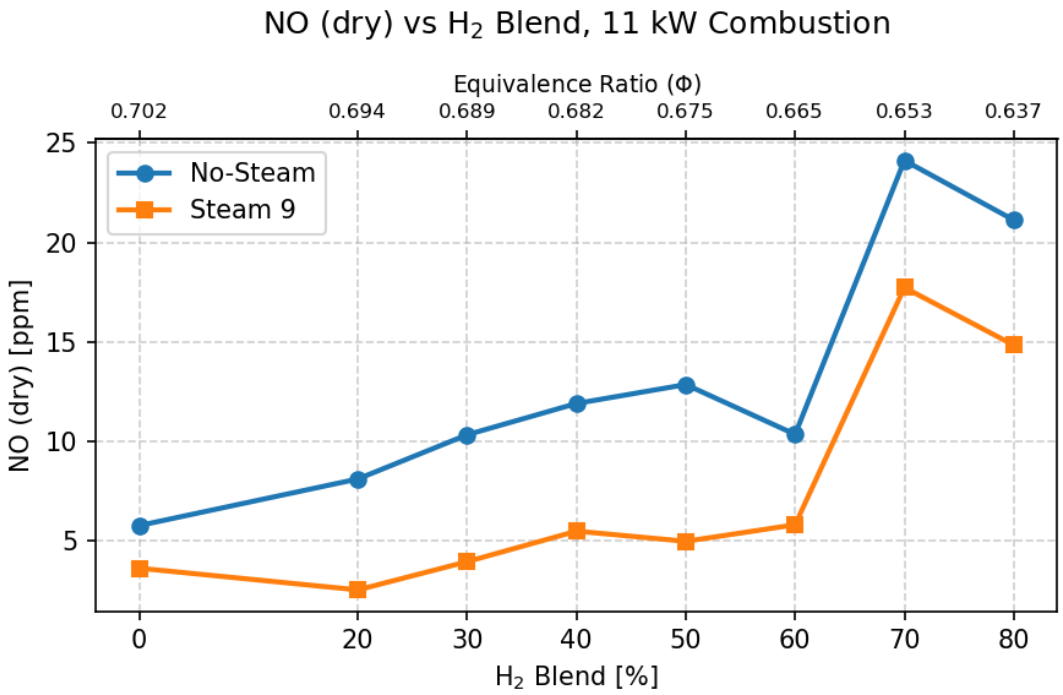


Figure 9.8: Experiment-B1: NO (dry) vs H_2 blend fraction at 11 kW with and without side steam injection (Steam 9 = 24.4 g/min). The upper axis shows the corresponding equivalence ratio ϕ.

In the absence of steam, dry NO increases steadily as the hydrogen fraction rises from 0–50%, reflecting the combined influence of higher turbulent burning velocity, greater concentrations of reactive radicals (O, H, OH), and the more compact flame shape associated with hydrogen enrichment. As hydrogen is introduced, its high diffusivity alters local mixing and promotes differential diffusion effects, which can generate spatial variations in equivalence ratio. Even though the global mixture remains lean, regions of locally higher equivalence ratio can form where hydrogen preferentially accumulates, creating pockets with higher reaction intensity and temperature. In addition, as the flame becomes shorter and more compact with increasing H_2 content, the relative influence of wall and hardware heat losses is reduced, because a smaller fraction of the flame surface area is exposed to cold boundaries. This allows higher effective temperatures to be sustained in the main reaction zone compared to methane-only operation. The combined increase in local temperature and radical pool availability accelerates thermal NO formation, which explains the experimentally observed rise in NO emissions with increasing hydrogen fraction from 0 to 50%.

At 60% H_2, NO decreases despite the higher hydrogen content. This coincides with the introduction of axial air injection (10%), which redistributes part of the total air away from the swirler. Previous studies on this burner have shown that axial air injection weakens the inner recirculation zone and promotes more jet-like stabilization in the outer shear layer, fundamentally changing the flame structure [110, 111]. At 70% H_2, NO rises sharply to its maximum value, as the stronger reactivity and enhanced radical pool outweigh the aerodynamic influence of 15% AAI. At 80% H_2, the further increase in AAI to 20% again modifies the stabilization pattern, leading to a slight decline in NO relative to 70%. The non-monotonic trend between 60–80% H_2 therefore reflects the competing influences of hydrogen enrichment, which drives reactivity and compact flames, and axial air injection, which alters flow partitioning and stabilization.

It can be observed in Table 9.8 and Figure 9.8 that steam injection lowers NO emissions across all blends. The data suggests that steam injection reduces NO emissions mainly around 6 ppm range in absolute terms, with some variation in some points. However, this absolute ppm drop corresponds to different values of % NO drop due the the different no-steam reference NO emissions. Nevertheless, steam injection manages to reduce NO emissions between 26-68% depending on the H_2 blend fraction. However, no conclusions on whether steam injection performs better in H_2 or in CH_4 can be drawn from the data. The

data suggests that steam injection is roughly equally effective in mitigation NO emissions in both H_2 and CH_4 flames.

The full emissions table for Experiment B-1 is provided in Table 9.9:

H_2 Blend [%]	AAI [%]	$\phi \pm 0.017$	Steam	NO (ppm, *dry*) (wet in parentheses)	O_2 [%]	CO [ppm]	CH_4 [ppm]	CO_2 [%]
0	0	0.702	No-Steam	5.78 (4.99 wet)	6.06	0.00	1.11	8.45
			Steam-9	3.64 (2.82 wet)	5.88	27.91	11.85	8.42
20	0	0.694	No-Steam	8.12 (6.96 wet)	6.31	0.00	1.15	7.88
			Steam-9	2.55 (1.96 wet)	6.31	22.87	3.60	7.87
30	0	0.689	No-Steam	10.34 (8.82 wet)	6.50	0.00	1.21	7.51
			Steam-9	3.97 (3.04 wet)	6.45	5.15	1.83	7.53
40	0	0.682	No-Steam	11.91 (10.11 wet)	6.72	0.00	0.97	7.07
			Steam-9	5.50 (4.20 wet)	6.66	0.00	1.51	7.10
50	0	0.675	No-Steam	12.86 (10.84 wet)	6.94	0.00	1.27	6.56
			Steam-9	4.99 (3.78 wet)	6.90	0.00	2.63	6.57
60	10	0.665	No-Steam	10.36 (8.67 wet)	7.83	0.00	1.32	5.66
			Steam-9	5.82 (4.38 wet)	7.82	2.24	2.01	5.66
70	15	0.653	No-Steam	24.11 (19.97 wet)	8.08	0.00	1.02	4.92
			Steam-9	17.73 (13.22 wet)	8.04	0.00	0.00	4.94
80	20	0.637	No-Steam	21.12 (17.27 wet)	8.31	0.00	0.99	3.94
			Steam-9	14.84 (10.93 wet)	8.23	0.00	0.28	3.97

Table 9.9: Full emissions for Experiment B1. Constant 11 kW burner power with varying H_2 fuel fraction. Values reported on a *dry* basis for NO; analyzer wet readings are shown in parentheses. O_2, CO, CH_4, and CO_2 are measured dry by the analyzer. Dry conversion via Equation 8.5. Side steam injection configuration was used.

The expanded emissions data in Table 9.9 provide further context to the NO behavior by including O_2, CO, CH_4, and CO_2 across the range of hydrogen fractions. The dry O_2 concentration increases gradually with higher H_2 content, consistent with the decreasing equivalence ratio from 0.702 at 0% H_2 to 0.637 at 80% H_2. The difference between steam and no-steam cases is minimal and within analyzer scatter, which confirms that steam injection did not alter the underlying air–fuel balance but instead affected the thermochemical environment. This mirrors the trends observed in A2, where O_2 signals remained insensitive to steam injection once values were reported on a dry basis.

The adjusted CH_4 data, corrected for analyzer offset, show that unburned methane remains low overall but is still detectable under steam injection at high methane fraction blend conditions. At 0% and 20% H_2, CH_4 concentrations rise slightly above the detection limit (roughly 3–10 ppm), while at higher H_2 fractions they converge to the no-steam reference values within the analyzer uncertainty. This suggests that localized quenching is present under steam dilution in methane-dominated flames, but increasing hydrogen content improves reactivity sufficiently to suppress detectable methane emissions. This indicates that while methane oxidation is improved with higher H_2 fractions, the effect of unburnt hydrogen cannot be evaluated since it was not measured by the analyzer.

CO_2 concentrations follow the expected monotonic decrease with hydrogen fraction, from about 8.4% at pure methane to below 4% at 80% H_2, reflecting the reduced carbon input at fixed burner power. Steam injection produces only small differences, always within the measurement uncertainty. This indicates that while CO and CH_4 measurements reveal minor pockets of incomplete combustion under steam injection at low H_2 fractions, these effects are not extensive enough to alter the bulk carbon balance. The combined emissions picture for B1 therefore reinforces the dual role of steam injection: while it consistently suppresses NO across the blend range, it can also introduce localized oxidation penalties.

After the raw emission results for Experiment-A2, the derived (dry) NO metrics are presented in Table 9.10. To provide a clear visualisation of the emission indices, Figure 9.9 provides the plots of EICO and EINO in mass basis.

H_2 [%]	ϕ	Steam	NO				CO			
			(dry) [ppm]	@15% O_2 [ppm]	EINO [mg/MJ]	EINO [g/kg]	(dry) [ppm]	@15% O_2 [ppm]	EICO [mg/MJ]	EICO [g/kg]
0	0.702	No-Steam	5.78	2.31	2.717	0.136	0.00	0.00	0.000	0.000
		Steam-9	3.64	1.44	1.711	0.086	27.91	11.02	12.244	0.612
20	0.694	No-Steam	8.12	3.30	3.801	0.198	0.00	0.00	0.000	0.000
		Steam-9	2.55	1.04	1.198	0.062	22.87	9.29	9.990	0.521
30	0.689	No-Steam	10.34	4.21	4.830	0.252	0.00	0.00	0.000	0.000
		Steam-9	3.97	1.62	1.874	0.098	5.15	2.11	2.243	0.120
40	0.682	No-Steam	11.91	4.84	5.602	0.294	0.00	0.00	0.000	0.000
		Steam-9	5.50	2.21	2.579	0.135	0.00	0.00	0.000	0.000
50	0.675	No-Steam	12.86	5.21	6.080	0.319	0.00	0.00	0.000	0.000
		Steam-9	4.99	2.02	2.360	0.124	0.00	0.00	0.000	0.000
60	0.665	No-Steam	10.36	4.11	4.585	0.241	0.00	0.00	0.000	0.000
		Steam-9	5.82	2.31	2.602	0.137	2.24	1.02	0.966	0.059
70	0.653	No-Steam	24.11	11.15	11.082	0.730	0.00	0.00	0.000	0.000
		Steam-9	17.73	8.17	8.146	0.537	0.00	0.00	0.000	0.000
80	0.637	No-Steam	21.12	9.94	9.637	0.707	0.00	0.00	0.000	0.000
		Steam-9	14.84	6.94	6.769	0.497	0.00	0.00	0.000	0.000

Table 9.10: Experiment B1. O_2-normalized and derived NO and CO metrics (*dry*) as described in Section 8.4.

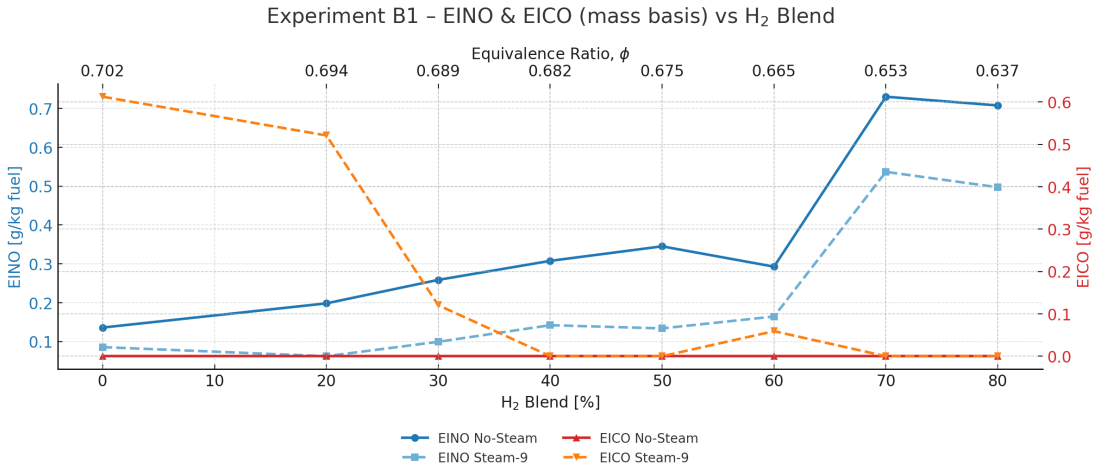


Figure 9.9: Experiment B1. Comparison of derived emission indices (EINO and EICO) on a mass basis for steam and non-steam cases.

O_2 normalized values of NO and CO once again confirm the trend that was observed with raw emissions values. This confirms that the steam effect is not an artifact of excess-air differences, but rather reflects genuine changes in flame temperature and radical chemistry.

The derived emission indices in Table 9.10 and Figure 9.9 reinforce the trends already observed in the raw emissions. EINO rises steadily with hydrogen enrichment up to 50%, before the introduction of axial air injection modifies the trajectory and produces the non-monotonic profile between 60–80% H_2. The EICO values, while small in absolute terms, highlight the localized quenching observed in the steam cases at high methane fraction blend conditions. An additional consideration is that hydrogen flames are more compact than methane flames at comparable thermal input, which likely reduces the degree to which side-injected steam penetrates the reaction zone. This reduced steam–flame interaction can partly explain why the mitigation effect is less pronounced at higher hydrogen fractions, consistent with previous studies on this burner that reported a shift of burning to the outer shear layer and reduced accessibility of the flame front to lateral injection [110, 111].



Pure CH_4, No-Steam | Pure CH_4, Steam-9 | 80% H_2, No-Steam | 80% H_2, Steam-9

Figure 9.10: Flame images for pure CH_4 and 80% H_2 cases at 11 kW, with and without side steam injection (Steam-9 = 24.4 g/min).

The flame images in Figure 9.10 illustrate the contrasting response of CH_4-rich and H_2-rich flames to steam injection. For pure methane, the flame is relatively tall and luminous, with steam injection producing visible broadening and increased fluctuations in the shear layer. This aligns with the emission data showing stronger quenching and incomplete combustion products at CH_4-rich conditions. In contrast, the 80% H_2 flame is more compact, consistent with the higher burning velocity of hydrogen. Steam injection in this case does not strongly change the overall flame shape but stretches the outer edges upward, suggesting that dilution and cooling occur mainly near the shear layer. Since the high hydrogen fraction flame is compact, the steam jets may not reach the reaction zones as effectively as in the larger methane flame, which reduces the overall mitigation effect. Similar behavior has been reported in previous studies of this burner, where flame compactness and changes in stabilization strongly affected the effectiveness of secondary injection through axial air injection [111, 110].

Experiment-B2: H_2 Fraction Variation with Constant 9 kW Power

Experiment B2 investigates the influence of hydrogen enrichment on NO emissions at a lower burner load of 9 kW. Compared to B1 (11 kW), these conditions are substantially leaner ($\phi \approx 0.47$–0.57 vs. $\sim$0.64–0.70). Axial air injection (AAI) begins at 60% H_2 in both B1 and B2, but the distribution of air differs: in B2, AAI is kept constant at 10% for 60–80% H_2 and only increases to 15% at 100% H_2, whereas in B1 it rises progressively (10/15/20%). This difference in air partition into AAI and swirl air is due to the stability regime of the flame at lower power and ϕ values, which consequently have effects on the flame dynamics and emissions profile.

The NO emission data for Experiment-B2 is given in Table 9.11 and illustrated in Figure 9.11:

H_2 Blend [%]	**AAI [%]**	**$\phi \pm$ 0.014**	**NO (ppm, *dry*) (wet in parentheses)**		**Dry reduction**	
			No-Steam	Steam-9	Abs [ppm]	%
20	0	0.568	1.00 (0.88 wet)	— (blowout)	—	—
30	0	0.563	1.46 (1.28 wet)	0.00 (0.00 wet)	1.46	100.0
40	0	0.558	2.22 (1.94 wet)	0.00 (0.00 wet)	2.22	100.0
50	0	0.552	3.63 (3.16 wet)	0.00 (0.00 wet)	3.63	100.0
60	10	0.544	3.98 (3.44 wet)	0.70 (0.54 wet)	3.28	82.4
70	10	0.534	11.55 (9.90 wet)	0.58 (0.45 wet)	10.97	95.0
80	10	0.521	13.20 (11.20 wet)	3.19 (2.43 wet)	10.01	75.8
100	15	0.476	7.72 (6.32 wet)	4.27 (3.15 wet)	3.45	44.7

Table 9.11: NO emissions for Experiment B2. Constant 9 kW burner power with varying H_2 fuel fraction. Side steam injection configuration was used. Values reported on a dry basis; analyzer wet readings are shown in parentheses. Dry conversion via Equation 8.5.

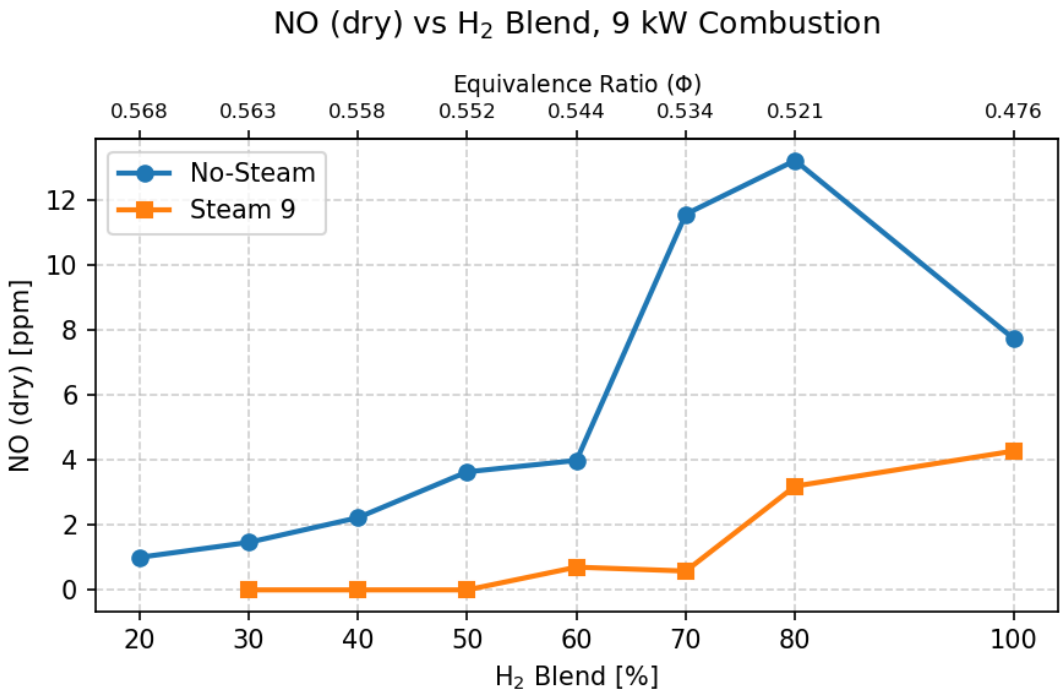


Figure 9.11: Experiment-B2: NO (dry) vs H_2 blend fraction at 9 kW with and without side steam injection (Steam 9 = 24.4 g/min). The upper axis shows the corresponding equivalence ratio ϕ.

In the no-steam reference, NO emissions increase with hydrogen fraction, from 1.0 ppm at 20% H_2 to 13.2 ppm at 80%. While hydrogen enrichment contributes through faster chemistry, this trend must also be viewed in the context of the changing equivalence ratio, which drops from 0.568 to 0.521 across these points. At 100% H_2, NO decreases to 7.7 ppm despite the higher reactivity of the mixture. This reduction reflects the combined influence of the lower ϕ (0.476) and the higher AAI share (15%), both of which moderate flame temperature and limit the effective time at high temperature. Overall, the trend is characterized by a steady increase in NO up to 80% H_2, followed by a decline at full hydrogen, showing how composition, equivalence ratio, and the resulting air–fuel mixing from the axial and swirl air distribution interact to govern emissions.

Steam injection produces very strong NO reduction throughout B2. Between 30–50% H_2, NO is completely suppressed to the analyzer detection limit, while at 60–80% H_2 reductions remain substantial, typically 75–95%. Even at 100% H_2, where the flame is most reactive, steam still cuts NO by nearly half. The effect is stronger at 9 kW than at 11 kW, which can be attributed to the larger relative heat losses and higher steam-to-fuel ratio at lower load, both of which enhance the quenching influence of steam. The only exception occurs at 20% H_2, where steam addition destabilized the flame and caused blowout, even though this point had the highest ϕ in B2. This reflects the lower burning velocity and weaker radical pool of methane-dominated mixtures, which makes them more vulnerable to dilution and cooling from steam injection, consistent with earlier observations on this burner [111, 110]. At higher H_2 fractions, however, the increased burning velocity and the stronger pool of chain-branching radicals (H, OH) enhance flame stability, preventing blowout even under the same steam injection [112].

The full emissions table for B2 is provided below in Table 9.12 to give more insight into the full emissions profile, including O_2, CO, CH_4, and CO_2 alongside NO:

H_2 Blend [%]	AAI [%]	$\phi \pm 0.014$	Steam	NO (ppm, *dry*) (wet in parentheses)	O_2 [%]	CO [ppm]	CH_4 [ppm]	CO_2 [%]
20	0	0.568	No-Steam	1.00 (0.88 wet)	9.19	24.03	2.42	6.29
			Steam-9	blowout	—	—	—	—
30	0	0.563	No-Steam	1.46 (1.28 wet)	9.23	1.89	0.00	6.07
			Steam-9	0.00 (0.00 wet)	9.44	1508.32	375.50	5.82
40	0	0.558	No-Steam	2.22 (1.94 wet)	9.36	0.00	0.00	5.75
			Steam-9	0.00 (0.00 wet)	9.47	972.13	162.90	5.59
50	0	0.552	No-Steam	3.63 (3.16 wet)	9.55	0.00	0.00	5.33
			Steam-9	0.00 (0.00 wet)	9.57	446.77	65.39	5.26
60	10	0.544	No-Steam	3.98 (3.44 wet)	10.23	4.96	0.00	4.62
			Steam-9	0.70 (0.54 wet)	10.32	1231.81	184.70	4.46
70	10	0.534	No-Steam	11.55 (9.90 wet)	10.51	0.00	0.00	3.98
			Steam-9	0.58 (0.45 wet)	10.55	296.91	16.08	3.93
80	10	0.521	No-Steam	13.20 (11.20 wet)	10.79	0.00	0.00	3.16
			Steam-9	3.19 (2.43 wet)	10.80	43.52	0.35	3.14
100	15	0.476	No-Steam	7.72 (6.32 wet)	12.26	0.00	0.00	0.03
			Steam-9	4.27 (3.15 wet)	12.23	0.00	0.00	0.03

Table 9.12: Full emissions for Experiment B2. Constant 9 kW burner power with varying H_2 fuel fraction. Values reported on a *dry* basis for NO; analyzer wet readings are shown in parentheses. O_2, CO, CH_4, and CO_2 are measured dry by the analyzer. CH_4 values close to the analyzer detection limit ($\sim$4 ppm) should be interpreted with caution. Dry conversion via Equation 8.5. Side steam injection configuration was used.

The expanded emissions data in Table 9.12 reinforce the observation that steam injection at 9 kW introduces significant combustion penalties compared to B1. In the no-steam reference, CO remains negligible and CH_4 is at or below the detection limit across all blends, consistent with stable lean combustion. With steam injection, however, both CO and CH_4 increase sharply, especially at 30–60% H_2 where CO reaches 400–1500 ppm and CH_4 rises to hundreds of ppm. These values are far larger than those observed in B1, indicating that the weaker flames at 9 kW are more sensitive to dilution. At higher hydrogen fractions (70–100% H_2), CO and CH_4 emissions decline again, which can be explained due to the lower carbon presence in the fuel. The overall picture is that while steam is highly effective at suppressing NO, its large heat capacity and dilution effect lead to extensive regions of incomplete combustion in high methane fraction flames at low load. This confirms that the strong NO reduction achieved in B2 comes at the expense of combustion efficiency, and that this trade-off is more severe than at higher power levels.

On the other hand, O_2 and CO_2 emissions readings act as expected. The differences between no-steam and steam injection cases are within the gas analyzer uncertainty, which confirms that steam injection does not alter the overall air–fuel balance or bulk carbon conversion. O_2 emissions rise with increasing H_2 fraction in the fuel, which is expected as the equivalence ratio also decreases. CO_2 emissions also decrease as the CH_4 content in the fuel decreases.

After the raw emission results for Experiment-A2, the derived (dry) NO metrics are presented in Table 9.13. To provide a clear visualisation of the emission indices, Figure 9.12 provides the plots of EICO and EINO in mass basis.

H_2 [%]	ϕ	Steam	NO				CO			
			(dry) [ppm]	@15% O_2 [ppm]	EINO [mg/MJ]	EINO [g/kg]	(dry) [ppm]	@15% O_2 [ppm]	EICO [mg/MJ]	EICO [g/kg]
20	0.568	No-Steam	1.00	0.51	0.580	0.030	24.03	12.16	13.017	0.679
		Steam-9	blowout	–	–	–	–	–	–	–
30	0.563	No-Steam	1.46	0.74	0.847	0.045	1.89	0.96	1.023	0.055
		Steam-9	0.00	0.00	0.000	0.000	1508.32	779.71	816.441	43.752
40	0.558	No-Steam	2.22	1.14	1.284	0.071	0.00	0.00	0.000	0.000
		Steam-9	0.00	0.00	0.000	0.000	972.13	503.85	524.839	29.087
50	0.552	No-Steam	3.63	1.89	2.093	0.121	0.00	0.00	0.000	0.000
		Steam-9	0.00	0.00	0.000	0.000	446.77	233.59	240.405	13.901
60	0.544	No-Steam	3.98	2.21	2.287	0.140	4.96	2.75	2.661	0.163
		Steam-9	0.70	0.39	0.402	0.025	1231.81	689.49	660.814	40.380
70	0.534	No-Steam	11.55	6.58	6.610	0.435	0.00	0.00	0.000	0.000
		Steam-9	0.58	0.33	0.332	0.022	0.00	0.00	0.000	0.000
80	0.521	No-Steam	13.20	7.73	7.509	0.551	0.00	0.00	0.000	0.000
		Steam-9	3.19	1.87	1.815	0.133	0.00	0.00	0.000	0.000
100	0.476	No-Steam	7.72	5.29	4.311	0.517	0.00	0.00	0.000	0.000
		Steam-9	4.27	2.91	2.384	0.286	0.00	0.00	0.000	0.000

Table 9.13: Experiment B2 (9 kW). O_2-normalized and derived NO and CO metrics (*dry*) as described in Section 8.4.

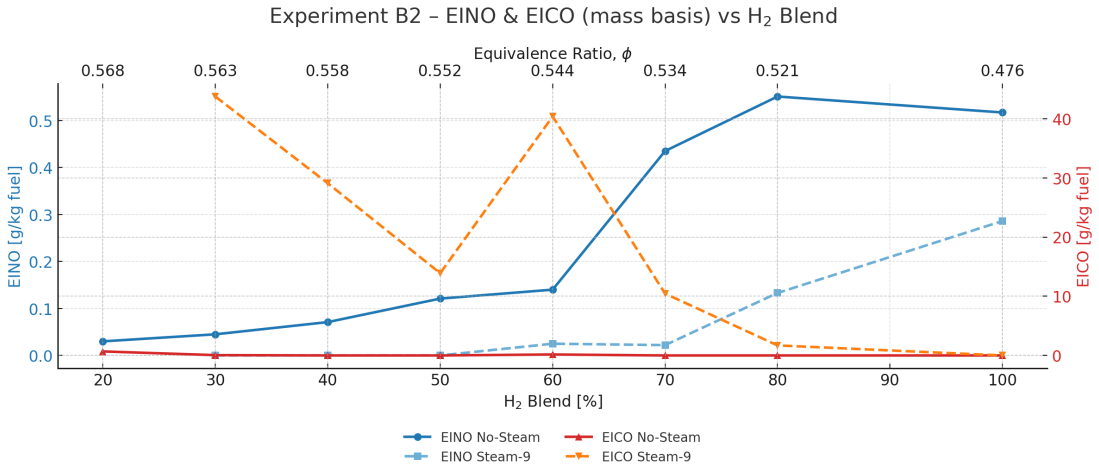


Figure 9.12: Experiment B2. Comparison of derived emission indices (EINO and EICO) on a mass basis for steam and non-steam cases.

The trends in Figure 9.12 are consistent with the raw emissions discussed earlier. The exceptionally high EICO values for the Steam-9 condition at 30–60% H_2 reflect the sharp rise in CO reported in Table 9.12. At 9 kW the flame is weak and strongly affected by steam dilution, which reduces reaction intensity and promotes incomplete oxidation, leading to substantial CO formation even though NO is effectively suppressed. This confirms that at low load, aggressive steam addition introduces a severe trade-off between NO reduction and combustion efficiency. The O_2-normalized emissions and emission indices support this conclusion: EINO decreases markedly with steam injection, whereas EICO increases sharply in the methane-dominated cases due to incomplete combustion. To further illustrate the impact of steam at different power levels, a comparison of the emission indices between Experiments B1 and B2 is presented below in Figure 9.13 and Figure 9.14:

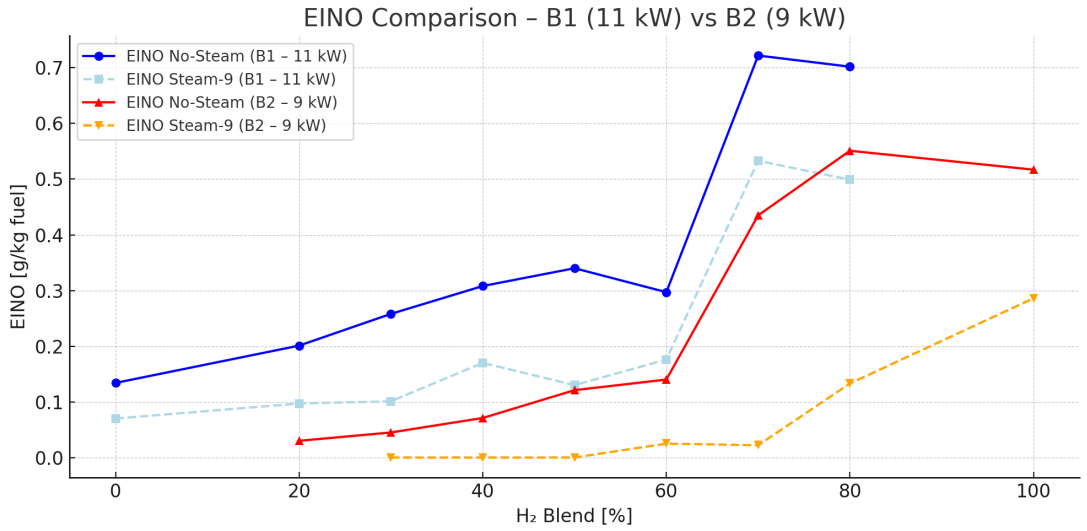


Figure 9.13: Comparison of EINO (mass basis, g/kg fuel) between Experiment B1 (11 kW) and Experiment B2 (9 kW) for varying H_2 fuel fractions under no-steam and Steam-9 conditions.

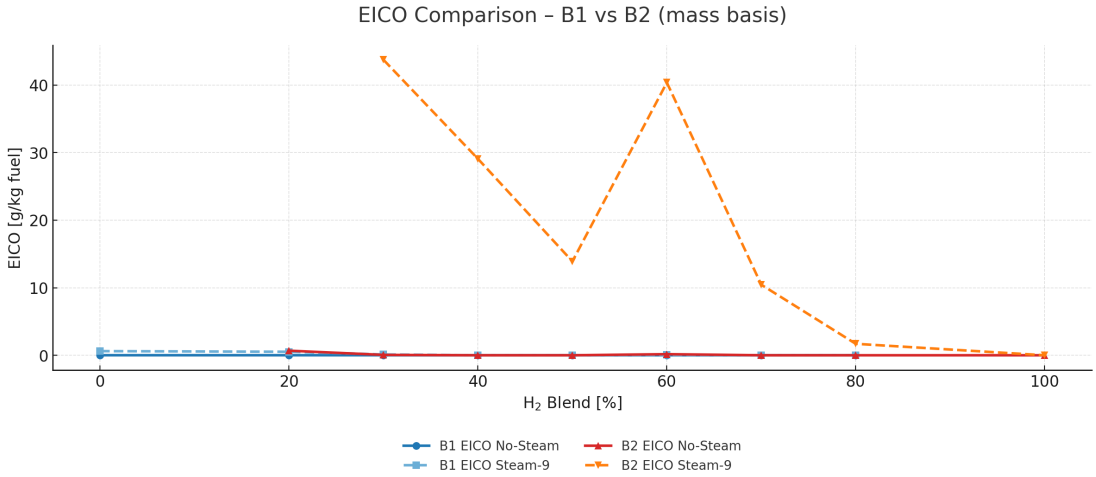


Figure 9.14: Comparison of EICO (mass basis, g/kg fuel) between Experiment B1 (11 kW) and Experiment B2 (9 kW) for varying H_2 fuel fractions under no-steam and Steam-9 conditions.

Comparisons of the EINO values confirm that at high burner powers where more fuel is present, the NO emissions still increase when normalized for the mass of the fuel injected. It can also be observed that the EINO drop is higher at 9 kW power at the higher H_2 blends. This indicates that at lower powers (lower equivalence ratio) steam dilution and heat absorption effect is much stronger so that steam injection achieves stronger NO mitigation even after normalized for the amount of fuel burned. The results are more obvious with the EICO comparison, where EICO values for 9 kW flame with steam injection are too high that the rest of the results are not visible.

Overall these results indicate that steam injection is consistently successful at mitigating NO emissions, while it is comparatively better in lower power, lower equivalence ratio flames at the same steam level. This can be explained by the higher steam-to-fuel ratio in such cases, where steam causes more pronounced dilution in the flame where local incomplete combustion regions may occur. This results in emissions that indicate inefficient combustion like CO and CH_4 in high methane fraction blends. Theoretically the same inefficiencies may be present in H_2 flames also, but that can not be confirmed in the current set-up.

9.4. Series C: Variation in Steam Injection Amount

The third series of experiments focuses on the direct effect of varying steam injection rates while keeping the fuel composition and burner power fixed. Unlike Series A and B, where either the burner power or the fuel blend fraction was systematically changed, the objective here is to isolate the influence of steam mass flow on flame behavior and emissions. This provides a clearer understanding of how the magnitude of steam injection impacts NO formation, combustion efficiency, and overall flame stability.

Experiment-C1: Steam-7 and 9 Injection at constant 10 kW Power

In Experiment-C1, the burner was operated with constant power of 10 kW and total air injection of 250 nlpm with H_2 blend vary from 10% to 100%. Alongside no-steam reference points, 2 steam levels were used: steam-7 [17.7 g/min] and steam-9 [24.4 g/min]. By comparing these conditions under otherwise identical operating points, the experiment provides a direct measure of the sensitivity of NO emissions and other exhaust species to the injected steam quantity.

It should be noted that certain points in the experimental matrix are missing due to time constraints in the lab. For example, the steam-7 case for the 10% H_2 blend could not be tested, and the 0% H_2 case was not included in this campaign at all. Nevertheless, the available results, namely what's available for 10% H_2, are presented here as they still provide meaningful insight into the influence of steam injection on flame behavior and emissions trends.

The NO emissions results for Experiment-C1 is presented below in Table 9.14 and Figure 9.15:

H_2 Blend [%]	AAI [%]	$\phi \pm 0.015$	Steam	NO (ppm, *dry*) (wet in parentheses)	Dry reduction vs No-Steam	
					Abs [ppm]	%
10	0	0.635	No-Steam	2.12 (1.85 wet)	—	—
			Steam-9	0.63 (0.49 wet)	1.50	70.50
20	0	0.631	No-Steam	2.57 (2.23 wet)	—	—
			Steam-7	0.82 (0.66 wet)	1.74	67.97
			Steam-9	0.73 (0.57 wet)	1.84	71.54
30	0	0.626	No-Steam	3.11 (2.69 wet)	—	—
			Steam-7	1.91 (1.53 wet)	1.20	38.45
			Steam-9	1.66 (1.29 wet)	1.45	46.61
40	0	0.620	No-Steam	4.89 (4.21 wet)	—	—
			Steam-7	3.72 (2.96 wet)	1.17	23.93
			Steam-9	0.99 (0.77 wet)	3.89	79.64
50	0	0.613	No-Steam	6.51 (5.58 wet)	—	—
			Steam-7	2.26 (1.79 wet)	4.25	65.30
			Steam-9	2.05 (1.58 wet)	4.46	68.49
60	10	0.604	No-Steam	6.60 (5.61 wet)	—	—
			Steam-7	3.27 (2.57 wet)	3.33	50.46
			Steam-9	2.35 (1.80 wet)	4.24	64.31
70	10	0.593	No-Steam	14.73 (12.42 wet)	—	—
			Steam-7	12.54 (9.78 wet)	2.19	14.87
			Steam-9	11.66 (8.84 wet)	3.08	20.87
80	15	0.579	No-Steam	16.98 (14.14 wet)	—	—
			Steam-7	12.65 (9.75 wet)	4.33	25.48
			Steam-9	9.43 (7.07 wet)	7.55	44.44
100	15	0.529	No-Steam	12.78 (10.22 wet)	—	—
			Steam-7	10.25 (7.60 wet)	2.52	19.75
			Steam-9	8.94 (6.45 wet)	3.83	30.00

Table 9.14: NO emissions for Experiment C1. Constant 10 kW burner power with varying H_2 fuel fraction and steam injection level (Steam-7 = 17.7 g/min, Steam-9 = 24.4 g/min). Values reported on a dry basis; analyzer wet readings are shown in parentheses. Dry conversion via Equation 8.5.

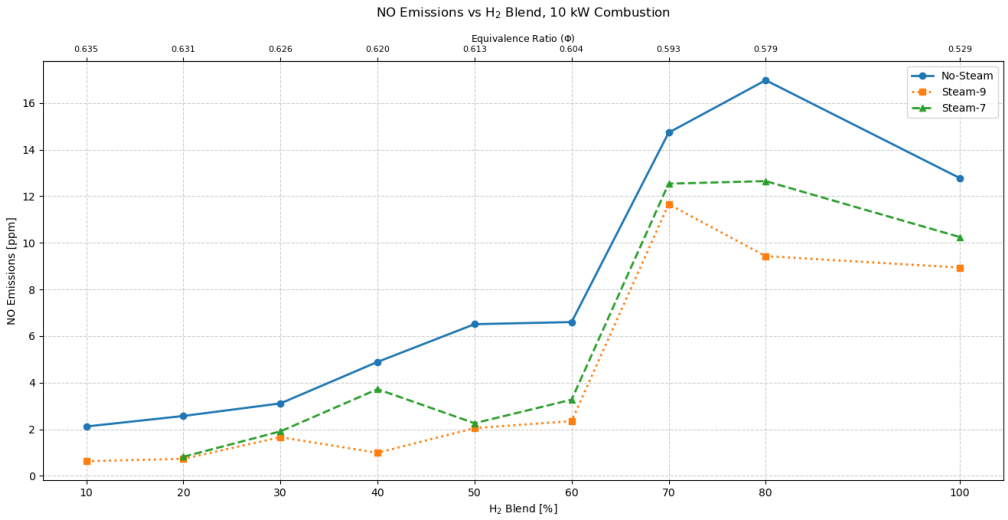


Figure 9.15: Experiment-C1: NO (dry) vs H_2 blend fraction at 10 kW with and without side steam injection (Steam 7 = 17.7 g/min; Steam 9 = 24.4 g/min). The upper axis shows the corresponding equivalence ratio ϕ.

The no-steam reference cases show a similar trend to Experiments B1 and B2, with NO emissions increasing as the H_2 fraction in the fuel rises. With the introduction of AAI, this increase becomes less linear, and a drop in NO is observed again at the 100% H_2 blend. This behavior can be attributed to the redistribution of air into an axial jet, which penetrates the swirling flow and weakens the central recirculation zone (CRZ). By accelerating the flow through the core, the axial jet reduces the residence time of hot gases within the CRZ, where peak temperatures and thermal NO formation are typically sustained. As a result, thermal NO production decreases, consistent with observations in swirl-stabilized flames [110].

With steam injection, NO emissions are once again reduced in all H_2 blend levels in both steam injection levels, and the trend seen in no-steam case is mostly preserved. Looking at the difference in NO emissions at different steam injection levels, the data suggests that the higher steam injection of steam 9 (24.2 g/min) resulted in more NO reductions compared to the relatively lower steam injection of steam 7 (17.7 g/min). However, in certain points the difference is very significant, while at some points the difference is very mininal. For example, at 40% H_2 steam 7 reduces NO emissions by 24% while steam 9 achieves 80% reduction. On the other hand, at 50% the reductions in NO emissions are very similar with 65 and 68% decrease in steam 7 and 9 respectively.

The data suggests that the effect of steam injection amount on NO mitigation is not entirely consistent. While some points indicate a clear advantage of the higher steam flow, others show only marginal differences between the two levels. From a theoretical perspective, a larger amount of injected steam should enhance the heat-sink effect, provide stronger dilution of reactive species, and therefore suppress NO formation more effectively. The fact that this expected trend is not uniformly observed may be linked to flame instabilities, uneven distribution of the injected steam, or experimental limitations such as fluctuations in steam delivery and mixing within the burner.

To better understand the dynamics of amount of steam injection, the full emissions table for Experiment-C1 is provided below in Table 9.15:

H_2 Blend [%]	AAI [%]	$\phi \pm 0.015$	Steam	NO (ppm, *dry*) (wet in parentheses)	O_2 [%]	CO [ppm]	CH_4 [ppm]	CO_2 [%]
10	0	0.635	No-Steam	2.12 (1.85 wet)	7.69	0.00	10.23	7.34
			Steam-9	0.63 (0.49 wet)	7.78	390.46	116.02	7.24
20	0	0.631	No-Steam	2.57 (2.23 wet)	7.99	0.00	1.11	6.92
			Steam-7	0.82 (0.66 wet)	7.99	102.53	16.16	6.92
			Steam-9	0.73 (0.57 wet)	8.02	238.26	55.37	6.90
30	0	0.626	No-Steam	3.11 (2.69 wet)	8.13	0.00	0.35	6.62
			Steam-7	1.91 (1.53 wet)	8.06	35.10	3.75	6.69
			Steam-9	1.66 (1.29 wet)	8.11	161.95	33.22	6.62
40	0	0.620	No-Steam	4.89 (4.21 wet)	8.27	0.00	0.33	6.26
			Steam-7	3.72 (2.96 wet)	8.20	4.01	5.03	6.34
			Steam-9	0.99 (0.77 wet)	8.23	70.52	8.83	6.27
50	0	0.613	No-Steam	6.51 (5.58 wet)	8.47	0.00	0.01	5.81
			Steam-7	2.26 (1.79 wet)	8.49	0.66	0.25	5.83
			Steam-9	2.05 (1.58 wet)	8.42	12.76	0.91	5.83
60	10	0.604	No-Steam	6.60 (5.61 wet)	9.27	0.00	0.00	5.01
			Steam-7	3.27 (2.57 wet)	9.25	79.74	2.84	5.01
			Steam-9	2.35 (1.80 wet)	9.30	231.53	13.29	4.97
70	10	0.593	No-Steam	14.73 (12.42 wet)	9.54	0.00	0.08	4.33
			Steam-7	12.54 (9.78 wet)	9.48	1.67	0.10	4.34
			Steam-9	11.66 (8.84 wet)	9.48	6.58	0.33	4.34
80	15	0.579	No-Steam	16.98 (14.14 wet)	9.81	0.00	0.00	3.43
			Steam-7	12.65 (9.75 wet)	9.83	0.00	0.11	3.42
			Steam-9	9.43 (7.07 wet)	9.85	0.00	0.14	3.42
100	15	0.529	No-Steam	12.78 (10.22 wet)	11.35	0.00	0.00	0.00
			Steam-7	10.25 (7.60 wet)	11.33	0.00	0.00	0.00
			Steam-9	8.94 (6.45 wet)	11.30	0.00	0.00	0.00

Table 9.15: Full emissions for Experiment C1. Constant 10 kW burner power with varying H_2 fuel fraction and steam injection level (Steam-7 = 17.7 g/min, Steam-9 = 24.4 g/min). Values reported on a *dry* basis for NO; analyzer wet readings are shown in parentheses. O_2, CO, CH_4, and CO_2 are measured dry by the analyzer. Dry conversion via Equation 8.5. Side steam injection configuration was used.

The full emissions table provide some strong evidence on the dilution effect of different steam injection levels. At lower H_2 blends, both the CO emissions and the $CH4_4$ rise with increasing steam injection levels. This clear difference between steam 9 and steam 7 for CO and CH_4 indicate that the difference in steam injection amount does result in significant effects on flame dynamics and emissions. Even in points such as 20, 30 and 60% where the difference in NO emissions between different steam injection levels were small, there is significant difference in CO and CH_4 between the levels. This can be interpreted as further evidence on the dilution effect of steam causing local regions of incomplete combustion. As the steam injection amount gets lower, these regions also decrease in size, which result in less incomplete combustion products like CO and CH_4.

Additionally, O_2 and CO_2 emissions act as expected between vary H_2 levels, and consequently equivalence ratio change. There is negligible change in O_2 and CO_2 emissions between steam injection amounts, so steam injection does no result in any unexpected results in these species.

One interesting result appears in the 60% H_2 case, where both CO and trace CH_4 emissions rise sharply compared to the neighboring blend fractions. This can be linked to the use of axial air injection at this operating point, which accelerates the core flow and reduces the residence time of the reacting gases in the central recirculation zone (CRZ). Similar behavior has been noted in previous studies with the same burner, where AAI was found to push the flame downstream and weaken the central recirculation zone. As a result, the flame no longer anchors tightly near the nozzle along the centerline but instead stabilizes further downstream in the outer shear layers, leaving a relatively cold and unreactive core. This change shortens the exposure of gases to high temperatures and can lead to incomplete burnout and higher CO

when large AAI fractions are used [113, 110, 114]. Combined with the lower flame temperature at $\phi \approx 0.60$ and the additional cooling effect of steam, this shortened residence time limits CO to CO_2 oxidation, while local stratification and quench pockets further promote incomplete combustion. These effects together provide a plausible explanation for the anomalous increase in CO and CH_4 emissions observed at this condition.

The derived emissions metrics, are presented below in Table 9.16 and Figure 9.16:

H_2 [%]	ϕ	Steam	NO				CO			
			(dry) [ppm]	@15% O_2 [ppm]	EINO [mg/MJ]	EINO [g/kg]	(dry) [ppm]	@15% O_2 [ppm]	EICO [mg/MJ]	EICO [g/kg]
10	0.635	No-Steam	2.12	0.95	1.101	0.056	0.00	0.00	0.000	0.000
		Steam-9	0.63	0.34	0.378	0.020	390.46	176.40	189.340	9.652
20	0.631	No-Steam	2.32	1.07	1.203	0.063	0.00	0.00	0.000	0.000
		Steam-7	0.91	0.42	0.472	0.025	102.53	47.07	49.623	2.588
		Steam-9	0.79	0.36	0.410	0.021	238.26	109.64	115.309	6.013
30	0.626	No-Steam	3.11	1.44	1.610	0.086	0.00	0.00	0.000	0.000
		Steam-7	1.91	0.88	0.988	0.053	50.39	23.29	24.241	1.288
		Steam-9	1.66	0.77	0.859	0.046	55.07	25.46	26.500	1.409
40	0.620	No-Steam	4.89	2.29	2.526	0.140	0.00	0.00	0.000	0.000
		Steam-7	3.72	1.74	1.921	0.106	85.49	40.36	41.905	2.297
		Steam-9	0.99	0.46	0.511	0.028	149.41	70.41	73.098	4.059
50	0.613	No-Steam	6.51	3.10	3.352	0.194	0.00	0.00	0.000	0.000
		Steam-7	2.26	1.08	1.164	0.067	260.14	127.20	130.656	7.553
		Steam-9	2.05	0.97	1.055	0.061	400.43	196.27	201.644	11.655
60	0.604	No-Steam	6.60	3.36	3.388	0.207	4.96	2.75	2.661	0.163
		Steam-7	3.27	1.66	1.678	0.103	287.58	156.71	157.947	9.730
		Steam-9	2.35	1.20	1.206	0.074	508.11	272.89	266.266	16.454
70	0.593	No-Steam	14.73	7.68	7.523	0.496	0.00	0.00	0.000	0.000
		Steam-7	12.54	6.51	6.404	0.422	0.00	0.00	0.000	0.000
		Steam-9	11.66	6.05	5.954	0.392	0.00	0.00	0.000	0.000
80	0.579	No-Steam	16.98	9.09	8.607	0.632	0.00	0.00	0.000	0.000
		Steam-7	12.65	6.77	6.411	0.471	0.00	0.00	0.000	0.000
		Steam-9	9.43	5.05	4.779	0.351	0.00	0.00	0.000	0.000
100	0.529	No-Steam	12.78	7.92	6.344	0.761	0.00	0.00	0.000	0.000
		Steam-7	10.25	6.34	5.087	0.610	0.00	0.00	0.000	0.000
		Steam-9	8.94	5.51	4.437	0.532	0.00	0.00	0.000	0.000

Table 9.16: Experiment C1. O_2-normalized and derived NO and CO metrics (*dry*) as described in Section 8.4.

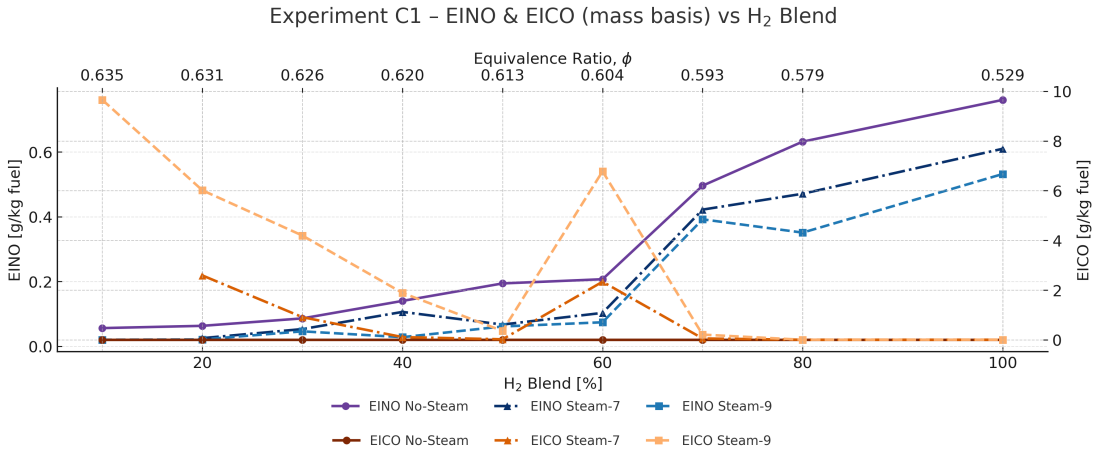


Figure 9.16: Experiment C1. Comparison of derived emission indices (EINO and EICO) on a mass basis for various steam injection cases.

The derived metrics are once again in agreement with the raw emissions data provided. O_2 normalized values of NO and CO show the same trends as before, indicating the difference in results are not due to dilution of oxygen. EINO and EICO metrics also

The derived metrics confirm the trends observed in the raw analyzer readings. The O_2-normalized concentrations of NO and CO closely follow the same patterns, demonstrating that the observed changes cannot be attributed solely to differences in oxygen dilution. Likewise, the emission indices (EINO and EICO), which account for the amount of fuel and energy input, reinforce these findings and provide a consistent basis for comparing the different steam injection levels and fuel blends.

Experiment-C1 demonstrates that the steam injection strongly suppresses NO across the NO across the full range of hydrogen blends. The distinction between moderate and higher steam injection rates is clearly visible in some points but it is not consistent across the different H_2 blend test points. To further investigate the effect of different steam injection rates, the following experiments of C2 and D1 utilize a larger range of steam injection amounts. While Experiment-C1 indicates a noteworthy relation between the NO suppression and steam injection amount, the following experiments will provide a deeper insight to either confirm or refute the theory.

Experiment-C2: Steam-6, 7, 8 and 9 Injection at constant 10 kW Power

As previously mentioned, Experiment-C2 intends to provide a deeper insight on the effect of steam injection amount. To do this, only 3 H_2 blend fractions were chosen: 40, 60, and 80% H_2. Additionally, the whole available commissioned range of steam injection amounts were used: Steam-6 = 13.7 g/min, Steam-7 = 17.7 g/min, Steam-8 = 22.8 g/min and Steam-9 = 24.4 g/min.

The NO emissions results for Experiment-C2 is presented below in Table 9.17 and Figure 9.17:

H_2 Blend [%]	AAI [%]	$\phi \pm$ 0.013	Steam	NO (ppm, *dry*) (wet in parentheses)	Dry reduction	
					NO Drop [ppm]	%
40	0	0.620	No-Steam	4.60 (3.96 wet)	—	—
			Steam-6	3.38 (2.74 wet)	1.22	26.5
			Steam-7	3.40 (2.71 wet)	1.20	26.1
			Steam-8	3.09 (2.41 wet)	1.51	32.8
			Steam-9	3.05 (2.36 wet)	1.55	33.7
60	10	0.604	No-Steam	6.66 (5.70 wet)	—	—
			Steam-6	3.96 (3.20 wet)	2.70	40.5
			Steam-7	2.43 (1.93 wet)	4.23	63.5
			Steam-8	1.07 (0.83 wet)	5.59	83.9
			Steam-9	1.54 (1.19 wet)	5.12	76.9
80	15	0.579	No-Steam	15.41 (13.04 wet)	—	—
			Steam-6	11.21 (8.97 wet)	4.20	27.3
			Steam-7	10.77 (8.48 wet)	4.64	30.1
			Steam-8	10.98 (8.48 wet)	4.43	28.7
			Steam-9	10.40 (7.98 wet)	5.01	32.5

Table 9.17: NO emissions for Experiment C2. Constant 10 kW burner power with varying H_2 fuel fraction and steam injection level (Steam-6 = 13.7 g/min, Steam-7 = 17.7 g/min, Steam-8 = 22.8 g/min, Steam-9 = 24.4 g/min). Side steam injection configuration was used. Values reported on a dry basis; analyzer wet readings are shown in parentheses. Dry conversion via Equation 8.5.

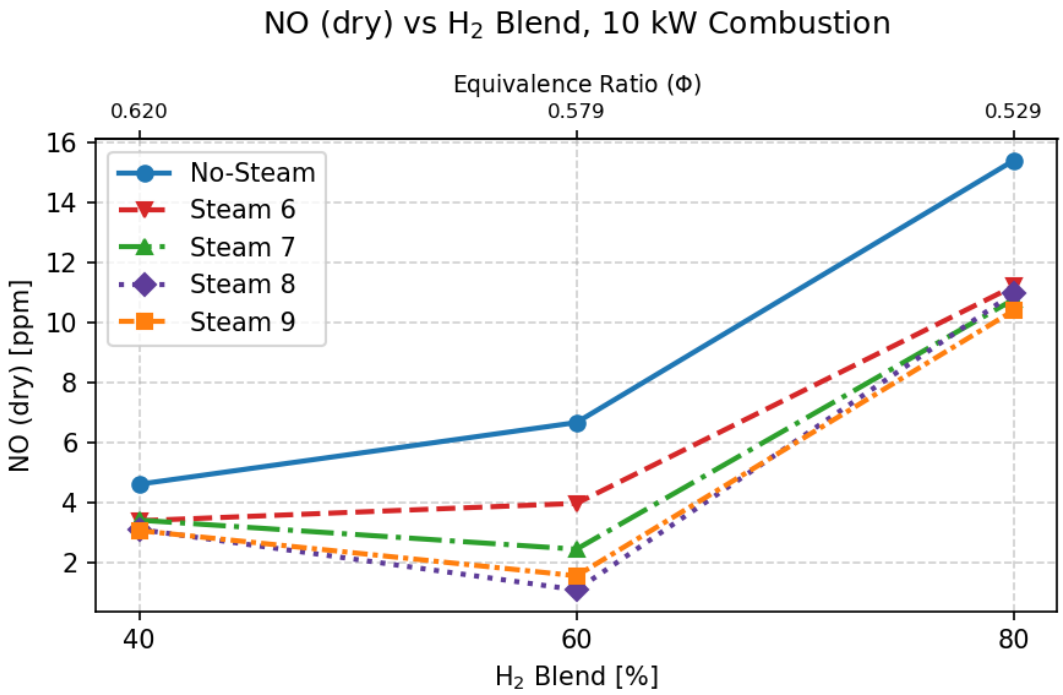


Figure 9.17: Experiment-C2: NO (dry) vs H_2 blend fraction at 10 kW with and without side steam injection (Steam 6 = 13.7 g/min; Steam 7 = 17.7 g/min; Steam 8 = 22.8 g/min; Steam 9 = 24.4 g/min). The upper axis shows the corresponding equivalence ratio ϕ.

The no-steam reference cases follow a similar trend to what has been observed in the previous experiments. NO emissions increase as the H_2 fraction rises from 40% to 80%. The higher hydrogen content intensifies the flame chemistry by producing larger amounts of reactive radicals (O, H, OH). This accelerates the thermal NO formation pathways and results in higher NO levels despite the modest drop in adiabatic flame temperature shown by Cantera simulation results [112].

The effect of steam injection amount shows a limited but discernible influence, with the extent of additional NO reduction depending on the hydrogen blend fraction. The trend is very clear in 60% H_2 blend, where with increasing steam injection there is a clear drop in NO emissions, between 40–77%. It is observed that in blends of 60 and 80% H_2, steam-8 (22.8 g/min) resulted in slightly more NO reductions than steam-9 (24.4 g/min). However, the wet NO reading difference between those points is within 0.50 ppm, which is susceptible to gas analyzer noise. Additionally, accounting for the uncertainties of steam injection amounts of around $\pm$0.4–0.6 g/min, any instability in the steam injection delivery may have contributed to the apparent crossover. However, looking at the overall trend of the lowest steam injection level of steam-6 (13.7 g/min) and comparing it to the higher steam injection levels of 8 and 9 (24.4 - 22.8 g/min), there is an observable difference in NO emissions levels, where increasing the steam injection amount resulted in lower NO emissions. Therefore, the results should be interpreted as indicating that higher steam injection generally promotes further NO reduction, while the small deviations between steam 8 and steam 9 are within the experimental uncertainty.

The full emissions table of Experiment-C2 is provided below in Table 9.18 to investigate the effect of different steam injection amounts on other emissions species:

H_2 Blend [%]	AAI [%]	$\phi \pm 0.013$	Steam	NO (ppm, *dry*) (wet in parentheses)	O_2 [%]	CO [ppm]	CH_4 [ppm]	CO_2 [%]
40	0	0.620	No-Steam	4.60 (3.96 wet)	7.93	0.00	0.19	6.48
			Steam-6	3.38 (2.74 wet)	7.93	0.00	0.78	6.48
			Steam-7	3.40 (2.71 wet)	7.93	0.00	0.95	6.47
			Steam-8	3.09 (2.41 wet)	7.95	5.42	0.85	6.46
			Steam-9	3.05 (2.36 wet)	7.96	11.76	1.11	6.46
60	10	0.579	No-Steam	6.66 (5.70 wet)	8.64	0.00	0.26	5.35
			Steam-6	3.96 (3.20 wet)	8.69	0.00	0.23	5.32
			Steam-7	2.43 (1.93 wet)	8.69	1.94	0.11	5.32
			Steam-8	1.07 (0.83 wet)	8.70	18.88	0.66	5.31
			Steam-9	1.54 (1.19 wet)	8.69	25.18	1.12	5.32
80	15	0.529	No-Steam	15.41 (13.04 wet)	9.39	0.00	0.00	3.66
			Steam-6	11.21 (8.97 wet)	9.39	0.00	0.05	3.66
			Steam-7	9.84 (7.75 wet)	9.40	0.00	0.22	3.66
			Steam-8	10.98 (8.48 wet)	9.40	0.00	0.40	3.66
			Steam-9	10.40 (7.98 wet)	9.40	0.00	0.18	3.66

Table 9.18: Full emissions for Experiment C2. Constant 10 kW burner power with varying H_2 fuel fraction and steam injection level (Steam-6 = 13.7 g/min, Steam-7 = 17.7 g/min, Steam-8 = 22.8 g/min, Steam-9 = 24.4 g/min). Values reported on a *dry* basis for NO; analyzer wet readings are shown in parentheses. O_2, CO, CH_4, and CO_2 are measured dry by the analyzer. Dry conversion via Equation 8.5.

The full emissions data provide additional context to the NO results by showing the accompanying O_2, CO, CH_4, and CO_2 levels. Across all three blend fractions, O_2 and CO_2 behave as expected, with only small variations between the different steam injection levels, confirming that the changes in NO are not simply due to shifts in oxygen availability. At 40% and 80% H_2, CO and CH_4 remain close to zero, indicating stable and complete combustion. In contrast, at 60% H_2 the introduction of higher steam flows leads to a noticeable rise in CO and trace CH_4, consistent with the earlier observation that axial air injection combined with steam can shorten residence times and promote incomplete burnout. Overall, the full emissions measurements support the interpretation that steam injection primarily reduces NO formation, while only under certain blend conditions (notably 60% H_2) it also leads to measurable increases in incomplete combustion products.

When comparing the full emissions data of C2 with the corresponding points in C1, noticeable differences in CO and trace CH_4 levels emerge, even though the operating power, steam rates, and AAI settings were nominally identical. These discrepancies are most likely linked to small variations in flame dynamics between the two experimental days. Since steam was supplied through the two side ports, slight differences in jet penetration or mixing efficiency could have produced local pockets of over- or under-dilution, which in turn influence the completeness of CO and CH_4 burnout. Moreover, the reacting system at $\phi \approx 0.60$ is inherently sensitive to instabilities, and minor changes in boundary conditions can shift the flame stabilization and residence times. While part of the variation is within the uncertainty band of the analyzer at such low concentrations, the consistent observation of elevated CO/CH_4 in C1 suggests that these results capture a real flame behavior rather than pure measurement noise.

Next, the derived emissions metrics of Experiment-C2 are presented below:

H_2 [%]	ϕ	Steam	NO				CO			
			(dry) [ppm]	@15% O_2 [ppm]	EINO [mg/MJ]	EINO [g/kg]	(dry) [ppm]	@15% O_2 [ppm]	EICO [mg/MJ]	EICO [g/kg]
40	0.620	No-Steam	4.60	2.10	2.376	0.132	0.00	0.00	0.000	0.000
		Steam-6	3.38	1.54	1.746	0.097	0.00	0.00	0.000	0.000
		Steam-7	3.40	1.55	1.756	0.097	0.00	0.00	0.000	0.000
		Steam-8	3.09	1.41	1.596	0.088	5.42	2.61	2.613	0.145
		Steam-9	3.05	1.40	1.575	0.087	11.76	5.39	5.669	0.314
60	0.579	No-Steam	6.66	3.22	3.579	0.219	0.00	0.00	0.000	0.000
		Steam-6	3.96	1.92	2.128	0.130	0.00	0.00	0.000	0.000
		Steam-7	2.43	1.18	1.306	0.080	1.94	0.97	0.973	0.059
		Steam-8	1.07	0.52	0.575	0.035	18.88	9.47	9.469	0.579
		Steam-9	1.54	0.75	0.827	0.051	25.18	12.22	12.628	0.772
80	0.529	No-Steam	15.41	7.93	8.622	0.633	0.00	0.00	0.000	0.000
		Steam-6	11.21	5.77	6.272	0.460	0.00	0.00	0.000	0.000
		Steam-7	10.77	5.07	5.505	0.404	0.00	0.00	0.000	0.000
		Steam-8	10.98	5.66	6.143	0.451	0.00	0.00	0.000	0.000
		Steam-9	10.40	5.36	5.818	0.427	0.00	0.00	0.000	0.000

Table 9.19: Experiment C2. O_2-normalized and derived NO and CO metrics (*dry*) computed from analyzer readings.

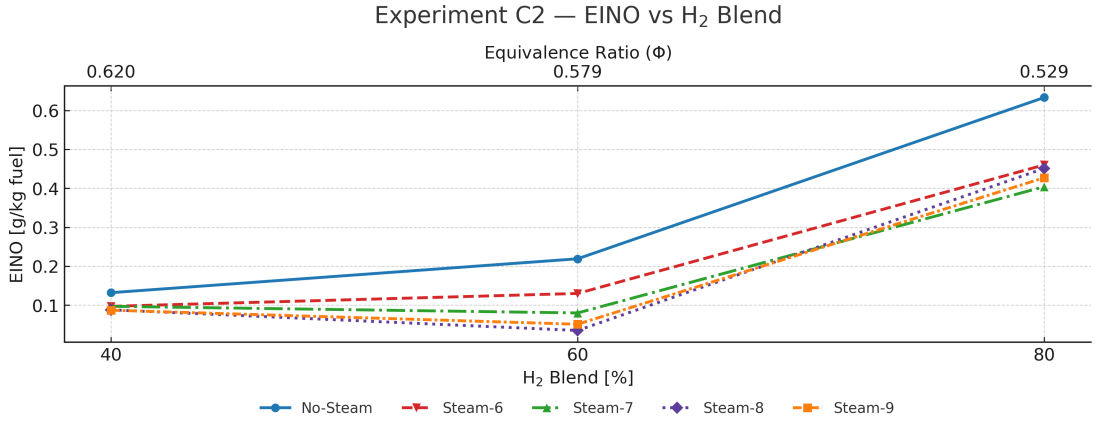


Figure 9.18: Experiment C2. Comparison of EINO on a mass basis for various steam injection cases.

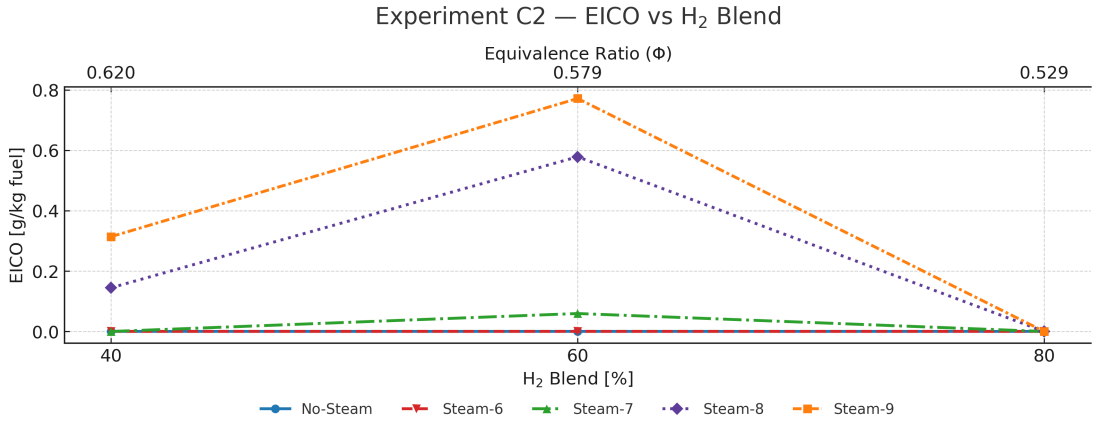


Figure 9.19: Experiment C2. Comparison of EICO on a mass basis for various steam injection cases.

The derived emissions metrics for Experiment C2 confirm the trends observed in the raw data. O_2-

normalized NO values and the calculated EINO metrics decrease with increasing steam injection across all three H_2 blends. Similarly, EICO results reiterate the notion that steam injection increases the CO emissions in high CH_4 fraction blends, likely due to local zones of incomplete combustion due to its dilution effect.

To complement these quantitative results, UV image sequences of the same operating points are examined. They provide a visual perspective on how steam injection modifies flame structure and luminosity at 40, 60, and 80% H_2, offering direct context for the observed changes in NO and CO emissions.

The UV image sequences in Figure 9.20 to Figure 9.22 present the 10 kW flames with side steam injection at 40, 60, and 80% H_2 for the cases No-Steam, Steam–6, Steam–7, Steam–8, and Steam–9. All frames were recorded under identical optical settings (gain and exposure time), ensuring that relative intensities can be directly compared across steam levels. The applied colormap is purely a visualization aid; the discussion focuses on relative intensity and flame structure. These images provide a qualitative complement to the emissions data, allowing changes in flame anchoring, luminosity, and shape to be directly linked to the observed NO and CO trends.

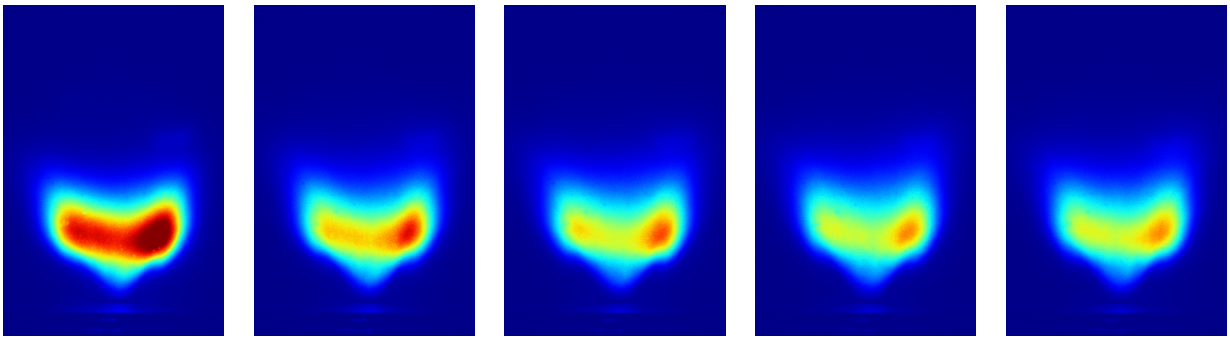


Figure 9.20: UV imaging of 10 kW 40% H2 blend flame under different steam injection settings.

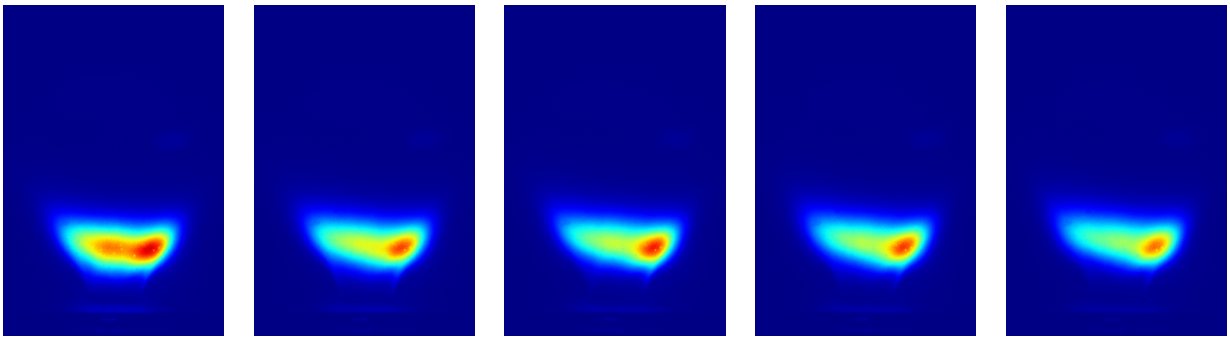


Figure 9.21: UV imaging of 10 kW 60% H2 blend flame under different steam injection settings.

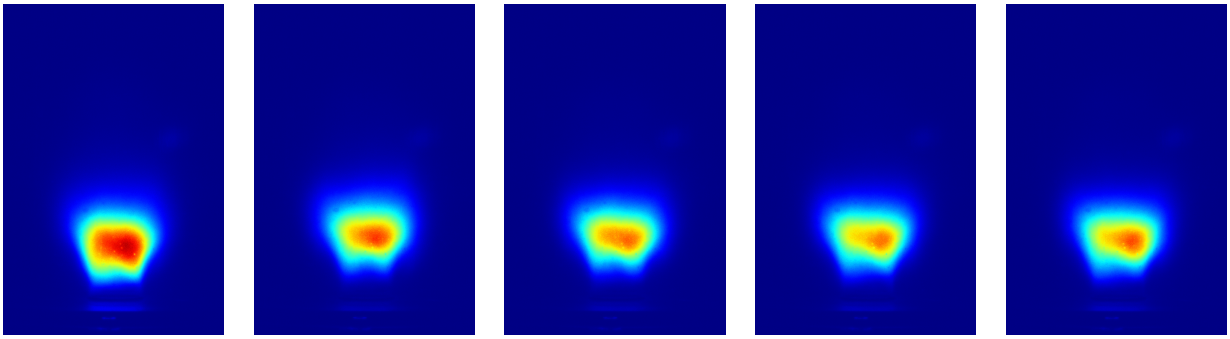


Figure 9.22: UV imaging of 10 kW 80% H2 blend flame under different steam injection settings.

The 40% H_2 blend shows the broadest UV envelope and the most pronounced structural response to steam addition. The no-steam flame is compact and anchored close to the nozzle with a relatively straight front. With increasing steam, the flame envelope broadens laterally, the front edges curve inward toward the centerline, and the apparent lift-off height increases by a few millimeters. This upward shift of the luminous region and modest increase in axial extent indicate reduced flame speeds under dilution [63], together with a weakened radical pool. The strongest evidence of this effect is the progressive dimming of OH^* emission with steam addition, which signifies reduced heat release and lower local flame temperatures. Since thermal NO formation is exponentially sensitive to temperature, this visible decrease in luminosity provides a clear counterpart to the measured NO reductions in Table 9.17 and the corresponding EINO decrease in Table 9.19.

At 60% H_2 no-steam, the flame is compact and intense, with OH^* emission concentrated near the nozzle. Unlike the 40% H_2 case, a distinct lift-off is not observable, likely due to the faster burning dynamics of hydrogen that help keep the flame anchored even under dilution. Adding steam (Steam–6 to 9) produces a clear monotonic reduction in integrated UV intensity, accompanied by a subtle narrowing of the bright core and a slight upward shift of the centroid. Although the structural changes are modest compared to the 40% case, the strong dimming of OH^* provides clear evidence of reduced radical concentrations and lower peak flame temperatures. This trend is consistent with the steep NO reductions in Table 9.17 and the corresponding drop in EINO in Table 9.19, while the simultaneous rise in CO and CH_4 suggests that dilution and shorter residence times hinder complete oxidation at this blend fraction.

The 80% H_2 no-steam flame is compact, bright, and tightly anchored at the nozzle. With increasing steam, no clear elongation is observed; instead, the most noticeable change is a monotonic reduction in luminosity, particularly near the flame root. This region is closest to the side steam injection ports, suggesting that local quenching and dilution effects are strongest there. The compactness of the flame at this high hydrogen fraction likely limits how effectively the injected steam can penetrate into the deeper reaction zones, reducing its overall impact compared to lower H_2 blends. This interpretation is consistent with the emissions data, where NO reductions are present but less pronounced than at 60% H_2, and CO levels remain negligible across all steam rates. The smaller overall change in luminosity, as well as the smaller differences between steam injection levels, further support this reduced sensitivity, in line with the modest NO reductions reported in Table 9.17 and the corresponding EINO trends in Table 9.19.

These results can be explained by the physical effects of steam on flame dynamics and chemistry. The UV camera records OH^* chemiluminescence at 309 nm, which serves as a marker of high heat release zones and radical activity near stoichiometric layers [11, 63]. Steam addition reduces OH^* chemiluminescence intensity and reshapes the flame through coupled mechanisms. Firstly, the high specific heat capacity of steam lowers the adiabatic flame temperature, suppressing thermal NO formation. Secondly, dilution decreases reactant partial pressures and laminar burning velocity, weakening flame anchoring and slowing reaction rates [11]. Thirdly, collisional quenching reduces the lifetime of excited OH^* species, directly diminishing observed luminosity. Finally, steam alters radical chemistry by promoting recombination and third-body stabilization, for instance through $H + O_2 + M \rightarrow HO_2 + M$ and $OH + H + M \rightarrow H_2O + M$, while suppressing chain-branching reactions such as $H + O_2 \rightarrow O + OH$ [115, 11]. The combined outcome is a reduction in the pool of reactive radicals (O, H, OH), weaker heat release, and progressively dimmer and more concave flames with increasing steam.

Taken together, the results of Experiment-C2 confirm and extend the main findings of the C-series. Steam consistently suppresses NO formation across all blends, with the most pronounced relative reductions observed at intermediate hydrogen fractions. At lower H_2 contents, the absolute NO levels are already modest, so the effect of additional steam remains limited in scope. At very high H_2 fractions, the flames become increasingly compact, and the side-injected steam is less able to penetrate the hot reaction zones, leading to smaller relative reductions. The intermediate blends therefore represent a regime where baseline NO levels are sufficiently high and flame structure sufficiently open for steam dilution and heat capacity effects to produce the clearest distinction. CO and CH_4 responses further highlight the role of local mixing and residence time in shaping emissions, particularly under AAI operation. Overall, the C-series demonstrates that while steam injection is a robust strategy for NO control, its effectiveness depends strongly on hydrogen fraction and on the flow-field configuration (i.e., the axial/swirl air split).

Overall, the C-series demonstrates that while steam injection is a robust strategy for NO control, its effectiveness depends strongly on hydrogen fraction and on the flow-field configuration (i.e., the axial/swirl air split).

9.5. Series D: Variation in Steam Injection Location

The D-series focuses on the role of steam injection location in shaping emissions and flame structure. In the previous experiments steam was introduced through two side ports downstream of the burner exit. In contrast, the D-series investigates axial injection through the burner's centerline. This comparison provides insight into whether injection geometry alters the effectiveness of steam as a diluent and coolant, and how it influences flame anchoring and burnout behavior.

Experiment-D1: Axial steam injection with constant 10 kW Power

Experiment D1 forms the sole test case in this series. It was conducted at 10 kW burner power with five selected H_2 blend fractions (40, 50, 60, 70, and 80%) and four steam injection levels (Steam–6 = 13.7 g/min, Steam–7 = 17.7 g/min, Steam–8 = 22.8 g/min, Steam–9 = 24.4 g/min). Unlike the previous experiments, where steam was injected from the side ports, here all steam was introduced axially through the burner centerline. Axial air injection (AAI) was kept at 0% throughout due to set-up constraints. This configuration enables a direct comparison to the side injection cases, highlighting whether axial delivery into the flame core produces stronger or weaker impacts on NO reduction and flame behavior.

The NO emissions results for Experiment-D1 is provided below in Table 9.20 and Table 9.20:

H_2 Blend [%]	AAI [%]	$\phi \pm$ 0.014	Steam	NO (ppm, *dry*) (wet in parentheses)	Dry reduction	
					NO Drop [ppm]	%
40	0	0.620	No-Steam	4.83 (4.13 wet)	—	—
			Steam-6	2.21 (1.77 wet)	2.62	54.2
			Steam-7	1.89 (1.49 wet)	2.94	60.9
			Steam-8	1.36 (1.05 wet)	3.47	71.8
			Steam-9	1.24 (0.95 wet)	3.59	74.3
50	0	0.613	No-Steam	5.52 (4.72 wet)	—	—
			Steam-6	3.00 (2.41 wet)	2.52	45.7
			Steam-7	2.62 (2.07 wet)	2.90	52.5
			Steam-8	2.04 (1.58 wet)	3.48	63.0
			Steam-9	1.77 (1.36 wet)	3.75	67.9
60	0	0.604	No-Steam	14.04 (11.99 wet)	—	—
			Steam-6	8.14 (6.55 wet)	5.90	42.0
			Steam-7	6.90 (5.46 wet)	7.14	50.9
			Steam-8	3.29 (2.55 wet)	10.75	76.6
			Steam-9	3.03 (2.33 wet)	11.01	78.4
70	0	0.593	No-Steam	14.57 (12.42 wet)	—	—
			Steam-6	9.82 (7.91 wet)	4.75	32.6
			Steam-7	8.98 (7.12 wet)	5.59	38.4
			Steam-8	7.33 (5.69 wet)	7.24	49.7
			Steam-9	7.00 (5.40 wet)	7.57	52.0
80	0	0.579	No-Steam	16.64 (14.14 wet)	—	—
			Steam-6	6.83 (5.50 wet)	9.81	59.0
			Steam-7	6.33 (5.02 wet)	10.31	62.0
			Steam-8	5.48 (4.26 wet)	11.16	67.1
			Steam-9	5.16 (3.99 wet)	11.48	69.0

Table 9.20: NO emissions for Experiment D1. Constant 10 kW burner power with varying H_2 fuel fraction and steam injection level (Steam-6 = 13.7 g/min, Steam-7 = 17.7 g/min, Steam-8 = 22.8 g/min, Steam-9 = 24.4 g/min). Values reported on a *dry* basis; analyzer wet readings are shown in parentheses. Dry conversion via Equation 8.5. Axial steam injection configuration was used.

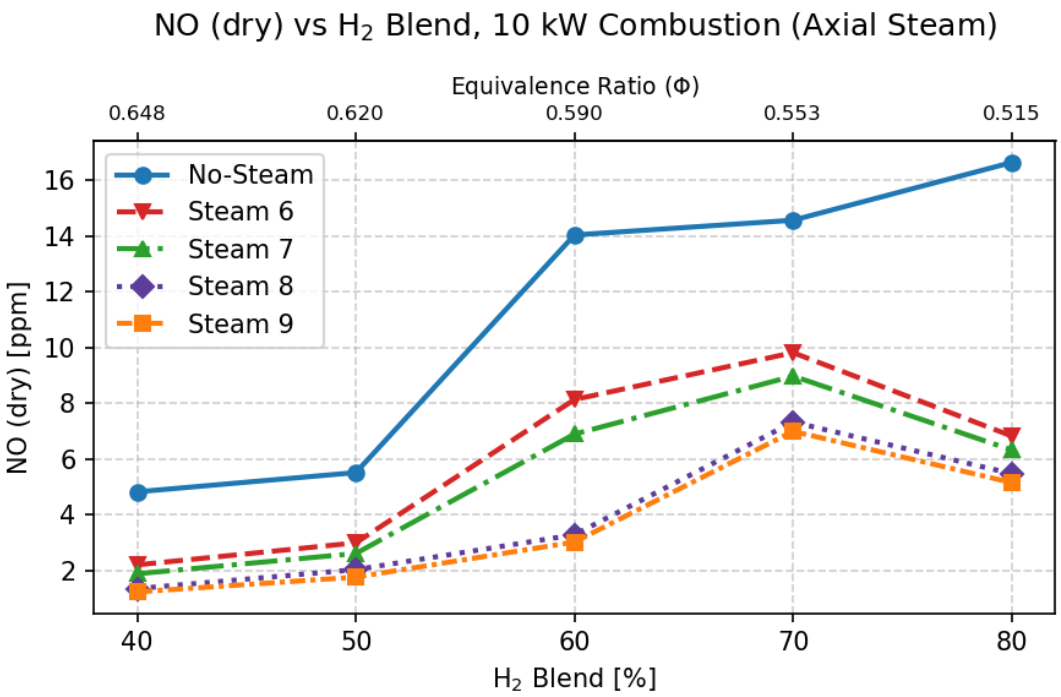


Figure 9.23: Experiment-D1: NO (dry) vs H_2 blend fraction at 10 kW with and without axial steam injection (Steam 6 = 13.7 g/min; Steam 7 = 17.7 g/min; Steam 8 = 22.8 g/min; Steam 9 = 24.4 g/min). The upper axis shows the corresponding equivalence ratio ϕ.

Without steam injection, the NO emissions trend is similar to the trends observed in the previous experiments. One major difference is the consistent increase of NO emissions with increasing H_2 blend fraction. In the previous experiments in B and C series, when the axial air injection was present, the points from 60% showed inconsistent NO emission behavior. This provides further evidence on the effect of AAI in NO emissions and flame dynamics, highlighting how it can alter flame stabilization and residence time in a way that decouples NO formation from the expected monotonic dependence on hydrogen content.

Introducing steam through the axial channel suppresses NO at all hydrogen fractions, with the degree of reduction scaling predictably with injection amount. At low blends (40–50% H_2), NO falls by roughly 50–70% depending on the steam rate, showing a clear progression as injection is increased. The effect is most pronounced at 60% H_2, where each step in steam flow yields a distinct drop and overall reductions reach almost 80%. At higher hydrogen fractions (70–80% H_2), absolute decreases remain substantial, but the percentage reductions narrow to about 30–70% and the steam levels cluster closer together. Even so, small but consistent differences between Steam-8 and Steam-9 confirm that the flame remains sensitive to incremental changes in injection.

It has been firmly established across the earlier experiments that steam injection into CH_4–H_2 flames leads to a clear and significant reduction in NO emissions. The objective of Experiment D1 is to assess the effect of axial steam injection in comparison to the side injection configuration. For a meaningful evaluation, comparisons must be made at identical operating points (burner power, ϕ, fuel blend, total air input, and steam injection level). Two earlier series provide such overlap. First, in Experiment C1, blends of 40, 50, 60, 70, and 80% H_2 were tested at 10 kW with 250 nlpm total air and steam injection levels of 7 and 9, conditions which are also present in D1. These points allow a direct side-by-side comparison of the two injection configurations. Second, Experiment C2 included blends of 40, 60, and 80% H_2 at 10 kW and 250 nlpm total air, with steam levels 6–9. These cases likewise overlap with D1 and provide an additional basis for evaluating the influence of steam injection location.

A comparative table showing the relevant dry emissions results in experiments D1, C1 and C2 is given below in Table 9.21:

H_2 [%]	Steam	D1 Axial				C1 Side				C2 Side			
		No-Steam	Steam	Drop [ppm]	Drop [%]	No-Steam	Steam	Drop [ppm]	Drop [%]	No-Steam	Steam	Drop [ppm]	Drop [%]
40	6	4.83	2.21	2.62	54.2	4.89	—	—	—	4.60	3.38	1.22	26.5
40	7	4.83	1.89	2.94	60.9	4.89	3.72	1.17	23.9	4.60	3.40	1.20	26.1
40	8	4.83	1.36	3.47	71.8	4.89	—	—	—	4.60	3.09	1.51	32.8
40	9	4.83	1.24	3.59	74.3	4.89	0.99	3.90	79.6	4.60	3.05	1.55	33.7
50	6	5.52	3.00	2.52	45.7	6.51	—	—	—	—	—	—	—
50	7	5.52	2.62	2.90	52.5	6.51	2.26	4.25	65.3	—	—	—	—
50	8	5.52	2.04	3.48	63.0	6.51	—	—	—	—	—	—	—
50	9	5.52	1.77	3.75	67.9	6.51	2.05	4.46	68.5	—	—	—	—
60	6	14.04	8.14	5.90	42.0	6.60	—	—	—	6.66	3.96	2.70	40.5
60	7	14.04	6.90	7.14	50.9	6.60	3.27	3.33	50.5	6.66	2.43	4.23	63.5
60	8	14.04	3.29	10.75	76.6	6.60	—	—	—	6.66	1.07	5.59	83.9
60	9	14.04	3.03	11.01	78.4	6.60	2.35	4.25	64.3	6.66	1.54	5.12	76.9
70	6	14.57	9.82	4.75	32.6	14.73	—	—	—	—	—	—	—
70	7	14.57	8.98	5.59	38.4	14.73	12.54	2.19	14.9	—	—	—	—
70	8	14.57	7.33	7.24	49.7	14.73	—	—	—	—	—	—	—
70	9	14.57	7.00	7.57	52.0	14.73	11.66	3.07	20.9	—	—	—	—
80	6	16.64	6.83	9.81	59.0	16.98	—	—	—	15.41	11.21	4.20	27.3
80	7	16.64	6.33	10.31	62.0	16.98	12.65	4.33	25.5	15.41	10.77	4.64	30.1
80	8	16.64	5.48	11.16	67.1	16.98	—	—	—	15.41	10.98	4.43	28.8
80	9	16.64	5.16	11.48	69.0	16.98	9.43	7.55	44.4	15.41	10.40	5.01	32.5

Table 9.21: Axial (D1) vs side (C1 and C2) comparisons at 10 kW, 250 NLPM total air. Values are dry NO; drops are computed series-by-series (i.e., against each series' own no-steam case). "—" indicates not tested.

The data show several important patterns when comparing axial and side steam injection. At 40% H_2, the axial configuration in D1 reduces NO by 54 to 74% across the tested steam levels. This is substantially higher than the 26 to 34% achieved in C2 under the same conditions, suggesting that the axial configuration may suppress NO more effectively at low to mid blends. The C1 results at 40% H_2 complicate this picture. Steam-7 shows a modest reduction of 24%, consistent with the weaker C2 results, but Steam-9 shows a reduction of nearly 80%, even greater than in the axial case. Since C1 and C2 were run at identical nominal conditions, such a divergence cannot be explained by AAI. More likely, it arises from subtle but impactful differences such as steam jet penetration, condensation in the lines, or even day-to-day flame stability. These sensitivities suggest that steam injection NO mitigation is prone to variability. However, it should be noted that for the 40% H_2 blend the absolute NO emissions are already at the lower end of the measurement range. As a result, the relative percentage drops observed with steam injection may appear more pronounced, even though the absolute reductions are modest. This indicates that the apparent effectiveness at low H_2 fractions should be interpreted with caution.

At 50% H_2, the comparison again highlights contrasting behavior. Side injection in C1 appears more effective overall, showing reductions between 65 and 69% in steam-7 and 9 respectively, while axial injection in D1 gives 53 to 68% at same steam conditions. In this case the two configurations converge, with the best axial result nearly matching the side injection. This indicates that at certain intermediate blends the relative performance of the two configurations is comparable, and no clear superiority emerges.

The case at 60% H_2 is particularly revealing. Here the percentage reductions overlap between axial and side cases, making direct comparison less straightforward. However, the absolute NO drops are much larger in D1, up to 11 ppm compared to around 5 ppm in the side-injection series at the highest steam setting of steam-9 (24.4 g/min). This is directly related to baseline levels: in D1 the baseline NO is more than twice that of C1 and C2, which can be traced to the absence of AAI. With all the air introduced through the swirler, the flame core remains hotter for longer and produces higher baseline NO, thereby increasing the potential scope for reduction.

At 70% H_2, the baselines for D1 and C1 are similar, which removes the confounding effect of different starting points noted in the 60% H_2 case. This convergence persists at even higher hydrogen fraction of 80% H_2, indicating that at high H_2 content the elevated flame temperature and strong reactivity dominate the influence of AAI, leaving little difference between axial and side no-steam conditions. In this context, the superiority of axial injection becomes very clear: reductions of 38 to 52% are achieved in D1, while C1 shows only 15 to 21% in steam-7 (17.7 g/min) and steam-9 (24.4 g/min) settings respectively. This points to axial steam being more effective when the flame is high hydrogen in fraction, where the hot reaction

zone is concentrated along the centerline and axial injection has a direct impact. The side injection jets in contrast may miss part of the core region or mix less effectively, which limits their effectiveness.

At 80% H_2, the baselines again align across D1, C1, and C2, which allows for a meaningful direct comparison. The results here confirm the trend already observed at 70%: axial steam achieves much stronger reductions, between 59 and 69%, while side injection produces only 27 to 44%. The data at this blend fraction provide some of the clearest evidence in favor of axial steam injection, as the separation between the two configurations is large and consistent across multiple steam levels.

It should be acknowledged, however, that the corresponding side steam injection operating points in experiments C1 and C2 show some variation in their emission results, which complicates a direct comparison with the D1 axial steam injection case. In addition, the no-steam reference cases also exhibit some variability across experiments, which makes the percentage NO reduction a more reliable metric for comparison. To better capture the general trends between axial (D1) and side (C1/C2) steam injection, a plot of percentage reductions is generated. The results of C1 and C2 are averaged to represent the side-injection performance, and where data for C2 are missing (e.g., 50 and 70 % H_2), the values from C1 are directly used. While this averaging approach may not be the most rigorous given the variability of the dataset, it still provides a useful representation of the overall trend. The comparison plot is provided below in Figure 9.24:

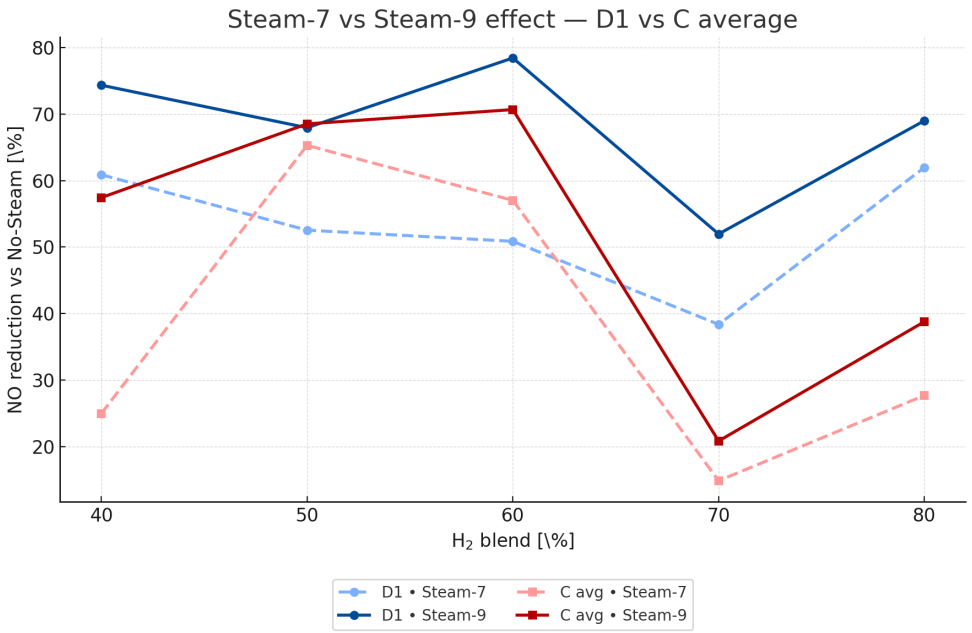


Figure 9.24: Percentage reduction in NO emissions with Steam-7 (17.7 g/min) and Steam-9 (24.4 g/min) injection compared to the no-steam case, for D1 (axial) and C-series average (C1 and C2, side steam injection). Steam-7 cases are shown with dashed lines, while Steam-9 cases are solid. Constant 10 kW burner power

The comparison graph above makes the previously observed trend clearer. At the lower to mid-level of H_2 content, the NO reduction percentages are comparable between axial steam injection and side steam injection, with a slightly better performance in axial injection. It should be noted that for the 40 % H_2 blend the absolute NO emissions are already low, so the large percentage reductions observed there should be interpreted with caution. However, the trend is very clear in higher H_2 content flames: axial steam injection results in considerably better NO mitigation compared to side steam injection. One explanation for that would be the smaller and more compact flame shapes of H_2 due to their faster burning dynamics and speed, which may cause side steam injection to not target the flame front as well as the wider high CH_4 fraction flames. This has been observed in the UV flame images in Experiment-C2 in Figure 9.22. With axial steam injection, however, the steam dilutes the hot flame core more efficiently and causes a more uniform temperature drop of the flame through its core.

To complement these quantitative findings, UV camera images are presented in Figure 9.25–Figure 9.27, comparing axial and side injection configurations across 40, 60, and 80 % H_2 blends. These visualizations illustrate how steam injection progressively reduces the luminosity and compactness of the flame, consistent with the observed decreases in NO.

It should be noted that the UV images shown for each operating condition were recorded with constant camera settings (gain and exposure time) across the different steam injection levels at a given blend. For example, the sequence from No-Steam to Steam-9 at 40 % H_2 under axial injection was acquired under identical settings, and the same applies to the side injection sequences at 40, 60, and 80 % H_2. This allows for a meaningful comparison of relative luminosity trends within each sequence. However, the camera settings used for the axial cases differ from those of the side injection cases, meaning that absolute intensity levels cannot be directly compared between injection locations.

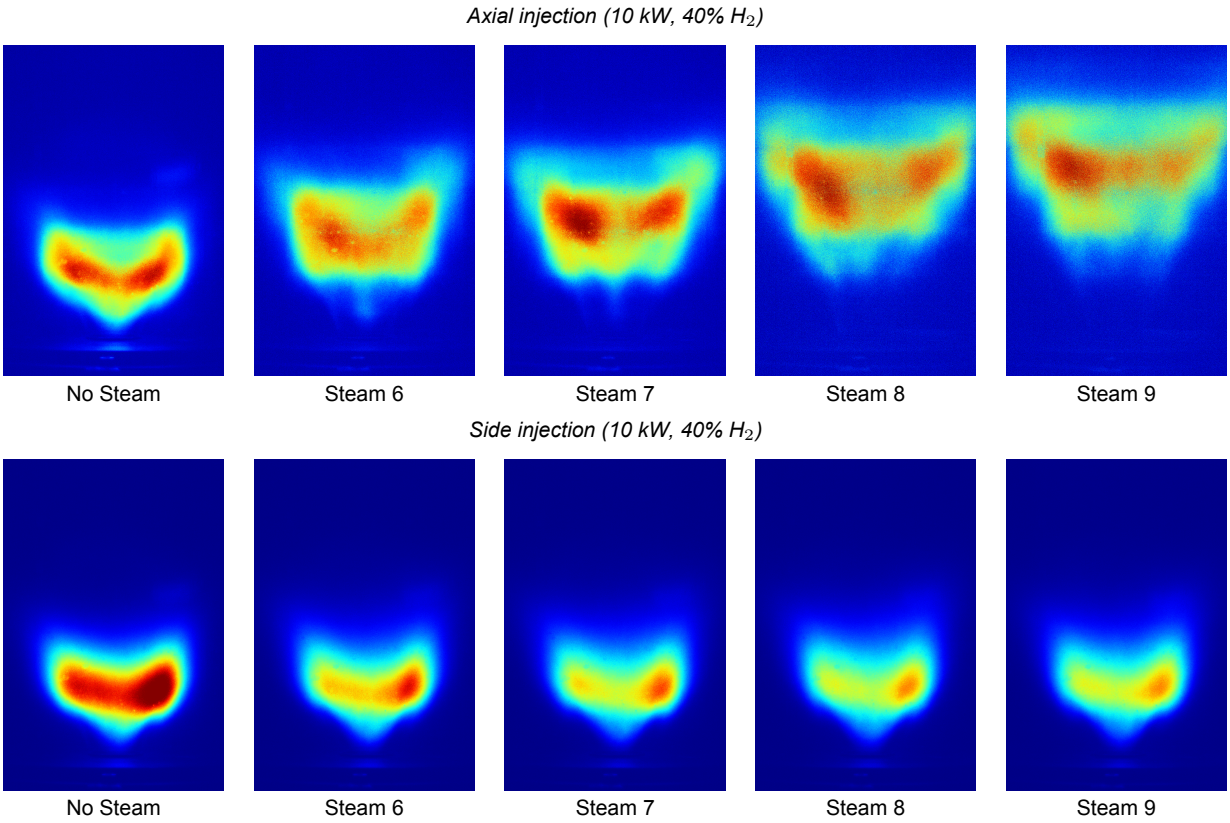


Figure 9.25: UV imaging at 10 kW, 40% H_2: axial (top row) vs side (bottom row) steam injection from No-Steam to Steam-9.

The difference in the effect of steam injection location is very clear in the 40 % H_2 blend. Axial steam injection causes a significant lift-off of the flame, and at the highest injection level (Steam-9) the flame appears to lose a clear anchor point altogether. As the steam amount increases, the flame is strongly stretched and the overall luminosity observed in the UV images becomes markedly dimmer. This indicates both a reduction in heat release intensity and a redistribution of the reaction zone further downstream, consistent with the higher sensitivity of axial injection to quenching. By contrast, side injection preserves a more compact and anchored flame even at Steam-9, with a gradual reduction in luminosity but without the pronounced lift-off. This visual evidence shows that side injection maintains a more attached and compact flame, whereas axial injection promotes a lifted flame with greater downstream displacement of the reaction zone. This lift-off does not on its own indicate instability but rather reflects a shift in the stabilization mechanism and heat release location, which can also reduce thermal loading on the burner surface.

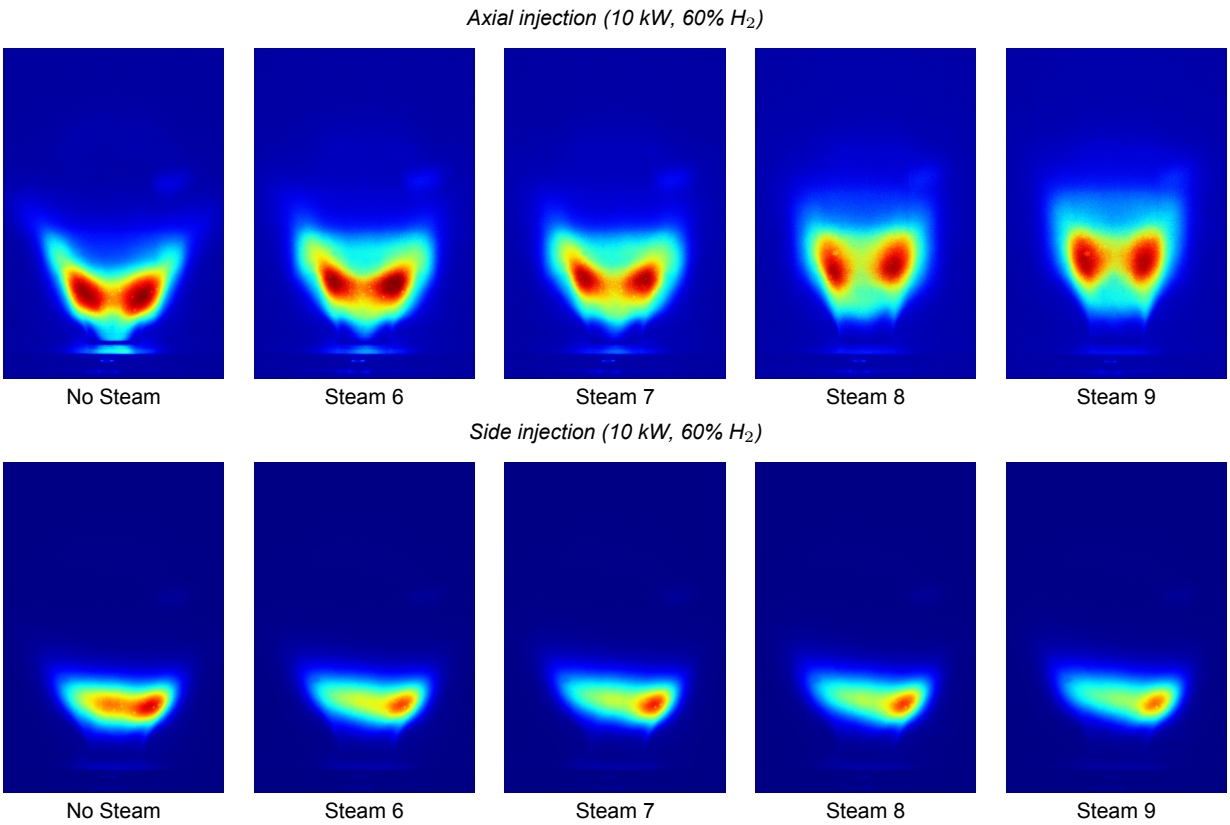


Figure 9.26: UV imaging at 10 kW, 60% H_2: axial (top row) vs side (bottom row) steam injection from No-Steam to Steam-9.

In the 60% H_2 blend, the flame behaviour is similar to that of 40% H_2, though the effects are less pronounced. A reduction in luminosity with increasing steam is still observed, but the magnitude of the change is smaller. Under axial steam injection the flame shows a visible lift-off, whereas with side injection no clear lift-off occurs. In the axial case the flame is also stretched upwards, which can be attributed both to the additional axial momentum of the injected steam and to the reduced burning velocity associated with steam dilution. This effect is more distinct in axial injection because of the more uniform introduction of steam through the core. The cooling influence of axial steam is evident when comparing the no-steam and Steam-9 cases: the luminosity near the anchoring region is significantly reduced, consistent with a lowered reaction intensity at the root of the flame. Another noticeable feature is that the flame shape under axial injection appears more symmetric compared to side injection, likely reflecting the centrally supplied steam producing a more balanced flow field and promoted better mixing, in contrast to the asymmetry introduced when dilution is applied from the side.

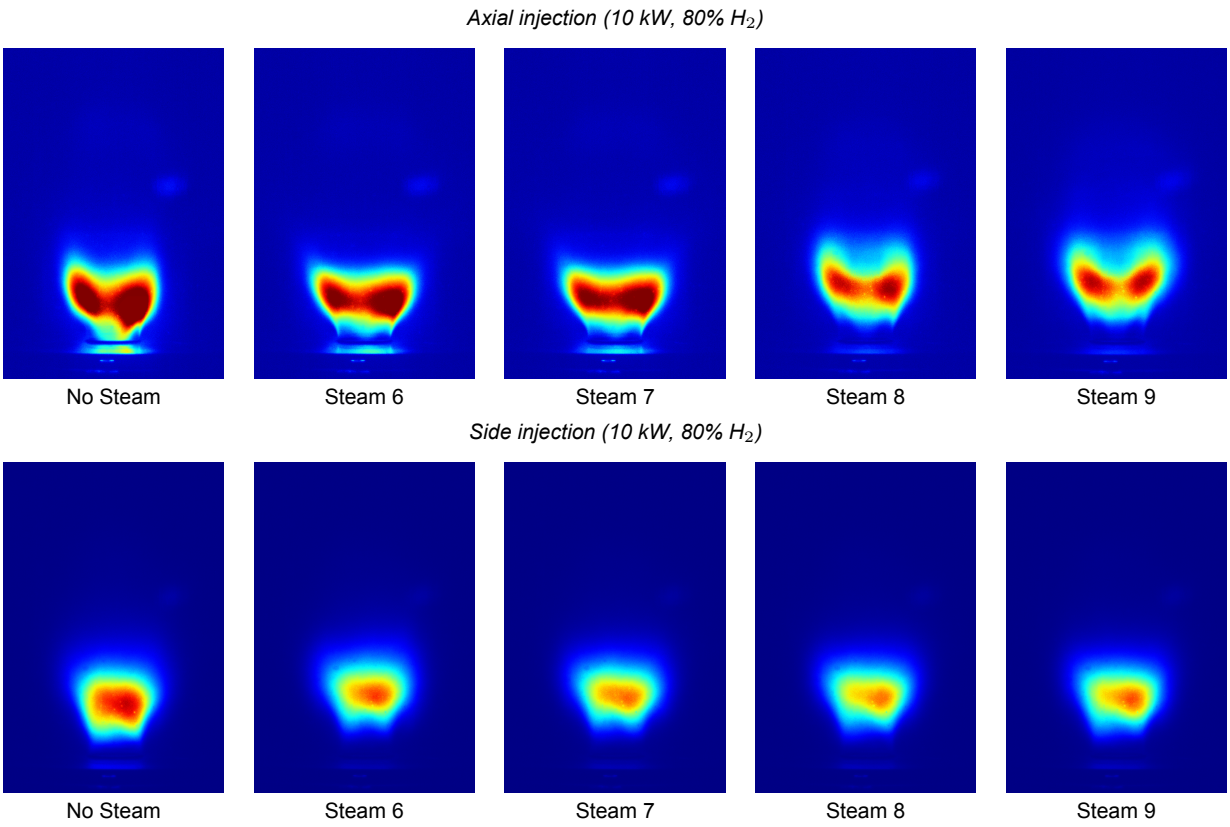


Figure 9.27: UV imaging at 10 kW, 80% H_2: axial (top row) vs side (bottom row) steam injection from No-Steam to Steam-9.

At 80% H_2 blends, the differences are even less pronounced. The decrease in luminosity is still present with axial steam injection, while even though a direct luminosity comparison between axial and side injection can not be made, the decrease in luminous intensity with axial steam injection seems to be stronger with respect to its no-steam reference case compared to side steam injection. The over-saturation points present in axial case no-steam diminishes strongly with increasing steam injection rate. This is in agreement with the higher NO reduction levels observed with axial steam injection at this H_2 blend fraction. Axial steam injection also causes observable lift-off in the flame, unlike side steam injection. The core-cooling effect of axial steam injection is again visible through the reduced luminosity of at the root of the flame.

At 80% H_2 blends, the differences between axial and side steam injection are less pronounced overall, yet several key distinctions can still be drawn from the flame development. Within the axial sequence, a marked decrease in luminosity is observed as the steam rate increases, and while absolute intensity comparisons with the side sequence cannot be made due to different imaging settings, the relative reduction from the no-steam baseline appears stronger in the axial configuration, which can be supported by the NO emissions data seen previously. A particularly notable feature is the disappearance of the oversaturated regions that dominate the no-steam axial case; by steam-9 these bright, saturated zones are strongly diminished, pointing to effective cooling of the flame core where NO formation is most intense. In addition to this, axial injection induces visible lift-off and elongation of the flame as steam is increased, consistent with the combined effects of axial momentum imparted by the injected steam and reduced burning velocity due to dilution. By contrast, the side-injection flames remain more compact and closely anchored across all steam levels, with structural changes limited mainly to a gradual softening and contraction of the core reaction zone. These contrasting behaviors suggest that axial steam penetrates more directly into the hottest central regions of the flame, enabling stronger suppression of NO formation compared to side injection, even though the overall differences between the two injection strategies narrow at this high hydrogen fraction.

To provide a fuller picture of the effect of axial steam injection, the full emissions table of Experiment-D1 is presented below in Table 9.22:

H_2 Blend [%]	$\phi \pm 0.013$	Steam	NO (ppm, *dry*) (wet in parentheses)	O_2 [%]	CO [ppm]	CH_4 [ppm]	CO_2 [%]
40	0.648	No-Steam	4.83 (4.13 wet)	7.77	0.00	0.00	6.52
		Steam-6	2.21 (1.77 wet)	7.76	0.00	0.00	6.53
		Steam-7	1.89 (1.49 wet)	7.77	0.00	0.00	6.52
		Steam-8	1.36 (1.05 wet)	7.76	0.00	0.00	6.52
		Steam-9	1.24 (0.95 wet)	7.77	0.00	0.00	6.52
50	0.620	No-Steam	5.52 (4.72 wet)	8.02	0.00	0.00	6.03
		Steam-6	3.00 (2.41 wet)	8.05	0.00	0.00	6.02
		Steam-7	2.62 (2.07 wet)	8.04	0.00	0.00	6.03
		Steam-8	2.04 (1.58 wet)	8.02	0.00	0.00	6.04
		Steam-9	1.77 (1.36 wet)	8.07	0.00	0.00	6.01
60	0.590	No-Steam	14.04 (11.99 wet)	8.29	0.00	0.00	5.45
		Steam-6	8.14 (6.55 wet)	8.22	0.00	0.00	5.49
		Steam-7	6.90 (5.46 wet)	8.24	0.00	0.00	5.48
		Steam-8	3.29 (2.55 wet)	8.27	0.00	0.00	5.47
		Steam-9	3.03 (2.33 wet)	8.28	0.00	0.00	5.46
70	0.553	No-Steam	14.57 (12.42 wet)	8.63	0.00	0.00	4.71
		Steam-6	9.82 (7.91 wet)	8.61	0.00	0.00	4.72
		Steam-7	8.98 (7.12 wet)	8.63	0.00	0.00	4.71
		Steam-8	7.33 (5.69 wet)	8.66	0.00	0.00	4.70
		Steam-9	7.00 (5.40 wet)	8.66	0.00	0.00	4.70
80	0.515	No-Steam	16.64 (14.14 wet)	9.81	0.00	0.00	3.49
		Steam-6	6.83 (5.50 wet)	9.00	0.00	0.00	3.75
		Steam-7	6.33 (5.02 wet)	9.01	0.00	0.00	3.75
		Steam-8	5.48 (4.26 wet)	8.99	0.00	0.00	3.76
		Steam-9	5.16 (3.99 wet)	8.97	0.00	0.00	3.76

Table 9.22: Full emissions for Experiment D1. Constant 10 kW burner power with varying H_2 fuel fraction and steam injection level (Steam-6 = 13.7 g/min, Steam-7 = 17.7 g/min, Steam-8 = 22.8 g/min, Steam-9 = 24.4 g/min). Values reported on a *dry* basis for NO; analyzer wet readings are shown in parentheses. O_2, CO, CH_4, and CO_2 are measured dry by the analyzer. Dry conversion via Equation 8.5. Axial steam injection configuration was used.

The full emissions profile for D1 shows a distinct pattern compared to the side injection configurations. Most notably, CO concentrations remain consistently below the detection limit across all blends and steam injection levels, even at high methane fraction conditions where side injection previously caused sharp CO rises under quenching. Similarly, CH_4 emissions stay below the analyzer detection limit throughout the entire matrix. This absence of measurable incomplete-combustion products indicates that axial steam injection dilutes the flame more uniformly, rather than creating localized zones of over-dilution and quenched flames. In contrast, the side injection configuration likely introduced steam in concentrated regions, disturbing flame anchoring and oxidation completeness in specific zones. The D1 results therefore suggest that axial delivery distributes steam more evenly across the reaction zone, suppressing NO formation without triggering the incomplete oxidation penalties observed in some C1 and C2 cases. This uniformity provides a possible explanation for why the steam–NO suppression trend in D1 is clearer and more consistent than in the side injection experiments.

When comparing the full emissions results of Experiment D1 (axial injection) to the side-injection cases in Series C1 and C2, a complication becomes immediately clear: the C-series data are not fully consistent with each other, even at nominally identical operating points. In principle, C1 and C2 should produce very similar values, since both were conducted at 10 kW with the same fuel blends, steam levels, and AAI fractions. Instead, notable discrepancies appear. For example, at 40% and 60% H_2, C1 reports CO levels

well above 100 ppm and CH_4 in the tens of ppm under steam addition, whereas C2 shows values much closer to the analyzer detection limit. This inconsistency within the C-series complicates efforts to isolate the effect of steam injection location, since it is difficult to know which of the two datasets better reflects the true behavior of the system.

By contrast, the D1 axial injection results are internally consistent and show a very different character: CO remains below detection across all conditions, and CH_4 levels stay below 4 ppm even at high steam rates and high methane fraction blends. O_2 and CO_2 trends behave as expected in all three series, with O_2 rising and CO_2 falling as hydrogen fraction increases, but the penalties in CO and CH_4 observed in C1 (and to a lesser degree in C2) are absent in D1. This difference could point to a genuine advantage of axial injection in avoiding localized quenching, but the inconsistencies between C1 and C2 prevent a definitive conclusion.

The discrepancies between C1 and C2 are not uniform across the matrix but occur at a limited number of operating points. The most pronounced differences appear at 40% and 60% H_2, where C1 reports CO levels exceeding 100 ppm and measurable CH_4 slip under steam addition, while C2 remains close to detection limits. At other blend fractions (e.g. 70 and 80% H_2), the two series are in much closer agreement, suggesting that the variation is concentrated in certain conditions rather than systematic across the whole dataset. In addition to day-to-day variability, the side-injection configuration itself is inherently less symmetric than the axial one, and imperfect steam distribution between the two side ports could have amplified localized quenching in C1 but not in C2. This system-level asymmetry therefore offers a plausible physical mechanism for why one series shows CO and CH_4 penalties while the other does not. Furthermore, in a swirl-stabilized partially premixed burner, the mixing of air, fuel, and steam is inherently non-uniform. The calculated global equivalence ratio, ϕ, does not capture local mixture variations that develop across the recirculation zone and shear layers. These inhomogeneities can create pockets of locally higher ϕ, where oxidation is incomplete and CO and CH_4 formation is promoted, while other regions remain lean and favor lower NO production.

Regardless of these discrepancies, the ϕ–NO trends remain consistent across all campaigns, reinforcing that the primary conclusions regarding NO suppression are robust even though the interpretation of CO and CH_4 penalties carries more uncertainty.

To gain further insight into the flame structure, Abel-inverted reconstructions of the UV images were produced for selected operating conditions (Figures 9.28–9.30). The images were first symmetrized by averaging the two flame halves, after which an inverse Abel transform was applied to approximate the local radial emissivity distribution. This approach highlights how reaction intensity is distributed across the centerline and radial directions. The faint vertical seam along the axis is a post-processing artifact of the inversion procedure and should not be interpreted as a physical feature of the flame.

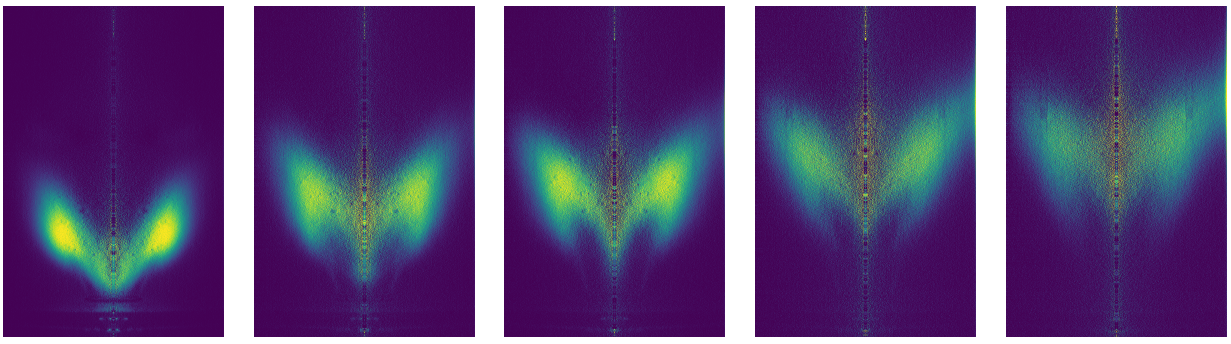


Figure 9.28: Abel-inverted UV imaging of a 10 kW flame with 40% H_2 blend under different axial steam injection settings.

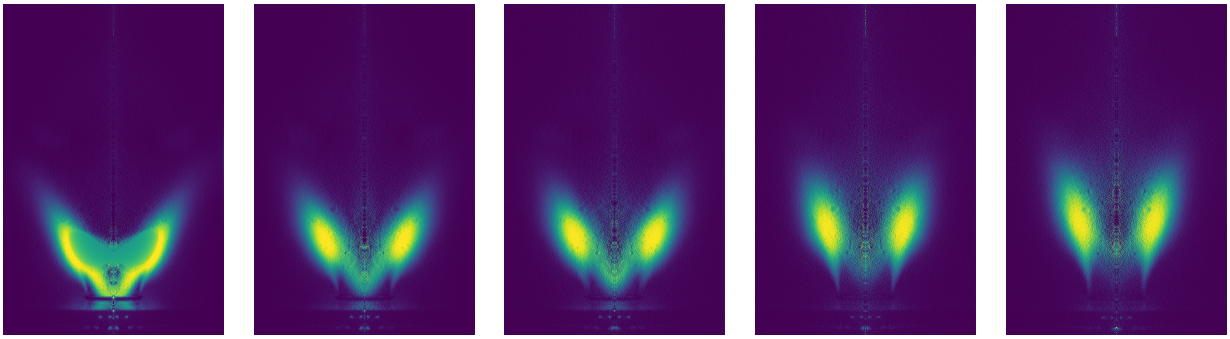


Figure 9.29: Abel-inverted UV imaging of a 10 kW flame with 60% H_2 blend under different axial steam injection settings.

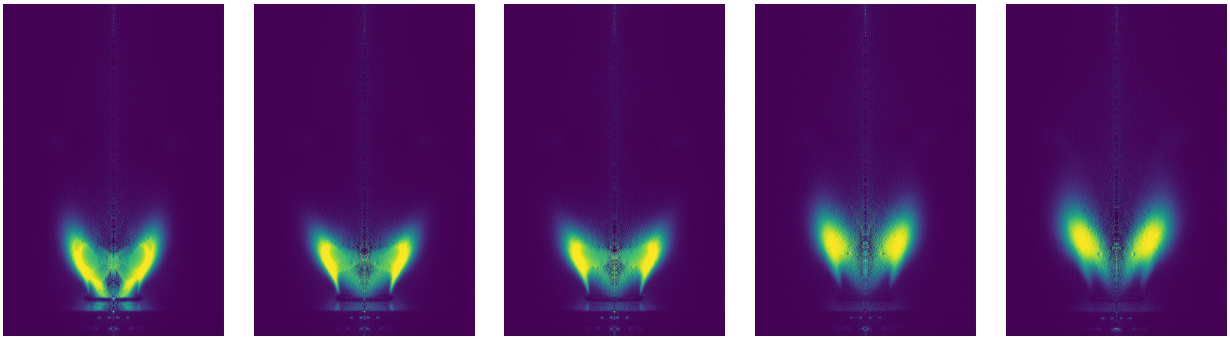


Figure 9.30: Abel-inverted UV imaging of a 10 kW flame with 80% H_2 blend under different axial steam injection settings.

In 40% H_2 flame, the no-steam flame is tall and wide, with intense lobes along the shear layers and a bright, cup-shaped root near the nozzle. When steam is injected axially, the structure changes dramatically. The flame lifts by several centimeters and stretches upwards, while the reaction zone loses its sharply defined outline and becomes less distinct. At higher steam rates a clear hollow forms in the flame core, cutting through the bright cup-shaped base that is present without steam. The Abel reconstructions confirm this centerline cooling effect, showing that axial steam penetrates directly into the root of the flame and weakens the hottest regions. Rather than forming a stable anchored front, the flame front appears disrupted and more irregular, reflecting both the reduced burning velocity and the additional momentum imparted by the steam jet. This behavior is consistent with the significant reductions in NO, achieved without measurable CO penalties, indicating that the weakening occurs globally across the reaction zone rather than as localized quenching.

The situation changes markedly at 60% and 80% H_2. In the no-steam cases, both flames exhibit a bright, sharply defined region along the centerline, producing a characteristic cup-shaped structure at the flame root. This feature reflects a highly concentrated and intense reaction zone in the flame core, typical of high hydrogen fraction mixtures with fast burning velocities and elevated temperatures. With axial steam injection, this bright cup structure is progressively disrupted. At Steam-6, a partial hollow already appears at the base of the flame. As the injection level is increased, the central maximum is eroded further, giving rise to a clear hole in the core of the flame at Steam-8 and Steam-9. The peak reaction intensity shifts outward, forming two off-axis lobes that incline toward the shear layers of the flow. This outward migration reflects both dilution and cooling of the flame center and the added axial momentum of the injected steam, which pushes the reaction away from the burner axis.

The hollowing trend is particularly pronounced at 60% H_2, where the transition from a single on-axis maximum to two off-axis peaks is very clear. The lobes tilt upward and outward with increasing steam, and the flame base becomes less well anchored, consistent with the lift-off observed in the raw UV images.

At 80% H_2, a similar pattern is observed, though the flame core is more resistant to quenching, and a remnant of the central bright zone persists even at high steam rates. This resilience is likely due to the very high burning velocity and reactivity of high hydrogen fraction mixtures, which stabilizes the reaction against full centerline suppression. Nonetheless, the “cup” zone becomes less defined and more diffuse, and the central oversaturated regions visible in the no-steam case are strongly diminished with steam addition.

Importantly, the Abel reconstructions confirm that axial steam injection targets the flame core most effectively. The dilution is introduced directly into the highest-temperature regions, producing a uniform cooling of the center and redistributing the reaction intensity outward. This explains why axial injection yielded larger and more consistent NO reductions at high hydrogen fractions compared to side injection. In the side-injection cases (see Experiment C2, Figure 9.22), the flame often retained a central bright core, while dilution mainly affected the periphery. The axial geometry therefore achieves a more direct suppression of the NO-forming zones without introducing strong asymmetry or incomplete combustion, as CO and CH_4 remained below detection in D1.

In summary, the Abel-inverted fields demonstrate that axial steam injection not only reduces the overall reaction intensity but also fundamentally reshapes the flame structure. The transformation from a tightly confined reaction zone to a more radially displaced heat release structure provides direct visual evidence of how steam penetrates and quenches the flame base. This structural reorganization aligns with the measured NO trends in Experiment D1 and highlights the importance of injection location in determining the effectiveness of steam as a diluent.

To complement the previous analysis, the derived NO metrics of Experiment-D1 is presented below in Table 9.23. Unlike the previous experiments, since D1 resulted in no CO emissions, so CO metrics are omitted in the results.

H_2 [%]	ϕ	Steam	NO (dry) [ppm]	NO@15% O_2 [ppm]	EINO [mg/MJ]	EINO [g/kg]	ΔEINO [%]
40	0.648	No-Steam	4.83	2.18	2.379	0.132	0.0
		Steam-6	2.21	1.00	1.088	0.060	-54.3
		Steam-7	1.89	0.85	0.931	0.052	-60.9
		Steam-8	1.36	0.61	0.670	0.037	-71.9
		Steam-9	1.24	0.56	0.611	0.034	-74.3
50	0.620	No-Steam	5.52	2.54	2.808	0.162	0.0
		Steam-6	3.00	1.38	1.526	0.088	-45.7
		Steam-7	2.62	1.21	1.332	0.077	-52.5
		Steam-8	2.04	0.94	1.037	0.060	-63.1
		Steam-9	1.77	0.82	0.900	0.052	-67.9
60	0.590	No-Steam	14.04	6.60	7.392	0.452	0.0
		Steam-6	8.14	3.80	4.285	0.262	-42.0
		Steam-7	6.90	3.23	3.632	0.222	-50.9
		Steam-8	3.29	1.54	1.732	0.106	-76.6
		Steam-9	3.03	1.42	1.595	0.097	-78.4
70	0.553	No-Steam	14.57	7.04	8.028	0.529	0.0
		Steam-6	9.82	4.73	5.411	0.356	-32.6
		Steam-7	8.98	4.34	4.948	0.326	-38.4
		Steam-8	7.33	3.55	4.039	0.266	-49.7
		Steam-9	7.00	3.39	3.857	0.254	-52.0
80	0.515	No-Steam	16.64	8.89	9.586	0.704	0.0
		Steam-6	6.83	3.40	3.935	0.289	-59.0
		Steam-7	6.33	3.15	3.646	0.268	-62.0
		Steam-8	5.48	2.73	3.157	0.232	-67.1
		Steam-9	5.16	2.56	2.972	0.218	-69.0

Table 9.23: Experiment D1. Derived NO metrics (*dry*). NO values were normalized to 15% O_2 using Eq. (8.16).

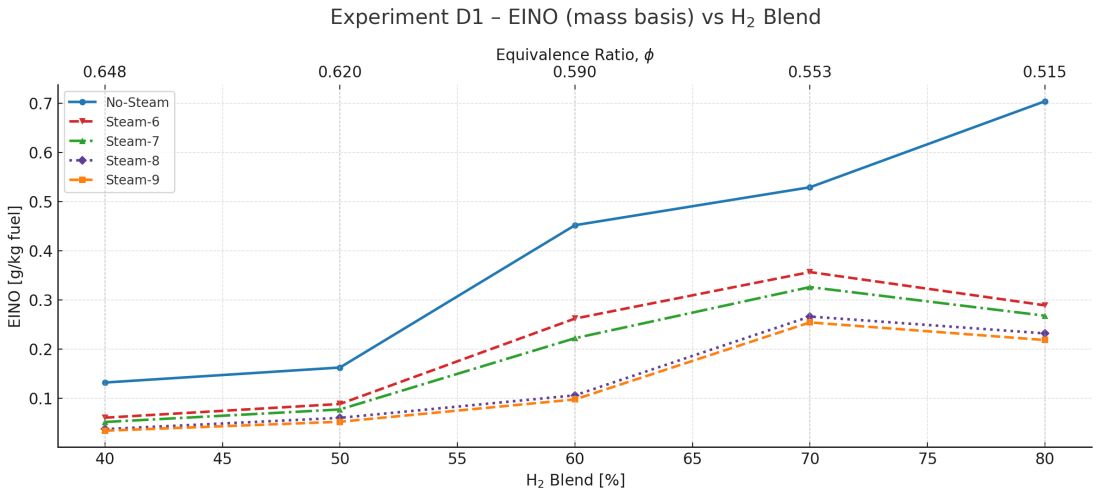


Figure 9.31: Experiment D1. Comparison of EINO on a mass basis for various steam injection cases.

The derived NO metrics confirm the suppression trends already observed in the raw emission data. Normalizing to 15% O_2 shows that reductions remain substantial across all blends, with decreases of more than 70% at 40–60% H_2 and nearly 70% even at 80% H_2 under the highest steam rate. The EINO values follow the same behavior, dropping by more than half in most cases and highlighting the strong impact of axial steam injection on thermal NO formation. Importantly, the absence of CO and CH_4 penalties indicates that these reductions are achieved without compromising combustion completeness. Overall, the D1 metrics reinforce that axial injection delivers consistent and effective NO mitigation across the tested hydrogen fractions.

In summary, the D1 results confirm that axial steam injection consistently suppresses NO emissions while maintaining complete combustion. Compared to side injection, axial delivery dilutes the flame more uniformly and avoids the localized quenching penalties observed in some C-series cases. The effect is especially clear in high hydrogen fraction conditions, where axial injection directly cools the flame core and achieves stronger reductions. These findings establish axial steam injection as a more stable and effective strategy for NO mitigation across a wide range of operating conditions tested in this burner set-up.

To conclude the results section, DSLR flame images are presented for all tested H_2 blends under No-Steam and Steam–9 conditions with side steam injection (Figure 9.32). These images are shown as supplementary evidence, complementing the emissions trends, UV chemiluminescence, and Abel inversions discussed earlier. While the UV camera isolates OH^* radicals and Abel processing provides spatially resolved intensity maps, the DSLR captures broadband visible emission (dominated by CH^* and C_2) and offers a more intuitive view of the flame structure. Presenting these images last allows for a qualitative confirmation of the impact of steam injection across the entire blending range in the side-injection configuration.

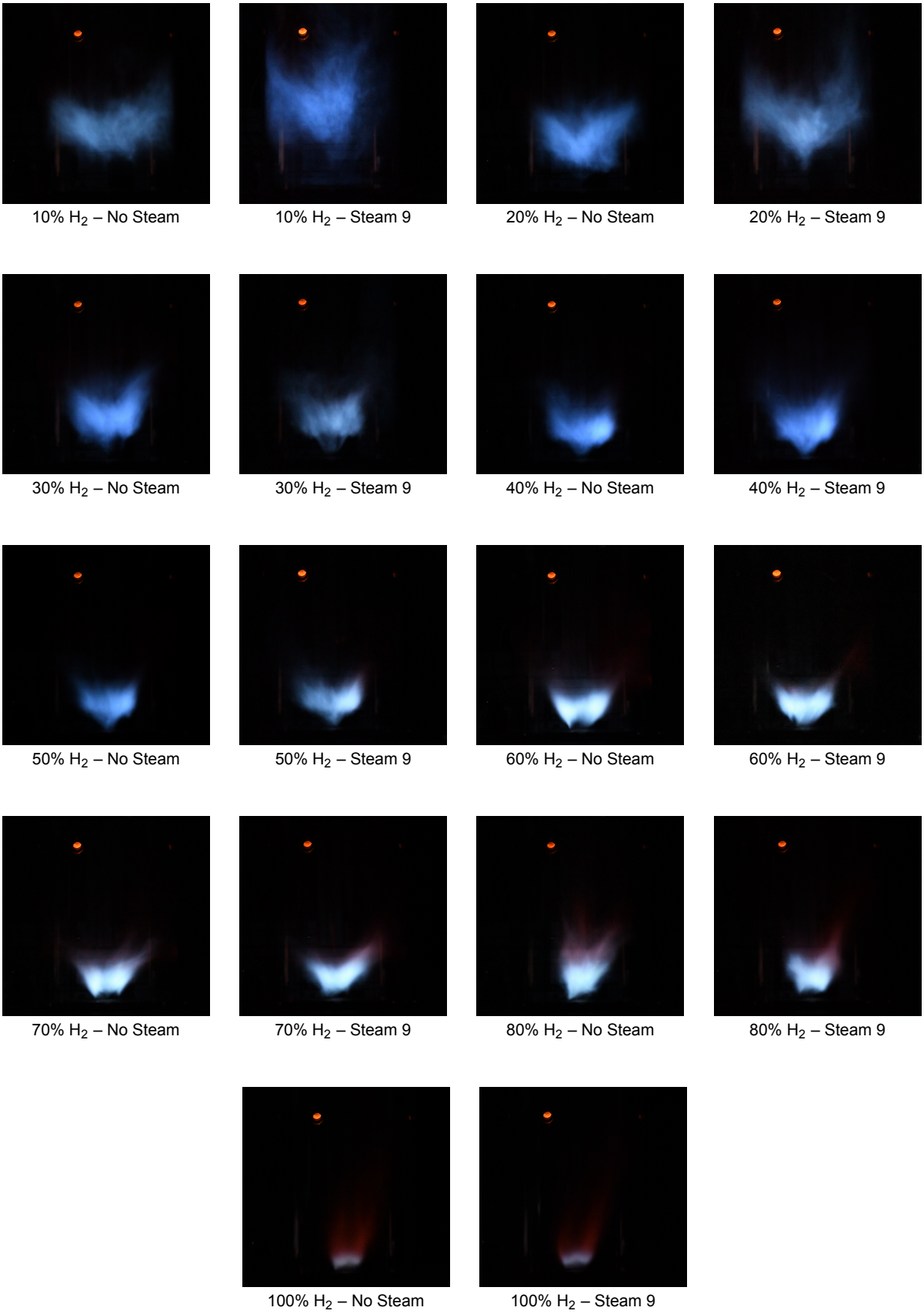


Figure 9.32: DSLR camera images of flame fronts for H_2 blends from 10% to 100%, each shown under No Steam and Steam 9 injection conditions. Side steam injection was used. Steam addition influences flame luminosity and shape across the hydrogen blending range.

The visible flame structures align well with earlier observations. At low H_2 blends (10–30%), the no-steam flames appear lifted and wide, with distinct high-intensity lobes, while Steam–9 cases are visibly stretched and weakened, consistent with increased dilution. At 40–60% H_2, where NO reductions were strongest, the DSLR frames clearly show diminished brightness and disrupted flame anchoring when steam is added. At high blends (70–100% H_2), the visible luminosity is already limited due to the lack of carbon radicals, yet steam injection still reduces the residual luminous core and smooths the flame outline. Notably, at 60 and 80% H_2, the characteristic “cup-shaped” bright zone seen in no-steam flames is visibly penetrated and eroded by the steam jet, leaving a darkened hole at the flame root in the Steam–9 cases.

These DSLR images therefore serve as a supplementary visualization of the side injection configuration, reinforcing that steam consistently suppresses flame luminosity and alters flame structure across all H_2 fractions. While less diagnostic than the UV and Abel analyses, they provide a straightforward visual confirmation of the steam effect and act as a closing illustration of the overall trends discussed throughout this chapter.

10

Discussion

The present study explored the effectiveness of steam injection as a method to reduce NO emissions in lean premixed flames of methane, hydrogen, and their blends within a swirl-stabilized burner configuration. Across all tested conditions, the addition of steam resulted in a clear reduction in NO emissions; however, the degree of suppression varied considerably with fuel composition, thermal power, and injection configuration. These variations are best interpreted in the context of established NO formation pathways and the impact of steam on the underlying combustion chemistry and flame structure.

Thermal NO, described by the Zeldovich mechanism, is the primary pathway under the higher temperature conditions of these experiments and becomes significant when local gas temperatures approach the 1800 K range. Not all operating points reach this level everywhere in the flame, particularly at lower power, with high steam dilution, or in methane-dominated cases. Hydrogen combustion, with higher peak temperatures and faster kinetics at comparable power and global equivalence ratio, strongly promotes this route. By contrast, methane–air flames reach relatively lower temperatures, typically about 100 to 300 K below hydrogen flames under similar conditions. Although this temperature difference may appear modest, it produces an observable change in NO because the Zeldovich rate depends exponentially on temperature. Under the lower temperature conditions more typical of methane or strongly diluted operation, additional pathways can contribute to the measured NO, including prompt NO near the flame front and, in some lean or low temperature cases, a minor nitrous-oxide intermediate route [11].

Steam influences NO formation through three coupled effects: a thermal effect (increased mixture heat capacity reduces flame temperature), a dilution effect (steam displaces reactive oxygen and lowers reactant partial pressures), and a chemical effect (third–body stabilization and radical recombination suppress the H/O/OH pool and chain branching). These mechanisms act simultaneously and are consistent with prior studies and the present observations [116, 117, 66].

A brief comparison between the simplified estimates in Section 9.1 and the measurements shows good first-order agreement. The analytical model predicted 35–55% NO reduction for the Steam-7 to Steam-9 range when thermal effects dominate. In the side-injection 10 kW series (C1/C2), measured reductions were typically 30–40% at Steam-7 and 45–55% at Steam-9 for 40–80% H_2, matching the predicted band; blend sweeps at 9–11 kW (B1/B2) follow the same trend, with larger relative drops at methane-richer points where baselines are lower. Deviations from the estimate are consistent with mechanisms outside the thermal-only picture: at methane-rich, low-power points, local quenching and incomplete mixing can yield reductions larger than purely thermal scaling, whereas at high H_2 some cases show slightly smaller percentage drops because compact hot cores sustain higher post-flame temperatures. Axial cases (D1) generally fall within the same envelope but occasionally exhibit smaller reductions at a given steam setting, attributable to residence-time and mixing differences introduced by the core jet; series-by-series normalization confirms the overall consistency of the simplified prediction with experiment.

In the experimental results, the role of fuel composition emerged as one of the most significant factors in determining the response to steam injection. While high hydrogen fraction flames consistently produced higher NO emissions than high methane fraction flames under similar thermal power settings, this cannot be solely attributed to adiabatic flame temperature. Under constant power operation, shifting the fuel blend toward higher hydrogen content slightly reduces the overall equivalence ratio, which in turn lowers the adiabatic flame temperature, as confirmed by equilibrium simulations conducted in Cantera. Nevertheless,

the experimental results showed increased NO formation in high hydrogen fraction flames, suggesting that the actual flame temperatures were higher. This discrepancy is explained by the turbulent flame structure that develops with hydrogen enrichment. The Cantera simulations represent ideal adiabatic, one-dimensional premixed flames, whereas the present flames are turbulent and swirl-stabilized, with heat transfer, mixing inhomogeneities, and finite-rate chemistry. As a result, the effective flame temperature is governed by the local flow field rather than by the adiabatic equilibrium value. These properties produce a narrower, more localized high-temperature zone, reducing the surface area for convective and radiative heat loss to the combustion chamber walls [118, 36]. As a result, hydrogen flames tend to retain more thermal energy locally, resulting in higher effective flame temperatures and greater thermal NO formation, even under nominally cooler adiabatic conditions.

Furthermore, hydrogen's high diffusivity introduces preferential diffusion effects in the present burner, which operates in a partially premixed mode. As a result, the mixture is not perfectly homogeneous even before combustion, and local variations in equivalence ratio are already present due to incomplete mixing of fuel and air. The addition of hydrogen amplifies these inhomogeneities because it diffuses more rapidly than methane, creating locally richer pockets even when the global mixture remains lean. These locally enriched regions can reach higher temperatures and therefore enhance thermal NO formation through the Zeldovich mechanism [13]. Although hydrogen has fast chemical kinetics, this does not necessarily suppress NO formation, since most thermal NO is formed not at the flame front itself but in the post-flame region, where gases remain at elevated temperatures. In this region, the residence time is governed primarily by the flow field and recirculation dynamics rather than by the laminar flame speed. Consequently, NO formation in hydrogen-enriched cases is mainly controlled by the sustained high temperatures in the post-flame zone rather than by reaction rate alone, leading to a net increase in NO emissions.

Consistent with the trade-offs discussed above, the carbon-species response mirrors the NO behavior but with a different emphasis. In the no-steam reference cases, CO is negligible and CH_4 is at or below the detection limit across all blends, indicating robust carbon oxidation under no-steam operation. With steam injection, however, both species become measurable, revealing steam-induced penalties in carbon conversion. These penalties are smaller at higher hydrogen fractions, which is expected both because the fuel contains less carbon and because hydrogen addition generally strengthens reaction rates and shortens oxidation paths. Accordingly, reduced CO and CH_4 at higher H_2 should be read primarily as evidence of more complete carbon oxidation, not as a direct measure of overall combustion efficiency. A full efficiency assessment would also require information on hydrogen present in the product gasses, which was not measured by the analyzer; while the higher reactivity of hydrogen may improve overall efficiency, this cannot be confirmed without H_2 measurements and a complete species balance.

In contrast, high methane fraction flames exhibited a sharper trade-off. While NO suppression was more pronounced in relative terms, increased steam addition often pushed these flames close to the quenching limit, particularly at lower power levels. This was evidenced by elevated CO and residual CH_4 concentrations in the exhaust gases. Such behavior is consistent with previous findings by Li et al. [119] and Göke et al. [120], who reported that methane combustion, though inherently lower in NO formation, is more sensitive to dilution due to its slower chemical kinetics and greater susceptibility to local extinction. The present results confirm that although methane flames can achieve high NO reductions, sometimes exceeding 80%, these gains are constrained by a narrowing combustion stability margin.

The location of injection had a significant influence on NO emissions and combustion stability. While side injection was initially expected to be more effective due to its interaction with high-temperature regions, particularly near the outer recirculation zones, it instead diluted the post-flame gases rather than the reactants, which occasionally induced localized quenching in high-methane flames and led to CO and unburned hydrocarbon penalties. Conversely, axial injection of steam through the burner core offered a more homogeneous premixing with the air stream, leading to similar or slightly better NO suppression without combustion efficiency losses. These findings are in agreement with the conclusions of Tao and Zhou[121] and Göke *et al.*[122], who showed that steam injection placement and uniformity are key for lowering NO while avoiding instability and incomplete oxidation. The implication is that for swirl-stabilized lean premixed combustion, uniformity in steam distribution may be more important than spatial targeting of high-temperature zones, especially in compact geometries where mixing length is limited.

Images of flame structures under different steam injection strategies revealed distinct morphological differences, especially at low-to-moderate power levels. Side steam injection in high methane fraction

flames led to noticeable asymmetry, elongation, and flickering of the flame front. These distortions intensified at higher steam flow rates, suggesting that the lateral jet introduced localized quenching and interfered with the swirl-induced internal recirculation zones. The broader spatial extent of methane flames made them more susceptible to aerodynamic disturbances, but also allowed the side-injected steam to more effectively intersect with high-temperature reaction zones. In this configuration, side injection may therefore be particularly suitable for high methane fraction operation, offering targeted NO suppression without compromising combustion stability.

In contrast, high hydrogen fraction flames exhibited a compact and intense reaction zone attached close to the rim. Under these conditions, side injection interacts mainly with the post-flame region rather than the reactants, which limits its influence on peak flame temperature and reduces its effectiveness in thermal NO suppression. Conversely, axial injection introduces steam upstream in the mixing tube where it blends with the reactants before ignition, producing reactant dilution, acting as a heat sink and causing global reduction in flame temperature. This explains why axial steam injection consistently achieved stronger NO reduction in high hydrogen blend conditions. This configuration produced more symmetric flame shapes and maintained combustion completeness, as indicated by low CO and CH_4 levels. A notable effect was the increased flame lift-off observed in methane-dominated and low-H_2 blends. Moderately lifted flames can be beneficial, as the longer mixing length between the burner exit and the stabilization point promotes improved fuel–air homogenization and can reduce NO formation. However, excessive lift-off introduces a risk of blow-off at higher steam rates or under leaner conditions. These trends align with Li *et al.* [119] and Tao & Zhou [121], who reported that steam premixing enhances NO reduction and flame symmetry but also modifies stabilization dynamics depending on operating conditions. These findings indicate that the effectiveness of steam injection depends not only on injection rate but also on how early steam can mix with the incoming oxidizer stream.

Placing the present measurements alongside prior work on steam injected premixed hydrogen and hydrogen–methane flames shows close agreement in both trend and magnitude of NO suppression. Göke and Paschereit reported that when the steam–to–air mass fraction exceeded approximately 20% in premixed configurations at atmospheric pressure, both hydrogen and natural gas flames achieved single–digit NO_x at 15% O_2 across a wide equivalence–ratio range, with all wet cases lying below their corresponding no-steam baselines at the same firing conditions [25]. The present lean, swirl–stabilized data at 7–11 kW and $\phi \approx 0.48$–0.98 exhibit the same systematic downward shift of NO upon steam addition, including hydrogen–rich and blend flames where the thermal drive is intrinsically high. On a mass basis, EINO values here span roughly 0.05–0.75 g/kg for dry operation and frequently fall to ≤ 0.15 g/kg under the highest steam setting, which is consistent with the single–digit ppm regime reported for wet premixed operation at similar lean conditions [25]. Where literature sources provide only ppm at 15% O_2 and not $EINO_x$, direct mass–basis alignment is not possible without additional assumptions; nevertheless, the observed EINO range here matches the low–NO_x envelope that wet premixing enables in those studies.

High-pressure premixed swirl tests by Stathopoulos *et al.* [123] reported that increasing the steam-to-air mass ratio to 0.20–0.25 reduced NO_x from about 80–90 ppm to 20–40 ppm at 9 bar for 100% natural gas and from about 120–150 ppm to 40–70 ppm at 9 bar for a 90%NG/10%H_2 blend; at 1 bar their no-steam cases were roughly 5–15 ppm and steam injected cases decreased to approximately 5–10 ppm. The reactor-network analysis in that work attributes the suppression to combined thermal, dilution and chemical effects of H_2O on radical populations. In the present 7–11 kW atmospheric swirl tests steam injection produced single-digit NO_x in several steamed conditions with corresponding EINO values on the order of or below 0.2 g/kg. Although $EINO_x$ was not reported by Stathopoulos *et al.*, the ppm reductions they document are qualitatively consistent with the present mass-basis observations and with the same set of suppression mechanisms inferred here.

Göckeler et al. [124] increased steam content up to approximately 30% of the air mass and reported a strong, monotonic decrease in NO_x for both high methane fraction and high hydrogen fraction blends; wet cases with steam in the range 20%–30% produced NO_x below 10 ppm (15% O_2) across a wide equivalence–ratio window, while CO penalties appeared only as mixtures approached the lean stability limit. These outcomes align quantitatively with the present 7–11 kW results: blend points with steam frequently exhibit EINO values $\leq$0.15 g/kg, which correspond to single–digit ppm in several steamed conditions. The CO and CH_4 penalties observed by Göckeler et al. near lean blowout are also present in the current high methane fraction, high-steam, low-power cases, supporting the same trade-off between NO suppression and stability. Overall, Göckeler et al. provide a direct atmospheric-pressure benchmark

for the present data, showing that steam injected premixing to 20%–30% steam reliably reduces NO_x to the low-ppm regime while the present mass-basis EINO values rest within that performance envelope.

Concetti et al. [63] isolated the chemical contribution of steam by maintaining the adiabatic flame temperature and performing 1-D freely propagating flame simulations with the CRECK mechanism. Their parameter space covered equivalence ratios $\phi = 0.3$–0.8 and water loadings Y_W up to 0.10 (10% by mass). Under conditions close to stoichiometry and with $Y_W = 0.10$, the study reports an approximate 50% reduction in NO_x relative to the dry case, demonstrating that water vapour alone (through third-body efficiencies and changes in the H/O radical pool) can halve NO_x even at constant T_{ad}. The elementary process invoked in that analysis was expressed in the form

$$\mathrm{H} + \mathrm{O_2}\ (+\mathrm{M}) \rightleftharpoons\ \mathrm{H_2O}\ (+\mathrm{M}),$$

where M denotes a collisional third body. Termolecular (third-body) reactions of this type proceed via collisional stabilization of an energized intermediate; an increased concentration of a high-efficiency third body such as H_2O enhances the rate of radical recombination and chain-termination steps (for example, H + O_2 (+M) $\rightarrow$ HO_2 (+M) and related pathways), thereby reducing steady-state concentrations of H, O and OH radicals. Because the thermal Zeldovich routes to NO formation depend critically on these radical pools and on high temperatures, the promotion of radical termination by H_2O yields a chemical suppression of NO_x that complements the pure thermal and dilution effects of steam addition. The chemical effect is most pronounced at higher ϕ within the examined range, where the native radical concentrations are larger and third-body mediated termination produces a correspondingly larger fractional reduction in NO production.

The present experimental matrix exhibits larger percentage reductions in several lean, low-power points (often approaching the analyzer detection limit), which exceed the $\sim$50% chemical-only reduction reported by Concetti et al. This difference is consistent with the expectation that the experiments combine chemical and thermal/dilution effects: maintaining the adiabatic temperature in Concetti et al. intentionally removes the thermal cooling contribution, whereas steam injection in the present 7–11 kW tests provides both chemical third-body effects and a measurable drop in local flame temperature. Where Concetti et al. report relative reductions (mole-fraction or reaction-rate based) rather than mass-based EINO values, the present work reports EINO on the order of or below 0.15 g/kg in many steamed cases, indicating that the combined mechanisms in practical premixed burners can produce equal or greater emission reduction than the isolated chemical effect alone. [63]

Taken together, the results highlight a clear operational trade-off when applying steam injection for NO_x control. Hydrogen-dominated flames produce higher absolute NO but allow a wider operational window for steam dilution without provoking quench or large CO penalties, whereas high methane fraction flames deliver larger relative NO reductions at the cost of a markedly narrower stability margin. Intermediate hydrogen–methane blends (approximately 40%–60% H_2) provide a favorable compromise, enabling substantial NO reductions while retaining combustion stability across the tested 7–11 kW power range. This conclusion aligns with the blend-optimisation reported by Goeckeler et al. [124], who identified mid-blend compositions as offering low-NO operation with limited CO penalties under wet premixed conditions.

However, several experimental limitations present in this study must be acknowledged. NO_2 measurements were compromised by water vapor interference and therefore were not used for quantitative NO_x partitioning. Hydrogen emissions in the exhaust could not be quantified because the gas analysis suite did not include an H_2 channel; as a result, combustion completeness for pure hydrogen cases can only be inferred indirectly from CO and CH_4 traces. The steam generator introduced an uncertainty in the injected mass flow of approximately $\pm$ 1.6-3.4% ($\pm$0.4–0.6 g/min), which likely contributed to variability in Series C and to scatter in point-to-point comparisons. Despite these constraints, the consistency of $EINO_x$ suppression trends across series and the quantitative agreement with prior steam injected-premixed studies support the robustness of the core findings.

In summary, steam injection is an effective pathway to mitigate NO_x in hydrogen–methane premixed combustion, provided that fuel composition, injection strategy and operating parameters are jointly optimized. High hydrogen fraction operation tolerates higher steam loadings with little measurable loss in combustion completeness; high methane fraction operation achieves stronger proportional NO suppression but requires tighter control to avoid instability. Uniform steam–air mixing is particularly important in compact, swirl-stabilized geometries to achieve steady, low-NO operation without incurring CO or unburned-fuel penalties.

These observations motivate prioritizing uniform premixing and blend-level optimization in any practical steam-dilution strategy for hydrogen-capable burners.

11

Conclusion & Recommendations

11.1. Conclusion

The research objective of this thesis was **to experimentally investigate the effect of steam injection on NO emissions in premixed CH_4–H_2 flames within a swirl-stabilized burner, with a focus on how steam flow rate, injection location, fuel composition, and burner power influence emission outcomes, and on understanding the underlying mechanisms of NO suppression**.

This objective was addressed through a systematic experimental matrix conducted in the TU Delft High Speed Laboratory. Tests covered burner thermal powers in the 7–11 kW range, fuel compositions from 0% to 100% H_2, and multiple steam dosing levels and injection configurations (side and axial). Measurements included dry NO (15% O_2 normalization) and other relevant species (O_2, CO_2 CO, CH_4), chemiluminescence imaging (OH* narrowband), and calibrated steam flow metrology. Experimental design emphasized series-level replication and consistency so that trends in NO and EINO could be attributed to controllable variables rather than to single-point scatter.

The following sections answer the research questions directly by outlining the measured effects of steam rate, injection location, fuel blend and burner power on NO emissions, identifying the dominant suppression mechanisms inferred from combined emissions and imaging diagnostics, and translating these findings into practical recommendations for steam-based NO control in hydrogen-capable burners.

Research Question 1

What are the design considerations for implementing steam injection in a hydrogen combustion system?

The experiments highlight three practical design messages for implementing steam injection in hydrogen-capable swirl combustors. First, reliable steam delivery is essential because small changes in steam amount alter both emissions and stability. In the present campaign the steam generator exhibited a flow variability of roughly $\pm$0.4–0.6 g/min (≈1.6–3.4%), which contributed measurable scatter in NO and EINO trends and therefore must be treated as a performance risk in control logic. Rather than reporting only absolute flows, control strategies and test reports should use relative setpoints and tolerances (for example target steam-to-fuel ratio with $\pm$X% allowed deviation) so that emission targets remain reproducible.

Second, injection location and fuel composition determine the suppression–stability trade-off. Side ports that impinge steam into the recirculation zones produced the largest local NO reductions in high methane fraction conditions, but these cases also showed the greatest sensitivity to quench and produced CO/CH_4 penalties when dosing was aggressive. High methane fraction test points commonly achieved relative NO reductions greater than 50% and in several points exceeded 80%, at the cost of a narrowed stability margin. Hydrogen-dominated flames produced higher absolute NO but tolerated substantially larger steam fractions with smaller relative reductions (typical relative reductions $\sim$30–40%), and in some high hydrogen fraction conditions modest steam addition expanded the usable stability envelope such that axial-air staging (AAI) became unnecessary. Mid-blend compositions (≈40%–60% H_2) were found to provide the best compromise between strong relative NO suppression and retained stability across the 7–11 kW matrix.

Third, several constraints are laboratory-specific and must be made explicit. Condensation in unheated or non-metallic piping and the use of PVC sections produced delivery artifacts and measurement bias

in the present tests; in practical systems steam delivery is expected to be via heated metallic lines with condensate traps, eliminating those artifacts. Similarly, NO_2 and hydrogen could not be measured in the current analyzer suite. Ideally, extended system-level studies should include wet-capable NO/NO_2 analyzers and an H_2 measurement channel to permit direct assessment of combustion completeness rather than indirect inference from CO and CH_4.

A final practical consideration concerns the source of steam in full-scale hydrogen combustion systems. In laboratory environments steam is typically supplied by an external evaporator, but in industrial applications such as the HySIITE engine concept by General Electric or hydrogen-fueled gas turbines, steam can be produced internally by recovering water from the exhaust. In such systems a fraction of the exhaust is condensed and reinjected into the combustor as steam, enabling internal steam recirculation. This approach reduces dependence on external steam generation equipment, improves thermal efficiency, and provides inherent temperature moderation while still achieving NO reduction through dilution and heat-capacity effects.

In summary, design choices must balance metering accuracy, injection distribution and blend-aware stability margins.

Research Question 2

How does steam injection impact NO emissions in hydrogen and hydrogen–methane blended combustion?

Steam injection reduced NO in every test point. In high methane fraction flames the reductions were strongest, often exceeding 50%, although excessive dilution sometimes produced higher CO and residual CH_4. Mid-range blend fuels resulted in strong NO reduction with limited side effects of CO and CH_4. High hydrogen fraction flames showed smaller relative reductions, typically around one third, because high flame temperatures and fast chemistry sustain NO formation. In several cases suppression reached the analyzer detection limit ($\approx$100% relative reduction), while in a few points reductions were as low as $\sim$10%. Across the matrix steam produced a consistent downward shift in NO at all fuel compositions.

The reduction is attributed to three coupled effects: thermal cooling via the increased heat capacity of the reactants, reactant dilution that reduces the available O atom pool, and chemical (third-body / radical-pool) effects that lower steady-state H/OH concentrations. Evidence for the chemical contribution has been demonstrated in controlled studies that hold T_{ad} constant and still observe substantial NO suppression with added H_2O [63]; the combined thermal and dilution mechanisms are well documented in wet premixing experiments and swirl combustor tests [25, 124, 123]. These effects act together, but their relative importance depends on the fuel mix: methane flames are more sensitive to thermal and chemical suppression because of slower kinetics and greater susceptibility to local quench, whereas hydrogen flames are more tolerant of dilution owing to higher burning velocity and compact flame structure. This interaction and its implications for stability and emissions are discussed in greater detail in the Discussion. [124, 63]

Research Question 3

How does steam injection affect overall combustion characteristics in fully hydrogen and hydrogen–methane flames?

Steam injection altered flame shape, local reaction rates, and emissions in ways that depended on fuel composition and injection strategy. In high methane fraction blends with side steam injection, high steam injection rates frequently reduced oxidation completeness: CO and residual CH_4 increased at the largest steam settings, indicating localized quenching where steam caused over-dilution. However, these emissions and effects were not observed with axial steam injection, implying axial steam injection results in a more uniform dilution by targeting the reactants directly. Blended fuels showed intermediate behavior, with mid-range mixtures delivering substantial NO reductions and only modest CO/CH_4 penalties when steam remained within the stability margin. High hydrogen fraction blend flames showed the highest NO emissions even with steam injection and the lower relative NO emission reductions, in both side and axial injection configuration. This can be attributed to the faster burning dynamics of hydrogen, which sustain high peak flame temperatures and limit the impact of dilution-based NO suppression. However, the effect of steam injection on hydrogen combustion efficiency was not quantified in this study because H_2 content in the flue gasses could not be measured. Although NO decreased significantly, a full assessment of

trade-offs should also examine co-emitted species and byproducts, including CO, unburned hydrocarbons, H_2, and NO_2, to characterize overall emissions and pollutant impacts.

Optical diagnostics corroborate these emission trends and highlight effects of steam injection on the flame stability. Side injection produced a dimmer, elongated flame with the brightest reaction region displaced upward and lateral features that grew with steam level; this signals a weakened near-field reaction zone and increased downstream reaction extent. Axial injection weakened the centerline core while preserving overall symmetry; flame images and Abel-inverted chemiluminescence revealed a reduced on-axis emissivity and growing off-axis activity as steam increased. These structural changes are consistent with a lengthened reaction zone, lower peak emissive temperature and redistribution of the region of strongest reactions away from the immediate swirler exit.

Stability effects were blend and injection location dependent. At low ϕ and 20% H_2 one methane-lean point that was stable without steam blew off at the highest steam setting (Steam-9) in side steam configuration, demonstrating that aggressive steam injection can erode anchoring by lowering local burning velocity and extending the flame base away from the exit. Conversely, several high hydrogen fraction points tolerated high steam loading without loss of attachment, and in some cases axial steam injection allowed stable operation without the previously required axial-air staging (AAI). Thus, steam can both reduce the need for auxiliary staging in some high hydrogen fraction conditions and simultaneously shrink the usable steam range in methane-lean conditions; this trade-off must guide setpoint selection.

The observed structural and stability changes arise from three coupled effects: the heat-capacity increase from H_2O lowers peak temperatures, reactant dilution reduces the available O-atom pool and slows reaction rates, and third-body and radical-pool effects reduce steady-state H/OH concentrations. In addition to these thermochemical mechanisms, steam injection also introduces a momentum source that modifies the local flow field. At sufficiently high steam velocities this jet momentum can alter the recirculation zones that anchor the flame, change the shear layer structure, and shift the location of heat release. These combined thermal, chemical, and aerodynamic effects produce the measured NO suppression while also modifying burning velocity and anchoring. Practically, side injection is effective for targeted NO reduction but demands conservative steam limits for high-methane operation, whereas axial steam injection causes more uniformly distributed dilution and achieves robust NO reduction with fewer CO and unburned-fuel penalties and can expand the operating envelope for high hydrogen fraction systems.

11.2. Recommendations

Improvements

While the present campaign produced consistent and meaningful results, several practical improvements could enhance accuracy and reproducibility if the work were repeated. These recommendations focus on instrumentation, measurement reliability, and experimental procedure.

Steam delivery accuracy. The steam generator used in this study required separate calibration because its specifications only provided electrical input power rather than output flow. Future work would benefit from generators with documented or adjustable steam mass flow rates, reducing the need for indirect estimation. Steam lines could be heated in further experimentation to minimize condensation losses and verify the effect of water vapor on the emission reduction.

Measurement robustness. The ABB AO2020 analyzer proved reliable for NO, CO, CH_4, CO_2, and O_2, but NO_2 readings were strongly affected by water interference. Using a gas analysis system designed to better handle wet exhaust conditions would improve reliability and allow NO and NO_2 to be measured with confidence. While time-consuming, routine calibration checks during runs would further reduce day-to-day variability.

Diagnostics for flame structure The present imaging employed an OH^* narrowband filter (narrowband chemiluminescence), which provided useful qualitative maps of the luminous reaction zone and lift-off behavior. To obtain spatially resolved, quantitative flame structure, planar laser diagnostics are recommended. OH-PLIF can resolve the radical field and attachment surfaces, and NO-LIF can provide local NO concentration fields. Combining these planar measurements with PIV and synchronized high-speed imaging would permit direct separation of thermal, dilution, and chemical effects and support model validation.

Campaign design. Standardizing the stabilization time and measurement duration for each operating point would improve comparability and reduce variability between nominally identical runs. Replicates should be performed on the same day where possible to minimize sensitivity to ambient conditions.

Data handling. Results would be easier to compare and interpret if all measurement and imaging data were archived with consistent metadata, including stabilization times, analyzer settings, and camera exposure parameters.

Axial air injection with axial steam injection. The current axial configuration did not allow simultaneous axial air injection with axial steam injection due to hardware limitations. Modifying the steam delivery system, for example by adding heated metallic lines, condensate traps, and one-way valves, would enable both to operate together. This would allow a direct comparison of side versus axial strategies under equivalent aerodynamic staging, clarifying whether differences in NO suppression arise from steam distribution alone or from combined staging effects.

Further Research

Beyond practical improvements, several directions for further study could expand the findings of this work and address open questions regarding steam injection in hydrogen-based combustion.

Injection strategy. The current experiments compared side and axial steam injection, but results were not conclusive on which approach offers the greatest suppression potential. A broader parametric study, including combinations of axial steam with axial air staging, is needed to isolate aerodynamic from dilution effects and to clarify how location influences flame stability and emissions.

Operating conditions. All tests were carried out at atmospheric pressure and relatively modest thermal loads. Extending the work to elevated pressures, higher power densities, and preheated air would bring the conditions closer to gas turbine practice and reveal how steam dilution performs under realistic engine settings.

Suppression mechanisms. This thesis focused on emissions, with only qualitative imaging of the flame front. Future campaigns should combine emission measurements with quantitative diagnostics, such as laser-based temperature fields, species concentrations, planar OH-LIF, and planar NO-LIF. These tools would help separate the thermal, dilution, and chemical pathways through which steam reduces NO.

Combustion efficiency and stability. While high hydrogen fraction flames tolerated steam without penalties, high methane fraction and mid-blended flames showed trade-offs between NO suppression and complete oxidation. Future studies should investigate blow-off, flashback, and lean stability systematically under steam dilution, to map safe operational windows for practical combustor design. Additionally, adding H_2 measurement to the gas analyzer would provide better insight on the completeness of H_2-rich flames.

Scaling and modeling. The compact laboratory combustor used here likely amplified heat losses and residence-time effects. Computational fluid dynamics (CFD) and detailed chemical-kinetic modeling could extend the present results, helping to generalize the findings to larger combustors. Coupling the models with experimental validation would provide a more complete framework for applying steam injection in engine development.

Residence time effects. Thermal NO formation depends strongly on how long the gases remain in the high-temperature core. The present work suggests that steam alters residence time by lifting flames and redistributing hot zones, but this effect was not quantified. Future studies should employ PIV to resolve the velocity field, which would allow residence time changes to be quantified and linked directly to NO suppression.

References

[1] Hannah Ritchie et al. “Fossil Fuels”. In: *Our World in Data* (2023). URL: https://ourworldindata.org/fossil-fuels.

[2] Natural Resources Defense Council (NRDC). “Fossil Fuels: The Dirty Facts”. In: (2023). URL: https://www.nrdc.org/stories/fossil-fuels-dirty-facts.

[3] ClientEarth. “Fossil Fuels and Climate Change: The Facts”. In: (2022). URL: https://www.clientearth.org/latest/news/fossil-fuels-and-climate-change-the-facts/.

[4] Environmental et al. “Climate, Environmental, and Health Impacts of Fossil Fuels”. In: (2021). URL: https://www.eesi.org/papers/view/fact-sheet-climate-environmental-and-health-impacts-of-fossil-fuels-2021.

[5] International Civil Aviation Organization (ICAO). “Impact of Aviation NOx Emissions on Climate and Air Quality”. In: (2022). URL: https://www.icao.int/environmental-protection/Documents/EnvironmentalReports/2022/ENVReport2022_Art18.pdf.

[6] David S. Lee et al. “Transport impacts on atmosphere and climate: Aviation”. In: *Atmospheric Environment* 44.37 (2010), pp. 4678–4734. DOI: 10.1016/j.atmosenv.2009.06.005. URL: https://www.sciencedirect.com/science/article/pii/S1352231009003574.

[7] Intergovernmental Panel on Climate Change (IPCC). “Hydrogen as a Sustainable Fuel for Aviation”. In: (2022). URL: https://www.ipcc.ch/site/assets/uploads/2018/03/av-en-1.pdf.

[8] U.S. Department of Energy. *Does the use of hydrogen produce air pollutants such as nitrogen oxides?* URL: https://www.energy.gov/eere/fuelcells/does-use-hydrogen-produce-air-pollutants-such-nitrogen-oxides.

[9] M. Keim et al. “Flame stabilization and flashback behaviour of hydrogen–air flames in a generic swirl combustor”. In: *Combustion and Flame* 162.9 (2015), pp. 3249–3263. DOI: 10.1016/j.combustflame.2015.05.018.

[10] Pratt & Whitney. *Pratt & Whitney Launches Hybrid Steam Injected, Intercooled Turbine Engine (HySIITE) Project*. https://prattwhitney.com. Accessed: 2025-01-10. 2022.

[11] Stephen R. Turns. *An Introduction to Combustion: Concepts and Applications*. 3rd. McGraw-Hill, 2012.

[12] Irving Glassman et al. *Combustion*. 5th. Amsterdam: Academic Press, 2014.

[13] Chung K. Law. *Combustion Physics*. Cambridge, UK: Cambridge University Press, 2006. DOI: 10.1017/CBO9780511754517.

[14] Gregory P. Smith et al. *GRI-Mech 3.0: An optimized mechanism for methane/natural gas combustion*. https://combustion.berkeley.edu/gri-mech/version30/. Accessed: 2025-10-01. 1999.

[15] Steven Ashley. “Hydrogen-powered aircraft may be getting a lift”. In: *Physics Today* 73.12 (2020), pp. 27–30. DOI: 10.1063/PT.3.4625. URL: https://pubs.aip.org/physicstoday/article/73/12/27/390636/Hydrogen-powered-aircraft-may-be-getting-a.

[16] Airbus. *How to store liquid hydrogen for zero-emission flight*. 2021. URL: https://www.airbus.com/en/newsroom/news/2021-12-how-to-store-liquid-hydrogen-for-zero-emission-flight.

[17] Airbus. *Hydrogen*. 2023. URL: https://www.airbus.com/en/innovation/energy-transition/hydrogen.

[18] The Engineer. *Comment: Addressing the challenges of hydrogen-based aviation*. 2021. URL: https://www.theengineer.co.uk/content/opinion/comment-addressing-the-challenges-of-hydrogen-based-aviation/.

[19] Resources for the Future. *Navigating Sustainable Skies: Challenges and Strategies for Greener Aviation*. 2023. URL: https://www.rff.org/publications/reports/sustainable-aviation-challenges-strategies-policies-for-greener-aviation/.

[20] Thierry Poinsot et al. *Theoretical and Numerical Combustion*. 2nd ed. Philadelphia, PA: R.T. Edwards, Inc., 2005.

[21] S. Matthes et al. “Hydrogen-powered aviation and contrail climate effects”. In: *Atmospheric Environment* 244 (2021), p. 117834. DOI: 10.1016/j.atmosenv.2020.117834.

[22] John H. Seinfeld et al. *Atmospheric Chemistry and Physics: From Air Pollution to Climate Change*. 2nd. John Wiley & Sons, 2006.

[23] World Health Organization. *Ambient Air Pollution: A Global Assessment of Exposure and Burden of Disease*. https://www.who.int/publications/i/item/9789241511353. Accessed 2025-10-02. 2016.

[24] IPCC. *Climate Change 2013: The Physical Science Basis. Contribution of Working Group I to the Fifth Assessment Report of the Intergovernmental Panel on Climate Change*. Ed. by Thomas F. Stocker et al. Cambridge University Press, 2013. DOI: 10.1017/CBO9781107415324.

[25] Sebastian Göke et al. “Influence of Steam Dilution on NOx Formation in Premixed Natural Gas and Hydrogen Flames”. In: *AIAA SciTech Forum (AIAA Paper 2012-1272)*. 2012. DOI: 10.2514/6.2012-1272. URL: https://doi.org/10.2514/6.2012-1272.

[26] Y. B. Zeldovich. “The Oxidation of Nitrogen in Combustion and Explosions”. In: *Acta Physicochimica U.R.S.S.* 21 (1946), pp. 577–628.

[27] Jinje Park et al. “Experimental study on flameless combustion and NO emission with hydrogen-containing fuels”. In: *International Journal of Energy Research* (2022). DOI: 10.1002/er.7324. URL: https://doi.org/10.1002/er.7324.

[28] *Chemical-Kinetic Mechanisms for Combustion Applications (San Diego Mechanism)*. https://web.eng.ucsd.edu/mae/groups/combustion/mechanism.html. Accessed 2025-10-02.

[29] Peter Glarborg et al. “Modeling nitrogen chemistry in combustion”. In: *Progress in Energy and Combustion Science* 67 (2018), pp. 31–68. DOI: 10.1016/j.pecs.2018.01.002.

[30] Yuan Jiang. “Development and Validation of Updated San Diego Mechanism for Combustion Applications”. PhD thesis. University of California, San Diego, 2019. URL: https://escholarship.org/uc/item/6n02n8fc.

[31] Henry J. Curran. “Developing detailed chemical kinetic mechanisms for fuel combustion”. In: *Progress in Energy and Combustion Science* 72 (2019), pp. 1–144. DOI: 10.1016/j.pecs.2018.12.002.

[32] C. P. Fenimore. “Formation of nitric oxide in premixed hydrocarbon flames”. In: *Symposium (International) on Combustion* 13.1 (1971), pp. 373–380. DOI: 10.1016/S0082-0784(71)80039-3.

[33] James A. Miller et al. “Mechanism and modeling of nitrogen chemistry in combustion”. In: *Progress in Energy and Combustion Science* 15.4 (1989), pp. 287–338. DOI: 10.1016/0360-1285(89)90017-8.

[34] IPCC. *Climate Change 2021: The Physical Science Basis. Contribution of Working Group I to the Sixth Assessment Report of the Intergovernmental Panel on Climate Change*. 2021. DOI: 10.1017/9781009157896.

[35] Barbara J. Finlayson-Pitts et al. *Chemistry of the Upper and Lower Atmosphere: Theory, Experiments, and Applications*. San Diego: Academic Press, 2000.

[36] S. M. Correa. “A Review of NO_x Formation Under Gas-Turbine Combustion Conditions”. In: *Combustion Science and Technology* 87.1-6 (1993), pp. 329–362. DOI: 10.1080/00102209208947221.

[37] Arthur H. Lefebvre et al. *Gas Turbine Combustion: Alternative Fuels and Emissions*. 3rd. CRC Press, 2010.

[38] K. Göke et al. "NO_x Emissions of Premixed Hydrogen- and Natural Gas-Fueled Flames with Steam Dilution at Atmospheric Pressure". In: *Journal of Propulsion and Power* 28.2 (2012), pp. 280–287. DOI: 10.2514/1.B34284.

[39] R. W. Anderson et al. "The Effects of Water and Steam Injection on NO_x Emissions from Gas Turbines". In: *Journal of Engineering for Gas Turbines and Power* 123.1 (2001), pp. 190–196. DOI: 10.1115/1.1338940.

[40] Pratt & Whitney. *Alternative Fuel — HySIITE*. https://www.prattwhitney.com/en/future-of-flight/alternative-fuel. Accessed 3 October 2025. 2025.

[41] Moshe Matalon. "Intrinsic Flame Instabilities in Premixed and Nonpremixed Combustion". In: *Annual Review of Fluid Mechanics* 39 (2007), pp. 163–191. DOI: 10.1146/annurev.fluid.38.050304.092153.

[42] Norbert Peters. *Turbulent Combustion*. Cambridge University Press, 2000.

[43] James F. Driscoll. "Turbulent Premixed Combustion: Flamelet Structure and Its Effect on Turbulent Burning Velocities". In: *Progress in Energy and Combustion Science* 34.1 (2008), pp. 91–134. DOI: 10.1016/j.pecs.2007.04.002.

[44] Shuguo Shi et al. "Cellular structures of laminar lean premixed H_2/CH_4/air polyhedral flames". In: *Applications in Energy and Combustion Science* 13 (2023), p. 100105. DOI: 10.1016/j.jaecs.2022.100105.

[45] Halit Kutkan. *Modelling Turbulent Premixed CH_4/H_2/air Flames with Effects of Stretch, Heat Loss and Non-unity Lewis Number for Flame Stabilization and Dynamics*. Preprint on ResearchGate. DOI proxy on RG: 10.13140/RG.2.2.17990.65603. 2023. URL: https://www.researchgate.net/publication/371667075_Modelling_Turbulent_Premixed_CH4H2air_Flames_with_Effects_of_Stretch_Heat_Loss_and_Non-unity_Lewis_Number_for_Flame_Stabilization_and_Dynamics.

[46] Longjuan Ji et al. "Structure and thermoacoustic instability of turbulent swirling lean premixed methane/hydrogen/air flames in a model combustor". In: *International Journal of Hydrogen Energy* 60 (2024), pp. 890–901. DOI: 10.1016/j.ijhydene.2024.02.162.

[47] Ravi K. Bompelly. "Lean Blowout and Its Robust Sensing in Swirl Combustors". PhD thesis. Atlanta, GA: Georgia Institute of Technology, 2013. URL: http://hdl.handle.net/1853/47529.

[48] Martin Kröner et al. "Flashback Limits for Combustion Induced Vortex Breakdown in a Swirl Burner". In: *Journal of Engineering for Gas Turbines and Power* 125.3 (2003), pp. 693–700. DOI: 10.1115/1.1568121.

[49] Bonnie J. McBride et al. *Coefficients for Calculating Thermodynamic and Transport Properties of Individual Species*. Tech. rep. NASA/TP-4513. Cleveland, OH: NASA Glenn Research Center, 1996. URL: https://ntrs.nasa.gov/citations/19940013151.

[50] B. Ashok, ed. *NOx Emission Control Technologies in Stationary and Automotive Internal Combustion Engines: Approaches Toward NOx Free Automobiles*. English. Amsterdam: Elsevier, 2022. DOI: 10.1016/C2020-0-01213-2.

[51] Eugenio Giacomazzi et al. "Hydrogen Combustion: Features and Barriers to Its Exploitation in the Energy Transition". In: *Preprints* (2023). Not peer-reviewed. DOI: 10.20944/preprints202309.1834.v1. URL: https://doi.org/10.20944/preprints202309.1834.v1.

[52] D. R. Dowdy et al. "The use of expanding spherical flames to determine burning velocities and stretch effects in hydrogen/air mixtures". In: *Symposium (International) on Combustion*. Vol. 23. Elsevier, 1991, pp. 325–332.

[53] O. Kwon et al. “Flame/stretch interactions of premixed hydrogen-fueled flames: measurements and predictions”. In: *Combustion and Flame* 124 (2001), pp. 590–610. DOI: 10.1016/S0010-2180(00)00213-8.

[54] S. D. Tse et al. “Morphology and burning rates of expanding spherical flames in H_2/O_2/inert mixtures up to 60 atmospheres”. In: *Proceedings of the Combustion Institute*. Vol. 28. 2000, pp. 1793–1800. DOI: 10.1016/S0082-0784(00)80578-2.

[55] M. Kuznetsov et al. “Flammability limits and laminar flame speed of hydrogen–air mixtures at sub-atmospheric pressures”. In: *International Journal of Hydrogen Energy* 37 (2012), pp. 17580–17588. DOI: 10.1016/j.ijhydene.2012.08.068.

[56] Anupam Ghosh et al. “Laminar burning velocity of hydrogen, methane, ethane, ethylene, and propane flames at near-cryogenic temperatures”. In: *Applications in Energy and Combustion Science* 12 (2022), p. 100094. DOI: 10.1016/j.jaecs.2022.100094. URL: https://www.sciencedirect.com/science/article/pii/S2666352X2200094.

[57] R. T. E. Hermanns et al. “Laminar burning velocities of methane–hydrogen–air mixtures”. Submitted to *Combustion and Flame*. 2007.

[58] M. Goswami et al. “The effect of elevated pressures on the laminar burning velocity of methane+air mixtures”. In: *Combustion and Flame* 160 (2013), pp. 1627–1635. DOI: 10.1016/j.combustflame.2013.02.002.

[59] A. Mazas et al. “Effects of water vapor addition on the laminar burning velocity of oxygen-enriched methane flames”. In: *Combustion and Flame* 158 (2011), pp. 2428–2440. DOI: 10.1016/j.combustflame.2011.05.014.

[60] M. Metghalchi et al. “Laminar Burning Velocity of Propane–Air Mixtures at High Temperature and Pressure”. In: *Combustion and Flame* 38 (1980), pp. 143–154. DOI: 10.1016/0010-2180(80)90046-2. URL: https://james-keck-memorial-collection.unibs.it/JCKeck-papers/MetghalchiKeck-CombustionFlame-38-143-1980.pdf.

[61] M. Ó Conaire et al. “A comprehensive modeling study of hydrogen oxidation”. In: *Combustion and Flame* 139.1-2 (2004), pp. 1–24. DOI: 10.1016/j.combustflame.2004.06.017.

[62] Michael P. Burke et al. “Comprehensive H_2/O_2 kinetic model for high-pressure combustion”. In: *International Journal of Chemical Kinetics* 44.7 (2012), pp. 444–474. DOI: 10.1002/kin.20603.

[63] Riccardo Concetti et al. “On the Chemical Effect of Steam Addition to Premixed Hydrogen Flames with Respect to NO_x Emissions and Flame Speed”. In: *Flow, Turbulence and Combustion* 113 (2024), pp. 519–534. DOI: 10.1007/s10494-024-00551-5.

[64] Ivan Langella et al. “Flashback Prevention in a Hydrogen-Fueled Reheat Combustor by Water Injection Optimized With Global Sensitivity Analysis”. In: *Journal of Engineering for Gas Turbines and Power* 147.6 (2025), p. 061021. DOI: 10.1115/1.4066895.

[65] Cheng Lu et al. “The effects of N_2 and steam dilution on NO emission for a H_2/Air micromix flame”. In: *International Journal of Hydrogen Energy* 47 (2022), pp. 27266–27278. DOI: 10.1016/j.ijhydene.2022.06.050.

[66] Katharina Goeckeler. “Mitigation of NO_x Emissions from Dry Low Emission Combustion with Hydrogen-Enriched Natural Gas Using Steam Injection”. MA thesis. Technische Universität München, 2021.

[67] P. Stathopoulos et al. “Emissions of a Wet Premixed Flame of Natural Gas and a Mixture with Hydrogen at High Pressure”. In: *Proceedings of ASME Turbo Expo 2016: Turbomachinery Technical Conference and Exposition*. GT2016-57745. Seoul, South Korea, June 2016. DOI: 10.1115/GT2016-57745.

[68] Stephan Eugen Maximilian Lellek. “Pollutant Formation in Premixed Natural Gas Swirl Flames with Water Injection”. Fakultät für Maschinenwesen, Lehrstuhl für Thermodynamik. PhD thesis. Garching, Germany: Technische Universität München, Oct. 2017.

[69] A. Farokhipour et al. “A numerical study of NOx reduction by water spray injection in gas turbine combustion chambers”. In: *Fuel* 212 (2018), pp. 173–186. DOI: 10.1016/j.fuel.2017.10.033.

[70] Rolls-Royce NASA Glenn Research Center Boeing. *Water Injection on Commercial Aircraft to Reduce Airport NOx Emissions*. Tech. rep. NASA/TM-2010-216807. Accessed: 2025-01-30. NASA Glenn Research Center, 2010. URL: https://ntrs.nasa.gov/api/citations/20100021949/downloads/20100021949.pdf.

[71] Marco Novelo et al. “Experimental Investigation of Gas Turbine Compressor Water Injection for NOx Emission Reductions”. In: *Journal of Engineering for Gas Turbines and Power* 141.4 (2019), p. 041020. DOI: 10.1115/1.4043292. URL: https://asmedigitalcollection.asme.org/gasturbinespower/article/141/4/041020/368630/Experimental-Investigation-of-Gas-Turbine.

[72] Mohammad Zahid. “Impact of Water Injection on Emissions of Nitrogen Oxides from Aircraft Engines”. Accessed: 2025-01-30. Master’s Thesis. Massachusetts Institute of Technology (MIT), 2022. URL: https://dspace.mit.edu/handle/1721.1/143907.

[73] A. Mohamed et al. “Exploring the Benefits of Hydrogen-Water Injection Technology in Internal Combustion Engines: A Path Towards NOx Reduction and Efficiency Improvement”. In: *International Journal of Hydrogen Energy* 49.3 (2024), pp. 1137–1152. DOI: 10.1016/j.ijhydene.2023.11.041. URL: https://www.sciencedirect.com/science/article/pii/S0360319923026456.

[74] Puyan Xu et al. “Effects of direct water injection on engine performance in a hydrogen (H_2)-fueled engine at varied amounts of injected water and water injection timing”. In: *International Journal of Hydrogen Energy* 45 (2020), pp. 13523–13534. DOI: 10.1016/j.ijhydene.2020.03.011.

[75] A. Dhyani et al. “NOx and Backfire Control in a Hydrogen Spark Ignition Engine Using Water Injection and EGR”. In: *Energy Conversion and Management* 188 (2019), pp. 314–327. DOI: 10.1016/j.enconman.2019.03.056. URL: https://www.sciencedirect.com/science/article/pii/S0196890419302411.

[76] P. Novella et al. “Numerical Assessment of Water Injection in Medium-Duty Hydrogen Engines: Performance and NOx Reduction Analysis”. In: *Applied Thermal Engineering* 234 (2024), p. 120980. DOI: 10.1016/j.applthermaleng.2024.120980. URL: https://www.sciencedirect.com/science/article/pii/S1359431124000394.

[77] Scott Londerville et al. “Water/Steam Injection for NOx Reduction in Process Burners”. In: *Journal of Combustion Science and Technology* 190 (2018), pp. 45–62. DOI: 10.1080/00102202.2018.1452019. URL: https://www.tandfonline.com/doi/full/10.1080/00102202.2018.1452019.

[78] Sarah Link et al. *Vertical Combustor Manual - Swirl Stabilized Flame*. Version 3.0. Internal operating manual, Delft University of Technology. Dec. 2023.

[79] U.S. Department of Energy, National Energy Technology Laboratory. *Lean premixed combustion design for low NOx emissions in gas turbines*. Lean premix combustion produces lower NOx than diffusion flame technology (see §3.2.1.2 in the Gas Turbine Handbook). 2005. URL: https://netl.doe.gov.

[80] Sarah Link et al. “Experimental analysis of dual-fuel (CH_4/H_2) capability in a partially-premixed swirl stabilized combustor”. In: *International Journal of Hydrogen Energy* 101 (2025), pp. 427–437. DOI: 10.1016/j.ijhydene.2024.12.286. URL: https://doi.org/10.1016/j.ijhydene.2024.12.286.

[81] P. Sayad et al. “Experimental investigation of the stability limits of premixed syngas–air flames at two moderate swirl numbers”. In: *Combustion and Flame* 164 (2016), pp. 270–282. DOI: 10.1016/j.combustflame.2015.11.026. URL: https://doi.org/10.1016/j.combustflame.2015.11.026.

[82] Iacopo La Ferla. “Water Injection in a Swirl-Stabilized Hydrogen Burner: Flame Behavior and Emission Characteristics”. Supervised by Dr. Arvind Gangoli Rao and Dr. Sarah Link. Master’s Thesis. Delft, The Netherlands: Delft University of Technology, 2023.

[83] Sarah Link. *Stability Regime of the Vertical Combustor Excel Data Sheet*. 2023.

[84] Fabrizio Reale et al. “Effects of Steam Injection on the Permissible Hydrogen Content and Gaseous Emissions in a Micro Gas Turbine Supplied by a Mixture of CH_4 and H_2: A CFD Analysis”. In: *Energies* 15.8 (2022), p. 2914. DOI: 10.3390/en15082914.

[85] Unknown et al. “Investigating the Impact of Steam Enhancement on ...” In: *ASME Journal of Gas Turbines and Power* 147.1 (2024), p. 011001. DOI: 10.1115/1.1203032.

[86] Iacopo La Ferla et al. *Risk Inventarisation and Evaluation: Water Droplets Spray System*. TU Delft Internal Document. Version 1, dated 26-01-2024. HSL Compressor Hall, 2024.

[87] ABB Measurement & Analytics. *AO2000 Continuous Gas Analyzers — Data Sheet*. DS/AO2000-EN Rev. C. 2021.

[88] ABB Measurement & Analytics. *AO2000 Continuous Gas Analyzers — Operating Instructions*. OI/AO2000-EN Rev. B. 2021.

[89] ABB Measurement & Analytics. *Magnos28 — Paramagnetic Oxygen Measurement*. Product notes/technical description. 2018.

[90] ABB Measurement & Analytics. *AO2000 Continuous Gas Analyzers — Commissioning Instructions*. CI/AO2000-EN Rev. C. 2021.

[91] Raymond L. Speth et al. *Cantera: An Object-Oriented Software Toolkit for Chemical Kinetics, Thermodynamics, and Transport Processes*. Version 3.0.0. Cantera. 2024. URL: https://cantera.org.

[92] Esfahanian Vahid et al. “Laminar flame speed correlations for methane, ethane, propane and their mixtures and natural gas and gasoline for spark-ignition engine simulations”. In: *Fuel* 194 (2017). Accessed via ResearchGate, pp. 528–540. DOI: 10.1016/j.fuel.2017.01.017. URL: https://www.researchgate.net/publication/318794643_Laminar_flame_speed_correlations_for_methane_ethane_propane_and_their_mixtures_and_natural_gas_and_gasoline_for_spark-ignition_engine_simulations.

[93] Alberto Frassoldati et al. “Optimal Reduction of the C1-C3 Combustion Mechanism for the Simulation of Flaring”. In: *Combustion and Flame* 157.7 (2010). Accessed via ResearchGate, pp. 1364–1371. DOI: 10.1016/j.combustflame.2009.12.013. URL: https://www.researchgate.net/publication/230794366_Optimal_Reduction_of_the_C1-C3_Combustion_Mechanism_for_the_Simulation_of_Flaring.

[94] Yan Wang et al. “A Comprehensive Review on Fluid Dynamics and Transport of Suspension/Liquid Droplets and Particles in High-Velocity Oxygen-Fuel (HVOF) Thermal Spray”. In: *Progress in Materials Science* 77 (2016). Accessed via ResearchGate, pp. 118–204. DOI: 10.1016/j.pmatsci.2015.09.002. URL: https://www.researchgate.net/publication/282817619_A_Comprehensive_Review_on_Fluid_Dynamics_and_Transport_of_SuspensionLiquid_Droplets_and_Particles_in_High-Velocity_Oxygen-Fuel_HVOF_Thermal_Spray.

[95] International Civil Aviation Organization. *Annex 16 to the Convention on International Civil Aviation, Volume II: Aircraft Engine Emissions*. Definitions of EI, carbon-balance method, corrections. 2023.

[96] *ARP1533: Gas Turbine Engine Exhaust Emissions Measurement and Sampling Procedures*. Aerospace Recommended Practice. Data reduction and EI calculation (carbon-balance). SAE International, 2014.

[97] Federal Aviation Administration. *Advisory Circular 34-1B: Aircraft Engine Emissions Data Reductions and Reporting*. Tech. rep. Defines EI, handling of wet/dry, converter efficiency, reference corrections. 2011.

[98] *ISO 11042-1: Gas Turbines — Exhaust Gas Emission — Measurement and Evaluation*. International Standard. Stack/flow route and EI from rates; terminology. International Organization for Standardization, 1996.

[99] Environment and Climate Change Canada. *Guidelines for the Reduction of Nitrogen Oxide Emissions from Natural Gas-Fired Stationary Combustion Turbines*. Tech. rep. Sets output-based NO_x

limits in g/GJ of energy output. Government of Canada, 2017. URL: https://www.canada.ca/content/dam/eccc/documents/pdf/cepa/CEPA-Guidelines-CombustionTurbines-2-en.pdf.

[100] Environment Agency (UK). *Pollution Inventory Reporting – Combustion Activities Guidance*. https://www.gov.uk/government/publications/pollution-inventory-reporting-guidance-notes/combustion-activities-pollution-inventory-reporting. Emission factors reported in g/GJ of fuel energy input. 2023.

[101] European Environment Agency. *EMEP/EEA Air Pollutant Emission Inventory Guidebook 2023 – Combustion in Energy Industries (1.A.2)*. Provides default NO_x emission factors in g/GJ for multiple combustion categories. European Environment Agency, 2023. URL: https://www.eea.europa.eu/publications/emep-eea-guidebook-2023/part-b-sectoral-guidance-chapters/1-energy/1-a-combustion/1-a-2-combustion-in.

[102] U.S. Environmental Protection Agency. *Compilation of Air Pollutant Emission Factors (AP-42), Volume I: Stationary Point and Area Sources – Chapter 1: External Combustion Sources*. Tech. rep. Reports NO_x emission factors in g/GJ for propane, natural gas, and fuel oil combustion. U.S. EPA, 2018. URL: https://www.epa.gov/air-emissions-factors-and-quantification/ap-42-compilation-air-emission-factors.

[103] U.S. Environmental Protection Agency. *Method 19—Determination of Sulfur Dioxide Removal Efficiency and Particulate Matter, Sulfur Dioxide, and Nitrogen Oxides Emission Rates*. https://www.epa.gov/emc/method-19-determination-so2-removal-efficiency-and-so2-nox-emission-rates. Accessed: 2025-09-01. 2017.

[104] Environmental Protection Agency, Ireland. *Air Guidance Note AG3: Guidance on the Use of Continuous Emissions Monitoring Systems*. https://www.epa.ie/publications/compliance--enforcement/air/air-guidance-notes/AG13-CEMS-Guidance_.pdf. Accessed: 2025-09-01. 2018.

[105] U.S. Environmental Protection Agency. *Gas Turbine Emission Test Procedures and Performance Standards*. https://www.epa.gov/stationary-sources-air-pollution/gas-turbine-compliance-emission-testing. Accessed: 2025-09-01. 2016.

[106] European Commission. *Best Available Techniques (BAT) Reference Document for Large Combustion Plants (LCP BREF)*. Tech. rep. Accessed: 2025-09-01. Joint Research Centre, 2017.

[107] M. J. Rubleski et al. “Chemical Kinetic Study of Nitrogen Oxides Formation”. In: *Journal of Chemistry* 2012.898742 (2012). Discusses thermal NO formation via the Zeldovich mechanism and its strong sensitivity to flame temperature, pp. 1–15. DOI: 10.1155/2012/898742.

[108] M. Abian et al. “Formation of NO from N_2/O_2 mixtures in a flow reactor”. In: *Combustion Processes* (2015). States that thermal NO or Zeldovich mechanism remains the most important source of NO in gas combustion.

[109] Calqlata. *Steam (thermal properties) | entropy enthalpy volume*. Accessed: 2025-09-18. URL: https://www.calqlata.com/Science/Steam.html.

[110] Sarah Link et al. “Impact of hydrogen enrichment and air injection strategies on lean swirl-stabilized flames”. In: *International Journal of Hydrogen Energy* 50.6 (2025), pp. 1133–1147. DOI: 10.1016/j.ijhydene.2025.01.015.

[111] Federico Concetti et al. “Influence of axial air injection on swirl-stabilized hydrogen-methane flames”. In: *Combustion and Flame* 258 (2024), p. 112783. DOI: 10.1016/j.combustflame.2024.112783.

[112] A. R. Choudhuri et al. “Intermediate radical concentrations in hydrogen–natural gas flames”. In: *International Journal of Hydrogen Energy* 29.8 (2004), pp. 823–832. DOI: 10.1016/S0360-3199(03)00140-4.

[113] Sarah Link et al. “Experimental and numerical investigation of mixing in a partially premixed CH_4/H_2 combustor”. In: *International Journal of Hydrogen Energy* 141 (2025), pp. 176–192. DOI: 10.1016/j.ijhydene.2025.05.070.

[114] Kaushal A. Dave et al. “Kerosene–H_2 blending effects on flame properties in a multi-fuel combustor”. In: *Fuel Communications* 23 (2025), p. 100139. DOI: 10.1016/j.jfueco.2025.100139.

[115] Robert J. Kee et al. *CHEMKIN-II: A Fortran Chemical Kinetics Package for the Analysis of Gas-Phase Chemical Kinetics*. Tech. rep. SAND89-8009B. Sandia National Laboratories, 1989. DOI: 10.2172/5685759.

[116] Prateek Jain et al. “NO_x and CO emissions from lean premixed H_2/CH_4 combustion with steam dilution”. In: *Applied Energy* 345 (2023), p. 120357.

[117] Cheng Yu et al. “NO_x Emission Characteristics of Hydrogen-Enriched Lean Premixed Methane Flames with Steam Addition”. In: *International Journal of Hydrogen Energy* 46.18 (2021), pp. 10544–10556.

[118] R. Vasudevan et al. “NO_x emissions of turbulent jet flames: effects of jet diameter, fuel, and nozzle configuration”. In: *Combustion and Flame* 150.1–2 (2007), pp. 67–85.

[119] Mao Li et al. “Influence of the Steam Addition on Premixed Methane Air Combustion at Atmospheric Pressure”. In: *Energies* 10.7 (2017), p. 1070. DOI: 10.3390/en10071070.

[120] S. Göke et al. “Limits of Flame Stability and Emissions in Lean Premixed Methane Combustion under Dilution Effects”. In: *Journal of Engineering for Gas Turbines and Power* 136.3 (2014), p. 031502. DOI: 10.1115/1.4025805.

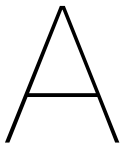
[121] C. Tao et al. “Effects of superheated steam on combustion instability and NOx emissions in a model lean premixed gas turbine combustor”. In: *Fuel* 288 (2021), p. 119646. DOI: 10.1016/j.fuel.2020.119646.

[122] Sebastian Göke et al. “Influence of steam dilution on the combustion of natural gas and hydrogen in premixed and rich-quench-lean combustors”. In: *Fuel Processing Technology* 107 (2013), pp. 14–22. DOI: 10.1016/j.fuproc.2012.07.032.

[123] Panagiotis Stathopoulos et al. “Emissions of a Wet Premixed Flame of Natural Gas and a Mixture with Hydrogen at High Pressure”. In: *Journal of Engineering for Gas Turbines and Power* 139.4 (2017), p. 041507. DOI: 10.1115/1.4034687. URL: https://doi.org/10.1115/1.4034687.

[124] Katharina Göckeler et al. “Laminar Burning Velocities and Emissions of Hydrogen–Methane–Air–Steam Mixtures”. In: *Journal of Engineering for Gas Turbines and Power* 137.3 (2015), p. 031503. DOI: 10.1115/1.4028460. URL: https://doi.org/10.1115/1.4028460.

[125] Joint Committee for Guides in Metrology (JCGM). *Evaluation of measurement data – Guide to the expression of uncertainty in measurement (GUM)*. Technical Note NIST TN-1297. See Section 5 on combining standard uncertainties. Gaithersburg, MD, USA: National Institute of Standards and Technology (NIST), 2000. URL: https://emtoolbox.nist.gov/publications/nisttechnicalnote1297s.pdf.



Appendix: Additional Document

Risk Inventarisation and Evaluation

Steam Injection System / HSL Compressor Hall

Risk Inventarisation and Evaluation

1 Object information

Location of Setup	HSL Compressor Hall
Location Responsible (TRA Matrix)	
Location Type	Tunnel Hall
Device or setup name	Steam Injection System

2 Document information

Status	**Not authorized for use**
Start date	02-06-2025
Version	1
Version date	25-05-2025
Replaces version	N/A
Location of Authorised hardcopy	Wind Tunnel Archives
Distribution list (Scan By email)	Author Coördinator Windtunnels LSO (if applicable) Technical Staff Archive

3 Officials

Coördinator Windtunnels	Henk-Jan Siemer
RI&E Author	Doruk Çelebi
Location Responsible	Henk-Jan Siemer, Adam Head
LSO	Dennis
Designated Users	Doruk Çelebi, Francesca De Domenico, Kaushal Dave, Alam Garciduenas, Sarah Link, Andre' Silva Correia

4 Authorisation

Author RI&E	**Coördinator Windtunnels**	**LSO**
	Date, paraf	*Date, paraf*

5 Equipment fixed setup

The goal of this experiment is to inject steam into Ch4-H2 flames to experimentally validate the theoretical prediction of NOx reduction via the addition of steam to the flame.

The modified experimental setup is based on the swirl combustion CH4 – H2 and the kerosene spray system developed in 2023 by Kaushal Dave. The current setup is used in combination with a different arrangement.

The experimental installation is housed in the HSL Compressor Hall. The configuration includes a swirl-stabilized burner assembly, air supply line, and a single steam generator (1 kW electric unit) positioned on a stable, elevated platform. This platform is non-conductive and located away from walkways to avoid splash or trip hazards. This platform is located under the exhaust hood. While a second identical steam generator is available to extend the steam flow range, only one unit is installed and operational in the standard configuration. The second unit will only be connected temporarily if required for specific tests.



Figure 1 Steam Generator to be used

There are 2 potential configurations present for the steam injection experimental set-up. First configuration, which is the default set-up, involves the steam to be mixed with the axial air injection before the combustor, where later the steam/axial air mixture is injected into the combustion chamber through the centre of the base plate/combustion platform. In the second configuration, the steam flow is directed into 2 separate flows where each flow is directed to the sides of the combustion platform. This aims to introduce “injection location” variable into the experiment, where this second configuration theoretically aims the steam towards the flame reaction zone, where the majority of NOx production occurs. The two set-ups have slightly different configurations, which they will be explained in detail below:

1. **Axial Air – Steam Injection Configuration**

In this first configuration, the steam is conveyed via a heat-resistant silicone hose extending from the generator. This hose is connected via a fixed T-union to the axial air-line. To mitigate the risk of thermal degradation of the original PVC air-line, the section of the air line where steam is introduced has been replaced with thermally insulated metal piping. The metal section begins upstream of the T-junction and continues to the combustor inlet to handle elevated temperatures caused by the steam-air mixture.

The combined air-steam flow is directed to the combustor through additional insulated metal tubing, securely fixed along its path using clamps and brackets. All piping, including the silicone and metal sections, is routed in a manner that avoids sharp bends or mechanical stress, with special attention given to strain relief near the steam injection junction.

Heat insulators are used to ensure that the heated pipes are not heating up the surrounding tubes.

A simplified schematic of the relevant steam connections for the 1st configuration is presented below:

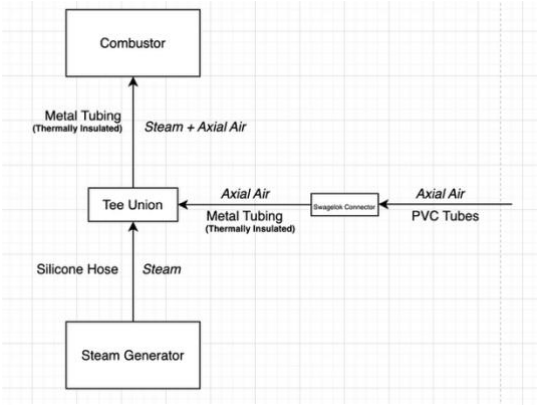


Figure 2 Simplified Schematics of Steam Connection 1st Configuration

Combustion occurs in a partially enclosed chamber constructed of borosilicate glass and metal framing, which serves both as a containment structure and optical access area for diagnostics. The chamber is supported on a rigid platform equipped with heat shielding and exhaust venting to ensure safe dispersion of combustion products.

Instrumentation, including thermocouples, pressure sensors, and any optical diagnostics (e.g., PLIF or OH* chemiluminescence cameras), are mounted either externally the ATEX zone or under the hood on fixed stands or shielded brackets and do not interfere with operator access or hose routing. Electrical cables are routed overhead or along cable trays and kept away from floor areas prone to condensation or foot traffic.

All components in the setup, while technically removable, are treated as fixed for the duration of the experimental campaign and are immobilized through supports or platform constraints to ensure operational stability and personnel safety.

One natural concern one may have with this set-up is the backpropagation of steam into the fuel line, which will cause a potential danger of combustion of the fuel early in the fuel line. However, this current system has been previously extensively tested without the steam injection into the axial air line, and no backpropagation of air into the fuel line or backpropagation fuel into the axial air line is observed. Since the steam will be injected into the axial air line, this subsequently implies that no steam can backpropagate into the fuel line or vice versa. Consequently, this also implies no water condensation is possible in the fuel lines.

All steam line fittings, including hose barbs, unions, and metal tubing connectors, are made of stainless steel to prevent corrosion and maintain mechanical integrity under thermal cycling.

The bottom figure displays the simplified schematic diagram of the modified steam injection system for the 1st configuration.

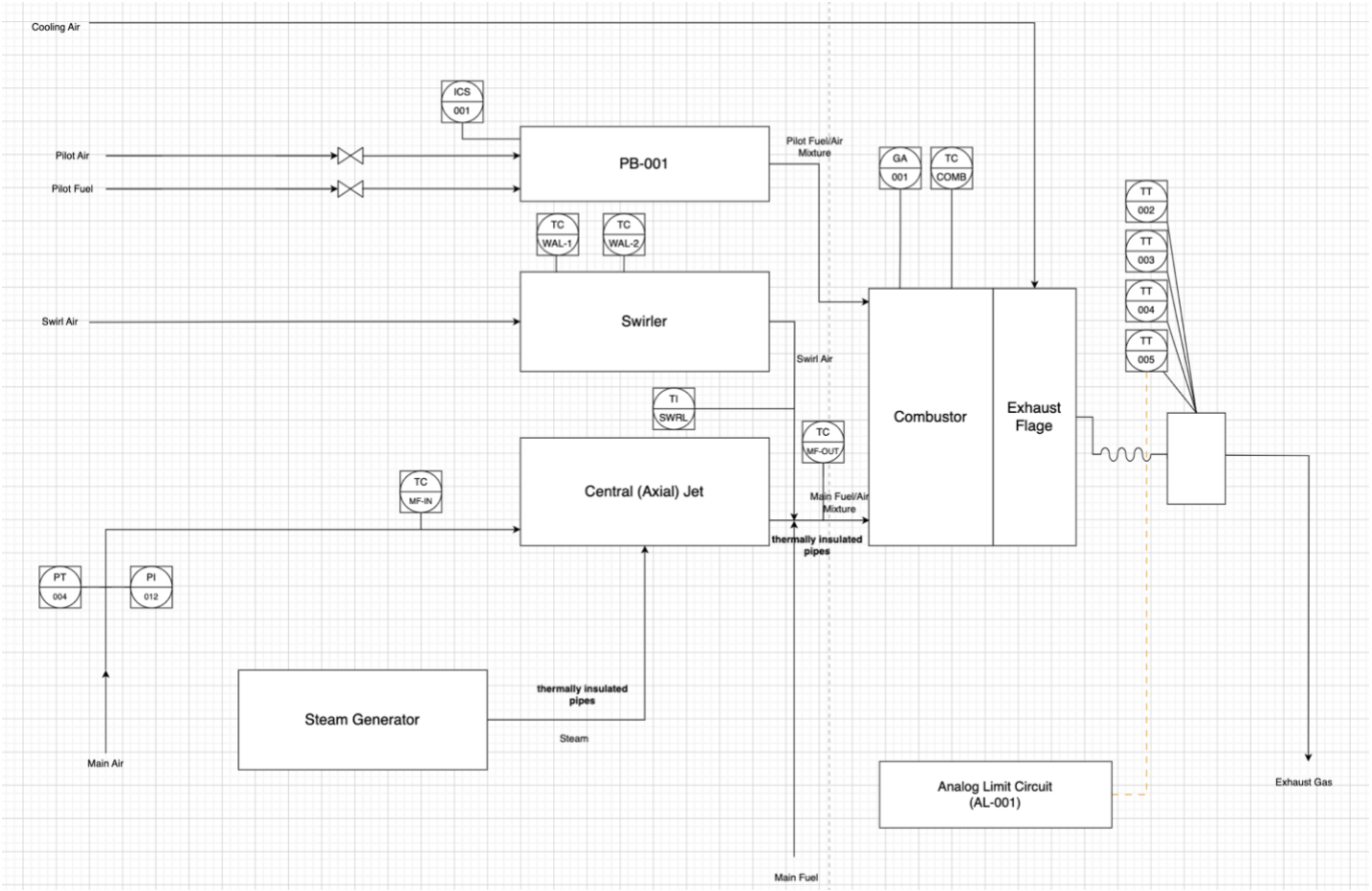


Figure 3 P&ID Lab Set-up 1st Configuration

2. Side Position Steam Injection Configuration

In the second configuration, the steam is injected directly into the combustion chamber through 2 nozzles attached to the sides of the base plate. The steam is emitted through the steam generator into the heat-resistant silicone hose, which is connected to a tee union through a hose barb and hose clamps. The other 2 ends of the tee union are connected to metal piping through tube fitting. Then the metal tubes are connected to the injector which is connected to the base plate at the locations indicated on the image on the right.

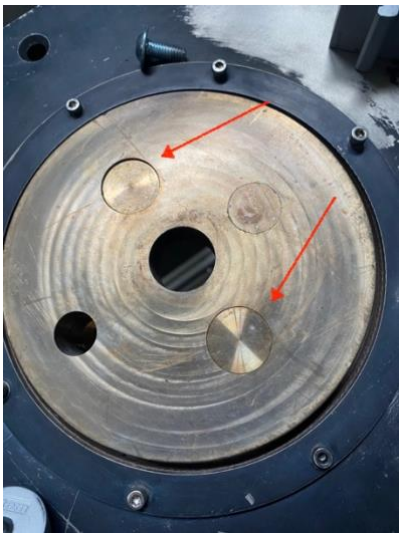


Figure 4 Combustion Base Plate

The only difference of this second configuration takes place in the piping of the steam system which is described above. The rest of the system is identical to the specifications described in configuration 1. Additionally, there are no differences between the operational procedures of the 2 configurations.

A simplified schematic of the relevant steam connections for the 2nd configuration is presented below:

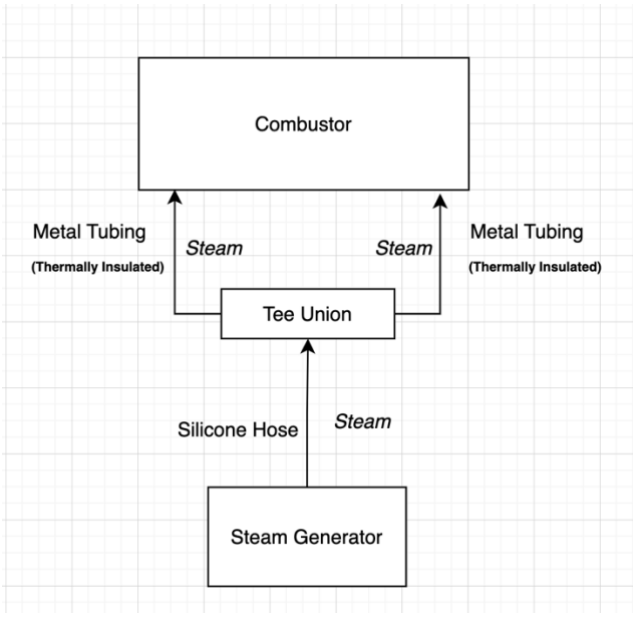


Figure 5 Simplified Schematic of Steam Connections 2nd Configuration

The bottom figure displays the simplified schematic diagram of the modified steam injection system for the 2nd configuration.

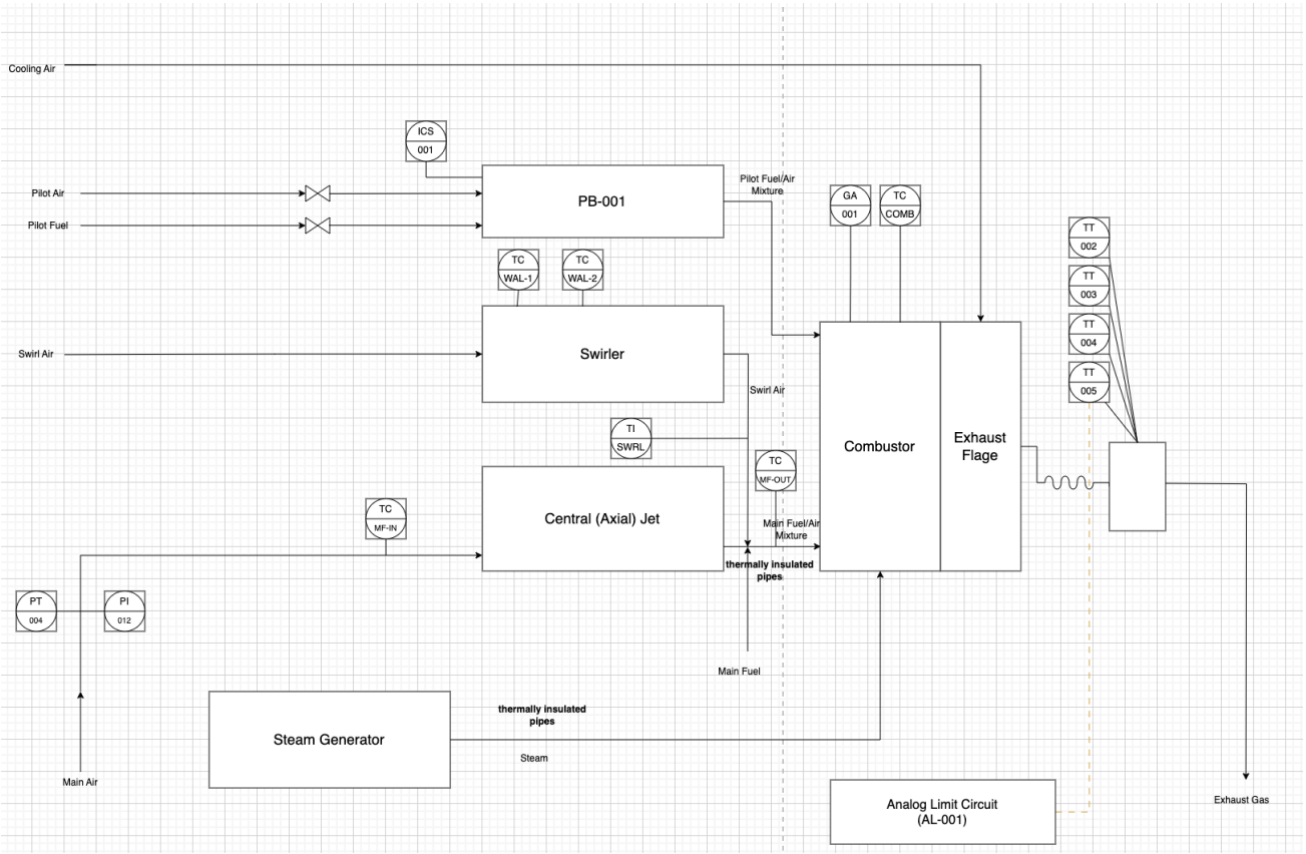


Figure 6 P&ID Lab Set-up 2nd Configuration

6 Non-reactive commissioning of the experiment

The system has already been characterised as a stand-alone system in the IRIS room. Before performing the combustion experiment, a cold-flow testing in the combustion setup will be performed to check the mechanical integrity of the parts. All assumptions regarding steam temperature, mass flow rate, and condensation behavior have been previously validated in isolated tests. Final validation in the combustor environment is part of the cold-run commissioning process.

COMMISSIONING OF SYSTEM FROM THE AAI SIDE

1) Mounting of the system: all the connections will be tested with air to ensure that they are leak free
2) Removal and shielding of all electronics around the steam generator to ensure that, in case of any leaks
3) Cold air will be passed through the Axial air system in small steps (10 lpm – 20 lpm – 30 lpm – 40 lpm – 50 lpm) to the maximum nominal level of AAI expected in the combustor. Visual inspection of the system will be carefully made to ensure that the system is functioning correctly
4) Remote switching of the steam system.
5) Switching off after 5 minutes to verify that there is no accumulation of water in the line. If successful, proceed repeat for 10 and 15 minutes provided that the chamber does not fill with water.
6) Continuous monitor of temperature with thermocouples

COMMISSIONING OF SYSTEM FLASH MOUNTED ON THE PLATE

1) Mounting of the system: all the connections will be tested with air to ensure that they are leak free
2) Removal and shielding of all electronics around the steam generator to ensure that, in case of any leaks
3) Initialisation of AAI
4) Remote switching of the steam system.
5) Switching off after 5 minutes to verify that there is no accumulation of water in the line. If successful, proceed repeat for 10 and 15 minutes provided that the chamber does not fill with water.
6) Continuous monitor of temperature with thermocouples

7 Setup description / processes at the site

The experiment is conducted in the HSL Compressor Hall, where a hydrogen combustion setup has been modified to allow the injection of steam into the axial air stream upstream of the combustor. The goal is to study the effect of steam dilution on flame temperature and NO_x emissions. A single 1 kW electric steam generator is used to deliver saturated steam at atmospheric pressure to the axial air-line. The process involves the following phases:

1. **Preparation and Filling Phase**
   Before operation, the steam generator is filled manually with up to 3 L of distilled water. Filling is performed while the unit is powered off and fully cooled. The generator is checked

for cable integrity and correct grounding. Any residual water in the silicone hose is drained, and thermocouples and data acquisition systems are activated. The behaviour of the system has already been tested outside of the combustor.

2. **Steam Generation and Preheating**
   Before ignition, the steam generator is powered on and allowed to heat up. The warm-up period typically takes 5 minutes, during which the generator builds internal temperature and begins producing visible steam at the outlet. This phase is required to ensure that the generator is ready to deliver steam promptly when reactivated later in the sequence. Once a consistent steam flow is observed at the end of the silicone hose, the steam generator is turned off temporarily. This pause prevents premature cooling of the combustion zone during ignition and ensures a stable flame establishment.

   The steam hose remains connected during this phase, and the system is monitored for any signs of steam leakage or excessive condensation. The axial air line section where steam is injected is made of thermally insulated metal piping to tolerate residual heat and any trace steam remaining in the system.
3. **Combustor Operation**
   Following the preheating phase, hydrogen and air flows are activated and adjusted to achieve the desired equivalence ratio. The combustion process is initiated using the existing ignition system, and the flame is stabilized under dry (non-steamed) conditions. Once a stable flame is achieved, the steam generator is turned back on, and steam injection is resumed. The previously warmed-up unit ensures rapid delivery of steam into the axial air-line.

   The steam-air mixture is conveyed through insulated metal piping and enters the combustor via the central axial inlet. As steam is introduced gradually, the effect on flame structure and emissions is observed. Combustor operation is visually monitored throughout, and advanced diagnostics such as PLIF and OH* chemiluminescence imaging may be used to analyse flame response. Thermocouples track the temperatures at key points along the steam line and combustor surfaces during this phase.
4. **Observation and Data Acquisition**
   During combustion, the system is operated under steady-state conditions. All temperature, pressure from the gas rack, as well as exhaust gas measurements and optical diagnostic data are recorded. The effect of steam on flame structure and emissions is observed in real time and/or post-processed. Two operator presence is mandatory at all times during combustion, with immediate access to emergency shutdown protocols. Emergency shut down protocol is the same of the swirl burner, since the presence of steam flowing through the chamber without the flame does not create any issue. Once the flame is shut down, the steam generator could be turned off. It is also important to note that the injection of steam into the combustor does not interfere with the normal operation of the gas analyser, as water is an allowed species for the equipment.
5. **Shutdown Phase**
   After each test run, hydrogen and air flows are shut down, and the flame is extinguished. The steam generator is turned off and allowed to cool before any handling or refill operations. All equipment is powered down in an orderly manner, and surface temperatures are checked before dismantling any part of the system. Steam condensation is wiped from exposed surfaces, and the floor is inspected and dried to avoid slipping hazards.

The laboratory is equipped with a ventilation system that provides continuous air exchange. Operator actions are limited to outside of the heat-affected zone and are coordinated with the lab supervisor when needed. No refilling or servicing of the steam generator is allowed while it is hot or in operation. All processes are executed according to standard operating procedures and monitored in real time.

Prior to full operation, a commissioning procedure will be carried out to verify system functionality and safety. This includes dry tests of the steam routing and silicone hose integrity using inert gas or low-temperature water vapor (already performed), with verification of thermocouple and data logging function, and a cold flow test of the steam-air injection path into the combustor without ignition. Once leak-free operation and stable steam delivery are confirmed, a live flame test with minimal hydrogen flow will be performed to observe system behavior under real conditions before starting the full experimental campaign. Since the research aims to assess how steam affects NO_x formation via both thermal and chemical mechanisms, the use of optical diagnostics such as PLIF and OH* chemiluminescence is essential. Therefore, the investigation of characteristic radicals such as OH and NO is crucial to confirm or refute the hypothesized reduction mechanisms. To these, the author refers to the risk assessment of the LIF system.

Non-standard components used in this setup:

- 1 kW electric steam generator (non-lab standard model)
- Heat-resistant silicone hose (custom routed for steam delivery)
- OH* chemiluminescence camera
- PLIF optics and filters
- Gas analyser for exhaust species

As a reference, a simplified schematic of the lab set-up with respect to the physical placements of the components is drawn and presented below:

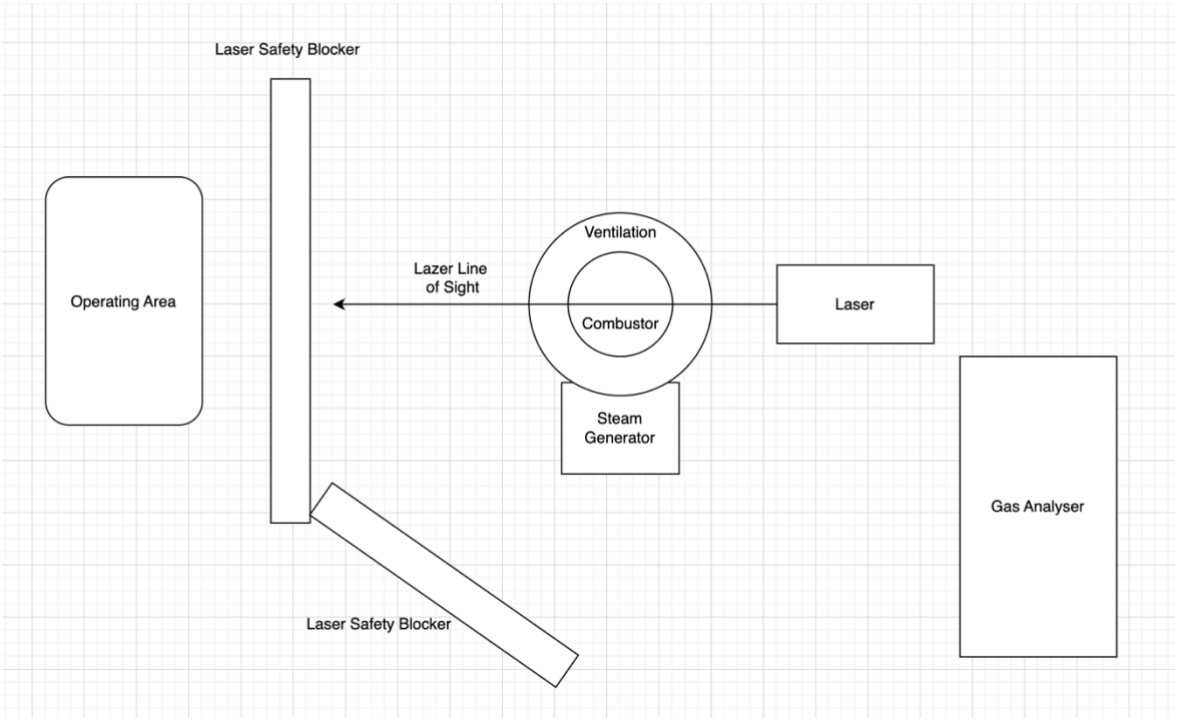


Figure 7 Schematic of the Lab During Operation

8 Risk groups and sources

Applicable risk group	No	Yes	Measure number
Juveniles, <18 years	X		
Elderly, >55 years	X		
Pregnant	X		
Disabled	X		
Foreigners (Language)		X	1,2
Asbestos	X		
Chrome-6	X		
PFAS	X		
CO2	X		
Lead	X		
Biological agentia	X		
Dangerous goods or substances in general	X		
Deviation of regular working hours	X		
Working with dangerous chemicals at home	X		
Physical load		X	3,4
Sound		X	5,6
Imaging Screens / monitors	X		
Ionising radiation	X		
Non-Ionising radiation	X		
Explosion Hazard *(either in use or storage)*		X	7,8
High Temperatures		X	8,9, 31
Low Temperatures	X		
Aggressive Chemicals (Either in use or storage)	X		
Toxic substances (Either in use or storage)	X		
Bacteria, parasites and fungi (Either in use or storage)	X		
Radiation (e.g. Laser, Röntgen, EMC but also visible light)		X	10,11,12,13
Mechanical violence		X	8, 14
Electrical hazards / risks		X	15, 33
Large scale experiments		X	16
Noise and vibrations		X	5,6
Long-term repetitive movements (RSI)	X		
Danger of crushing or cutting		X	3,17,18
Working at height / risk of falling		X	30
Use of hoisting equipment	X		

Describe the detailed safety precautions / measures per measure number in chapter 10

9 Risks due to external circumstances

Subject	No	Yes	Measure number
Power failure		X	19,20
Water supply or drain failure	X		
Gas or compressed air supply failure		X	19,21
Ventilation failure		X	22
Control failure mechanical or electrical		X	19,22
Clogged equipment or samples		X	23, 32
Equipment or sample leakage or rupture		X	24,25,26,31,32
Change of reaction conditions or recipe	X		
Transport and storage failure of sample or output	X		

Subject	No	Yes	Measure number
Fill and drain failure	X		
Startup process failure		X	27,28,29
Shutdown process failure		X	28
Drain and clean after use		X	30
Discard and storage by-products	X		

Describe the detailed safety precautions / measures per measure number in chapter 10

10 Safety judgement of author

	Standards and measures		Standard Operating Procedures / PPM
X	Meets low voltage standard	X	Safety goggles mandatory
X	Meets machine directive	X	Hearing protection mandatory
X	Meets EMC directive	X	Safety clothing mandatory
X	Protection against unauthorized personelle	X	Safety shoes mandatory
X	Adequate Ventilation		Others mandatory (note all applicable)
X	Adequate fire detection / protection	X	Clean any spillage or condensation
X	Lighting		
X	Emergency Lighting		
X	Emergency escapes		
X	Measures from chapter 10 adequate	X	Mandatory signing in place (Laser, Radio-active, etc)
X	Heat-resistant gloves		
X	Safety goggles (thermal and laser rated)		
X	Lab coat with long sleeves		

11 Detailed description of all safety and control measures from 7, 8 and 9.

Nr.	Description	Action owner	Due date	Finalised
1	Erroneous communication can lead to accidents Write all documentation in English	Doruk Çelebi		
2	Erroneous communication can lead to accidents Provide all communication in English	Doruk Çelebi		
3	Heavy lifting can cause injuries Lift any heavy loads using your legs, not your back	Doruk Çelebi		
4	Heavy lifting can cause injuries Use the crane for any loads that are too heavy (>23 kg). Always request help (take it out)	Doruk Çelebi		
5	Loud sounds/noise can cause hearing damage Wear hearing protection during operation	Doruk Çelebi		
6	Loud sounds/noise can cause hearing damage Warn others in the area and have them wear earpads as well	Doruk Çelebi		
7	Always close the ATEX zone in front of the building before operating the combustor	Doruk Çelebi		
8	When the combustor is running, no one is allowed in the ATEX zones and every person present needs to stand behind the protection glass (follow the ATEX guidelines for operating and designing the set-up)	Doruk Çelebi		
9	After the combustor was running, only operate on the combustor (e.g. removing the steel plate) with heavy protection gloves	Doruk Çelebi		
10	Direct/indirect exposure to laser light can cause harm to skin / eyes Operators shall be using laser protective glasses	Doruk Çelebi		

Risk Inventarisation and Evaluation

Nr.	Description	Action owner	Due date	Finalised
11	Direct/indirect exposure to laser light can cause harm to skin / eyes The LASER-ON light shall be turned on. Always let the LSO check the set-up before the first fire	Doruk Çelebi		
12	Direct/indirect exposure to laser light can cause harm to skin / eyes The laser shall be pointing away from the operator on eye-level	Doruk Çelebi		
13	LSO (currently Dennis) shall check the laser arrangement before starting the experiment	Doruk Çelebi		
14	Heavy parts are fixed at the metal frame of the combustor	Doruk Çelebi		
15	Insulate cables and use cable ducts if necessary	Doruk Çelebi		
16	Make use of already existing infrastructure for air and fuel supply	Doruk Çelebi		
17	Injuries(cuts, fractures)to operators When lifting heavy loads, protective gloves will be worn to prevent pinched fingers	Doruk Çelebi		
18	Injuries (cuts, fractures)to operators When using a sharp knife, always cut away from yourself	Doruk Çelebi		
19	Damage to the setup or injured operators Close the valve regulating the fuel flow - Shut down the laser	Doruk Çelebi		
20	Gas and fuel supply have integrated power failure mechanism for the combustion hood.	Doruk Çelebi		
21	Damage to the setup or injured operators Press the emergency button, this will stop the main gas supply (from outside) and manually shutdown the laser	Doruk Çelebi		
22	Immediately shut down the experiments when detecting a ventilation malfunction	Doruk Çelebi		
23	Damage to the setup or injured operators from erroneous setup operation Prior to the system assembly ensure injector orifice is free from visible impurities	Doruk Çelebi		
24	Damage to equipment or injured operators In case of rupture of any tubes from the manual valve should be immediately closed and the liquid medium drained.	Doruk Çelebi		
25	Damage to the setup or injured operators from erroneous setup operation - Prior to the system assembly if possible remove electronic and corrosion sensitive equipment and components. Ensure that pipes are at a sufficient distance from equipment sensitive to water. Leak tests with air the lines at lower pressure before operating at high pressure.	Doruk Çelebi		
26	Damage to the setup or injured operators In case of a loss of pressure, close the respective valve	Doruk Çelebi		
27	Damage to the setup or injured operators Stop start-up sequence in case one step is not fulfilled	Doruk Çelebi		
28	Have a proper start-up and shut-down philosophy in place	Doruk Çelebi		

Nr.	Description	Action owner	Due date	Finalised
29	Always plan a HAZOP of the set-up with trained personal after building up the set-up	Doruk Çelebi		
30	Check for water/steam leakages and slippery surfaces Ensure no water/steam leakage occurs during operation. Ensure floor is dry before, during, and after each run.	Doruk Çelebi		
31	Steam contact can cause skin burns or eye irritation Wear heat-resistant gloves and safety goggles. Avoid standing near steam hose.	Doruk Çelebi		
32	Unexpected overpressure in silicone hose Steam system is to remain unpressurized; inspect hose before every use and never obstruct outlet.	Doruk Çelebi		
33	Power and water interaction risk Place steam generator on elevated dry surface. RCD protection must be confirmed before each test.	Doruk Çelebi		

12 Attachments

Nr.	Description

B

Appendix B: Steam Generator Characterization Experiment

The steam generator has controllable time and power settings. It also arrives with a remote controller to control the settings, which is very convenient as getting close to the combustor during its operation is extremely dangerous. The steam generator has 9 power settings, from the lowest power setting 1 to the highest power setting of 9. However, no documentation was available on the difference between different power settings. Knowing amount of steam mass flow rate injected into to combustor is very important to characterize the effect of steam injection, so it was necessary to quantify the mass flow rates of steam and the temperature of steam at each different power setting. To achieve this, a side experiment was conducted to characterize performance of the steam generator. An experimental set-up was created outside the building to safely emit the steam. There were no available steam mass flow readers for such a small device and flow rate, so alternate methods to determine the mass flow rate were required. As a solution, the steam generator was filled with water and put on a scale. The device was turned on and after about 10 minutes of warm-up time, the device began to emit steam. An overview of the set-up is presented below in Figure B.1:

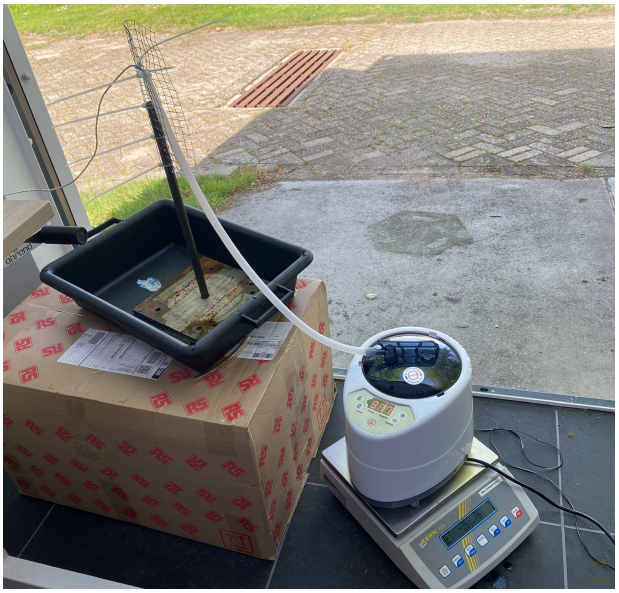


Figure B.1: Experimental set-up to characterize the performance of the steam generator

A K-Type thermometer from RS (1319A) was placed at the exit of the silicone hose. This was done to determine the potential temperature drop of the steam due to heat loss as it passes through the 40cm long silicone hose.



Figure B.2: Placement of the thermometer on the silicone hose



Figure B.3: K-Type thermometer 1319A

The scale used was from Kern with an uncertainty of 0.02 grams. However, due to the nature of the experiment the actual uncertainty of the mass readings were higher. The readings were done in 5 minute intervals for each power setting, and the starting and end weight measurements were noted down. As the measurements for the weights had to be done through human observation for a constantly changing measurement value, it is assumed that the uncertainties for the start and end weight readings to be ± 1 grams.

The steam generator was tested beginning at power setting 9, the highest available setting. After the first visible release of steam, a short stabilization period was required before a steady flow could be observed. At this point, the initial weight of the steam generator (filled with water) was recorded, and after 5 minutes of operation the final weight was measured. This procedure was repeated nine times for each power setting. During testing, it was noted that some phase change effects in the silicone tubing led to minor condensation, particularly at lower power settings. Since any condensed liquid water would remain at approximately $100°$C, this effect did not alter the steam temperature itself but could reduce the effective steam mass flow rate delivered to the combustor. The influence of condensation became more noticeable at power settings 8 and below, where intermittent droplets were observed at the hose outlet. To mitigate these losses, insulation sleeves were added to the steam line, which significantly reduced visible condensation. Nevertheless, at and below power setting 5 the generator consistently produced excessive liquid water carryover, making these settings unsuitable and unreliable for the main experimental campaign. As a result, only power settings 9 through 6 were selected for further use.

It was observed that during power setting 8, the steam generator was emitting minuscule amount of water at times due to heat losses in the silicone tubing. The effect was more visible in power 7 and 6, as the power setting decreased. During the testing, it was observed that at and below power setting 5, the steam generator emitted large amounts of water, which was deemed unsuitable and unreliable for the purpose of the main experiment. Hence, it was decided that only power settings 9 through 6 were to be used in the experimental campaign.

The method for the calculation of the steam mass flow rate is given below in Equation B.1:

$$\dot{m}_{steam}[g/min] = \frac{M_{start} \pm 1[g] - M_{end} \pm 1[g]}{time} = \frac{M_{start} \pm 1[g] - M_{end} \pm 1[g]}{5[min]} \tag{B.1}$$

The results for the steam generator performance characterization is given in Table B.1. It was also found during the testing that the steam generator emitted steam at a constant temperature of $100°C$ at power settings through 9 to 6. It was deduced that the heat losses through the silicone tube only had an effect on the phase change of the steam, and not the temperature of the steam or even the condensed water inside

the tube. To validate this the temperature of the condensed water was measured and found to be between $100°C$ and $99.5°C$, which is within the error range of the thermometer.

Calculated Steam Mass Flow Rate [g/min ± 0.4]										
Steam Power	**Run 1**	**Run 2**	**Run 3**	**Run 4**	**Run 5**	**Run 6**	**Run 7**	**Run 8**	**Run 9**	**Average**
Steam 9	24.1	24.5	24.0	23.8	24.4	24.6	24.7	24.6	24.5	24.4
Steam 8	20.5	23.0	23.1	22.6	24.3	23.2	24.0	22.8	22.0	22.8
Steam 7	15.3	16.4	19.2	18.6	18.2	19.8	16.5	17.6	17.4	17.7
Steam 6	13.2	13.9	13.7	14.0	13.5	13.2	13.8	14.1	13.7	13.7

Table B.1: Calculated steam mass flow rates for the power settings of the steam generator

However, it can be observed from Table B.1 that the values are not consistent in each run. Due to this spread of values, the total uncertainty of the average must be refined more. To estimate the uncertainty in a measured quantity based on repeated trials, both the instrumental (systematic) uncertainty and the repeatability (random) uncertainty should be considered in the final average steam mass flow rate value.

Let $x_1, x_2, \ldots, x_n$ be n independent measurements of the same quantity. The sample mean is computed as:

$$\bar{x} = \frac{1}{n} \sum_{i=1}^{n} x_i \tag{B.2}$$

The sample standard deviation s, which quantifies the spread of the individual measurements, is given by:

$$s = \sqrt{\frac{1}{n-1} \sum_{i=1}^{n} (x_i - \bar{x})^2} \tag{B.3}$$

To quantify the uncertainty associated with the mean value due to this spread, the standard error of the mean is used:

$$u_{\text{rep}} = \frac{s}{\sqrt{n}} \tag{B.4}$$

Combining the systematic uncertainty u_{measure} and the random uncertainty u_{rep}, the total uncertainty for the steam mass flow rates can be determined. Assuming the two sources of uncertainty are independent, the combined uncertainty is calculated using the root-sum-square (RSS) method [125]:

$$u_{\text{total}} = \sqrt{u_{\text{rep}}^2 + u_{\text{meaure}}^2} \tag{B.5}$$

The final reported result is:

$$x = \bar{x} \pm u_{\text{total}} \tag{B.6}$$

This method ensures that both the random variability of the repeated trials and the limitations of the measurement technique are taken into account in the total uncertainty estimation. The calculations and the results of this methodology is given below in Table B.2:

Steam Power	Mean [g/min]	Std. Dev. [g/min]	Std. Error u_{rep}	Total Uncertainty u_{total}
Steam 9	24.4	0.31	0.10	0.4
Steam 8	22.8	1.1	0.37	0.6
Steam 7	17.7	1.4	0.48	0.6
Steam 6	13.7	0.32	0.11	0.4

Table B.2: Uncertainty analysis for steam mass flow rate measurements

With this calculation, the mass flow rate of the steam generator corresponding to each power setting has been defined.

Steam Power	Mass Flow Rate [g/min]
Steam 9	24.4 $\pm$0.4
Steam 8	22.8 $\pm$0.6
Steam 7	17.7 $\pm$0.6
Steam 6	13.7 $\pm$0.4

Table B.3: Steam mass flow rates at different power settings